THE GEOCHEMISTRY OF CENOZOIC BASALTS AND PERIDOTITE XENOLITHS FROM HANNUOBA REGION, EASTERN CHINA: IMPLICATION FOR THEIR PETROGENESIS AND SUBCONTINENTAL MANTLE HETEROGENEITY

by

YAN SONG

B.S. CHANGCHUN GEOLOGY INSTITUTE
(1975)

M.S. BOSTON COLLEGE
(1983)

SUBMITTED TO THE DEPARTMENT OF EARTH ATMOSPHERIC, AND PLANETARY SCIENCES IN PARTIAL FULFILLMENT OF THE REQUIREMENTS FOR THE DEGREE OF

DOCTOR OF PHILOSOPHY

at the
MASSACHUSETTS INSTITUTE OF TECHNOLOGY

Signature of Author_____
Department of Earth Atmospheric, and Planetary Sciences

Certified by_____
Fred A. Frey
Thesis Supervisor

Accepted by_____
Chairman, Department Committee on Graduate Students

THE GEOCHEMISTRY OF CENOZOIC BASALTS AND PERIDOTITE XENOLITHS FROM HANNUOBA REGION, EASTERN CHINA: IMPLICATION FOR THEIR PETROGENESIS AND SUBCONTINENTAL MANTLE HETEROGENEITY

by
YAN SONG

SUBMITTED TO THE DEPARTMENT OF EARTH ATMOSPHERIC, AND PLANETARY SCIENCES, IN PARTIAL FULFILLMENT OF THE REQUIREMENTS FOR THE DEGREE OF DOCTOR OF PHILOSOPHY

ABSTRACT

The Cenozoic Hannuoba basaltic province, 200 km northwest of Beijing, China, is composed of intercalated tholeiitic, transitional and alkalic basalts. Although the alkalic basalts contain abundant upper mantle xenoliths, they range in MgO content from 5.7 to 10.6% MgO. Most of the major and trace element abundance variations in the alkalic basalts can be explained by segregation of a clinopyroxene-rich assemblage containing significant amounts of garnet and minor Fe-Ti oxides. Incompatible element abundances and Sr-Nd-Pb isotope compositions in these alkalic basalts are remarkably similar to those of alkalic basalts from oceanic islands. Obviously, there is a world-wide source for alkalic basalts that can be tapped in oceanic and continental settings.

Compared with Hannuoba alkalic basalts of similar MgO content Hannuoba tholeiitic lavas have lower incompatible element abundances, and different incompatible element abundance ratios (e.g., Ba/La, La/Sm, Sm/Nd, Zr/Nb and Zr/Hf). However, these tholeiitic lavas are not anomalously depleted in Nb and Ta; therefore, they are not similar to arc basalts and many continental flood basalts. Although radiogenic isotope data (Sr, Nd and Pb) show that the alkalic and tholeiitic lavas are isotopically distinct, variations in incompatible element abundances and abundance ratios in all lava types define coherent trends suggestive of a mantle mixing process.

The alkalic and tholeiitic lavas from the Hannuoba region formed from different mantle sources. The alkali basalts were generated by small degrees of partial melting of asthenosphere, perhaps a PREMA component, whereas the tholeiites were generated by partial melting of an enriched component (EMI-like) in the oceanic mantle. Subsequent contamination in the lower crust may have occurred. The enriched component may have resided in the upwelling

asthenosphere or subcontinental crust lithosphere. Mixing between the PREMA and EMI-like mantle components created the linear trends of radiogenic isotopic ratios defined by Hannuoba lavas. This mixing between mantle components may have occurred during the rifting event that caused extension in northeast China ~40my ago; that is, uprising asthenosphere may have caused rifting and the partial melting of continental lithosphere. The proximity of upwelling asthenosphere and heated, former continental lithosphere enabled mixing of isotopically diverse components. This proposal is consistent with the transition from dominantly alkalic to dominantly tholeiitic volcanism at Hannuoba.

Based on geochemical studies of six anhydrous spinel peridotite xenoliths in basanites, the upper mantle beneath Hannuoba, eastern China is compositionally heterogeneous. These samples range in Sr and Nd isotopic ratios from MORB-like to near bulk-earth estimates. The low $^{87}Sr/^{86}Sr$ and high $^{143}Nd/^{144}Nd$ xenoliths contain the largest amount of a basaltic component (e.g., CaO and Al_2O_3), but they are relatively depleted in light rare earth elements compared to chondrites. Other xenoliths have U-shaped chondrite-normalized REE patterns.

Trace element and radiogenic isotopic data for the peridotite require enrichment processes acting on depleted mantle. Constraints on these processes are: (a) inverse correlations between basaltic constituents, such as CaO and Al_2O_3, and La/Sm, and (b) samples most depleted in CaO and Al_2O_3 have the highest $^{87}Sr/^{86}Sr$ and lowest $^{143}Nd/^{144}Nd$. These trends can be explained by a model whereby garnet peridotite zoned in isotopic composition undergoes partial melting. Because of a gradient in degree of melting, e.g., from the wall-rock contact to hotter interior, or as a function of depth in a diapir, melts initially segregate from regions where the degree of melting is high. Subsequently the recently created residues are infiltrated by slower segregating incipient melts. Preferential mixing of these incipient melts with residues from high degrees of melting can explain the observed complex geochemical trends seen in Hannuoba and many other peridotite xenolith suites. Clinopyroxene-rich veins in some of the peridotites may reflect pathways of ascending melt.

Thesis Supervisor: F.A. Frey, Professor of Geochemistry

ACKNOWLEDGEMENTS

First, I would like to express my deep gratitude to my advisor, Fred Frey, for his scientific insight, guidance and his patience, and his willingness to discuss anything with me whenever I walked in his office. His helpful advice and constant support throughout my graduate years at M.I.T has been invaluable to me. This thesis would never have been completed without his enormous help. I greatly benefited from the privilege of being his graduate student.

I am also grateful to Stan Hart for allowing me to spend three years in his isotope laboratory, and for his interesting and helpful discussions regarding my study.

I benefited from discussions with T. Grove and N. Shimizu. I also would like to thank S.-S. Sun for his continuous thoughtful discussions and his willingness to help during the writing of this thesis. Thanks go to K. Hodges for being on both my generals and thesis committees.

I express my gratitude to J. Dostal, T. Grove, S. Hart, J. Rhodes and N. Shimizu for the use of their laboratories. I thank D. Hickmott and V. Salters for collecting the clinopyroxene REE and TE data by ion-probe, and D. Gerlach for obtaining REE data in two samples by isotope dilution.

I thank my past and present office-mates: A. Leinbach (who also has been my analytical cohort for RNAA analyses), P. Gurriet, R. Kinzler and D. Silverberg for their friendship, and willingness to spend much of their valuable time to help me. I thank K. Bartels, J. Blusztajn, T. Furman, L. Gulen, R. Hickey, T. Juster, A. Kennedy, Y. Lu, O. Navon and T. Sisson for their help during my research.

I also thank my Chinese colleagues: X. Zhi who has been my co-worker for Chapter 1 while he was a Visiting Scientist at MIT; J.L. Zheng for his collaboration during my field trips to the Hannuoba region. I was also significantly aided by B. Cong and R. Zhang.

Thanks to S. Recca for help with the microprobe and computer problems, and thanks to K. Burrhus for maintaining the mass specs, and P. ILa for maintaining the INAA lab. Thanks to Ms. N. Hearst for correcting my English.

This thesis has benefitted from constructive review comments by F. Albarede, D. Gerlach, B.M. Jahn, M. Menzies, N. Shimizu, S.-S. Sun, and especially detailed comments by T. Grove, S. Hart, M.F. Roden and A. Zindler.

Finally, but not least important, I thank my husband, Jiansheng Jin, who has shared my life in the U.S., for his constant support and deep understanding when I needed it most during these years. Thanks for editing and help with computer problems, and also thanks for taking all the responsibilities for taking care our son during the last few weeks (except for cooking). I also deeply thank my dear parents for their understanding and for taking care of my young son for the first four years I studied in America. I also thank my lovely son for excusing his mother for being so busy these past years that he hasn't yet had the chance to visit Disneyland.

TABLE OF CONTENTS

ABSTRACT 2
ACKNOWLEDGEMENTS 4
TABLE OF CONTENTS 6
LIST OF FIGURES 9
LIST OF TABLES 11

INTRODUCTION 13
Geologic Setting of Cenozoic Basalts of China 13
Geology and Petrology of the Cenozoic Basalts of Northeastern China 14
Geology of Hannuoba Basalts and Purpose of This Study 15
FIGURES 17

Chapter 1
Major and Trace Element Geochemistry of Hannuoba Basalts, Eastern China
Constraints on the Origin of Continental Alkalic and Tholeiitic Basalt 22

1-1. INTRODUCTION 23
1-2. GEOLOGIC SETTING AND SAMPLING 24
1-3. SAMPLE PREPARATION AND ANALYTICAL PROCEDURES 25
1-3.1. Sample Preparation 25
1-3.2. Analytical Methods 25
1-4. BASALT TYPES AND STRATIGRAPHY OF HANNUOBA LAVAS 26
1-4.1. Normalized Data 26
1-4.2. Classification and Stratigraphy 27
1-5. MACROSCOPIC AND PETROGRAPHIC CHARACTERISTICS 28
1-5.1. Alkalic Basalts 28
1-5.2. Tholeiitic Basalts 29
1-5.3. Transitional Basalts 30
1-5.4. Summary 30
1-6. GEOCHEMICAL RESULTS 31
1-6.1. Major and Minor Oxide Compositions 31
1-6.2. Trace Element Abundances - Rare Earth Elements (REE) 32
1-6.3. Trace Element Abundances - Incompatible Elements 33
1-6.4. Trace Element Abundances - Compatible Elements 34
1-7. DISCUSSION 35
1-7.1. Origin and Evolution of the Mantle Xenolith-Bearing Alkalic Basalts 35
1-7.2. Origin of Compositional Range from Tholeiitic to Alkalic Basalt 41
1-7.3. Geochemical Constraints on the Mantle Source of Hannuoba Lavas 44
1-8. CONCLUSIONS 49
TABLES 51
FIGURES 72

CHAPTER 2
GEOCHEMISTRY OF MEGACRYSTS IN HANNUOBA ALKALI BASALTS
EVIDENCE FOR HIGH-PRESSURE FRACTIONAL
CRYSTALLIZATION 97

2-1. INTRODUCTION 98
2-2. MEGACRYST AND BASANITE DESCRIPTION 101
2-3. CHEMICAL COMPOSITIONS OF MEGACRYSTS and HOST
BASANITE 103
2-4. IMPLICATIONS OF THE MEGACRYST COMPOSITIONS 106
2-5. EVALUATION OF FRACTIONAL CRYSTALLIZATION FOR
THE HANNUOBA ALKALI BASALTS 110
2-5.1. Major Element Modelling 111
2-5.2. Trace Element Modelling 114
2-6. CONCLUSIONS 115
TABLES 116
FIGURES 128

Chapter 3
Isotopic Characteristics of Hannuoba Basalts
Implications for their Petrogenesis and the
Composition of Subcontinental Mantle 134

3-1. INTRODUCTION 135
3-2. ANALYTICAL TECHNIQUES 137
3-3. RESULTS 138
3-4. DISCUSSION 140
3-4.1. Summary of Geochemical Characteristics 140
3-4.2. Evidence For Mixing 142
3-4.3. Endmember Components Represented in
Hannuoba Alkalic Basalts 144
3-4.4. Endmember Components Represented in
Hannuoba Tholeiitic Basalts 144
3-4.5. Proposed Petrogenetic Model for Hannuoba
Lavas 153
3-4.6. Plate Tectonic Interpretations of the
Origin of the Hannuoba Basalts 157
TABLES 160
FIGURES 166

Chapter 4
Geochemistry of Peridotites in Basalt from Hannuoba
Implications for Subcontinental Mantle
HeterogeneitY 182

4-1. INTRODUCTION 183
4-2. GEOLOGICAL SETTING 184
4-3. PETROGRAPHY 185
4-4. SAMPLE PREPARATION AND ANALYTICAL TECHNIQUES 187
4-4.1. Sample Preparation 187

4-4.2. Analytical Techniques 188
4-5. RESULTS 190
4-5.1. Major Elements 190
4-5.2. Trace Elements 191
4-5.3. Radiogenic Isotopes (Sr and Nd) 192
4-5.4. Group II xenoliths 193
4-6. DISCUSSION OF MANTLE PROCESSES 195
4-6.1. Constraints from Whole-Rock Major Element Chemistry 195
4-6.2. Constraints from Mineral Composition 198
4-6.3. Constraints from Trace Element Geochemistry 201
4-6.4. Constraints from Isotope Geochemistry
4-6.5. Timing of Depletion and Enrichment Events in the Subcontinental Mantle 218
4-7. DEVELOPMENT OF A METASOMATIC MODEL 219
4-8. SUMMARY OF CONCLUSIONS 228
TABLE 231
FIGURES 246

REFERENCES 273

Appendix 292
A-1. Classification and Nomenclature 292
A-2. Analytical Techniques 294

LIST OF FIGURES

INTRODUCTION

I-1 Distribution of active volcanism in the western Pacific. 18
I-2 Distribution of Cenozoic basalts in eastern China 19
I-3 Simplified tectonic map of eastern China 20
I-4 Distribution of the Cenozoic basalts and Hannuoba basalts in the North China Fault Block 21

CHAPTER 1

1-1 Geological map of Hannuoba Region. 75
1-2 Five stratigraphic sections through the Hannuoba basaltic plateau. 77
1-3 CIPW normative plot of Hannuoba basalts 78
1-4 Major oxide - MgO variation diagrams of Hannuoba basalts 79
1-5 Chondrite - normalized REE diagram for Hannuoba basalts 80
1-6 La/Yb vs. MgO variation diagrams of Hannuoba basalts 81
1-7 Incompatible element abundances vs. Th content 82
1-8 MgO and Th versus compatible trace element 83
1-9a Ni/Co versus MgO for Hannuoba basalts 84
1-9b MgO Versus CaO/Al_2O_3, Sc and Yb, Sc Versus Zr/Y 85
1-10a Various incompatible element ratios vs. MgO content 86
1-10b Sm/Nd, La/Ce, Nb/Ta and Zr/Nb versus Th 92
1-11 Geochemical trends of MgO versus Ti/Zr and Zr/Y 93
1-12 Normalized incompatible element diagrams 94
1-13 Ba/Nb - La/Nb plot of Hannuoba basalts and oceanic island basalts 96

CHAPTER 2

2-1 Ca-Mg-Fe components for clinopyroxene megacrysts 129
2-2 Chondrite-normalized REE patterns for Hannuoba garnet and clinopyroxene megacrysts 130
2-3 Ternary plot of end-member proportions for garnet megacrysts 132
2-4 Ternary plot for feldspar megacrysts in the alkaline basalts 133

CHAPTER 3

3-1 Sr-Nd isotope correlation for Hannuoba basalts 168
3-2 $^{143}Nd/^{144}Nd$ versus Sm/Nd for Hannuoba basalts 169
3-3 Pb isotope correlation for Hannuoba basalts 170
3-4 Mg number versus Nd and Sr isotopes 172
3-5 a) Nd-Pb and b) Sr-Pb isotope correlation diagrams 173
3-6 $^{143}Nd/^{144}Nd$ versus 1/Nd and $^{87}Sr/^{86}Sr$ vs. 1/Sr variations for Hannuoba basalts 175
3-7 Ba/Nb versus a) delta 8/4 and b) delta 7/4 176
3-8 $^{143}Nd/^{144}Nd$ versus Sm/Nd and $^{87}Sr/^{86}Sr$ 178

3-9 SiO2 versus Sm/Nd for Hannuoba basalts 180
3-10 Sketched diagram for model A and model B 181

CHAPTER 4
4-1 Variation diagrams of MgO versus CaO, Al_2O_3, Na_2O, TiO_2, FeO and SiO_2 in Hannuoba peridotites 250
4-2 MgO abundances versus Ni, Cr, Sc, V, Ga and Y contents in six Hannuoba peridotites 251
4-3 MgO and CaO abundances versus Sr and La contents in six Hannuoba peridotites 252
4-4 Chondrite-normalized REE diagrams for clinopyroxenes and host peridotites 253
4-5 $^{143}Nd/^{144}Nd$ versus $^{87}Sr/^{86}Sr$ for clinopyroxenes from six Hannuoba peridotites 255
4-6 Comparision diagrams of MgO versus CaO, Al_2O_3, Na_2O, TiO_2, FeO and SiO_2 in Hannuoba GroupI and Group II xenoliths 256
4-7 Comparision diagrams of MgO abundances vs. Ni, Cr, Sc, and Co contents in Hannuoba Group I and Group II inclusions 259
4-8 Chondrite-normalized REE diagrams for Group II inclusions 261
4-9 Variation diagram of whole rock Mg# vs. mineral Mg# 262
4-10 Variation diagram of Na_2O/CaO cpx versus Na_2O/CaO whole rock 262
4-11 Variation diagram of LnK versus 1/T (C^O) for clinopyroxenes from host peridotites and veins 263
4-12 Al_2O_3 contents of coexisting orthopyroxenes and spinels in Hannuoba peridotites 264
4-13 Variation diagram of Sr/Nd versus $^{87}Sr/^{86}Sr$ in Clinopyroxenes and Hannuoba basalts 265
4-14 Variation diagram of Rb/Sr versus $^{87}Sr/^{86}Sr$ in bulk peridotites 266
4-15 $^{143}Nd/^{144}Nd$ and $^{87}Sr/^{86}Sr$ of clinopyroxene versus (Mg/(Mg+Fe)) of bulk peridotites 267
4-16 Variation diagram of Rb/Sr versus Mg # in bulk peridotites 268
4-17 Variation diagram of La versus Sr in clinopyroxenes 268
4-18 $^{143}Nd/^{144}Nd$ versus $^{147}Sm/^{144}Nd$ in clinopyroxenes 269
4-19 Correlation of whole-rock CaO in anhydrous peridotite with $(Yb)_N$ abundances and La/Yb ratios 270
4-20 Evolution of REE abundance patterns in a 1km section of porous mantle using the chromatographic column model (Navon and Stolper, 1987) 271
4-21 Mixing models, residue plus partial melt, proposed to explain U-shaped REE patterns 272

LIST OF TABLES

CHAPTER 1

1-1	Major Element Abundances of Hannuoba Basalts	51
1-2	Trace Element Abundances of Hannuoba Basalts	59
1-3a	Major Element Composition for Standard Rock BHVO-1	66
1-3b	Trace Element Composition for Standard Rock BHVO-1	66
1-3c	Precision Estimates for Data Obtained by INAA	67
1-4	Chemical Analyses of Olivines in basanite D-1	68
1-5	Estimated Incompatible Element Abundance Ratios in Sources of Alkalic Basalts from Hannuoba and Oceanic Islands	71

CHAPTER 2

2-1a	Chemical Analyses of Clinopyroxene (Cpx) Megacryst and its Rim	116
2-1b	Clinopyroxenes in Basalts D-1	118
2-1c	Clinopyroxenes in Group I and Gruop II Xenoliths	118
2-2	Chemical Analyses of Megacryst Garnet (GT)	119
2-3	Chemical Analyses of Megacryst Anorthoclase and Magnetite	120
2-4a	Trace Element Abundances in Megacryst Gt and Cpx	121
2-4b	REE Abundances in Gt and Cpx Megacrysts	122
2-5a	TE Abundance Ratios of Megacryst Garnet and Clinopyroxene Over Chondrite and Basalts	123
2-5b	REE Abundance Ratios of Clinopyroxene and Garnet Megacrysts over J-14	123
2-6	Least-Square Calculation Based on Major Elements	124
2-7	Trace Element Modelling the Fractionation Model	127

CHAPTER 3

3-1a	Leaching Experiment on Sr-Nd Isotopic Composition	160
3-1b	Leaching Experiment on Pb Isotopic Compositions	161
3-1c	Leaching Experiment on Sr-Rb Concentrations	161
3-2	Sr and Nd Isotope Ratios of Hannuoba Basalts	162
3-3	Pb Isotope Ratios for Hannuoba Basalts	164

CHAPTER 4

4-1	Modal Proportions of Hannuoba Peridotites	231
4-2a	Major Element Abundances of Group I Peridotites	232
4-2b	Comparison of Major Element Analyses of Hannuoba Group I Peridotites	233
4-2c	Major Element Abundances of Average Group I Peridotites Worldwide	234
4-3a	Chemical Analyses of Olivines	235
4-3b	Chemical Analyses of Orthopyroxene	235

4-3c	Chemical Analyses of Clinopyroxene	236
4-3d	Chemical Analyses of Spinel	236
4-4	Petrography of Hannuoba Peridotites	237
4-5	Trace Element Abundances in Hannuoba Peridotites	238
4-6	Rare-Earth Element Abundances in Peridotites	239
4-7	Rare Earth Element Abundance in Clinopyroxene	241
4-8	Isotope Ratios and Trace Element Concentrations	242
4-9	Model Age Calculation	244
4-10	Major and Trace Element Abundances of Hannuoba Group II Xenoliths	245

INTRODUCTION

Geologic Setting of Cenozoic Basalts of China

Beginning at approximately the Mesozoic-Tertiary boundary, most of the Pacific coastal region of the Eurasian continent was subjected to intermittent but extensive basaltic volcanism ranging from continental tholeiites to alkali olivine basalts and basanites. The volcanoes are within a zone extending from the Kurile Volcanic arc in the north and the Honshu, the Ryukyu and the Philippines volcanic arcs in the south to approximately 3000 km westward.

In China, the post Mesozoic volcanism is largely restricted to the Marginal Pacific Tectonic Domain (Fig. I-1) with a clear pre-dominance of volcanic activity in northeastern China, off the coast of the Yellow Sea and the Sea of Japan, in the provinces of Shandong, Hebei, Liaoning, Jilin, Heilongjian, and the Inner Mongolia Autonomous Region. In fact, within China, more than 85% of these volcanics are found north of latitude 40^{o}N and east of longitude 115^{o}E (Fig. I-2). The Marginal Pacific Domain is underlain by two Precambrian shields: the North China Fault Block (NCFB) to the north and the Yangtze Block to the south (Fig. I-3). In between and around the two Precambrian shield blocks are various Phanerozoic fold systems: the

Heilongjiang-Jilin Fold System in the northeast, the Tsinling Fold System in between the two blocks and the South China Fold System to the south.

Geology and Petrology of the Cenozoic Basalts of Northeastern China

The Cenozoic basalts of northeast China can be classified either on the basis of geochemical affinities or by age. On the basis of geochemical affinities, there are two distinct basaltic suites (Cong et al., 1979): a). subalkaline-alkaline, and b). alkaline-peralkaline; and by age, they are: a). Early Tertiary basalts, b). Late Tertiary basalts, and c). Quaternary basalts. The subalkaline to alkaline suite includes basaltic types varying from a transitional tholeiite through mildly alkalic continental tholeiite to alkali olivine basalts. Basalts of this suite show only one generation of olivine as phenocrysts, no olivine in the matrix, predominance of plagioclase over ferromagnesian silicates and often minor amounts of residual glass in the matrix. By contrast, the alkaline to peralkaline suites consist of strongly alkalic basalts to basanites, often containing ultramafic nodules and megacrysts of clinopyroxene, alkali feldspar (anorthoclase) and more rarely opaques and garnet.

Cong et al (1979) have shown that there is a tendency towards an increase in alkalinity and decrease in Na_2O/K_2O

ratio with decreasing age. Most of the Early Tertiary basalts are subalkalic whereas the later Tertiary basalts are alkalic and most of the Quaternary basalts are peralkalic; for example in this sequence Na_2O/K_2O ratios decreases from 4.00 to 1.84.

Geology of Hannuoba Basalts and Purpose of This Study

The thick continental crust and complex evolution of continental lithosphere make the study of the sub-continental mantle more difficult than the study of the sub-oceanic mantle. However, access to the sub-continental mantle is provided by peridotite xenoliths and their host alkali basalts. The latter are believed to be unaffected (or less affected than the xenolith-free tholeiitic basalts) by crustal contamination so they provide indirect evidence for the composition and evolution of mantle melts. Peridotite xenoliths in these basalts are especially important because they provide direct insight into the chemical constitution and evolutionary history of the sub-continental mantle.

The Hannuoba basaltic plateau, 200 km northwest of Beijing, is near several deep faults in the North China Fault Block (Fig. I-4). It is an important occurrence among the Cenozoic basalts because of its size (>1700 km^2), the presence of intercalated tholeiitic and alkalic basalt and the abundant mantle xenoliths in the alkalic basalts. The locality is well known because the xenoliths have

accumulated in zones (hundreds of meters in size) where they form up to 90% of the outcrop (Feng, 1980). In addition to providing abundant samples of subcontinental mantle these zones are a source of gem quality olivine. Since the province was first surveyed and named (Barbour, 1929), there have been many studies of the basalts and their xenoliths (Lacroix, 1928; BHTHED, 1978; Zheng, 1980; Feng et al., 1982; Cong et al., 1983; Cong and Zhang, 1983; Huang et al., 1982; Wang et al., 1982; Feng and Han, 1983; Fan, et al., 1983; Zhai, 1983, 1984), but there have been no detailed geochemical studies involving major and trace element abundances and radiogenic isotope ratios. In this study the author has obtained such data. In Chapter 1 (Zhi et al., 1989) and Chapter 2, we report and interpret major and trace element abundance data for Hannuoba basalts and their megacrysts. In Chapter 3 we present and interpret the radiogenic isotope data for the basalts, and in Chapter 4 (Song and Frey, 1989), geochemical data for the mantle xenoliths are used to infer and characterize subcontinental mantle composition and processes beneath this region of eastern China, and to understand the petrogenesis of these continental basalts and mantle xenoliths.

FIGURES

FIGURE CAPTIONS

Figure I-1. Distribution of active volcanism in the western Pacific.

Figure I-2. Distribution of Cenozoic basaltic rocks in eastern China, on a base map showing the extent of the Marginal Pacific Tectonic Domain (from Geological Map of China, 1976; Zhou and Armstrong, 1982)

Figure I-3. Simplified tectonic map of eastern China, showing the nature of the basement rocks in the Marginal Pacific Tectonic Domain (From Zhou and Armstrong, 1982).

Figure I-4. Sketch map showing Cenozoic basalts northwest of Beijing (adapted from Tectonic Map of Asia (Number 4) compiled by the Research Institute of Geology, Chinese Academy of Geological Sciences). Recent rifted areas east and south of Beijing are shown, as are northeast-southwest and east-west faults and fracture systems. Some of these fractures are believed to control the location of eruption centers (e.g., Zhai, 1983).

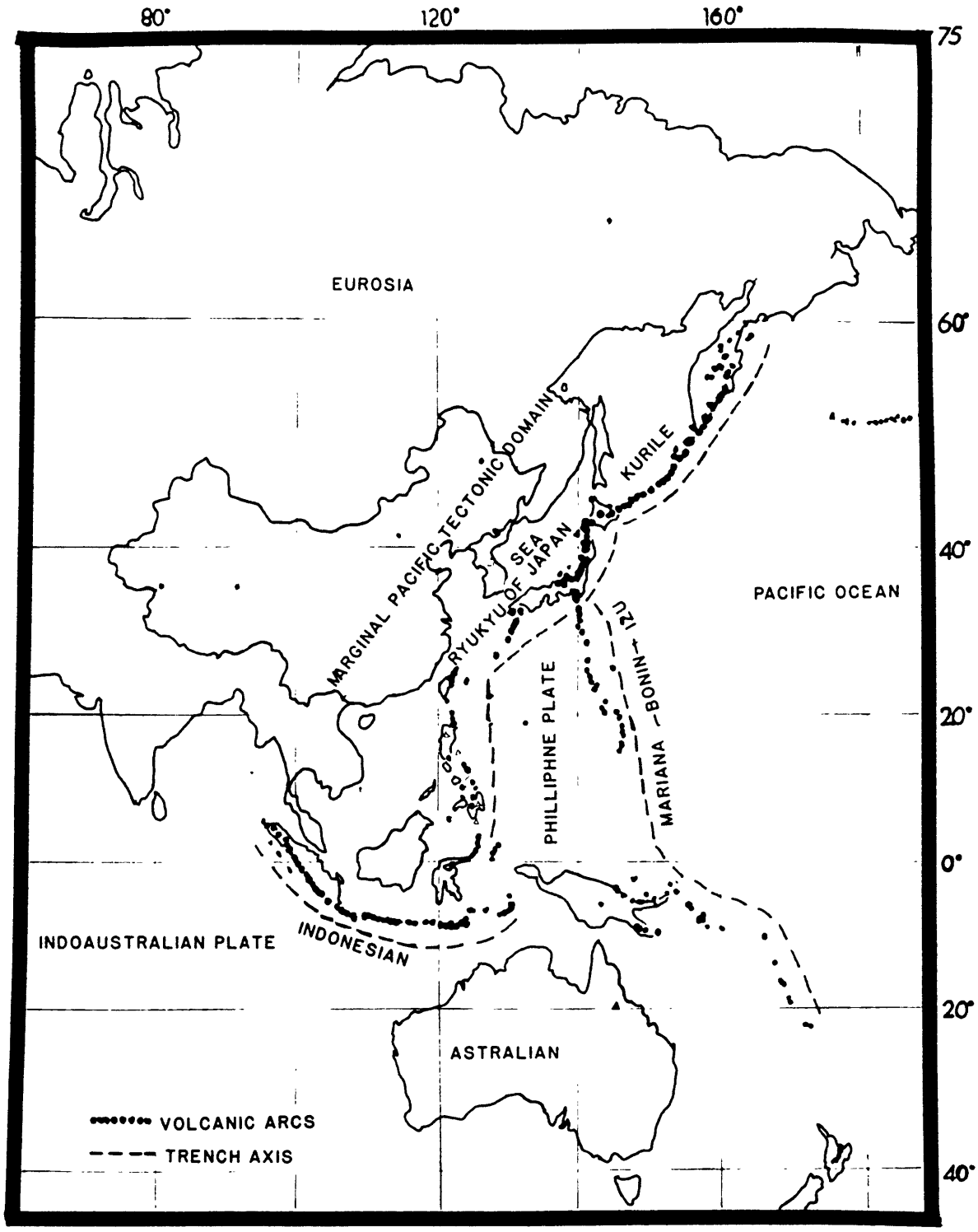
80°
120°
160°
75
60°
40°
20°
0°
20°
40°
EUROSIA
MARGINAL PACIFIC TECTONIC DOMAIN
KURILE
SEA OF JAPAN
RYUKYU
PACIFIC OCEAN
IZU
MARIANA - BONIN
PHILLIPHNE PLATE
INDOAUSTRALIAN PLATE
INDONESIAN
ASTRALIAN
VOLCANIC ARCS
TRENCH AXIS

FIGURE I-1

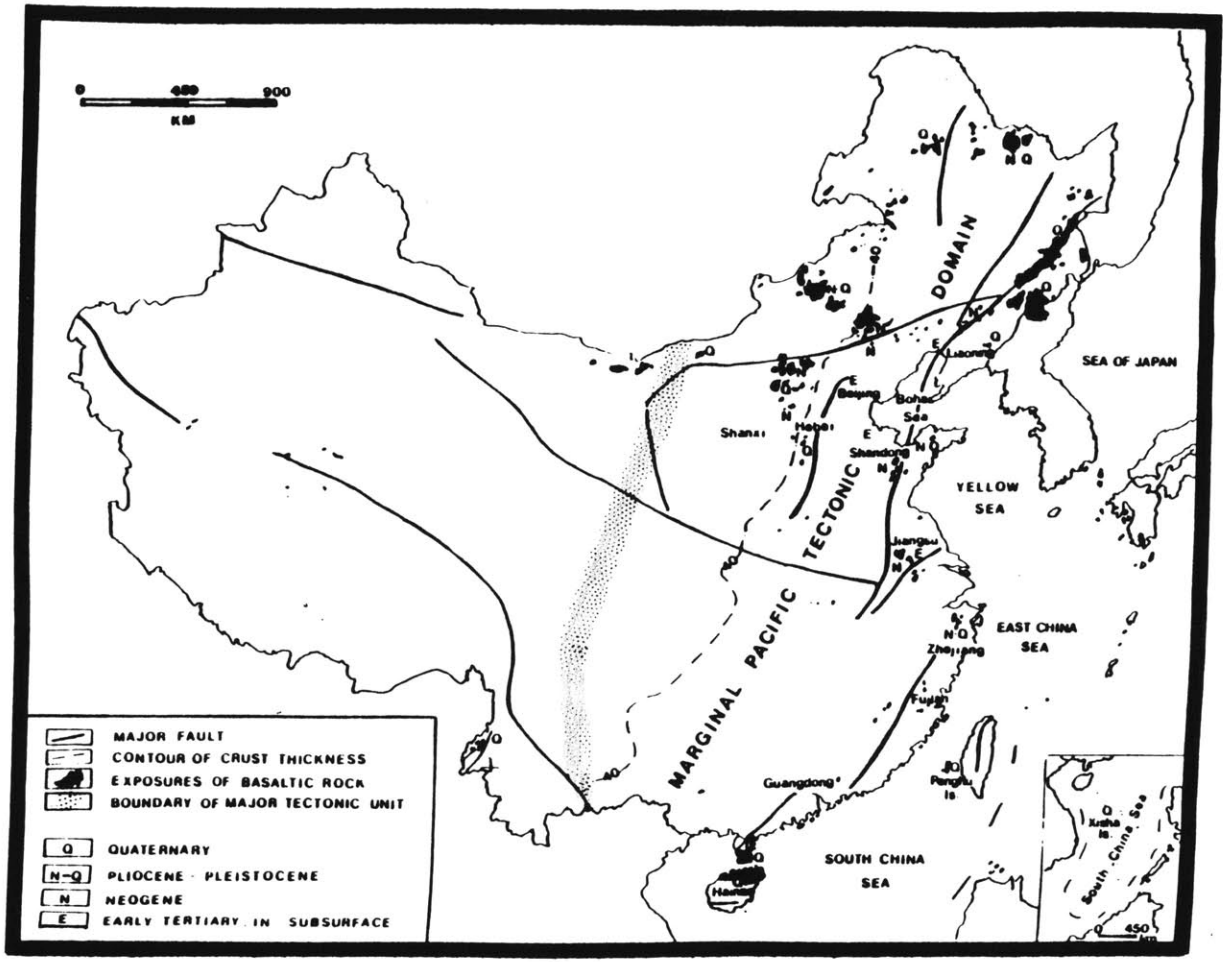
0
900
KM
SEA OF JAPAN
YELLOW SEA
EAST CHINA SEA
SOUTH CHINA SEA
MARGINAL PACIFIC TECTONIC DOMAIN
Shanxi
Hebei
Shandong
Guangdong
Hainan
Bohai Sea
South China Sea
MAJOR FAULT
CONTOUR OF CRUST THICKNESS
EXPOSURES OF BASALTIC ROCK
BOUNDARY OF MAJOR TECTONIC UNIT
Q QUATERNARY
N-Q PLIOCENE - PLEISTOCENE
N NEOGENE
E EARLY TERTIARY IN SUBSURFACE

FIGURE I-2

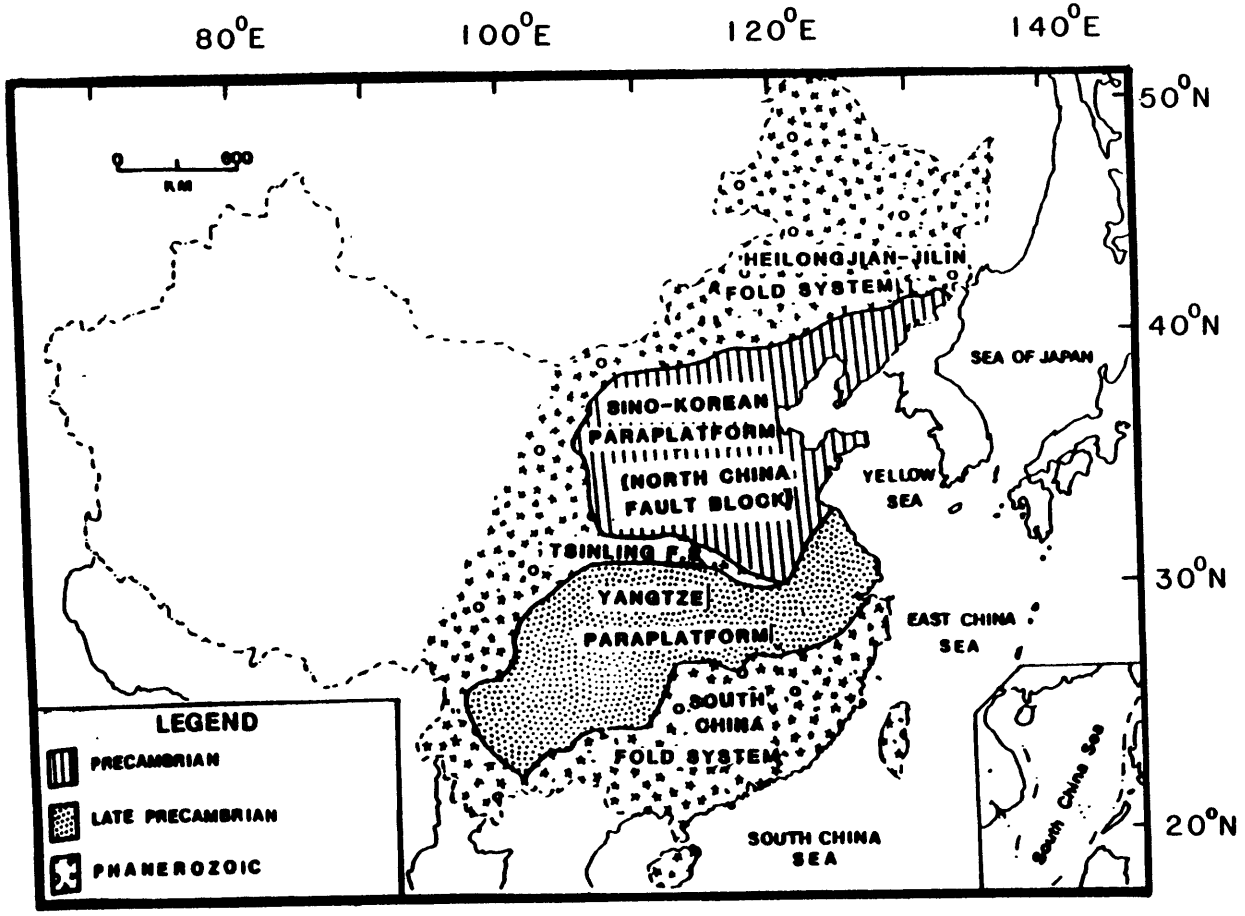
80°E
100°E
120°E
140°E
50°N
40°N
30°N
20°N
0
900
KM
HEILONGJIAN-JILIN
FOLD SYSTEM
SEA OF JAPAN
SINO-KOREAN
PARAPLATFORM
(NORTH CHINA
FAULT BLOCK)
YELLOW
SEA
TSINLING F.
YANGTZE
PARAPLATFORM
EAST CHINA
SEA
SOUTH
CHINA
FOLD SYSTEM
SOUTH CHINA
SEA
South China Sea
LEGEND
PRECAMBRIAN
LATE PRECAMBRIAN
PHANEROZOIC

FIGURE I-3

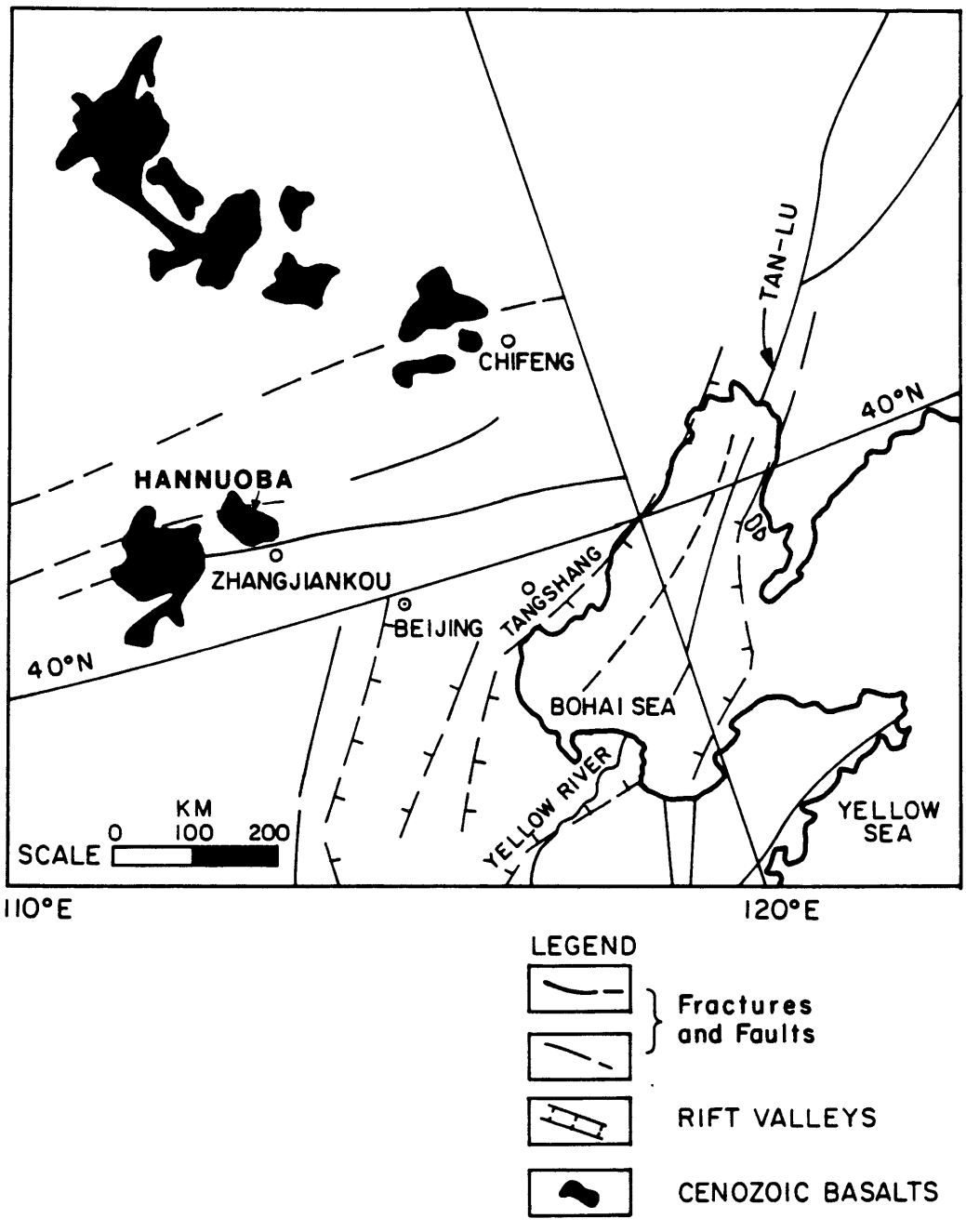
CHIFENG
HANNUOBA
ZHANGJIANKOU
BEIJING
TANGSHANG
TAN-LU
40°N
40°N
BOHAI SEA
YELLOW RIVER
YELLOW SEA
SCALE
KM
0
100
200
110°E
120°E
LEGEND
Fractures and Faults
RIFT VALLEYS
CENOZOIC BASALTS

FIGURE I-4

CHAPTER 1: MAJOR AND TRACE ELEMENT GEOCHEMISTRY OF HANNUOBA BASALTS, EASTERN CHINA: CONSTRAINTS ON THE ORIGIN OF CONTINENTAL ALKALIC AND THOLEIITIC BASALT

1-1. INTRODUCTION

Cenozoic basalts are widely distributed in eastern China (e.g., Zhou and Armstrong, 1982). Northwest of Beijing in Hebei province and the Inner Mongolia Autonomous Region there are large (~20,000 km^2) plateaus of Miocene and Pliocene basalt (Fig. I-4). The Hannuoba region is an excellent locality for determining the relative importance of mantle and crustal components in continental basalts because:

(1) the intercalated tholeiitic and alkalic basalts provide a geochemical diversity that is usually not available;

(2) the occurrence of mantle xenoliths provides local mantle samples for study; and

(3) the presence of dense xenoliths in the alkalic lavas provides evidence that they ascended more rapidly from their mantle source than the tholeiitic lavas; therefore, the alkalic lavas are probably less contaminated by continental crust.

In addition, we have previously studied tholeiitic to alkalic transitions in an oceanic environment (Chen and Frey, 1985) and we want to understand the nature of this transition in a continental setting. In this Chapter, We have obtained and interpret major and trace element data on Hannuoba basalts with the objective of understanding the petrogenesis of these continental basalts.

1-2. GEOLOGIC SETTING AND SAMPLING

The Hannuoba basaltic tableland 10-20 km northwest of Zhangjiakou city forms a southern edge of the Inner Mongolia plateau on the Yanshang fault system (Fig. I-4). Zhai (1983) interpreted that Hannuoba volcanism was controlled by intersecting deep fractures. Country rocks include Archean metamorphic rocks, Jurassic sediments and granites and Cretaceous to Quaternary sediments (Fig. 1-1; BHTHED, 1978). Based on stratigraphy, paleontology and geochronology, Hannuoba basalts range in age from Miocene in the east to Pliocene in the west (Fig. 1-1). Samples for this study were collected from the central and eastern parts of the region, mapped as Miocene, along the steep southern edge of the plateau. Along this scarp a stratigraphic succession (100 to 300 m) of about 20 to 30 flows is exposed. We studied 67 samples primarily collected from five cross sections, Xiliuling, Bailongdong, Damaping, Zhouba and Erdaobian; the first three are exposed within 5 km along the southern edge of the plateau, and the Zhouba and Erdaobian sections are approximately 25 km to the east (Fig. 1-1). Although each section contains intercalated tholeiitic and alkalic lavas (Fig. 1-2), it has not been possible to correlate individual lavas between sections.

1-3. SAMPLE PREPARATION AND ANALYTICAL PROCEDURES

1-3.1. Sample Preparation

The basalts were sawn to remove weathering surfaces and hammer marks. The saw marks were ground away with silicon carbide, then samples were carefully washed in distiled water without being directly touched by hand. The basalt samples were wrapped in clean cotton towel passed once through a jawcrusher, the resulting pieces were further reduced to small pieces (~ 1cm) by hammer. To avoid metal contamination the samples were wrapped in clean plastic plates surrounded by cotton towels during all hammering procedures. The basalt chips with vesicles, small inclusions and megacrysts were picked out before shatterboxing. All handling of the samples was with a gloved (poly) hand. All samples were prepared by crushing (in an agate shatterbox) ~150 grams of the freshest, inclusion free fragments, except for samples from the Xiliuling and Damaping (subset labeled ZX and ZB) which were aliquots of powders studied by Zhai (1983).

1-3.2. Analytical Methods

Major and some trace element (Rb, Ba, V, Cr, Ni, Zn, Ga, Y, Zr and Nb) abundances were determined by X-Ray fluorescence (XRF) at the University of Massachusetts at

Amherst according to the methods described by Rhodes (1983). Abundances of rare earth elements, Sc, Co, Cr, Hf, Ta and Th were determined by instrumental neutron activation (INAA) at MIT using the methods described by Ila and Frey (1984). H_2O and CO_2 contents of the samples were determined with a CHN analyzer (Perkin Elmer) at the Woods Hole Oceanographic Institute. Data and precision estimates are reported in Tables 1-1, 1-2 and 1-3. Detailed analytical techniques are reported in Appendix.

1-4. BASALT TYPES AND STRATIGRAPHY OF HANNUOBA LAVAS

1-4.1. Normalized Data

The relatively higher Fe_2O_3/FeO (Song, 1983) and higher H_2O content of some samples indicate variable degrees of weathering. The higher content of Fe_2O_3 has a pronounced effect on the normative calculation and therefore on the Mg# values ($Mg/(Mg+Fe^{+2})$). As an example, if the rock contains more Fe_2O_3 than FeO, then the normative olivine and nepheline contents are critically affected by the artificial lowering of their values and in some instances will even result in normative quartz. Such distortion clearly may affect classification of some of the basalts.

To remove the effect of weathering, the data from whole rock analyses in Table 1-1 are renormalized to 100%, H_2O-free basis with the molar ratio of $Fe_2O_3/(Fe_2O_3+FeO)=0.10$,

which equals to Wt% of $Fe_2O_3/(Fe_2O_3+FeO)=0.22$. This is the ratio of the least oxidized Hannuoba basalts analyzed by wet chemistry technique in China (Song, 1983). This ratio is same as the molar ratio of 0.10 and Wt ratio of 0.22 of the least oxidized Hawaiian basalts (Macdonald and Katsura, 1964; Macdonald and Powers, 1968; Wright, 1971; Clague and Frey, 1982). The calculated CIPW normative compositions are presented in Table 1-1.

1-4.2. Classification and Stratigraphy

Based on normative proportions (Table 1-1) Hannuoba basalts range from quartz tholeiites to basanites (Fig. 1-3). All lavas containing ultramafic mantle xenoliths are nepheline normative; for simplicity we label this group of 26 samples as alkalic basalt. A second group (30 samples), tholeiitic in normative proportions (Fig. 1-3) and containing more than 50% SiO_2 (Fig. 1-4) is labelled tholeiitic. Finally, a group of 11 samples is variable in normative proportions with compositions intermediate to the alkalic and tholeiitic lavas (Fig. 1-3). None contain mantle xenoliths and all have less than 50% SiO_2 (Fig. 1-4). We designate these compositionally intermediate lavas as a transitional group.

These three lava types are intercalated in the stratigraphic sections. However, in each section the oldest lavas are alkalic basalts with mantle xenoliths; the

youngest lavas in most sections are transitional (Fig. 1-2). Based on intercalated alkalic flows Feng et al. (1986) interpreted that the Hannuoba sections represent 4 to 6 cycles of older alkalic to younger tholeiitic lavas. In most sections tholeiitic lavas are dominant, but 15 of 23 flows in the Erdaobian section are alkalic basalt (Fig. 1-2).

1-5. MACROSCOPIC AND PETROGRAPHIC CHARACTERISTICS

1-5.1. Alkalic Basalts:

The alkalic basalts are fine-grained, dark grey and massive. Megacrysts, dominantly clinopyroxene and anorthoclase with rare titanomagnetite and garnet, and a wide range of xenoliths are abundant (Feng et al., 1982). Hannuoba alkali basalts have a lower degree of crystallization and higher glass content (10-20%) than both transitional and tholeiitic basalts. The texture of Hannuoba alkali basalts usually is vitrophyric and rarely porphyritic. The phenocrysts are mainly olivine, with rarely plagioclase (0.1-0.3 mm) in few samples. The total abundance of phenocrysts is less than 5% and the grain size of olivine and clinopyroxene is mainly 0.03-0.05 mm, and can be up to 1.5 mm. The texture of matrix is intersertal, and the grain sizes of minerals in the matrix are 0.001-0.01 mm. The matrix consists of granular pink titanaugite, titano-magnetite, and/or laths of plagioclase occurring in ophitic

intergrowth, between these phases are irregular pools of glass and/or alkali-feldspar, with minor granular olivine, and rare nepheline, apatite, and analcite.

Most of the phenocrystic olivines are not euhedral in shape, the crystal forms often modified by corrosion or fragmentation, suggesting that they are not phenocrysts but rather xenocrysts. For more detailed petrographic descriptions see Chapter 2.

1-5.2. Tholeiitic Basalts:

The Hannuoba tholeiitic lavas are coarser in grain size, grey to brown grey color, and outcrops are more intensely weathered, often forming spheroidal boulders. Megacrysts and xenoliths are absent. Hannuoba tholeiites show a relatively high degree of crystallization with porphyritic and holocrystalline texture. The texture of matrix usually is intergranular, intersertal and poikilitic. The holocrystalline rocks composed of laths of plagioclase and interstitial augite and olivine. In porphyritic rocks, the phenocrysts are composed mainly of plagioclase, olivine, in addition augite. The large grains of plagioclase are 0.1-0.5mm in length, and the lager grains of olivine and clinopyroxene are 0.1-0.5mm. The matrix often shows laths of plagioclase and interstitial augite, and rare apatite. Opaque minerals are mainly acicular ilmenite.

1-5.3. Transitional Basalts:

This type of basalt has transitional petrographic characteristics. The mineral grain size is coarser than in the alkali basalts, and the content of glass is more similar to the tholeiites. The texture of the matrix usually is interseptal, intersertal and intergranular. The phenocryst assemblage is dominantly olivine, with lesser amounts of titanaugite and plagioclase. The matrix is composed of plagioclase, olivine, titanaugite, and rare alkali-feldspar and apatite. Opaque minerals are granular titano-magnetite and acicular ilmenite.

1-5.4. Summary

In all three types of basalts, clinopyroxene is mostly pink-colored titanaugite and rare diopside. The olivines (xenocrysts, phenocrysts and in matrix) are often serpentinized, or iddingsitized, especially along rims or partings. Most of the plagioclase phenocrysts (in tholeiites) are labradorites, less commonly andesines, and labradorites to andesines in matrix (Zhai, 1984). Vesicles are more abundant in the alkalic basalts than in tholeiitic basalts. They are filled with zeolites and carbonates.

The alkalic and tholeiitic basalts are easily distinguished both in handsample and in thin section: the alkalic basalts are much finer grained, darker black in color, and less weathered. In thin section: alkali basalts

are more fine grained with few phenocrysts (no plagioclase, minor clinopyroxene phenocrysts), contain less than 5% xenocrysts (mainly olivine). Tholeiitic rocks are coarser with a high degree of crystallization and porphyritic and holocrystalline texture. Abundant coarse plagioclase and clinopyroxene occur in tholeiites. The opaque minerals are mainly granular titano-magnetite in alkalic basalts, and acicular ilmenite in tholeiitic basalts, they are easily distinguished under the microscope.

1-6. GEOCHEMICAL RESULTS

1-6.1. Major and Minor Oxide Compositions:

The three compositional groups, alkalic, transitional and tholeiitic, are readily distinguished in a SiO_2-MgO variation diagram (Fig. 1-4). Also, at a given MgO the alkalic lavas have higher FeO^*, TiO_2, Na_2O, K_2O and P_2O_5 (Fig. 1-4). The tholeiitic group has a limited range in MgO, 6.39 to 8.66%, in contrast to the mantle xenolith-bearing alkalic basalts which range from 5.69 to 10.62 % MgO. If adjusted to the same $Fe_2O_3/(FeO+Fe_2O_3)$ ratio (e.g., 0.1) the Mg/(Mg+Fe) ratios of alkalic and tholeiitic lavas overlap (50 to 63) (Table 1-1). Compositional variations within the tholeiitic and transitional groups do not form well-defined trends. The most systematic trends are exhibited by the alkalic basalts; with decreasing MgO, abundances of Al_2O_3, Na_2O and P_2O_5 increase while CaO and TiO_2 decrease. Some of

the scatter in these MgO trends, e.g., in K_2O, reflects late-stage alteration; whole rock H_2O^+ contents range from 0.38 to 4.60% (Table 1-1).

Although H_2O^+ and K_2O contents are not highly correlated, strong evidence for post-magmatic alkali metal mobility is illustrated by data for two alkalic basalt samples from the same flow Zh14-1 and 14-2 (Tables 1-1 and 1-2). They have high H_2O^+, 3.29 and 2.45 % respectively, and differ significantly in alkali metal and Ba contents; factors of 0.76, 1.84, 1.44 and 1.16 for Na, K, Rb and Ba, respectively (Tables 1-1 and 1-2). All other major and trace element abundances in these two samples are less variable; specifically, varying by less than 12% with most within 5%. Data for two samples, Bai-6-1 and -6-2, from a tholeiitic flow with slightly lower H_2O^+ (2.40 and 1.39%) do not show similar mobility of alkali metals (Table 1-1).

1-6.2. Trace Element Abundances - Rare Earth Elements (REE):

The three compositional groups are well defined on chondrite-normalized REE plots (Fig. 1-5). Light REE (LREE) increase from tholeiitic to alkalic lavas whereas heavy REE (HREE) decrease. As a result REE patterns for tholeiitic and alkalic lavas intersect (Fig. 1-5), and there is a systematic increase in LREE/HREE from tholeiitic to transitional to alkalic lavas. $(La/Yb)_N$ ratios range from 5 to 12 in the tholeiites and 16 to 50 in alkalic lavas (Fig. 1-6). Among the alkalic basalt lavas, six samples (Zh-1, Zh-

3, ZX-44, R-4, R-6 and R-8) with relatively high MgO contents (8.1-10%) have lower LREE/HREE than other alkalic basalts (Fig. 1-6); hence even within the alkalic basalt group there are intersecting REE patterns (Zhouba and Erdaobian sections, Fig. 1-5).

1-6.3. Trace Element Abundances - Incompatible Elements (P, Rb, Sr, Ba, Y, Zr, Hf, Nb, Ta, LREE and Th):

The post-magmatic mobility of alkali metals is indicated by the large Rb abundance range, a factor of 3.5 for alkalic basalts and 7.1 for tholeiitic basalts, and the poor correlation with abundances of other incompatible elements (e.g., Rb-Th in Fig. 1-7). Sample D-1 has anomalously high Rb (63 ppm, Fig. 1-7) and a very high H_2O^+ content (4.26%).

The anomalously high Ba in sample Z-2 (1136 ppm, Fig. 1-7) correlates with atypically high K_2O (2.82%, Fig. 1-4) and abundant potassium feldspar in the groundmass which interpret as an alteration feature. In contrast to alkali metals, other incompatible elements in these groups have similar abundance ranges, factors of 1.7 to 2 in alkalic basalts and 1.4 to 2.8 in tholeiitic basalts. The highest incompatible element abundances are in the alkalic basalts and the lowest in the tholeiitic basalts. Among all the Hannuoba lavas and within each compositional group, abundances of Sr, LREE, Zr, Hf, Nb and Ta are positively correlated (Fig. 1-7). Intercepts on the La, Ce, and Nb

versus Th plots are near zero (Fig. 1-7) indicating that these elements were highly incompatible during formation and evolution of the Hannuoba lavas. As a result, LREE/Th, and Nb/Th ratios are similar in all Hannuoba lavas. Ba and Th abundances are positively correlated in the tholeiitic and transitional basalts but not in the alkalic basalts (Fig. 1-7).

1-6.4. Trace Element Abundances - Compatible Elements (Ni, Cr, Co, Sc and V):

In contrast to incompatible element abundances which systematically increase from tholeiitic to transitional to alkalic lavas, abundances of compatible trace elements overlap in the various groups. Although abundances of these elements are not correlated with highly incompatible elements, Ni, Cr and Co are positively correlated with MgO content (Fig. 1-8). Nickel contents vary from 69 to 271 ppm and most are lower than calculated values for primary lavas (Sato, 1977; Hart and Davis, 1978); that is, the majority of lavas containing mantle xenoliths have Ni contents less than 200 ppm (Fig. 1-8). Consistent with these low Ni contents, Cr in the alkalic basalts ranges from 86 to 240 ppm. Several of the alkalic, mantle xenolith bearing lavas have lower compatible element contents than the tholeiitic lavas (Fig. 1-8).

Most (20 of 26) alkalic basalts have lower Sc (9-15 ppm) and HREE (Yb and Lu) contents than the tholeiitic and

transitional lavas (Fig. 1-8). The six alkalic basalts (Zh-1, Zh-3, ZX-44, R-4, R-6 and R-8) with relatively high Sc and heavy REE are low in normative Ne and have atypically low LREE/HREE ratios (Tables 1-1 and 1-2, Figs. 1-6 and 1-8).

1-7. DISCUSSION

1-7.1. Origin and Evolution of the Mantle Xenolith-Bearing Alkalic Basalts

The covariation of MgO, Ni and Cr abundances, their large abundance range (factor of ~4 for Ni) and absence of alkalic basalts with Ni > 271 and Cr > 240 requires that these basalts were not primary melts of average upper mantle as expressed by mantle xenoliths and alpine peridotites (e.g., Ni vs. MgO in Fig. 1-8, this Chapter; Maaloe and Aoki, 1977; Hart and Davis, 1978; Sato, 1977; Figure 2 of Hart and Allegre, 1980). The extreme sample supporting this interpretation is Zh-20 which contains mantle xenoliths but has only 5.69% MgO, 90 ppm Ni and 91 ppm Cr (Tables 1-1 and 1-2).

It is possible that these alkalic lavas were partial melts of compositionally diverse sources including sources with low Ni and Mg/Fe; e.g., a veined pyroxenite-garnet lherzolite mantle. An alternative explanation is that despite the presence of high density mantle xenoliths these lavas have fractionated mafic minerals. This fractionation

may have occurred subsequent to xenolith incorporation (Sparks et al., 1977) or more likely before incorporation of the mantle xenoliths (Irving and Price, 1981; Spera, 1984).

The large range in Ni content is consistent with olivine segregation (Hart and Davis, 1978). However, compatible element trends are not consistent with fractionation of only olivine. For example, it is well established that Ni/Co ratios in olivine exceed those in an equilibrium melt by a factor of ~4 (e.g., Henderson, 1982). However, Ni/Co ranges over only a factor of 1.7 (except for sample D-1) as MgO decreases from 10.0-5.7% (Fig. 1-9a). Segregation of phases, such as pyroxene and garnet, with a lower Ni/Co ratio are required by the data.

Consistent with this conclusion, other geochemical trends require segregation of phases such as clinopyroxene and garnet. For example, the positive correlation between CaO/Al_2O_3 and MgO (Fig. 1-9b) can be best explained by segregation of clinopyroxene. The positive Sc-MgO trend and inverse Zr/Y-Sc trends (Fig. 1-9b) could be explained by either clinopyroxene or garnet fractionation. However, the Yb-MgO correlation (Fig. 1-9b) and crossing REE patterns of the alkalic basalts (Fig. 1-5) can be best explained by segregation of garnet. The presence of clinopyroxene and garnet megacrysts (e.g., in sample J-14) in the Hannuoba alkalic basalts is complementary evidence for high pressure fractionation of these phases. Moreover, garnet in sample J-

14 has $^{143}Nd/^{144}Nd$ and $^{87}Sr/^{86}Sr$ similar to the host rock (see Table 3-2 and Fig. 3-1).

We interpret that the least evolved alkalic lavas are those with CaO/Al_2O_3 > 0.65, Sc > 18 ppm, Zr/Y = 10 to 12 (Fig. 1-9b) and La/Yb ~25 (Fig. 1-6). Five of the seven lavas with these characteristics have MgO contents of 9 to 10% and Ni contents of ~200 ppm. We suggest that these parental lava compositions evolved to alkalic basalts with lower MgO, Sc, Yb, CaO/Al_2O_3 and higher Zr/Y (Fig. 1-9b) by clinopyroxene and garnet fractionation. An important role for eclogite (i.e., clinopyroxene plus garnet) fractionation during the high pressure evolution of basaltic magmas has also been inferred from phase equilibria and major element constraints (e.g., O'Hara and Yoder, 1967; O'Hara, 1968; O'Hara et al., 1975).

As discussed in Chapter 2, if the Hannuoba megacrysts and peridotite xenoliths are used as guides for the compositions of segregated minerals, the major element trends of the alkali basalts (Fig. 1-4) can be matched by segregation of a clinopyroxene-rich, garnet-bearing assemblage. A clinopyroxene/garnet ratio of ~ 2 is required, and these proportions explain the decrease in CaO/Al_2O_3 with increasing differentiation (Fig. 1-9b). Segregation of an Fe-Ti-bearing oxide is also required to lower the TiO_2 content of the most evolved lavas (Fig. 1-4). Using a least squares mixing model involving clinopyroxene, garnet and titanomagnetite the most evolved alkalic lavas (Zh-20 with

5.7% MgO) can be derived from high MgO alkalic basalts (e.g., R-4 and ZX-44, 10% MgO) by ~ 44% fractionation. This amount of fractionation is sufficient to explain the observed enrichment of incompatible elements (Fig. 1-7). For example, the observed incompatible element enrichment factors, Zh-20/R-4 and Zh-20/ZX-44, range from ~ 1.5 to 1.6 which is less than the ~ 1.8 enrichment factor expected for a perfectly incompatible element.

However, the trend of Ba abundances in the alkalic basalts (Fig. 1-7) is not explained by an eclogite fractionation model. As stated earlier two samples from the same flow, Zh-14-1 and Zh-14-2 (Table 1-2), differ significantly (16%) in Ba contents; consequently, the poor Ba-Th trend (Fig. 1-7) may reflect the post-magmatic mobility of Ba. Nevertheless, the positive correlation of MgO content with Ba/Th, Ba/La and Ba/Nb (Fig.1-10a) is more consistent with magmatic processes. The proposed eclogite fractionation model cannot explain the absence of Ba enrichment in the most evolved lavas unless a Ba-rich phase, perhaps anorthoclase which occurs as an abundant megacryst, is part of the segregating assemblage. As discussed by Irving and Frey (1984) anorthoclase occurs as a phenocryst in highly evolved lavas such as benmoreites, phonolites and trachytes. Therefore, it is an unlikely fractionating phase in the Hannuoba alkalic basalt suite. However, the presence of anorthoclase megacrysts requires that highly evolved alkalic lavas existed. Therefore, it is possible that the

incompatible element abundance trends defined by the alkalic lavas (Fig. 1-7) reflect mixing of relatively primitive and evolved lavas.

Another magmatic interpretation of the Ba trend is that the small variation in Ba abundance reflects control by a mineral (e.g., phlogopite) during partial melting. In this case, the incompatible element trends (Fig. 1-7) reflect different degrees of partial melting. The crossing REE patterns (Fig. 1-5) could result from partial melting of a garnet-bearing source.

In Fig. 1-6 the alkalic basalt trends could be interpreted as resulting from two different parental basalts; i.e., a group of lavas with low and relatively constant La/Yb ranging in MgO from ~ 10% (R-4 and ZX-44) to 8% (Zh-3), and a group of lavas with variable La/Yb with sample D-1 (10.6% MgO) as a possible parent. However, this sample contains xenocrystic olivine. It contains 5 to 10% olivine ranging in size from 0.5 to 2 mm. The larger (1-2 mm) olivine xenocrysts are complexly zoned ranging from forsterite-rich (Fo) to forsterite-poor (Fo) regions (Table 1-4). Regions with low forsterite content overlap in composition with matrix olivine whereas the forsterite-rich regions overlap with olivine compositions in the mantle xenoliths (Table 1-4). The average X_{Fe}/X_{Mg} of four olivine grains in the matrix of basanite D-1 (Table 1-4) is 0.41, which requires an equilibrium melt with Mg number equal to 42 based on $K_d^{ol} = 0.30$. The rims of olivine xenocrysts also

have relatively high X_{Fe}/X_{Mg} (up to 0.43, olivine A-7 in Table 1-4) comparing to the core of olivine xenocrysts (down to 0.097, olivine A-1 in Table 1-4). These high X_{Fe}/X_{Mg} ratios in matrix olivine and xenocryst rims reflect equilibration with a melt that has a lower Mg number than that of the D-1 whole rock composition (Mg number = 63). The low CaO content of the Mg-rich olivine xenocrysts indicates that these olivines are not in equilibrium with the host basalt at low pressure (Watson, 1979). Also one Cr-spinel grain is included in an olivine xenocryst (D in Table 1-4). Apparently, these olivine xenocrysts were disaggregated from the abundant peridotite xenoliths during ascent. This xenocrystic olivine perturbs the bulk-rock composition of D-1 to anomalously high MgO/CaO (Fig. 1-4) and Ni/Co (Fig. 1-8) and causes an offset in the CaO/Al_2O_3-MgO trend (Fig. 1-9b). Subtraction of 6-7% Fo-rich olivine from the bulk-rock composition lowers the MgO content of sample D-1 so it fits the trends defined by the other alkalic basalts with relatively high La/Yb (Fig. 1-6).

In summary, we conclude that the first order geochemical trends among Hannuoba alkalic lavas can be explained by eclogite fractionation. For example, a parental Hannuoba alkalic basalt magma with relatively high Sc, low La/Yb and low normative nepheline, could evolve to the low Sc, high La/Yb and high normative nepheline magmas by fractionation of clinopyroxene, garnet and minor amounts of Fe-Ti oxide. This interpretation is consistent with the near

isotopic homogeneity of the Hannuoba alkalic lavas; e.g., $^{87}Sr/^{86}Sr$ = 0.7038 to 0.7040; $^{143}Nd/^{144}Nd$ = 0.51287 to 0.51297 and $^{206}Pb/^{204}Pb$ = 17.78 to 17.94 (Chapter 3).

Studies of alkalic lavas from other mantle xenolith localities have also concluded that: (1) post-melting mineral fractionation occurs in the mantle (e.g., Irving and Price, 1981); and (2) high pressure clinopyroxene segregation is a significant process in the evolution of alkalic basalts (e.g., Duda and Schmincke, 1985; Liotard et al., 1988). Complementary evidence for such upper mantle processes are pyroxenite, some containing garnet, layers in alpine peridotites. Typically, these layers have compositions consistent with an accumulate origin (e.g., Suen and Frey, 1987).

Alternatively, different degrees of melting of a garnet-bearing source can also explain the incompatible element trends of the alkalic basalts. If this source is veined pyroxenite-garnet lherzolite with variable Fe/Mg it may also explain much of the major element abundance variations among the alkalic basalts. This model has been recently proposed for mantle xenolith-bearing Quaternary alkalic basalts erupted in the northern Canadian Cordillera (Francis and Ludden, 1988).

1-7.2. Origin of Compositional Range from Tholeiitic to Alkalic Basalt

In all geochemical characteristics, i.e., major elements (Fig. 1-4), trace elements (Figs. 1-7 and 1-8) and isotopic ratios of Sr, Nd and Pb (Chapter 3), the transitional lavas are intermediate to the tholeiitic and alkalic groups. Trends defined by highly incompatible elements (Figs. 1-7 and 1-10b) and isotopic ratios (Chapter 3) are consistent with the transitional lavas representing mixtures of the alkalic and tholeiitic lavas. In contrast, trends involving major and compatible trace elements (Figs. 1-4, 1-8 and 1-10a) are not consistent with simple magma mixing. If mixing was important, subsequent crystallization has severely perturbed the major and compatible element trends. In subsequent discussion we focus on understanding the endmember compositional groups, i.e., the tholeiitic and alkalic lavas. Because of their intermediate geochemical characteristics, we anticipate that the transitional lava compositions will be readily explainable within the context of successful models for the tholeiitic and alkalic lavas.

The compositional differences between Hannuoba tholeiitic and alkalic lavas may reflect differences in source composition, degree of melting and post-melting fractionation processes. Evidence for different liquid lines of descent are the diverging trends in MgO variation diagrams, e.g., Ti/Zr and Zr/Y Vs. MgO (Fig. 1-11). Evidence

for differences in parental magma composition are provided by incompatible element abundance ratios. Abundances of general highly incompatible elements define a single coherent trend for Hannuoba tholeiitic, transitional and alkalic lavas. (Fig. 1-7). As a result, abundance ratios involving elements with very similar geochemical characteristics, are identical in all lava types, e.g., La/Ce and Nb/Ta (Fig. 1-10b); however, other incompatible element abundance ratios,such as Sm/Nd and Zr/Nb, vary systematically as a function of Th content (Fig.1-10a).

The simplest interpretation for this wide range in incompatible element abundances and systematic change in ratios is that parental lavas were derived by varying degrees of melting of a compositionally homogeneous source. This simple model is <u>not</u> appropriate for Hannuoba lavas. For example, abundance trends of compatible versus incompatible elements (Ni vs. Th, Fig. 1-8) are complex requiring at least extensive fractionation of mafic phases. Moreover, relative to the most primitive alkalic basalts, (e.g., ZX-44 and R-4) the tholeiitic lavas have lower abundances of incompatible elements <u>and</u> compatible elements (e.g., Ni, Fig. 1-8). Therefore, a simple fractionation relationship between these lava types is precluded. In addition, at similar MgO contents tholeiitic and alkalic lavas have different abundance ratios of Ba/La, La/Sm, Ce/Nd, Sm/Nd, Zr/Nb and Zr/Hf (Fig. 1-10b). The relative enrichment of the most incompatible elements in the alkalic basalts is clearly

shown in Fig. 1-12. The differences could result from varying degrees of melting of a compositionally homogeneous source. Alternatively, the tholeiitic and alkalic lavas were derived from compositionally different sources.

Strong evidence that compositionally different components have contributed to the Hannuoba tholeiitic and alkalic basalts are systematic differences in radiogenic isotopic ratios; $^{87}Sr/^{86}Sr$ = 0.7043 to 0.7048 and $^{143}Nd/^{144}Nd$ = 0.5127 - 0.5128 in tholeiitic lavas compared to 0.7038 to 0.7040 and 0.5129 to 0.5130 in the alkalic basalts (Chapter 3). These isotopic differences require that on a time-integrated basis the alkalic basalts were derived from more depleted sources than the tholeiitic lavas. Previous survey studies of Sr and Nd isotopic ratios in geographically associated and contemporaneous alkalic and tholeiitic lavas in eastern China also found that the alkalic basalts have isotopic ratios reflecting a long-term depleted source; i.e., lower $^{87}Sr/^{86}Sr$ and higher $^{143}Nd/^{144}Nd$ in alkalic lavas (Zhou and Armstrong, 1982; Zhou and Carlson, 1982).

In summary, we concluded that the Hannuoba tholeiitic and alkalic lavas were derived from different parental compositions. However, mixing of primary magmas or source components led to the coherent trends of incompatible element abundance ratios (Fig 1-10) and isotopic ratios (Chapter 3) defined by the tholeiitic transitional and alkalic lavas.

1-7.3. Geochemical Constraints on the Mantle Source of Hannuoba Lavas

Hannuoba tholeiitic basalts are isotopically heterogeneous (Chapter 3); therefore, it is difficult to constrain their source compositions. However, in normalized incompatible element abundance diagrams Hannuoba tholeiitic and alkalic lavas peak in the Nb-Ta region (Fig. 1-12a). In contrast, most tholeiitic continental flood basalts are relatively depleted in Nb and Ta (e.g., Thompson et al., 1983). The normalized trace element abundances of Hannuoba tholeiites are more similar to Hawaiian tholeiites (Fig. 1-12a). Also, the incompatible element similarities, such as peak at Nb-Ta, of Hannuoba tholeiitic and alkalic basalts are analogous to those of tholeiitic and alkalic basalts erupted along the Cameroon Line, a volcanic chain in the eastern Atlantic which straddles the transition from oceanic to continental volcanism (Fitton and Dunlop, 1985, figure. 8). Based on incompatible element abundances, it is evident that the petrogenesis of Hannuoba tholeiites was unlike that of continental flood basalts, such as the Columbia River and Parana, but similar to that of oceanic island tholeiites.

Because the alkalic Hannuoba lavas are a compositionally (this Chapter) and isotopically coherent group (Chapter 3), we have inferred the relative abundances of incompatible elements in their mantle source. Many incompatible element abundance ratios in these alkalic lavas

do not vary with MgO or Th content; e.g., La/Ce, Nb/Ta, Hf/Ta, and Zr/Nb (Fig. 1-10). We conclude that these ratios were not affected by melt/solid segregation during partial melting or subsequent crystal fractionation. Other abundance ratios, e.g., La/Sm, Ce/Nd, Ba/La and Ba/Sr, change systematically as a function of MgO content (Fig. 1-10a) and we can infer the ratios characteristic of the high MgO lavas. Using the trends in Fig. 1-10 we estimated incompatible element abundance ratios in the source of Hannuoba alkalic lavas (Table 1-5). The inferred source of these continental basalts from China is remarkably similar to inferred sources for alkalic basalts from oceanic environments (Table 1-5).

Another manifestation of the geochemical similarity of alkalic basalts from diverse tectonic settings (and by inference their source compositions) are similar patterns on normalized incompatible element diagrams (Fig. 1-12a). For example, patterns defined by alkalic basalts from continents, e.g., Germany, Australia and China, and from islands, e.g., Hawaii, peak at Ba and Ta-Nb; have smoothly decreasing trends from Ta-Nb to more compatible elements, such as Y and HREE; and scatter in the alkali metal - Th region partly because of alteration effects and partly because the relative abundances of Ba and Th vary within the mantle (e.g., Sun and McCullough, 1988).

A paradox is that Nd isotopic data for Hannuoba alkalic basalts require a depleted (Sm/Nd less than chondritic)

source whereas the inferred source (Table 1-5) is enriched. This paradox is characteristic of alkalic basalts and has been interpreted as requiring recent enrichment of incompatible elements (metasomatism) in the source or as resulting from Sm/Nd changes during melting; e.g., as expected for very low degrees of melting. In the latter case the inferred source characteristics in Table 1-5 are incorrect.

Our conclusions, based on element abundance data, that Hannuoba basalts and alkalic oceanic island basalts were derived from compositionally similar sources complements previous geochemical studies of Cenozoic Chinese basalts; i.e., (1) based on incompatible element abundance data, Nakamura et al. (1985) concluded that "the alkali basalts of northeastern China and Korea...are geochemically indistinguishable from ocean island alkali basalts;" and (2) based on Sr isotopic and incompatible element abundance data for Cenozoic basalts from eastern China, Zhou and Armstrong (1982) concluded that the tholeiitic magmas are melts of subcontinental mantle and that the alkalic magmas were derived from a deeper more depleted asthenosphere source. On a broader scale: Schwarzer and Rogers (1974) concluded that there are no systematic major element abundance differences between alkalic basalts erupted in different tectonic environments; Thompson et al. (1984) concluded that most alkalic basalts erupted in a continental setting have incompatible element abundance ratios similar

to alkalic basalts from oceanic islands, and alkalic basalts from the Cameroon line are a specific example (Fitton and Dunlop, 1985); and Allegre et al. (1981) found that radiogenic isotopic data "...show a close identity between oceanic island alkali basalts and intracontinental alkali volcanics." Clearly, the source of alkalic basalts can be tapped in continental and oceanic settings.

When comparing continental and oceanic alkalic basalts, it is important to recognize that oceanic island basalts can be divided into isotopic sub-groups (e.g., Zindler and Hart, 1986) which also have incompatible element abundance differences (e.g., Weaver et al., 1986; Sun and McDonough, 1988). Typically, there are differences in Ba/Nb and La/Nb; in this respect Hannuoba alkalic basalts have affinities with OIB having less than chondritic Ba/Nb and La/Nb (Fig. 1-13). Our main result is that the trace element abundance characteristics (Fig. 1-12) and isotopic ratios (Chapter 3) of Hannuoba alkalic basalts are well within the range exhibited by oceanic island basalts. That is, there is no obvious continental influence on the compositions of Hannuoba alkalic lavas. This conclusion contrasts with that of McDonough et al. (1985) who concluded that the isotopic composition of Cenozoic Australian alkalic basalts reflects a regional average of subcontinental lithosphere mantle. However, attempts to understand the isotopic heterogeneity of ocean island basalts have invoked an important role for delaminated subcontinental lithosphere (Hawkesworth et al.,

1986; Hart et al., 1986; Sun and McDonough, 1988). If true, compositional similarities of island and continental alkalic basalts might be attributed to subcontinental lithosphere. However, Chapter 3 shows that Hannuoba alkalic lavas have radiogenic isotopic ratios close to the PREMA component of Zindler and Hart (1986) rather than the more extreme isotopic end-members postulated to originate from subcontinental lithosphere.

1-8. CONCLUSIONS

Based on the major and trace element contents of the intercalated tholeiitic, transitional and alkalic basalts forming the Hannuoba plateau, our major conclusions are:

1) The alkalic basalts which contain mantle xenoliths range widely in composition. Much of this compositional range can be explained by segregation of clinopyroxene, garnet and minor Fe-Ti oxides. If these lavas formed from a magnesian (Mg/(Mg+Fe) > 88), compositionally homogeneous source, an important role for eclogite fractionation is inferred. Alternatively, these alkalic lavas formed from a compositionally heterogeneous source such as a veined garnet pyroxenite - garnet lherzolite mantle. However, Chapter 3 shows that the source of the alkalic basalts is nearly isotopically homogeneous, e.g., $^{87}Sr/^{86}Sr$ from 0.7038 to 0.7040.

2) The different lava types, tholeiitic, transitional and alkalic, at Hannuoba have followed different liquid lines of descent. However, the wide range of incompatible element abundances in these lavas define coherent trends consistent with a mantle mixing process or varying degrees of melting of a compositionally homogeneous source. The latter model is inconsistent with isotopic differences between the lava types, e.g., higher 87Sr/86Sr, lower 143Nd/144Nd and lower 206Pb/204Pb in the tholeiitic lavas (Chapter 3).

3) The geochemical characteristics of these continental basalts from eastern China are very similar to oceanic island lavas. For example, on mantle-normalized incompatible element plots the Hannuoba alkalic and tholeiitic lavas peak at Nb-Ta; i.e., very much unlike the Nb-Ta depletion characteristic of many continental flood basalts and arc lavas. Moreover, the inferred incompatible element abundances on the source of the alkalic Hannuoba lavas overlaps with that inferred from oceanic island alkalic basalts. Clearly, these continental alkalic basalts were derived from asthenospheric sources similar to the mantle sources which yield oceanic island basalts.

Table 1 Major Element Abundances in Hannuoba Basalts

Cross section	Zhouba								
sample	Zh-1	Zh-3	Zh-4	Zh-6	Zh-7	Zh-9	Zh-10	Zh-12	Zh-13
Lava Type	Ak	Ak	Th	Ak	Ak	Th	Th	Ak	Th
SiO_2	44.55	46.08	51.03	46.08	46.70	51.35	51.18	46.46	50.96
TiO_2	2.75	2.60	1.90	2.33	2.45	1.92	1.89	2.40	1.77
Al_2O_3	13.74	14.43	15.13	14.68	14.87	14.83	14.97	14.72	15.19
Fe_2O_3	14.38	13.64	11.64	13.01	13.23	11.37	11.13	13.12	11.04
MnO	0.19	0.17	0.14	0.17	0.17	0.12	0.13	0.16	0.13
MgO	9.16	8.07	7.53	6.65	6.91	6.85	7.95	6.49	7.87
CaO	9.88	8.92	9.25	7.75	8.16	8.85	8.46	8.27	9.11
Na_2O	2.84	2.78	2.74	5.75	4.44	2.95	2.73	4.30	2.69
K_2O	1.34	2.05	0.73	2.09	1.93	1.14	1.14	2.31	0.71
P_2O_5	0.94	0.84	0.36	1.16	1.16	0.36	0.36	1.14	0.33
Sum	99.81	99.58	100.45	99.67	100.02	99.74	99.94	99.37	99.80
H_2O^+	2.49	1.83	1.50	1.25	3.17	0.93	2.01	2.99	2.10
CO_2	0.85	0.41	0.37	0.00	0.00	0.21	0.83	0.25	0.16
Mg#	58	57	59	53	53	57	61	52	61
Q			1.2			1.0	0.7		1.2
Or	8.3	12.3	4.3	12.5	11.5	6.8	6.8	13.9	4.3
Ab	17.8	20.8	23.3	18.9	23.6	25.2	23.3	21.1	23.0
An	20.9	21.1	27.0	8.1	15.1	24.2	25.5	14.3	27.5
Ne	3.6	1.6		16.5	7.7			8.6	
Di	12.5	9.9	9.2	11.9	9.4	9.7	8.3	10.1	9.0
He	5.8	4.9	4.4	7.0	5.4	4.9	3.5	6.1	3.9
En			14.6			12.8	16.2		15.6
Fs			8.0			7.4	7.9		7.8
Fo	12.1	11.1		7.9	9.1			8.2	
Fa	7.1	6.9		5.9	6.6			6.3	
Mi	4.5	4.3	3.6	4.1	4.1	3.6	3.5	4.1	3.5
Il	5.3	5.0	3.6	4.5	4.7	3.7	3.6	4.6	3.4
Ap	2.2	2.0	0.8	2.7	2.7	0.8	0.8	2.7	0.8

-- AB = Alkali basalt
TH = Tholeiite
TR = Transitional basalt.
-- Mg# = $100(Mg/Mg+Fe^{2+})$ assuming $Fe_2O_3/(FeO+Fe_2O_3) = 0.1$.

Cross section	Zhouba								
sample	Zh-14-1	Zh-14-2	Zh-16	Zh-17	Zh-18	Zh-19	Zh-20	Zh-21	Zh-22
Lava Type	Ak	Ak	Th	Th	Th	Th	Ak	Th	Th
SiO_2	46.68	46.83	51.07	50.94	50.23	50.34	47.46	50.47	50.72
TiO_2	2.42	2.39	1.86	1.89	1.87	2.12	2.06	2.18	2.20
Al_2O_3	14.86	14.82	14.90	15.01	15.01	14.88	15.60	15.21	15.29
Fe_2O_3	13.24	13.03	11.35	11.19	11.35	11.58	12.20	11.66	11.68
MnO	0.16	0.16	0.14	0.14	0.15	0.15	0.16	0.11	0.11
MgO	6.54	6.37	7.90	7.88	8.66	7.48	5.69	6.39	6.39
CaO	8.32	8.30	8.39	8.48	8.38	8.61	7.82	8.80	8.82
Na_2O	4.14	5.40	2.98	2.82	2.79	2.96	4.11	3.44	3.05
K_2O	2.47	1.34	1.14	1.16	1.17	1.40	3.43	1.51	1.49
P_2O_5	1.18	1.17	0.36	0.37	0.36	0.44	1.04	0.48	0.46
Sum	100.01	99.81	100.09	99.88	99.97	99.96	99.57	100.25	100.21
H_2O^+	3.29	2.45	2.04	2.04	2.69	1.41	1.31	2.46	1.29
CO_2	0.55	0.27	0.15	0.24	0.66	0.50	0.05	0.18	0.27
Mg#	52	52	61	61	63	59	51	55	55
Q	16.3								
Or	18.4	8.0	6.8	6.9	7.0	8.3	20.6	9.0	8.9
Ab	14.0	26.0	25.4	24.1	23.9	25.3	17.2	29.3	26.0
An	9.2	12.4	24.1	25.1	25.2	23.4	14.1	21.8	23.8
Ne	10.1	11.0					9.8		
Di	6.1	11.0	8.7	8.4	8.2	9.3	9.1	10.1	9.2
He		6.7	3.9	3.7	3.3	4.3	6.0	5.4	4.9
En			14.4	15.8	13.4	10.9		5.1	10.4
Fs			7.3	7.9	6.2	5.8		3.1	6.4
Fo	8.2	7.7	1.0	0.1	3.2	2.5	7.1	4.4	1.0
Fa	6.3	5.9	0.6	0.0	1.6	1.5	5.9	3.0	0.7
Mi	4.1	4.1	3.5	3.5	3.6	3.6	3.8	3.6	3.6
Il	4.6	4.6	3.6	3.6	3.6	4.1	4.0	4.2	4.2
Ap	2.8	2.7	0.8	0.9	0.8	1.0	2.4	1.1	1.1

ZH-14-1 and -2 from same flow

Cross section sample	Erdaobian						
	R-2	R-4	R-6	R-8	R-9	R-11	R-19
Lava Type	Ak	Ak	Ak	Ak	Ak	Ak	Tr
SiO_2	45.51	44.9	45.35	45.37	45.55	45.81	45.94
TiO_2	2.89	2.68	2.67	2.72	2.72	2.49	2.80
Al_2O_3	14.33	13.83	14.01	14.05	14.54	14.70	14.53
Fe_2O_3	13.88	13.85	13.91	13.96	13.68	13.33	13.79
MnO	0.17	0.18	0.18	0.18	0.18	0.15	0.17
MgO	8.22	10.02	9.50	9.41	6.74	6.99	7.87
CaO	9.06	9.62	9.54	9.85	8.92	8.98	10.40
Na_2O	3.85	2.57	2.78	2.70	5.14	5.13	2.50
K_2O	1.64	1.51	1.20	1.14	1.33	1.42	1.14
P_2O_5	0.94	0.79	0.84	0.80	1.18	1.23	0.83
Sum	100.47	100.04	99.97	100.18	99.95	100.22	99.97
H_2O^+	3.28	3.50	2.93	3.22	2.34	2.34	2.82
CO_2	0.02	0.32	0.09	0.51	0.26	0.43	0.04
Mg#	57	61	61	60	52	54	56
Q							
Or	9.7	9.4	7.2	6.8	7.9	8.5	6.8
Ab	19.2	17.5	21.4	21.1	21.6	20.8	21.5
An	17.2	22.1	22.5	23.2	12.9	13.0	25.4
Ne	7.4	2.5	1.3	1.1	12.2	12.5	
Di	12.1	12.2	11.3	11.9	12.5	12.5	11.6
He	5.8	4.9	4.8	5.1	7.3	7.0	5.8
En							2.3
Fs							1.3
Fo	10.5	13.8	13.1	12.8	7.9	8.3	8.6
Fa	6.3	7.0	7.1	6.9	5.8	5.8	5.4
Mi	4.0	4.0	4.0	4.1	4.0	3.9	4.0
Il	5.5	5.2	5.1	5.2	5.2	4.8	5.4
Ap	2.2	1.9	2.0	1.9	2.8	2.9	1.9

Cross section	Bailongdong								
sample	Bai-1	Bai-2	Bai-3	Bai-4	Bai-5	Bai-6-1	Bai-6-2	Bai-7	Bai-8
Lava Type	Ak	Ak	Ak	Th	Th	Th	Th	Th	Th
SiO_2	45.74	45.76	46.25	51.17	51.16	50.33	50.29	50.21	49.94
TiO_2	2.75	2.83	2.70	1.88	1.88	2.01	2.05	2.12	1.98
Al_2O_3	14.29	14.29	14.68	14.96	15.06	15.58	15.88	15.73	15.15
Fe_2O_3	13.23	13.45	13.23	11.79	11.20	11.18	11.14	11.14	12.23
MnO	0.16	0.17	0.17	0.13	0.14	0.14	0.14	0.14	0.15
MgO	8.12	7.94	7.27	6.97	7.76	7.36	7.72	7.05	8.26
CaO	8.46	8.31	7.85	8.53	8.25	8.64	8.61	9.18	8.63
Na_2O	3.76	4.06	4.51	2.92	2.89	2.94	2.77	2.96	2.31
K_2O	2.29	2.02	1.55	1.18	1.14	1.34	1.31	1.38	0.66
P_2O_5	1.01	1.06	1.13	0.38	0.39	0.45	0.46	0.49	0.32
Sum	99.81	99.89	99.34	99.91	99.87	100.00	100.37	100.40	99.63
H_2O^+	2.63	2.47	2.95	0.96	2.37	2.40	1.39	1.42	2.66
CO_2	0.26	0.28	0.00	0.22	0.00	0.03	0.22	0.35	0.36
Mg#	58	57	55	57	60	59	60	58	60
Q				0.7	0.3				1.7
Or	13.7	12.1	9.3	7.0	6.8	8.0	7.8	8.2	4.0
Ab	17.8	20.0	26.2	25.0	24.7	25.3	23.5	25.1	19.8
An	15.5	15.0	15.5	24.5	25.0	25.5	27.1	25.7	29.4
Ne	7.8	8.0	6.8						
Di	11.2	10.8	8.9	8.4	7.7	8.2	7.2	9.3	6.6
He	5.2	5.2	4.6	4.4	3.4	3.8	3.1	4.3	3.0
En				13.6	15.9	11.2	13.4	9.2	17.8
Fs				8.2	8.1	5.8	6.6	4.9	9.4
Fo	10.7	10.5	10.0			2.4	1.8	2.9	
Fa	6.2	6.3	6.6			1.4	1.0	1.7	
Mi	4.1	4.2	4.2	3.7	3.5	3.5	3.5	3.5	3.8
Il	5.3	5.4	5.2	3.6	3.6	3.8	3.9	4.0	3.8
Ap	2.4	2.5	2.7	0.9	0.9	1.0	1.1	1.1	0.7

Samples Bai-6-1 and -2 from same flow.

Cross section	Bailongdong								
sample	Bai-9	Bai-10	Bai-11	Bai-12	Bai-13	Bai-15	Bai-17	Bai-18	Bai-19
Lava Type	Ak	Tr	Th	Th	Th	Th	Th	Th	Th
SiO_2	44.92	46.68	51.61	51.46	51.81	49.89	50.30	51.32	50.41
TiO_2	2.63	2.62	1.78	1.76	1.77	1.97	1.90	1.85	1.99
Al_2O_3	13.80	14.50	15.24	15.32	15.10	14.99	14.99	15.19	15.46
Fe_2O_3	13.40	13.18	11.21	11.08	11.30	12.40	11.90	11.13	11.03
MnO	0.18	0.17	0.13	0.13	0.14	0.15	0.12	0.15	0.12
MgO	9.18	8.42	7.54	7.61	6.87	7.61	6.65	6.86	7.73
CaO	9.20	9.06	8.82	8.64	9.04	8.41	9.61	8.83	8.49
Na_2O	3.08	2.69	2.76	2.71	2.70	3.21	3.06	3.27	2.85
K_2O	1.98	1.92	0.81	0.88	0.59	0.94	0.98	1.13	1.52
P_2O_5	1.09	0.83	0.31	0.31	0.28	0.33	0.31	0.36	0.43
Sum	99.46	100.07	100.21	99.90	99.60	99.90	99.82	100.09	100.03
H_2O^+	2.48	2.16	1.79	2.25	1.05	1.66	0.98	0.39	1.53
CO_2	0.00	0.00	0.12	0.30	0.20	0.20	0.80	0.27	0.00
Mg#	60	58	60	60	57	57	55	58	61
Q			1.8	1.8	3.9				
Or	11.9	11.5	4.8	5.2	3.5	5.6	5.9	6.7	9.0
Ab	16.8	22.5	23.5	23.2	23.1	27.4	26.2	27.8	24.3
An	18.3	22.0	27.0	27.3	27.7	24.0	24.5	23.6	25.1
Ne	5.2	0.2							
Di	11.8	9.9	8.4	7.8	8.5	8.6	11.3	9.8	8.3
He	5.0	4.5	3.9	3.5	4.4	4.4	6.3	5.0	3.5
En			15.0	15.5	13.4	9.5	9.1	10.7	11.5
Fs			8.0	8.1	7.9	5.5	5.8	6.3	5.6
Fo	12.4	11.6				3.9	1.7	1.4	2.8
Fa	6.7	6.6				2.5	1.2	0.9	1.5
Mi	4.2	4.1	3.5	3.5	3.5	3.9	3.7	3.5	3.4
Il	5.1	5.0	3.4	3.4	3.4	3.8	3.6	3.5	3.8
Ap	2.6	2.0	0.7	0.7	0.7	0.8	0.7	0.8	1.0

Cross section	Bailongdong					ZBG	Jieshaba	
sample	Bai-20	Bai-21	Bai-22	Bai-23	Bai-24	Z-2	J-1	J-14
Lava Type	Tr	Tr	Tr	Tr	Tr	Ak	Th	Ak
SiO_2	47.41	47.53	49.18	48.75	48.68	45.11	51.45	45.78
TiO_2	2.48	2.43	2.20	2.26	2.29	2.80	1.89	2.72
Al_2O_3	14.74	14.83	15.64	15.62	15.59	14.32	15.24	14.23
Fe_2O_3	13.00	12.95	11.35	11.55	11.73	13.85	10.98	13.95
MnO	0.17	0.16	0.13	0.15	0.14	0.18	0.15	0.17
MgO	8.83	9.01	7.64	6.47	5.98	7.57	6.60	8.40
CaO	9.02	8.91	9.33	9.44	9.67	7.95	9.30	8.77
Na_2O	2.52	2.04	2.61	3.38	3.11	4.40	3.15	3.76
K_2O	1.78	1.60	1.63	1.86	1.88	2.82	0.84	1.22
P_2O_5	0.63	0.60	0.50	0.53	0.55	1.12	0.35	0.91
Sum	100.58	100.06	100.21	100.01	99.62	100.11	99.93	99.90
H_2O^+	1.94	2.64	1.05	0.38	0.67	1.92	1.81	4.60
CO_2	0.04	0.52	0.28	0.04	0.14	0.26	0.43	0.04
Mg#	60	61	60	55	53	55	57	57
Q							0.9	
Or	10.6	9.5	9.7	11.1	11.2	7.3	5.0	7.3
Ab	21.4	17.4	22.3	25.6	26.4	21.4	27.0	23.8
An	23.7	26.8	26.3	22.1	23.3	22.5	25.2	18.6
Ne				1.8	0.1	1.3		4.6
Di	9.7	7.8	9.6	11.6	11.2	11.3	10.3	10.7
He	4.2	3.3	4.2	6.0	6.4	4.8	5.2	5.2
En	2.8	10.9	7.6				11.8	
Fs	1.4	5.3	3.7				6.9	
Fo	10.4	5.7	4.9	7.6	6.9	13.1		11.4
Fa	5.7	3.0	2.7	5.0	5.0	7.1		7.0
Mi	4.0	4.0	3.5	3.6	3.7	4.0	3.2	4.0
Il	4.7	4.7	4.2	4.3	4.4	5.1	3.6	5.2
Ap	1.5	1.4	1.2	1.2	1.3	2.0	0.8	2.1

Cross section	Damaping									
sample	ZB-111	ZB-41	ZB-49	ZB-51	ZB-53	ZB-83	ZB-77	D-1	D-3	D-5
Lava Type	Ak	Tr	Th	Th	Ak	Ak	Tr	Ak	Tr	Th
SiO_2	46.92	48.78	50.30	50.53	44.14	46.33	48.02	44.93	45.89	49.84
TiO_2	2.78	2.29	2.25	1.96	2.69	2.19	2.37	2.72	2.62	2.04
Al_2O_3	14.15	15.03	14.39	14.89	14.07	14.86	15.66	13.54	13.85	15.62
Fe_2O_3	13.37	12.53	12.92	12.27	15.04	13.67	11.78	13.48	13.52	11.01
MnO	0.16	0.21	0.16	0.16	0.17	0.18	0.15	0.17	0.18	0.13
MgO	7.56	6.29	6.62	6.96	7.26	6.12	6.76	10.62	9.15	7.36
CaO	8.23	9.84	8.58	9.20	9.04	7.49	9.47	8.18	9.66	8.87
Na_2O	4.37	2.99	3.27	2.80	4.46	5.64	3.87	3.52	2.20	3.42
K_2O	1.62	1.39	1.06	0.89	1.97	2.29	1.55	2.39	1.42	1.34
P_2O_5	0.88	0.66	0.38	0.32	1.26	1.27	0.57	0.89	0.70	0.46
Sum	100.04	100.01	99.93	99.98	100.08	100.04	100.20	100.44	99.19	100.08
H_2O^+				2.80	1.96	1.45	0.63	4.26	3.50	1.83
CO_2				1.57	0.47	0.41	0.33	0.32	0.09	0.51
Mg#	55	52	53	52	52	50	56	63	60	60
Q				0.6						
Or	9.7	8.3	6.3	5.3	11.8	13.7	9.2	14.2	8.6	8.0
Ab	24.8	25.6	27.9	23.9	14.0	19.9	24.4	12.7	19.0	29.2
An	14.4	23.7	21.7	25.6	12.7	8.5	20.9	14.2	24.3	23.6
Ne	6.8				13.1	15.3	4.7	9.5		
Di	11.4	10.8	9.7	9.7	12.3	10.0	12.3	12.4	11.3	10.0
He	5.7	6.5	5.7	5.3	7.6	6.9	6.1	4.5	4.9	4.4
En		4.4	9.9	13.0					4.2	3.6
Fs		3.0	6.7	8.2					2.1	1.8
Fo	9.6	4.5	1.6		8.8	7.5	7.9	14.7	9.7	7.2
Fa	6.1	3.4	1.2		6.9	6.6	5.0	6.7	5.3	4.0
Mi	4.2	3.9	4.0	3.8	4.7	4.3	3.7	3.9	4.0	3.2
Il	5.3	4.4	4.3	3.8	5.1	4.2	4.5	5.2	5.1	3.9
Ap	2.1	1.6	0.9	0.7	3.0	3.0	1.3	2.1	1.7	1.1

Cross section	Xiliuling					
sample	ZX-36	ZX-42	ZX-44	ZX-48	ZX-62	ZX-72
Lava Type	Ak	Th	Ak	Th	Th	Tr
SiO_2	45.17	50.64	45.19	50.95	49.85	47.76
TiO_2	2.50	1.82	2.65	1.84	2.21	2.38
Al_2O_3	14.06	15.21	13.90	15.34	16.11	15.93
Fe_2O_3	13.42	11.28	13.91	11.86	11.28	12.35
MnO	0.17	0.14	0.18	0.15	0.14	0.15
MgO	7.85	8.11	9.95	6.89	6.49	6.37
CaO	8.82	8.44	9.62	8.88	9.01	8.96
Na_2O	4.25	2.80	2.22	3.22	2.90	3.73
K_2O	2.16	1.02	2.06	0.62	1.84	2.11
P_2O_5	1.25	0.35	0.73	0.28	0.50	0.60
Sum	99.65	99.81	100.41	100.03	100.33	100.34
H_2O^+						
CO_2						
Mg#	56	61	61	56	56	53
Q				0.1		
Or	12.9	6.1	12.2	3.7	10.9	12.5
Ab	16.2	23.9	14.6	27.5	24.6	22.0
An	13.1	26.2	22.1	25.8	25.7	20.6
Ne	11.0		2.3			5.3
Di	12.4	7.8	12.1	8.9	8.7	10.5
He	6.3	3.4	5.0	4.8	4.4	10.5
En		15.9		13.2	6.6	
Fs		7.9		8.2	3.8	
Fo	9.9	0.6	13.5		4.0	7.8
Fa	6.3	0.3	7.0		2.5	5.6
Mi	4.2	3.5	4.3	3.7	3.5	3.8
Il	4.8	3.5	5.1	3.5	4.2	4.5
Ap	3.0	0.8	1.7	0.7	1.2	1.4

Table 2 Trace Element Abundances in Hannuoba Basalts

Cross section	Zhouba							
sample	Zh-1	Zh-3	Zh-4	Zh-6	Zh-9	Zh-12	Zh-14-1	Zh-14-2
Lava Type	Ak	Ak	Th	Ak	Th	Ak	Ak	Ak
P%	0.41	0.37	0.16	0.51	0.16	0.50	0.51	0.51
Rb	18.1	32.1	6.0	45.3	17.6	49.6	51.5	35.7
Sr	913	897	459	1218	459	1526	1595	1429
Ba	542	531	244	557	281	610	622	536
Sc	20	18	21	11	21	10	10	10
Ti%	1.65	1.56	1.14	1.40	1.15	1.44	1.45	1.43
V	192	167	151	129	147	125	117	126
Cr	225	164	178	123	183	125	125	124
Co	60	56	48	47	48	47	47	47
Ni	209	156	142	121	137	124	125	132
Zn	140	142	119	198	116	172	167	168
Ga	22	23	20	27	21	27	28	27
Y	24	23	18	22	19	21	21	21
Zr	293	252	134	389	147	376	383	376
Hf	6.8	5.6	3.2	8.1	3.5	8.3	8.4	8.2
Nb	75	61	22	100	25	96	95	97
Ta	4.4	3.6	1.3	5.6	1.4	5.8	6.0	5.9
Th	6.0	4.5	2.2	8.1	2.2	8.6	8.6	8.2
La	49	41	16.1	66	17.3	65	66	67
Ce	100	80	34	126	37	130	131	130
Nd	47	38	18	55	19	56	58	58
Sm	10.1	8.8	4.8	11.5	5.0	11.4	10.5	11.9
Eu	3.19	2.82	1.62	3.73	1.72	3.61	3.71	3.71
Tb	1.10	1.07	0.61	1.14	0.74	1.22	1.27	1.20
Yb	1.75	1.66	1.46	0.96	1.53	0.97	1.10	1.09
Lu	0.23	0.21	0.22	0.13	0.20	0.13	0.13	0.13

Cross section	Zhouba			
sample	Zh-17	Zh-19	Zh-20	Zh-21
Lava Type	Th	Th	Ak	Th
P%	0.16	0.19	0.45	0.20
Rb	17.6	20.2	49.0	22.7
Sr	416	477	1184	497
Ba	254	284	445	305
Sc	20	20	9.4	20
Ti%	1.13	1.12	1.23	1.31
V	137	150	103	153
Cr	197	195	91	182
Co	49	51	41	44
Ni	143	135	90	113
Zn	121	114	168	115
Ga	21	22	27	21
Y	17	19	19	19
Zr	131	157	361	164
Hf	3.3	3.7	7.5	3.9
Nb	24	31	92	32
Ta	1.5	1.8	5.5	1.8
Th	2.1	2.5	7.8	2.8
La	16.8	19.8	55	20.7
Ce	34	41	105	44
Nd	18	21	47	23
Sm	4.8	5.2	9.8	5.5
Eu	1.66	1.81	3.18	1.93
Tb	0.64	0.70	1.01	0.73
Yb	1.26	1.39	0.83	1.40
Lu	0.20	0.21	0.12	0.21

Cross section	Erdaobian Section						
sample	R-2	R-4	R-6	R-8	R-9	R-11	R-19
Lava Type	Ak	Ak	Ak	Ak	Ak	Ak	Tr
P%	0.41	0.34	0.37	0.35	0.52	0.54	0.36
Rb	32.2	33.0	20.0	28.6	35.2	37.8	22.0
Sr	1118.2	820.1	815.0	832.5	1223.0	1325.3	838.0
Ba	590	540	560	520	650	570	510
Sc	13.23	18.95	19.66	19.75	12.45	13.35	19.78
Ti%	1.73	1.61	1.60	1.63	1.63	1.49	1.68
V	163.8	180.3	193.2	174.8	163.9	145.5	199.0
Cr	142.1	186.3	214.5	185.7	77.4	130.3	177.8
Co	55.8	57.8	57.1	56.5	49.3	47.5	54.1
Ni	182.0	211.0	203.0	189.0	116.0	149.0	175.0
Zn	137.6	129.5	136.1	128.6	170.0	161.2	156.8
Ga	24.0	20.0	20.5	21.5	25.5	25.3	23.1
Y	20.4	22.3	23.1	22.3	21.0	22.3	23.3
Zr	295.1	252.1	255.9	258.4	337.8	356.7	264.8
Hf	5.7	5.3	5.2	5.4	6.8	6.9	5.4
Nb	71.3	59.1	61.1	62.6	84.6	89.4	63.1
Ta	4.2	3.6	3.5	3.7	5.1	5.1	3.6
Th	5.3	4.5	4.5	4.5	6.9	7.1	4.2
La	47.8	36.9	39.3	38.3	57.9	62.6	37.6
Ce	101.3	79.1	84.2	81.1	122.1	130.1	79.9
Nd	46.4	38.2	40.3	38.3	55.5	57.5	38.5
Sm	9.24	7.8	8.32	8.21	10.5	10.9	8.34
Eu	2.95	2.55	2.66	2.62	3.33	3.48	2.61
Tb	1.21	0.91	1.09	1.06	1.12	1.22	0.97
Ho	0.65	1.09	1.05	0.88	0.67	0.51	0.71
Yb	1.07	1.34	1.57	1.49	0.97	1.11	1.64
Lu	0.16	0.19	0.21	0.20	0.13	0.16	0.20

Cross section	Bailongdong						
sample	Bai-1	Bai-2	Bai-3	Bai-4	Bai-6-2	Bai-7	Bai-9
Lava Type	Ak	Ak	Ak	Th	Th	Th	Ak
P%	0.44	0.46	0.49	0.17	0.20	0.21	0.48
Rb	45.7	21.1	22.3	14.1	15.8	16.6	26.8
Sr	1285	1172	1346	490	496	547	1162
Ba	702	661	695	262	260	292	591
Sc	12	12	9.5	22	20	20	15
Ti%	1.65	1.70	1.62	1.13	1.23	1.27	1.58
V	150	157	134	143	147	153	157
Cr	177	175	138	199	154	143	197
Co	54	55	48	49	49	47	56
Ni	153	157	139	128	131	121	175
Zn	148	157	164	115	114	110	142
Ga	25	25	27	21	21	22	23
Y	20	20	20	18	17	18	21
Zr	326	331	366	144	154	166	293
Hf	7.4	7.5	7.8	3.5	3.7	3.9	6.5
Nb	82	82	90	24	31	32	76
Ta	5.2	4.9	5.6	1.3	1.7	1.9	4.2
Th	6.2	7.3	7.0	1.9	2.5	2.2	6.6
La	58	60	65	18.6	19.4	21.4	54
Ce	113	122	128	42	43	45	114
Nd	51	55	58	22.3	22.8	23.4	51
Sm	10.5	10.9	11.4	5.1	5.5	5.8	9.9
Eu	3.40	3.57	3.72	1.80	1.88	1.95	3.23
Tb	1.18	1.20	1.15	0.81	0.74	0.78	1.03
Yb	0.94	0.96	0.88	1.42	1.37	1.46	1.26
Lu	0.14	0.14	0.11	0.20	0.19	0.22	0.17

Bailongdong

Cross section sample	Bai-10	Bai-13	Bai-17	Bai-18	Bai-20	Bai-22	Bai-23
Lava Type	Tr	Th	Th	Th	Tr	Tr	Tr
P%	0.36	0.12	0.14	0.16	0.27	0.22	0.23
Rb	28.2	7.0	13.2	12.8	23.7	17.4	20.0
Sr	890	419	428	481	721	631	662
Ba	488	196	224	265	418	299	343
Sc	20	21	21	20	20	19	19
Ti%	1.60	1.06	1.14	1.11	1.49	1.32	1.35
V	169	144	152	156	174	164	169
Cr	204	172	156	174	167	166	183
Co	59	47	50	48	56	49	45
Ni	170	121	129	135	162	119	109
Zn	125	120	124	114	125	105	106
Ga	23	20	21	21	22	21	23
Y	21	17	18	16	20	17	18
Zr	245	115	120	126	205	169	179
Hf	5.8	2.9	3.0	3.1	4.6	3.7	3.8
Nb	60	15	18	23	47	37	39
Ta	3.6	0.98	1.0	1.3	2.7	2.0	2.2
Th	5.3	1.1	1.2	1.4	3.1	2.5	2.4
La	42	11.7	13.1	15.2	33.4	21.5	22.8
Ce	85	26	30	34	60	47	46
Nd	40	14.9	17.1	18.2	29.2	23.6	22.2
Sm	8.2	4.2	4.5	4.6	6.9	5.3	5.6
Eu	2.77	1.52	1.61	1.62	2.24	1.84	1.87
Tb	1.15	0.66	0.69	0.73	0.93	0.80	0.80
Yb	1.54	1.47	1.39	1.29	1.38	1.24	1.32
Lu	0.23	0.21	0.20	0.18	0.24	0.19	0.19

Cross section	Damaping									
sample	ZB-111	ZB-22	ZB-41	ZB-49	ZB-53	ZB-83	ZB-77	D-1	D-3	D-5
Lava Type	Ak	Th	Tr	Th	Ak	Ak	Tr	Ak	Tr	Th
P%	0.38	-	0.29	0.17	0.55	0.55	0.25	0.39	0.31	0.20
Rb	24.8	15.4	21.0	13.3	35.0	37.0	16.3	62.9	17.3	15.4
Sr	1120	542	668	442	1085	1345	732	1151	839.6	541.6
Ba	667	294	367	259	453	460	396	681	432	280
Sc	12	21	20	20	12	9.5	19	11.80	19.04	18.27
Ti%	1.67		1.37	1.35	1.61	1.31	1.42	1.64	1.57	1.22
V	164	159	160	170	173	133	199	147.9	190.2	161.8
Cr	104	197	170	154	89	86	192	240.0	198.3	139.7
Co	50	41	55	46	53	41	44	61.0	49.3	41.0
Ni	132	128	172	111	133	105	69	272.0	182.0	134.0
Zn	153	114	132	154	179	186	99	142.4	139.1	117.7
Ga	24	21	21	22	25	27	22	20.8	19.6	20.3
Y	19	19	22	21	20	20	18	19.1	21.4	17.8
Zr	316	158	194	156	298	379	182	293.6	225.8	162.7
Hf	6.6	3.5	4.4	3.7	5.9	7.2	3.7	5.8	4.4	3.3
Nb	77	26	42	24	83	99	42	69.5	52.0	32.2
Ta	4.2	1.3	2.2	1.2	4.3	5.2	2.1	4.5	3.1	2.0
Th	6.1	1.5	3.1	1.6	5.4	6.9	2.4	6.0	3.9	2.6
La	49	19.4	31.0	16.6	55	61	23.8	44.30	28.10	18.80
Ce	97	42	64	36	110	120	49	94.70	65.79	41.28
Nd	44	22	31	20	49	53	24	40.70	33.49	22.81
Sm	9.3	5.4	7.4	5.3	10.6	10.8	5.7	8.40	7.20	5.10
Eu	2.94	18.6	2.44	1.86	3.30	3.44	1.91	2.80	2.34	1.77
Tb	0.95	0.80	0.96	0.78	1.08	1.08	0.84	1.08	0.91	0.81
Yb	0.96	1.53	1.65	1.71	0.95	0.96	1.17	0.87	1.40	1.30
Lu	0.15	0.23	0.25	0.24	0.13	0.11	0.17	0.13	0.20	0.20

Cross section	Xiliuling						ZBG	Jieshaba	
sample	ZX-36	ZX-42	ZX-44	ZX-48	ZX-62	ZX-72	Z-2	J-1	J-14
Lava Type	Ak	Th	Ak	Th	Th	Tr	Ak	Th	Ak
P%	0.55	0.15	0.32	0.12	0.22	0.26	0.50	0.15	0.40
Rb	28.8	10.5	30.2	3.2	18.8	22.6	47.0	10.9	49.3
Sr	1251	400	989	431	661	746	1228	473	1115
Ba	556	197	501	224	395	366	1136	241	641
Sc	13	20	19	21	18	18	10.3	20.2	10.2
Ti%	1.50	1.09	1.59	1.10	1.32	1.43	1.68	1.13	1.63
V	154	144	195	155	180	186	146.3	153.4	151.5
Cr	130	195	189	164	126	155	160.3	159.6	119.1
Co	50	48	58	46	40	46	47.3	39.7	45.3
Ni	144	154	193	122	76	119	166.0	113.0	138.6
Zn	159	114	123	126	101	112	177.7	115.3	170.3
Ga	25	20	21	21	22	24	26.6	20.3	25.1
Y	22	16	20	18	17	18	20.4	18.2	19.5
Zr	346	128	232	120	175	195	357	139	312
Hf	7.1	2.9	4.9	2.9	3.8	4.1	6.9	2.8	6.2
Nb	87	22	58	16	35	44	88.2	23.7	76.6
Ta	5.1	1.3	3.3	0.87	2.0	2.5	5.5	1.5	4.8
Th	6.7	1.4	4.4	0.9	2.1	2.7	7.4	2.0	6.7
La	62	14.5	34.5	11.8	22.8	25.3	54.8	14.3	49.8
Ce	126	30	71	27	49	52	118.6	33.9	101.6
Nd	56	17	34	15	23	25	55.4	18.3	48.5
Sm	11.0	4.4	7.4	4.2	5.3	5.7	11.2	4.45	9.97
Eu	3.57	1.57	2.42	1.58	1.88	1.97	3.52	1.59	3.10
Tb	1.21	0.70	0.96	0.65	0.75	0.75	1.26	0.76	1.11
Yb	1.09	1.26	1.33	1.35	1.24	1.24	0.90	1.30	1.00
Lu	0.14	0.18	0.18	0.20	0.18	0.18	0.13	0.20	0.14

Table 1-3a. Major Element Composition for Standard Rock BHVO-1

	SiO_2	TiO_2	Al_2O_3	Fe_2O_3	FeO	MnO
Mean[1]	49.94	2.71	13.80	2.82	8.58	0.168
SD	±0.54	±0.06	±0.21	±0.24	±0.09	±0.008
Mean[2]	50.149	2.763	13.792	12.214	-	0.176
STD.	0.1572	0.0078	0.0654	0.0186	-	0.0032
% ERROR	0.314	0.282	0.474	0.153	-	1.851

	MgO	CaO	Na_2O	K_2O	P_2O_5
Mean[1]	7.23	11.40	2.26	0.520	0.273
SD	±0.22	±0.17	±0.07	±0.035	±0.025
Mean[2]	7.081	11.453	2.312	0.535	0.275
STD.	0.0328	0.0236	0.0797	0.0196	0.0042
% ERROR	0.463	0.206	3.446	3.673	1.532

Table 1-3b. Trace Element Composition for Standard Rock BHVO-1

Au-Tube	Nb	Zr	Sr	Ni	Cr	V
Mean[1]	19	179	403	121	289	317
	±2	±21	±25	±2	±22	±12
Mean[2]	18.93	183.82	406.07	120.59	290.08	286.42
STD	0.40	8.77	3.65	1.82	2.50	3.87
% ERROR	2.13	4.77	0.90	1.51	0.86	1.35

Mo-Tube	Y	Sr	Ga
Mean[1]	27.6	403	21
	±1.7	±25	±2
Mean2	25.24	396.69	22.04
STD	0.41	1.68	0.74
% ERROR	1.62	0.42	3.38

Mean[1] BHVO-1 values from Gladney and Roelandts (1988).

Mean[2], STD and %ERROR are based on 13 replicated analyses of BHVO-1 at University of Mass by XRF method. These BHVO-1 were done at the same time as the analyses of the Hannuoba lavas. STD = standard deviation. % ERROR = 100 X STD/Mean.

Table 1-3c. Precision Estimates for Data Obtained by Neutron Activation

	MEAN	STD	% Error
La	26.22	0.21	0.79
Ce	66.18	1.40	2.12
Nd	41.30	0.90	2.19
Sm	10.74	0.13	1.20
Eu	3.63	0.04	1.02
Tb	1.63	0.18	11.05
Yb	3.34	0.11	3.40
Lu	0.47	0.01	2.66
Hf	8.06	0.18	2.21
Th	1.98	0.23	11.53
Ta	1.73	0.04	2.43
Cr	125.45	2.46	1.96
Co	43.92	0.83	1.89
Sc	30.80	0.66	2.15

Data from 6 replicated analyses of MKCore, the MIT standard rock. The Hannuoba data were obtained in 6 different irradiations and this standard rock was included in each irradiation set.
STD = standard deviation. % ERROR = 100 X STD/Mean.

TABLE 1-4a. Chemical Analyses of Olivines in Basanite D-1

	Olivine xenocryst A						
	1	2	3	4	5	6	7
SiO_2	40.65	40.04	39.05	38.99	39.33	37.44	37.33
TiO_2	0	0	0	0	0	0.01	0.04
Al_2O_3	0.01	0	0	0.01	0.02	0.06	0.13
Cr_2O_3	0	0.09	0.07	0.01	0.05	0.04	0.06
FeO	8.72	9.68	14.11	16.59	14.16	24.44	26.95
MnO	0.17	0.14	0.23	0.26	0.24	0.40	0.43
MgO	50.32	49.28	45.84	43.82	45.98	37.28	35.15
CaO	0.04	0.03	0.05	0.10	0.12	0.33	0.46
Total	99.91	99.25	99.36	99.79	99.91	99.99	100.55
Ca(ppm)	286	214	357	715	858	2358	3288
Fo	91.1	90.0	85.3	82.5	85.3	73.1	69.9
	STOICHIOMETRIC						
	1	2	3	4	5	6	7
Si	0.993	0.989	0.985	0.990	0.987	0.987	0.990
Ti	0.000	0.000	0.000	0.000	0.000	0.000	0.001
Al	0.000	0.000	0.000	0.000	0.001	0.002	0.004
Cr	0.003	0.003	0.001	0.000	0.001	0.001	0.010
Fe	0.178	0.200	0.298	0.352	0.297	0.539	0.598
Mn	0.003	0.003	0.005	0.006	0.005	0.009	0.010
Mg	1.831	1.815	1.724	1.658	1.719	1.465	1.390
Ca	0.001	0.001	0.001	0.003	0.003	0.009	0.013
Total	3.007	3.010	3.014	3.010	3.013	3.012	3.006

(continued)

	Olivine xegnocryst B						
	1	2	3	4	5	6	7
SiO^2	39.78	40.77	39.71	39.19	38.14	37.49	36.74
TiO_2	0	0	0	0	0	0	0.02
Al_2O_3	0	0	0	0.05	0.03	0.04	0.09
Cr_2O_3	0.06	0.05	0.04	0.07	0.03	0	0.05
FeO	8.96	8.76	13.38	17.35	18.06	20.22	24.39
MnO	0.14	0.13	0.21	0.19	0.31	0.28	0.41
MgO	50.10	49.79	46.30	43.81	42.30	40.93	37.34
CaO	0.04	0.04	0.04	0.12	0.12	0.25	0.38
Total	99.08	99.53	99.68	100.77	99.00	99.21	99.43
Ca(ppm)	286	286	286	858	858	1788	2716
Fo	90.9	91.0	86.0	81.8	80.7	78.3	73.2
	STOICHIOMETRIC						
	1	2	3	4	5	6	7
Si	0.982	0.999	0.993	0.988	0.985	0.977	0.976
Ti	0.000	0.000	0.000	0.000	0.000	0.000	0.000
Al	0.000	0.000	0.000	0.001	0.001	0.001	0.003
Cr	0.001	0.001	0.001	0.001	0.001	0.000	0.001
Fe	0.185	0.179	0.280	0.366	0.390	0.441	0.542
Mn	0.003	0.003	0.004	0.004	0.007	0.006	0.009
Mg	1.844	1.818	1.727	1.646	1.628	1.590	1.479
Ca	0.001	0.001	0.001	0.003	0.003	0.007	0.011
Total	3.017	3.001	3.006	3.010	3.014	3.022	3.021

TABLE 1-4b. Chemical Analyses of Olivines in Basanite D-1

Olivine-xenocryst			Olivine in matrix				Olivine in Lherzolite
	C	D	A	B	C	D	RANGE
SiO_2	40.11	40.98	37.11	37.78	36.26	36.51	40.37-41.65
TiO_2	0	0	0.01	0.02	0.05	0.04	0-0.03
Al_2O_3	0	0	0.10	0.13	0.14	0.12	0-0.05
Cr_2O_3	0	0.03	0.04	0.08	0.09	0.08	0-0.04
FeO	9.83	8.86	26.12	24.90	26.88	26.00	8.28-9.68
MnO	0.18	0.08	0.49	0.44	0.55	0.35	0-0.18
MgO	49.26	49.81	35.83	36.72	34.68	35.78	48.73-50.95
CaO	0.01	0.06	0.49	0.36	0.45	0.47	0.04-0.09
NiO		0.28					0.25-0.39
Total	99.38	100.11	100.18	100.43	99.09	99.34	
Ca(ppm)	72	429	3502	2573	3216	3359	357-643
Fo	89.9	90.9	70.5	72.4	69.2	70.6	89.9-91.3

--Olivine compositions were determined with an electron microprobe by Song in 1983, and olivine xenocryst D was analysed by T.Sisson in 1988 at MIT in lab of T. Grove.

--Olivine xenocrysts A and B are zoned, and 7 points have been counted crossing the grain for each olivine. Olivine xenocryst C and D is homogeneous in composition, and the data are the average of 5 point counts for C, and of 3 point counts for D.

--The data of 4 olivine grains (A, B, C and D) in the matrix are the average of 2-3 point couts for each.

--The range of olivine in lherzolite is based on olivines from six Hannuoba spinel-lherzolites and three Cr-diopside veins (Table 4-3a, Chapter 4).

Table 1-5. Estimated Incompatible Element Abundance Ratios in Sources of Alkalic Basalts from Hannuoba and Oceanic Islands

	Hannuoba	Marquesas	Honolulu, Hawaii	Chondrites
Ba/Nb	8.5±0.65	7.9	8.2-11.6	9.8
Ba/Th	114±11.2	-	164	83
Ba/La	13.5±1.20	8.6	13.5	9.9
Nb/Ta	17.0±0.34	-	13-14	17.6
La/Th	8.5±0.35	-	12.1	8.4
La/Nb	0.63±0.02	0.92	0.60-0.86	1.0
La/Ce	0.48±0.01	0.43	0.49	0.39
Ce/Nd	2.10±0.02	-	1.73	1.34
Sm/Nd	0.21±0.01	-	0.23	0.32
Sm/Eu	3.10±0.05	2.66	3.2	2.65
Zr/Nb	4.10±0.12	142	4.5-6.4	15.6
Zr/Hf	46.7±2.09	44	40	36
Sr/Nd	22.6±3.05	-	19.1-30.5	18.3
Th/Ta	1.27±0.33	-	0.7-1	1.74
$87/86^4$	0.70397			

1. Hannuoba data: mean of 6 samples (R-4, R-6, R-8, Zh-1, Zh-3 and ZX-44) which are interpreted to be the most primitive.

2. Marquesas source from Liotard et al., 1986.

3. Honolulu source from Clague and Frey, 1982.

4. Mean value of $^{87}Sr/^{86}Sr$ from Table 3-2.

FIGURES

FIGURE CAPTIONS

Figure 1-1. Geological map of Hannuoba Region (modified from BHTHED 1978). Sampling sections of Miocene basalt are indicated in lower right: 1 = Xiliuling, 2 = Bailondong, 3 = Damaping, 4 = Zhouba, 5 = Erdaobian, 6 = Jieshaba, 7 = Zhenbeiugou (ZBG).

Figure 1-2. Five stratigraphic sections through the Hannuoba basaltic plateau (see figure 1-1 for locations). Alkali basalts containing mantle xenoliths are indicated by diagonal lines; tholeiitic and transitional flows indicated by TH and TR, respectively. Cretaceous (K) and Quaternary (Q) sediments form the base and top of the sections. Samples studied (Tables 1-1 and 1-2) are indicated by number.

Figure 1-3. CIPW normative plot illustrating field of alkalic basalts, (open circles), containing mantle xenoliths; tholeiitic basalts (open triangles) with >50% SiO_2 and transitional basalts (open squares).

Figure 1-4. Major oxide - MgO variation diagrams showing fields of alkalic basalt (circles), tholeiitic basalt (asterisks) and transitional basalt (triangles). Note separation of alkalic and tholeiitic fields on SiO_2, FeO* (total iron), TiO_2, Na_2O, K_2O and P_2O_5 plots.

Figure 1-5. Chondrite - normalized REE diagram for alkalic (AB) and tholeiitic (Th) basalts from 5 Hannuoba stratigraphic sections. Values within parentheses indicate number of samples defining the range. Note that in all cases the fields defined by tholeiitic and alkalic lavas intersect in the HREE region. Transitional lavas have REE patterns intermediate to the Th and AB fields. Individual patterns (Zh-1, Zh-3, Bai-10) are for more mafic less evolved alkali basalts whose REE patterns intersect the fields defined by the more evolved alkalic basalts. This phenomenon is illustrated in the Erdaobian section where the three lavas with lower LREE have MgO of 9.4 to 10% whereas the three lavas with higher LREE have only 6.7 to 8.2% MgO.

Figure 1-6. La/Yb versus MgO showing higher LREE/HREE ratios in the alkali basalts and a broad inverse trend within the alkali basalt field. Sample D-1, discussed in the text, is labeled and the seven alkalic basalts with low Sc and HREE are circled.

Figure 1-7. Incompatible element abundances versus Th content illustrating a strong positive correlation, except for Rb which was mobilized by post-magmatic alteration.Lower right panel shows that Th is not correlated with MgO in Hannuoba lavas, although there is a broad inverse trend among the alkalic basalts.

Figure 1-8. Left. Compatible trace element abundances showing general positive correlations with MgO content. The outlined field at high Ni content on MgO-Ni plot indicates range of Ni in basalts containing high pressure xenoliths (from Hart and Allegre, 1980). Lines labeled 5% and 20% are for batch partial melts from a source with 2300 ppm Ni; lines labeled 5 and 10 are trajectories for olivine fractional crystallization (all theoretical lines from Hart and Davis, 1978).

Right. Ni-Th plot shows no correlation between compatible and incompatible element abundances. Yb and Sc versus Th shows a group of 7 alkalic basalt lavas (circled) with higher Yb and Sc but lower Th content. These lavas are also relatively high in MgO (see Yb and Sc versus MgO in Figure 1-9b).

Figure 1-9a. Ni/Co versus MgO. The decrease in Ni/Co ratio with decreasing MgO is not consistent with subtraction of only olivine (solid line labeled 1) calculated using DNi varying as a function of MgO (Hart and Davis, 1978) and a DNi/DCo = 4 for olivine. The data trend requires fractionation of phases with lower DNi/DCo; e.g., DNi/DCo ratios of 1.5 (line 2) or 1.2 (line 3) fit the data trend. Both clinopyroxene and garnet have DNi/DCo < 4. Subtraction of a solid with 62.5% Cpx and 28.5% garnet yield a DNi/DCo of ~1.60 based on data from Dupuy et al (1980) and Henderson (1980).

Figure 1-9b. Geochemical trends showing diversity within the alkalic basalts. Note that with decreasing MgO, Sc and Yb content decreases, CaO/Al_2O_3 decreases and Zr/Y increases. These trends are consistent with garnet and clinopyroxene control. Sample D-1 is offset in several trends (see text for an explanation).

Figure 1-10a. Various incompatible element ratios versus MgO content showing systematic differences between alkalic and tholeiitic lavas at a given MgO.

Figure 1-10b. La/Ce, Sm/Nd, Nb/Ta and Zr/Nb versus Th illustrating similar La/Ce and Nb/Ta in tholeiitic and alkalic lavas. However, tholeiitic lavas have variable and higher Sm/Nd and Zr/Nb than the alkalic lavas.

Figure 1-11. Geochemical trends of MgO vs. Ti/Zr and Zr/Y showing diversity within the alkalic basalts.

Figure 1-12a. Lower Panels: Normalized incompatible element diagrams comparing alkalic and tholeiitic lavas fromHannuoba, China (samples ZX-44 and ZX-42) and Hawaii; the same lava type from these diverse locations are remarkably similar.

Upper Panels: Normalized incompatible element diagrams for alkalic lavas from other continental locations.

Data Sources: Kilauea, Hawaii tholeiite - BHVO-1 (Govindaraju, 1984); Honolulu, Hawaii basanite - 68FS2 (Clague and Frey, 1982); Australia basanite - 2679 (Frey et al., 1978); Germany, Hessian Depression average alkali olivine basalt (Wedepohl, 1985); Tahiti-Nui basanite - 2S (Dostal et al., 1982); Samoa basanite - UPO-9 (Palacz and Saunders, 1986). Oceanic island average alkali basalt and primitive mantle normalizing values from Sun and McDonough, 1988.

Figure 1-12b. Incompatible element abundance ratios of the high MgO tholeiite ZX-42 over the primitive alkalic basalts ZX-44 and R-4.

Figure 1-13. Ba/Nb - La/Nb plot illustrating wide range among oceanic island basalts (from Weaver et al., 1986; Sun and McDonough, 1988) and similarity of alkalic Hannuoba lavas to oceanic island basalts with near chondritic Ba/Nb but less than chondritic La/Nb.

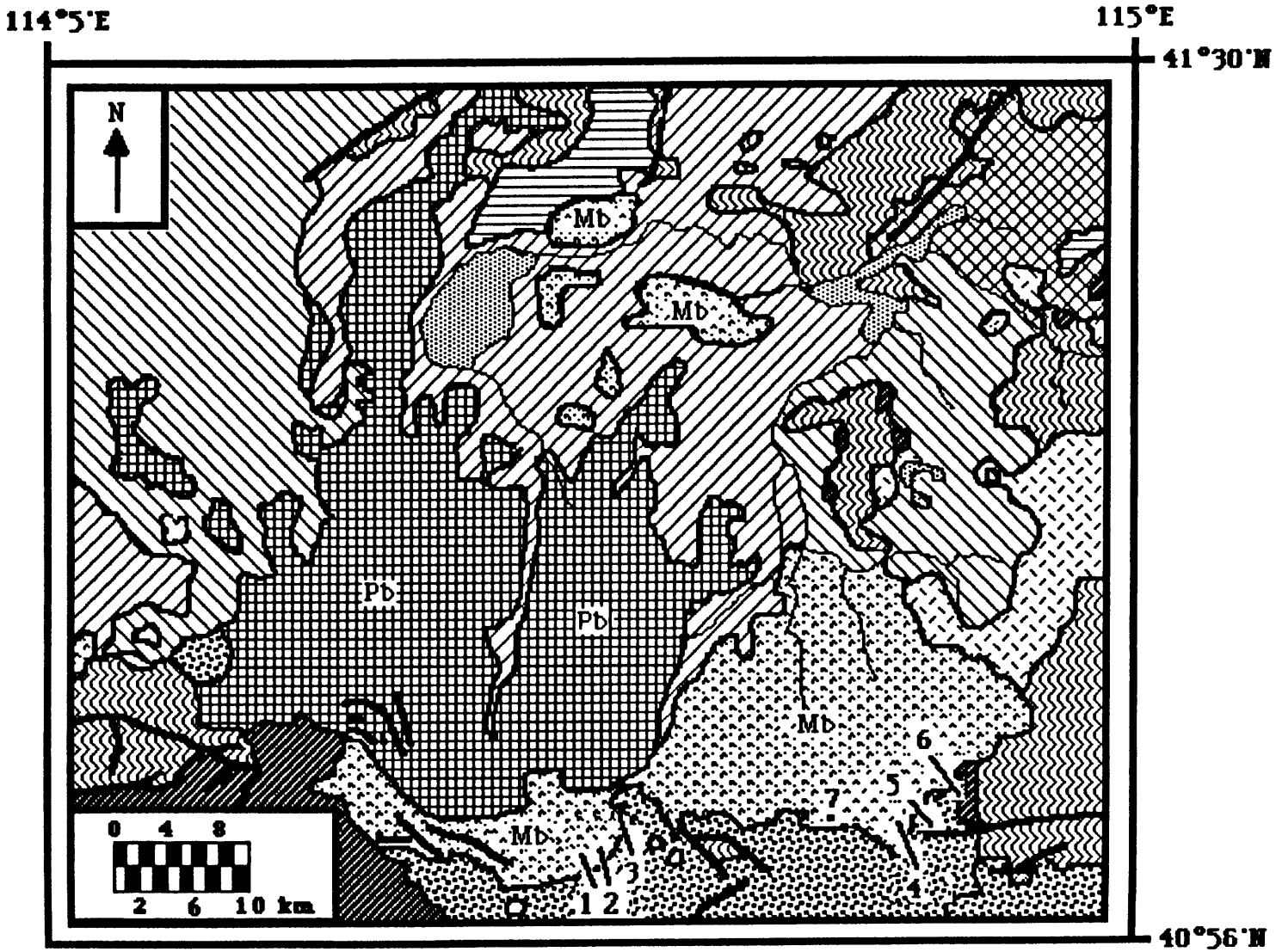

FIGURE 1-1

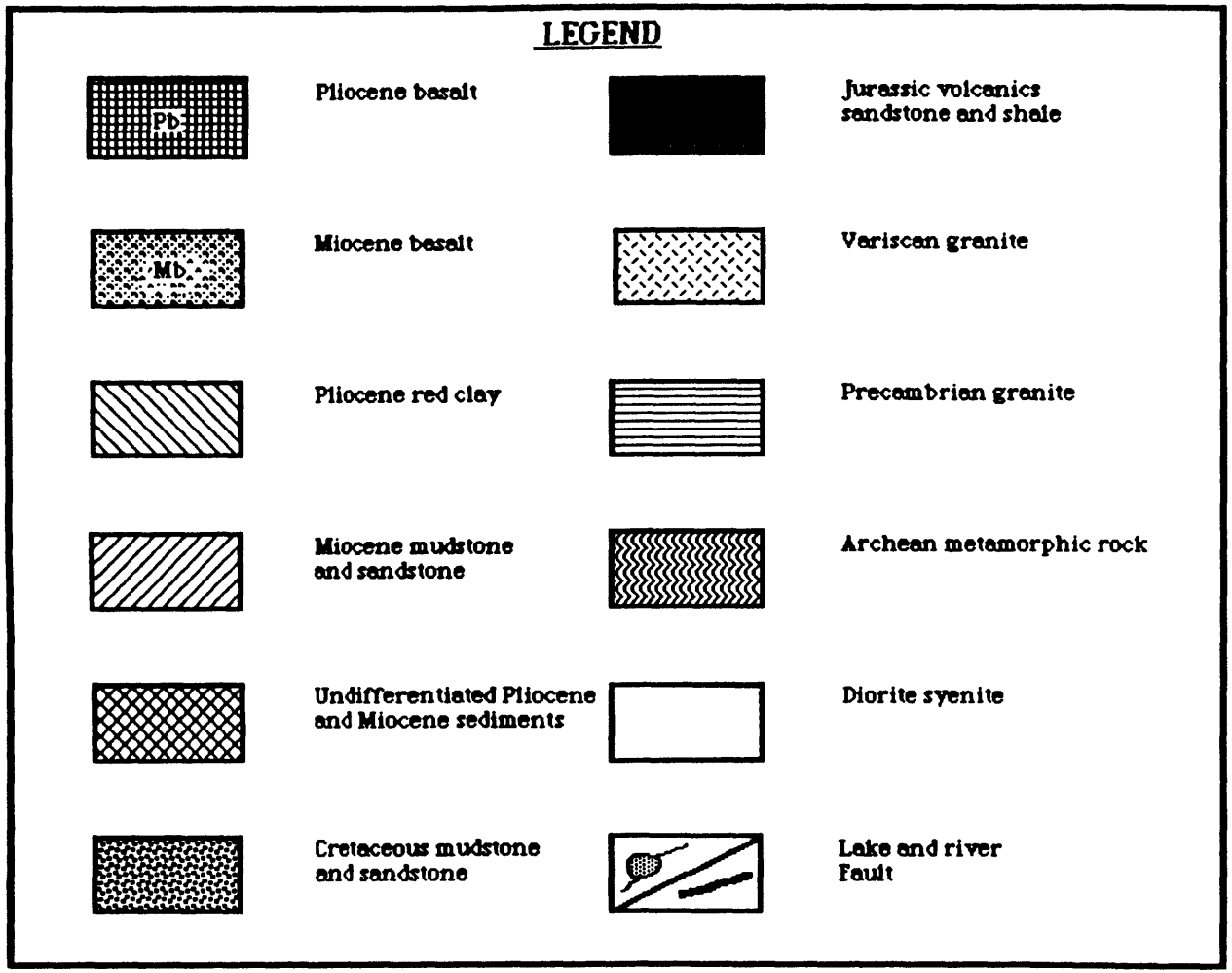
LEGEND
Pb
Pliocene basalt
Jurassic volcanics sandstone and shale
Mb
Miocene basalt
Variscan granite
Pliocene red clay
Precambrian granite
Miocene mudstone and sandstone
Archean metamorphic rock
Undifferentiated Pliocene and Miocene sediments
Diorite syenite
Cretaceous mudstone and sandstone
Lake and river
Fault

Stratigraphic Section

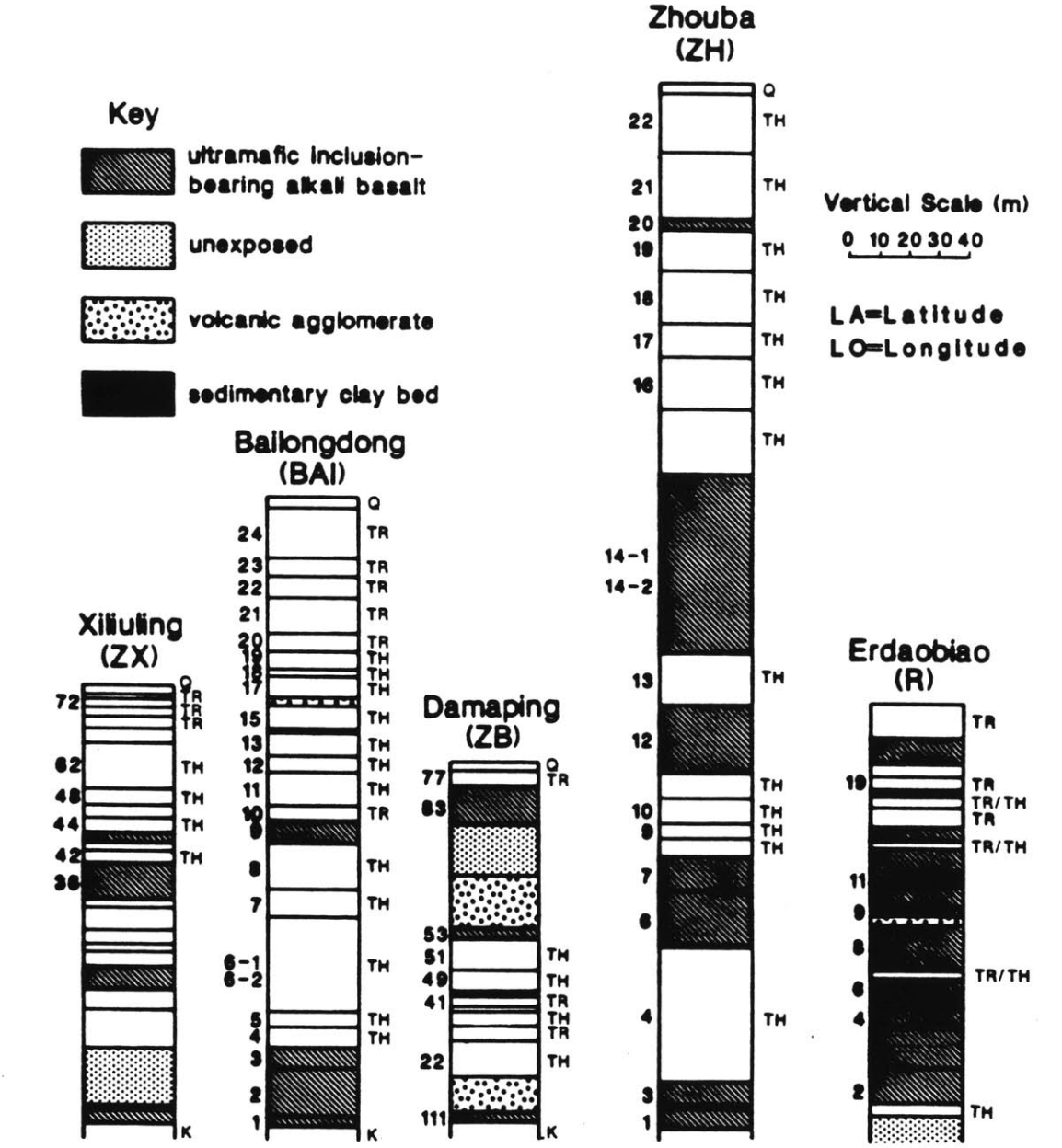

FIGURE I-2

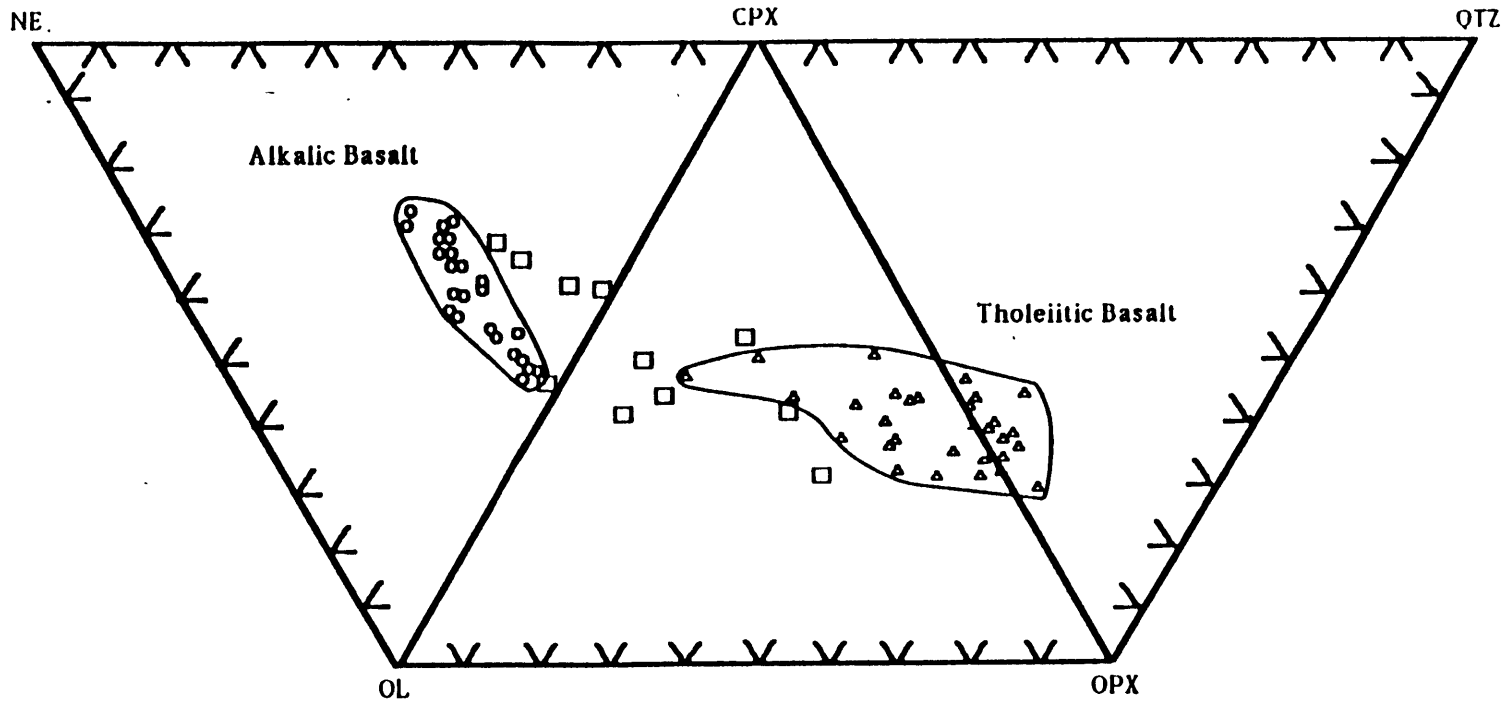

FIGURE 1-3

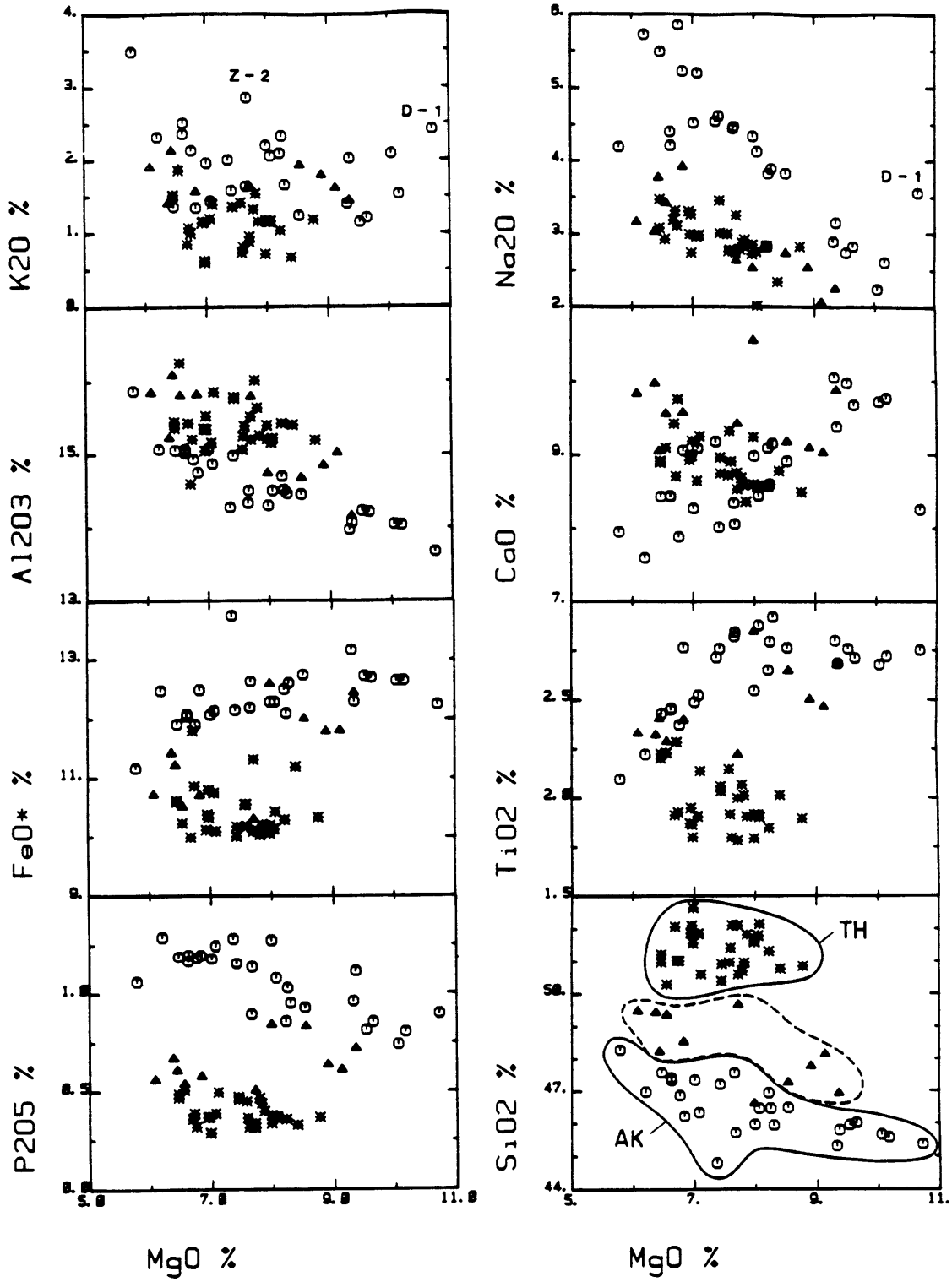

FIGURE I-4

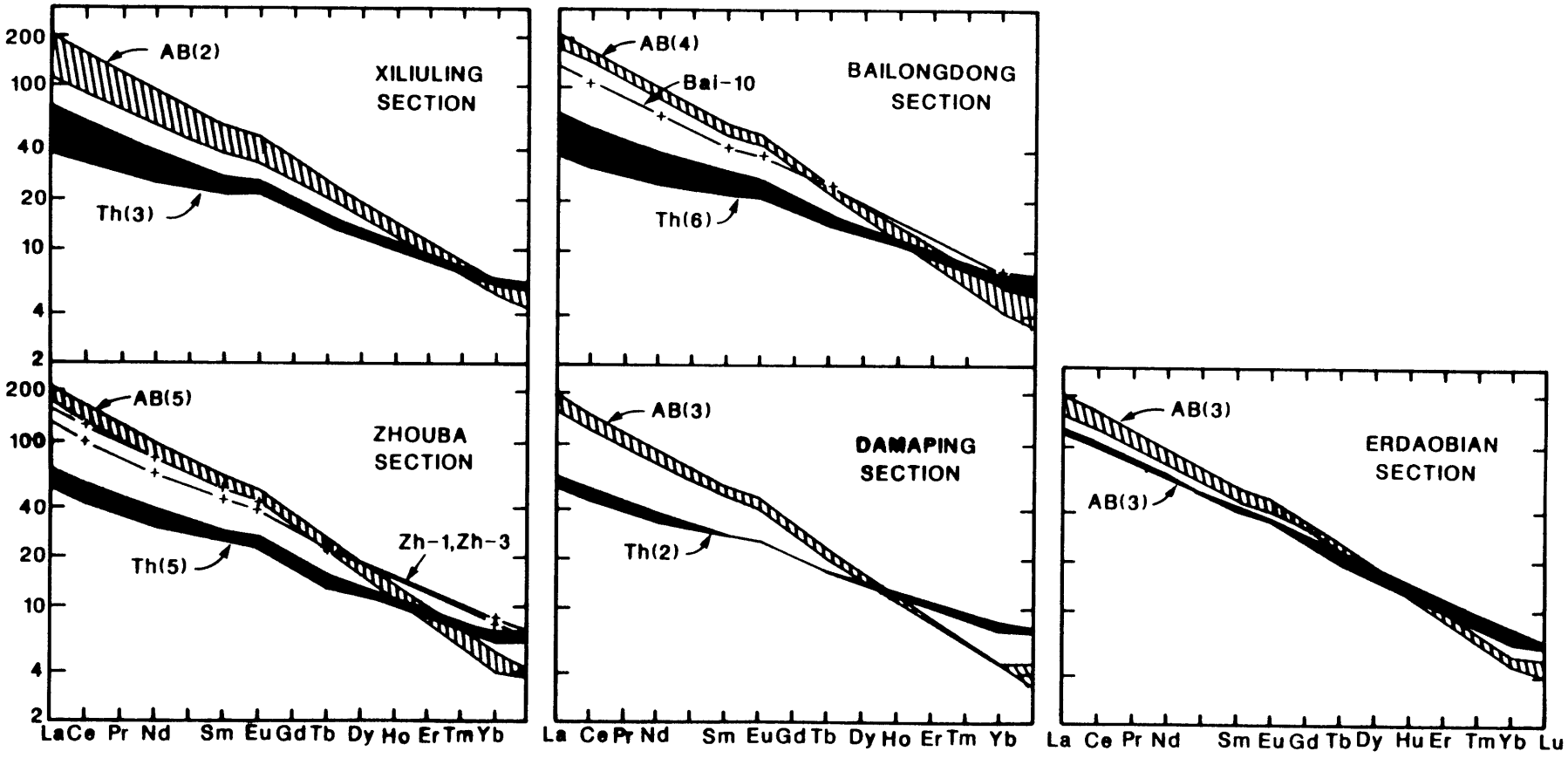
XILIULING SECTION
AB(2)
Th(3)
BAILONGDONG SECTION
AB(4)
Bai-10
Th(6)
ZHOUBA SECTION
AB(5)
Th(5)
Zh-1,Zh-3
DAMAPING SECTION
AB(3)
Th(2)
ERDAOBIAN SECTION
AB(3)
AB(3)
200
100
40
20
10
4
2
La Ce Pr Nd Sm Eu Gd Tb Dy Ho Er Tm Yb
La Ce Pr Nd Sm Eu Gd Tb Dy Ho Er Tm Yb
La Ce Pr Nd Sm Eu Gd Tb Dy Hu Er Tm Yb Lu

FIGURE I-5

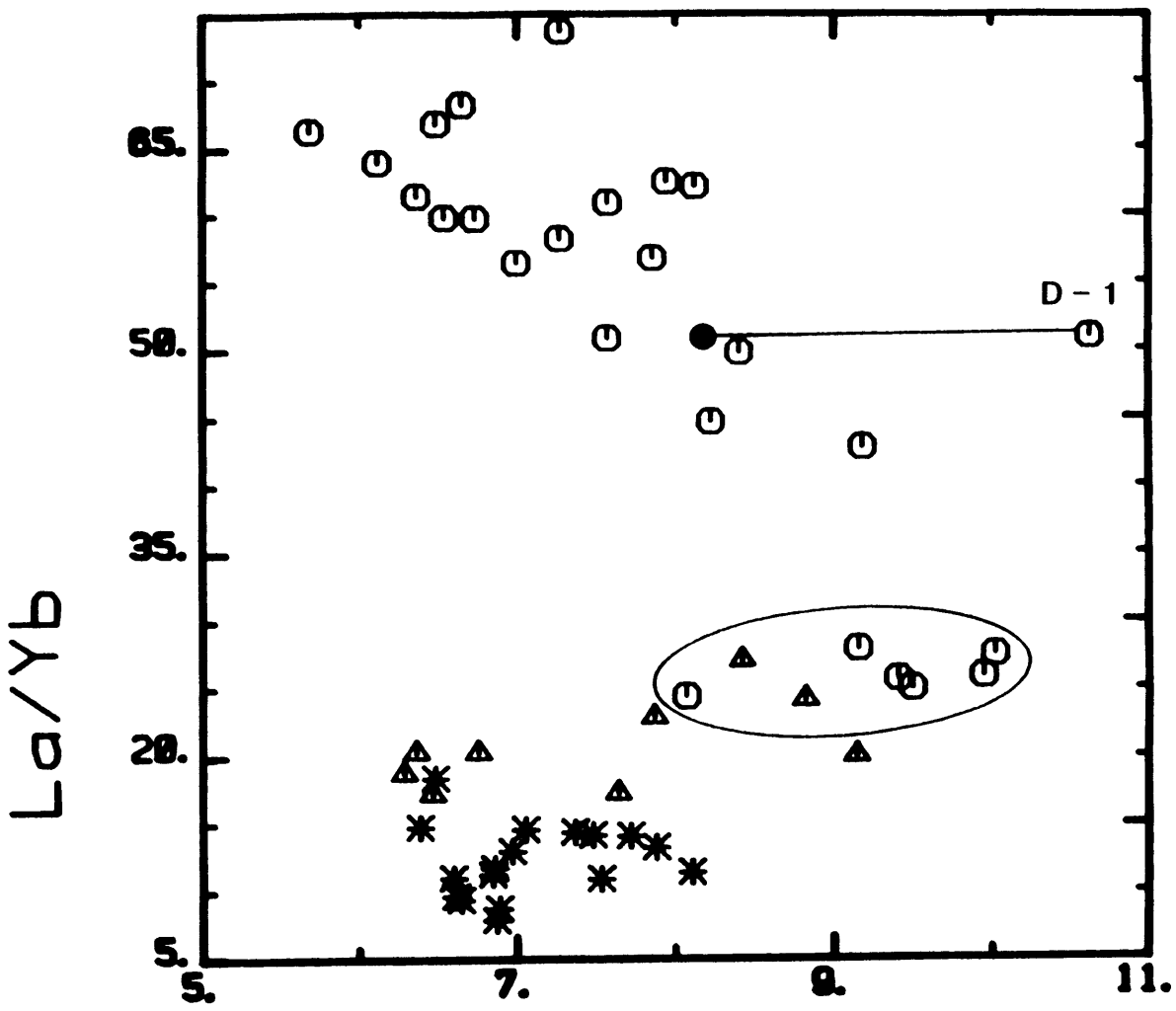

FIIGURE I-6

FIGURE 1-7

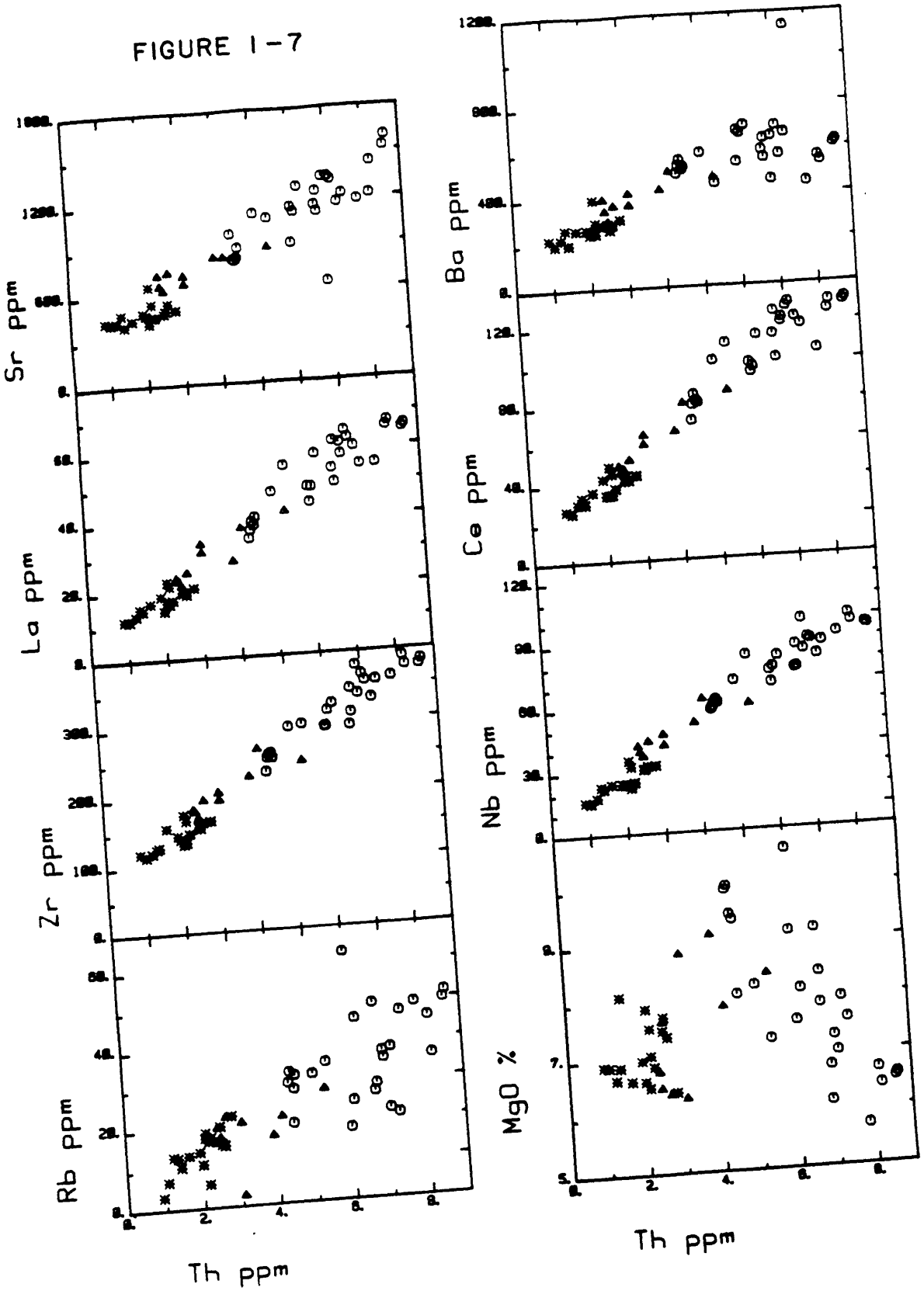

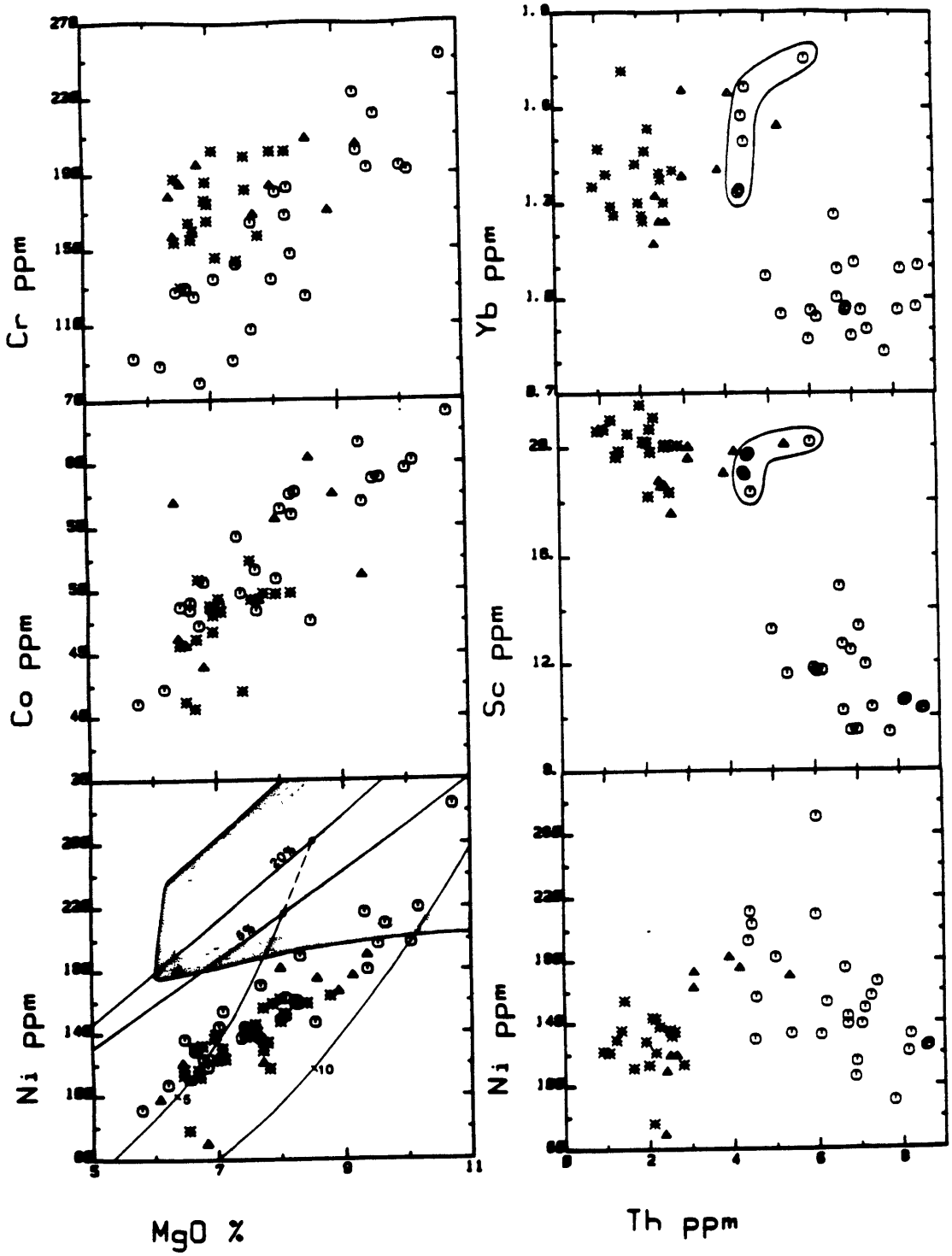

FIGURE 1-8

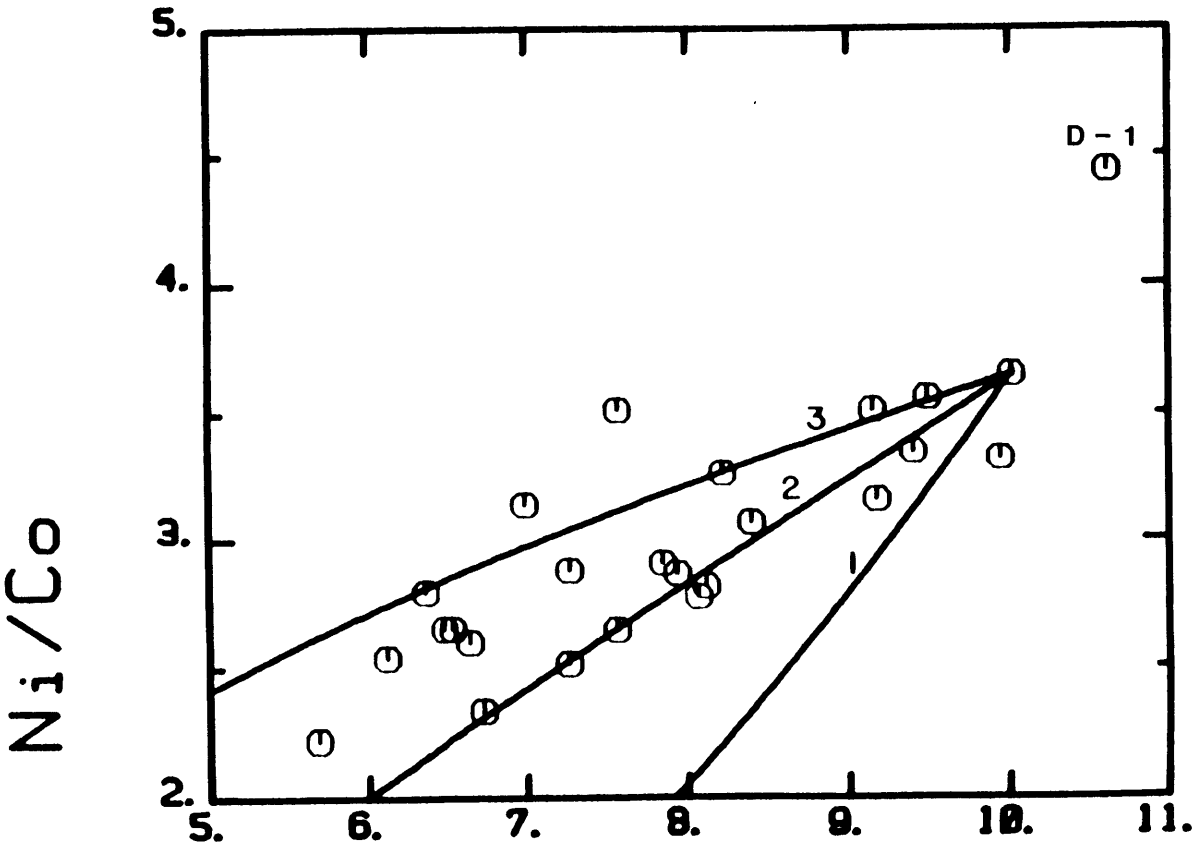

FIGURE I-9a

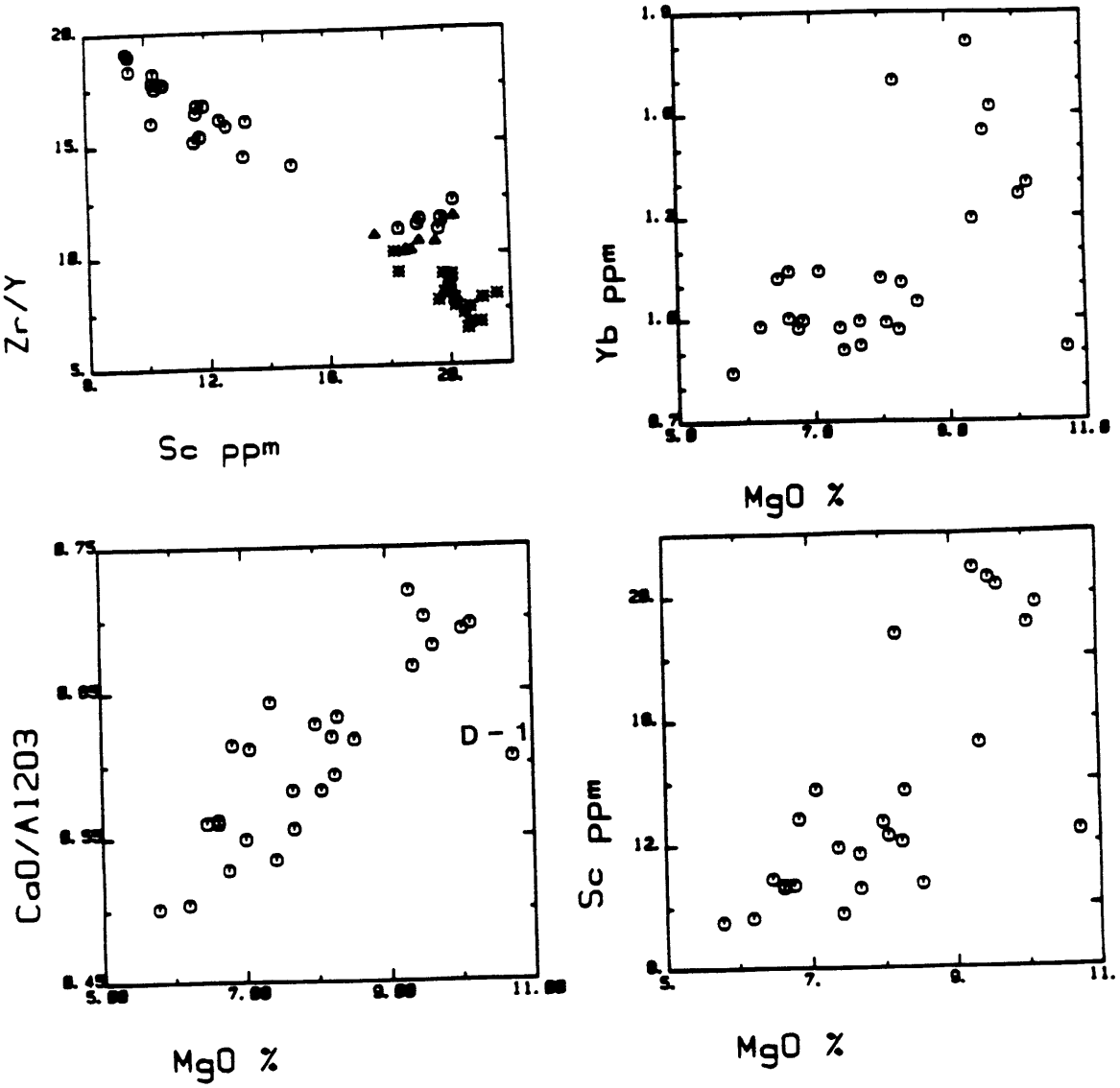

FIGURE I-9b

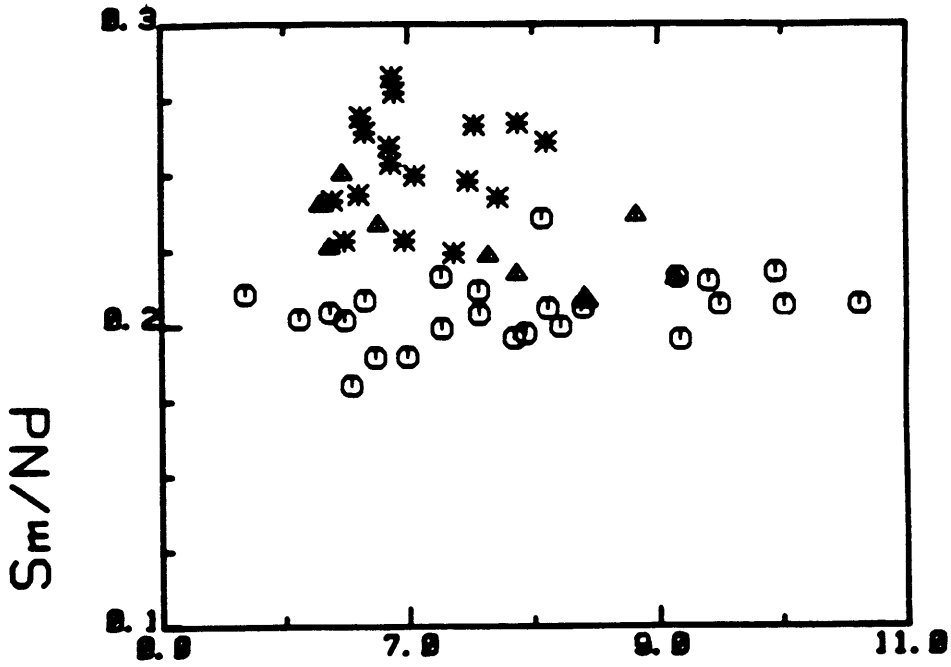

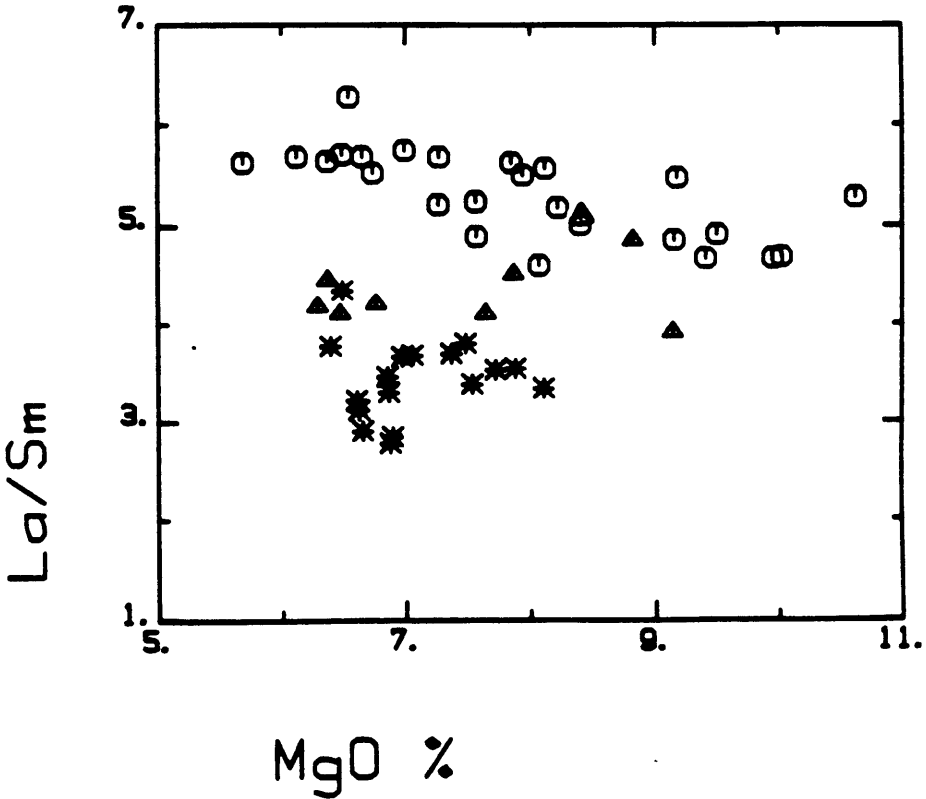

FIGURE 1-10a

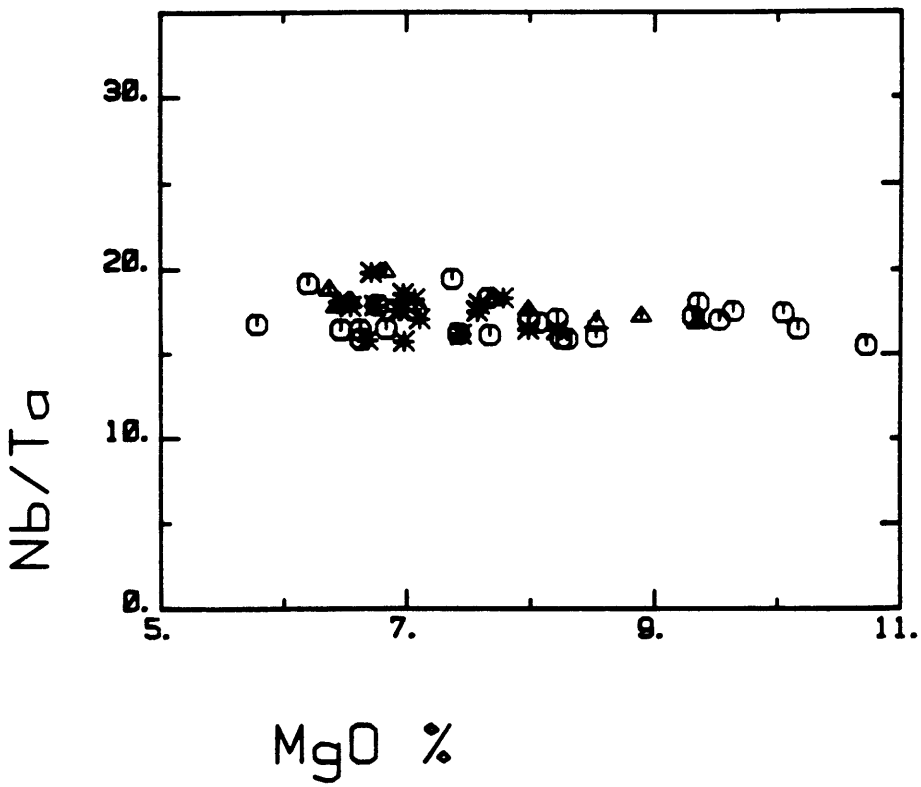
30.
20.
10.
0.
5.
7.
9.
11.
Nb/Ta
MgO %

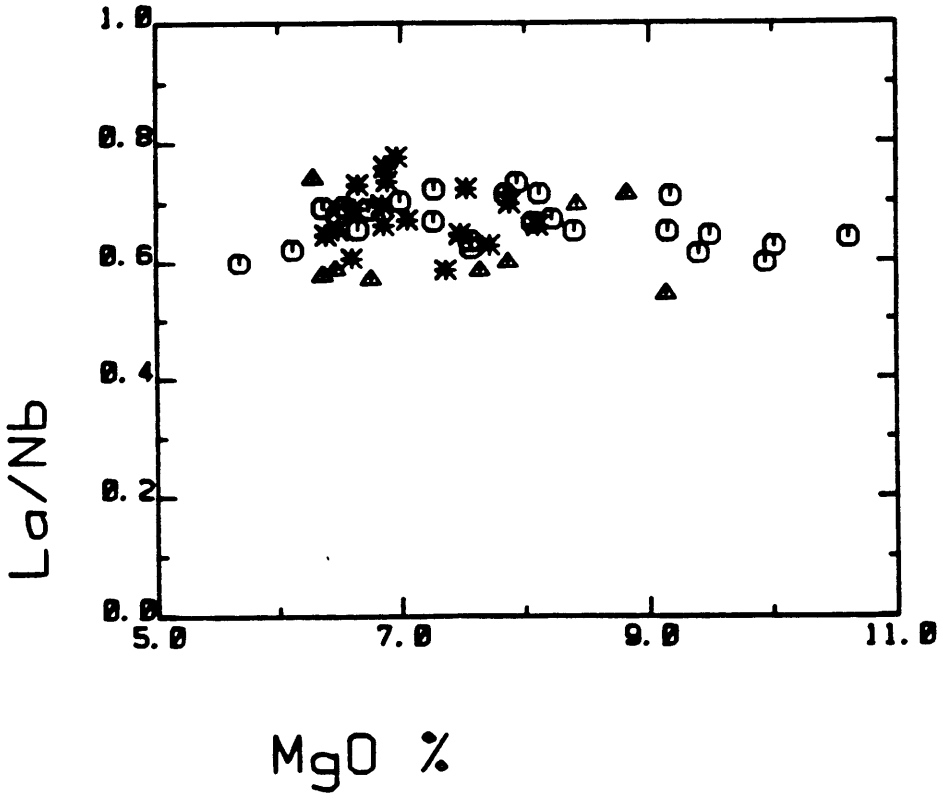
1.0
0.8
0.6
0.4
0.2
0.0
5.0
7.0
9.0
11.0
La/Nb
MgO %

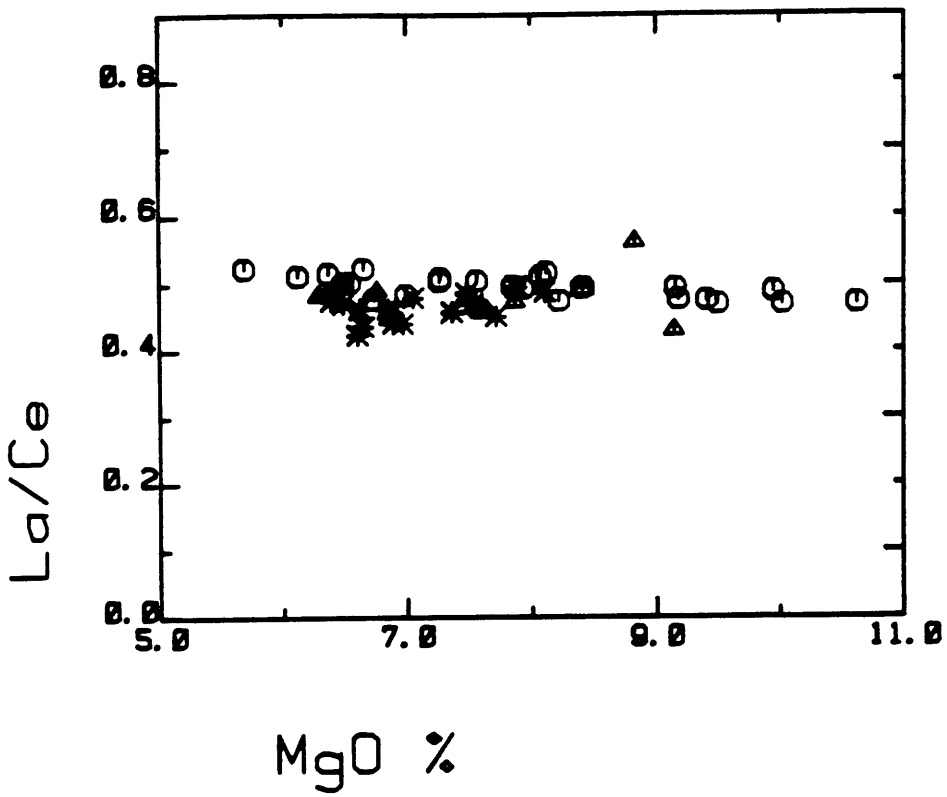
0.8
0.6
0.4
0.2
0.0
La/Ce
5.0
7.0
9.0
11.0
MgO %

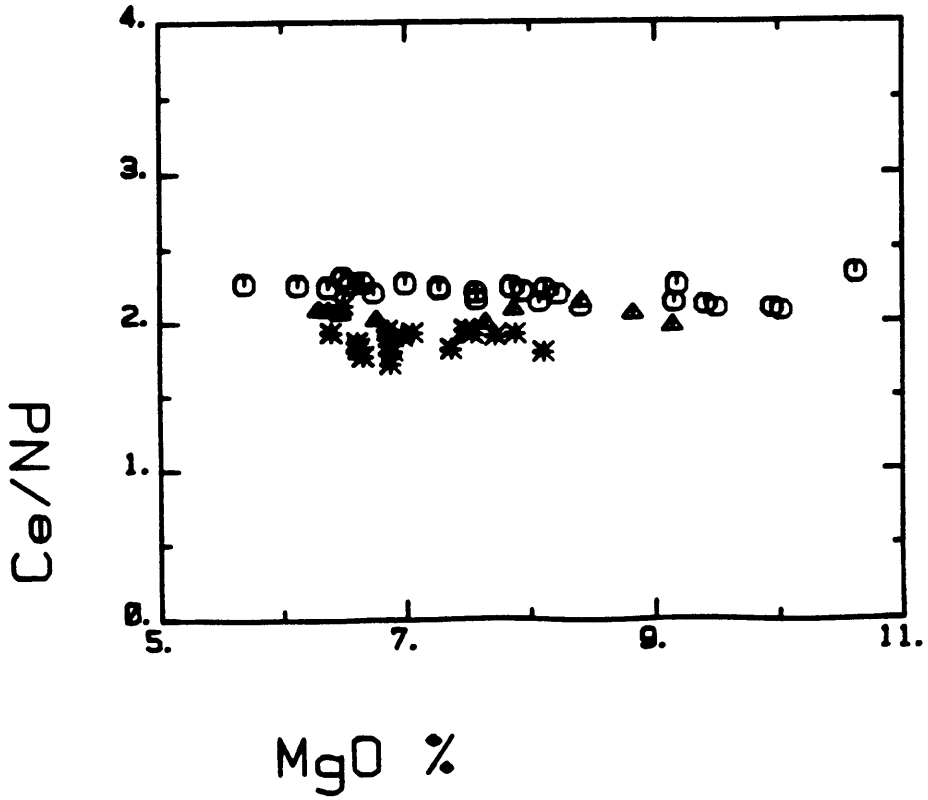
4.
3.
2.
1.
0.
Ce/Nd
5.
7.
9.
11.
MgO %

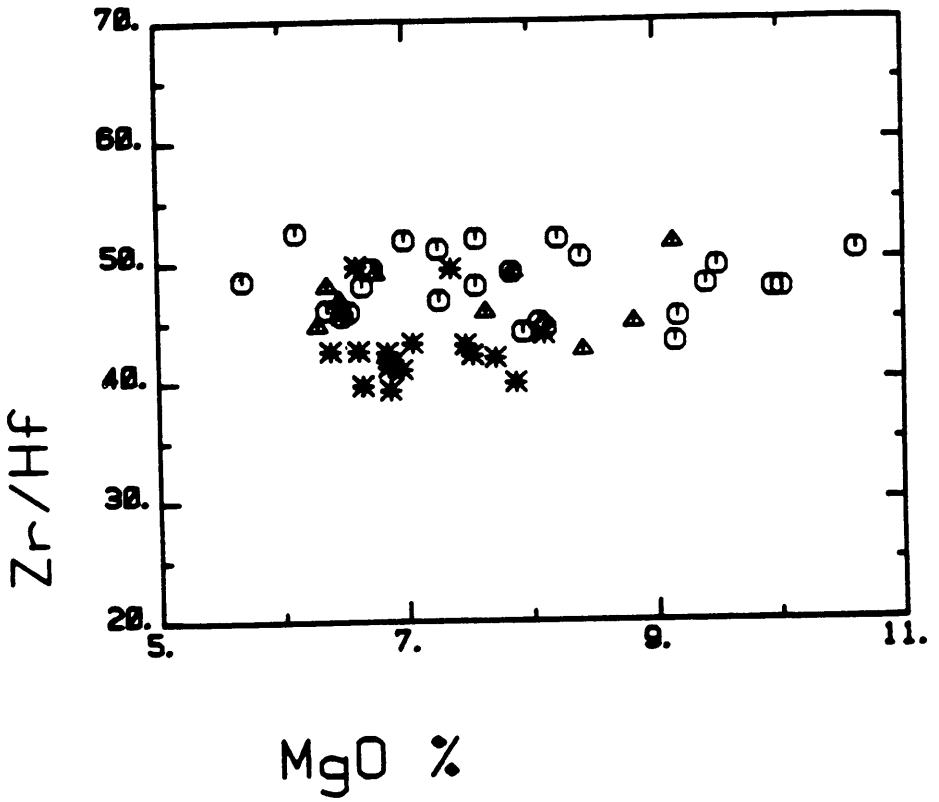
70.
60.
50.
40.
30.
20.
5.
7.
9.
11.
Zr/Hf
MgO %

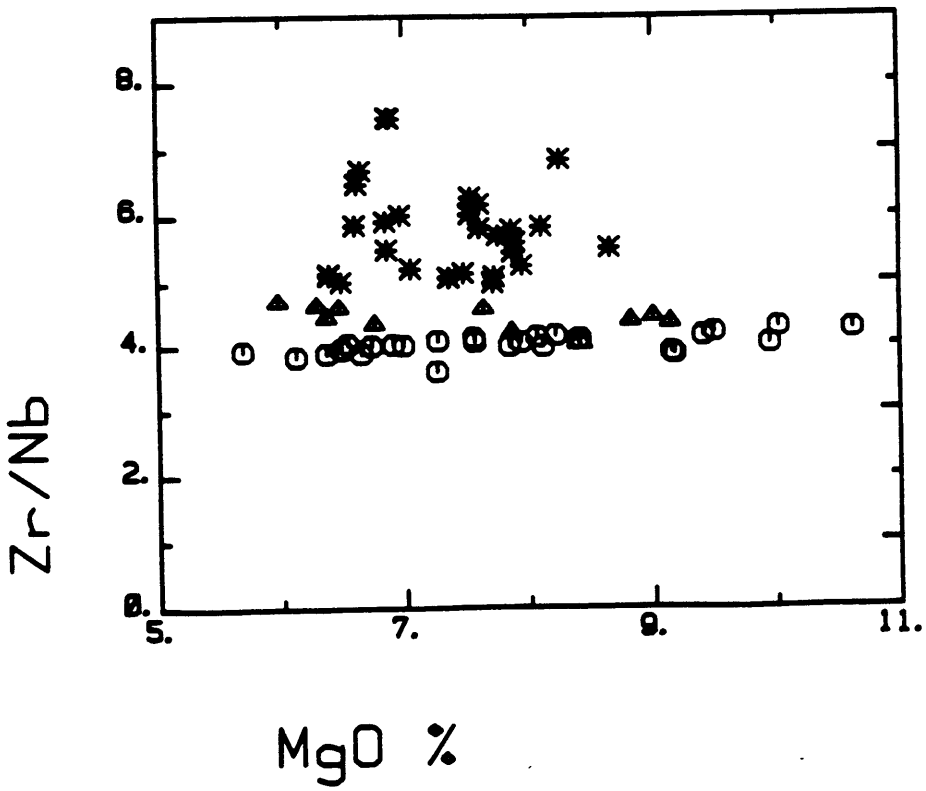
8.
6.
4.
2.
0.
5.
7.
9.
11.
Zr/Nb
MgO %

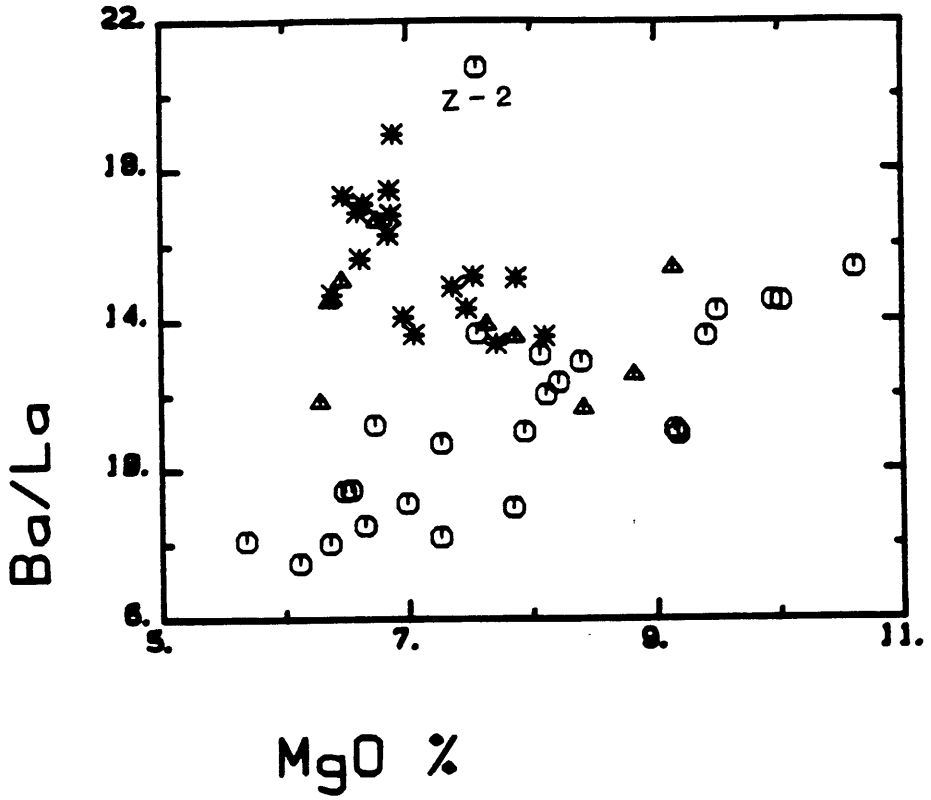
22.
18.
14.
10.
6.
5.
7.
9.
11.
Z-2
Ba/La
MgO %

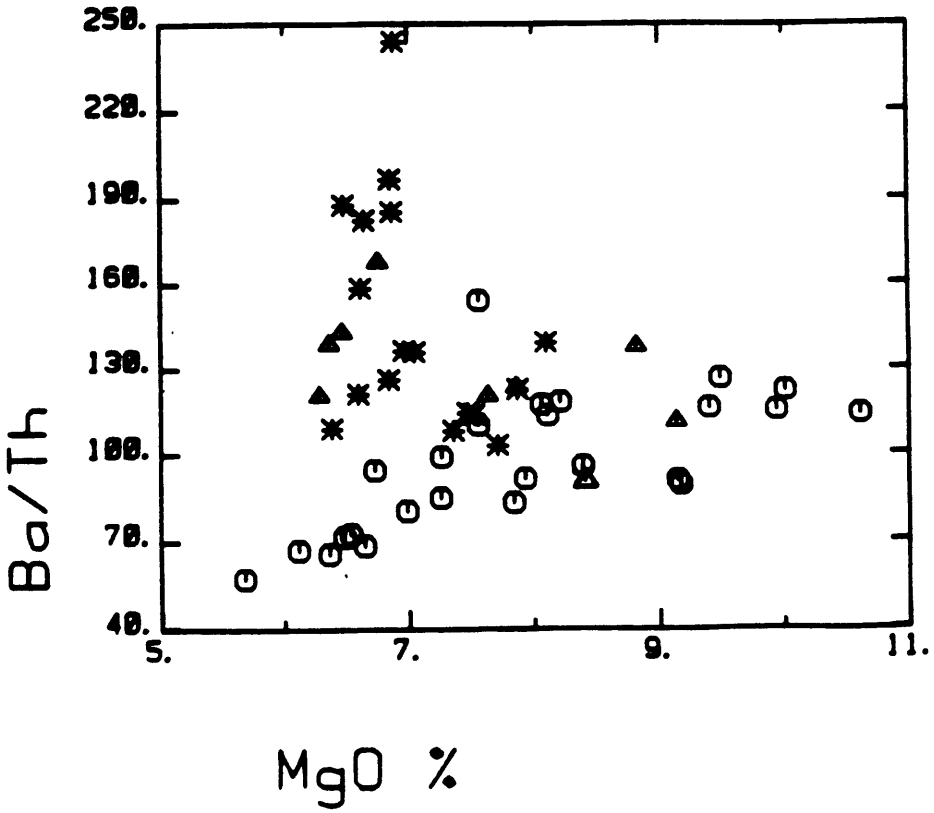
250.
220.
190.
160.
130.
100.
70.
40.
5.
7.
9.
11.
Ba/Th
MgO %

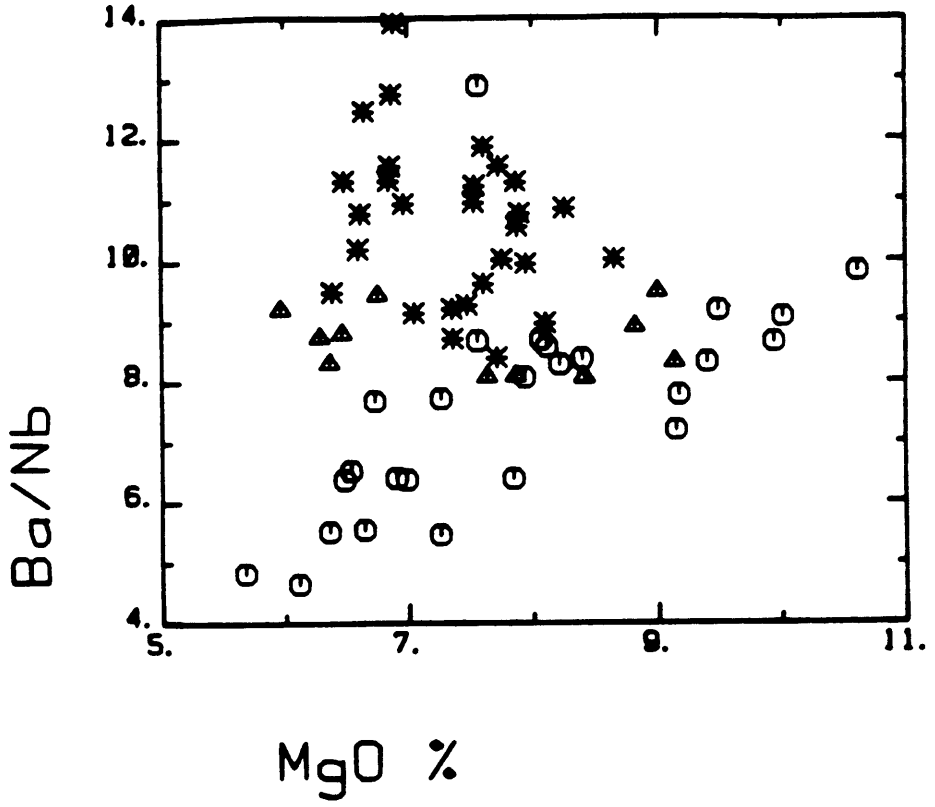
14.
12.
10.
8.
6.
4.
5.
7.
9.
11.
Ba/Nb
MgO %

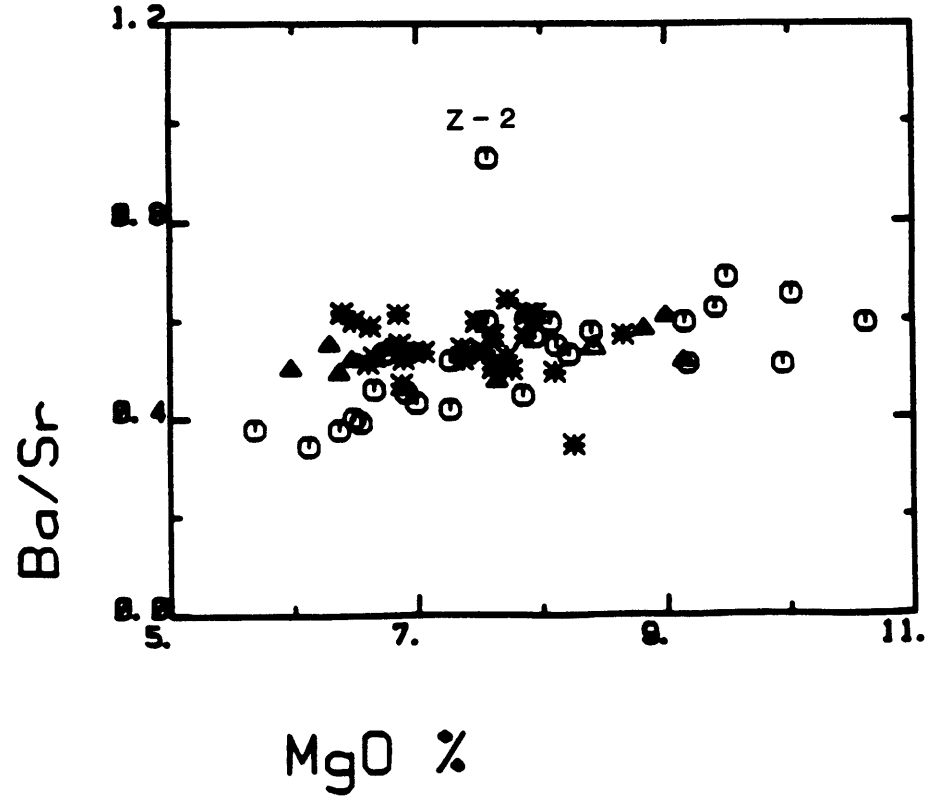
1.2
Z-2
5.
7.
9.
11.
Ba/Sr
MgO %

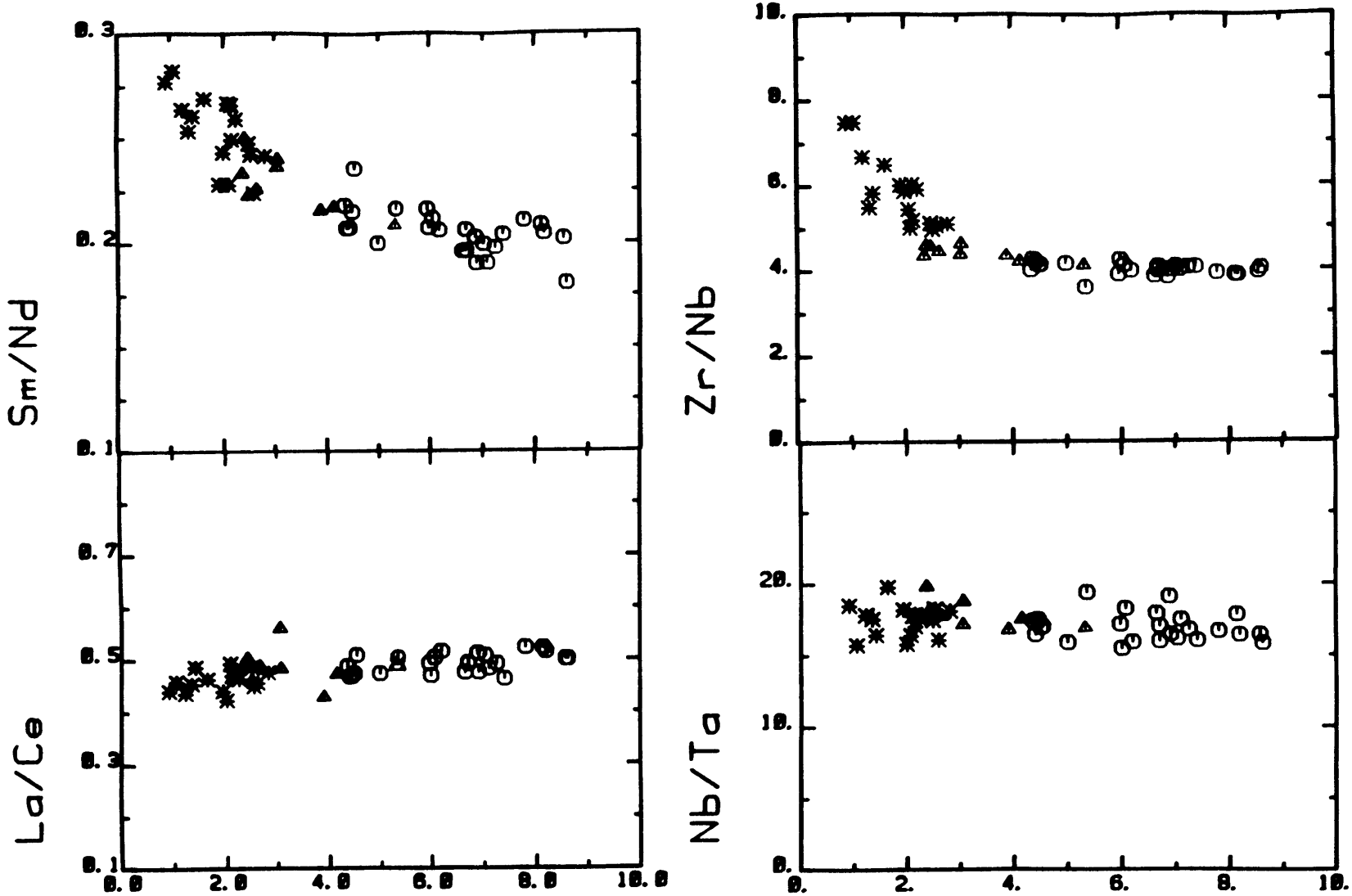
Sm/Nd
0.3
0.2
0.1
La/Ce
0.7
0.5
0.3
0.1
0.0
2.0
4.0
6.0
8.0
10.0
Th ppm
Zr/Nb
10.
8.
6.
4.
2.
0.
Nb/Ta
20.
10.
0.
2.
4.
6.
8.
10.
Th ppm

FIGURE 1-10b

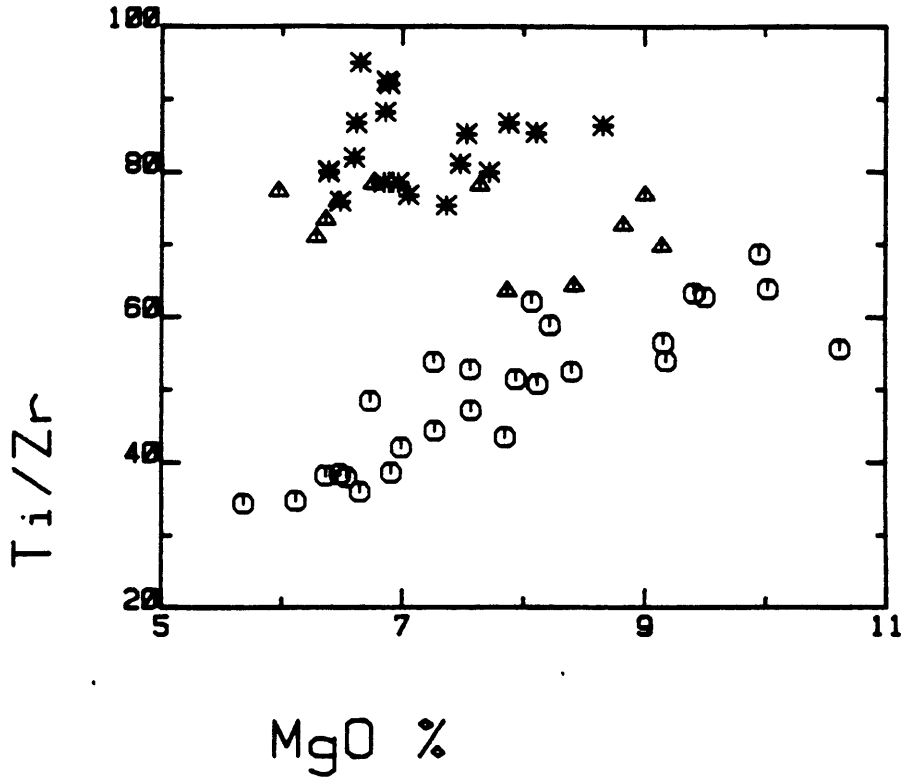

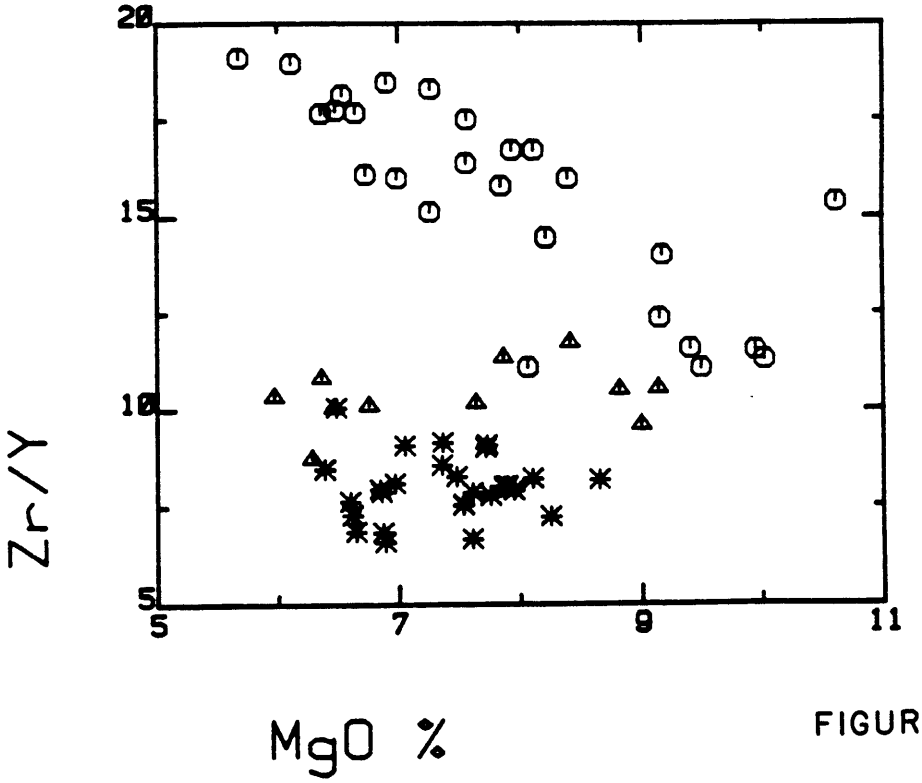

FIGURE I-11

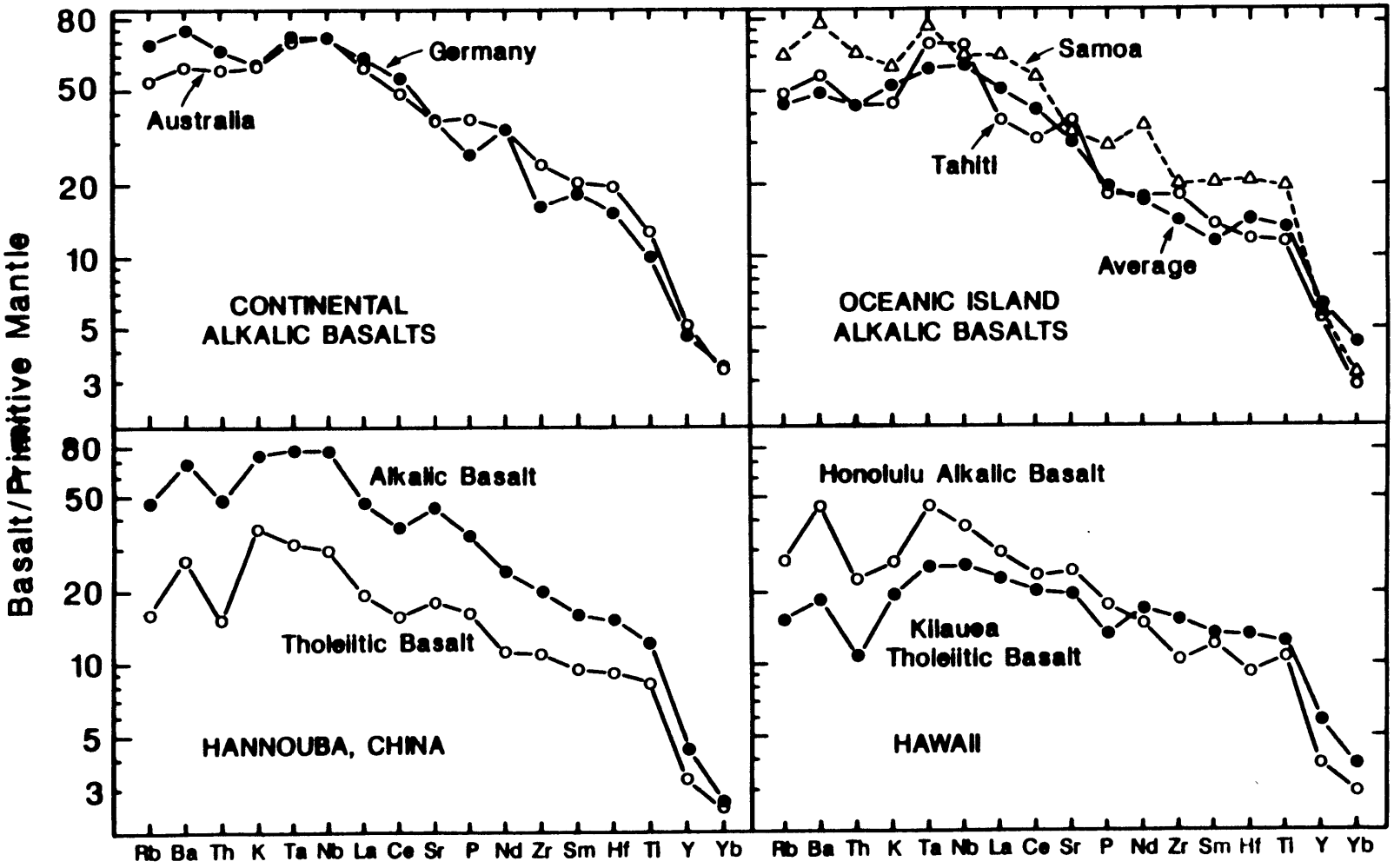
Basalt/Primitive Mantle
80
50
20
10
5
3
Germany
Australia
CONTINENTAL
ALKALIC BASALTS
Samoa
Tahiti
Average
OCEANIC ISLAND
ALKALIC BASALTS
Alkalic Basalt
Tholeiitic Basalt
HANNOUBA, CHINA
Honolulu Alkalic Basalt
Kilauea
Tholeiitic Basalt
HAWAII
Rb Ba Th K Ta Nb La Ce Sr P Nd Zr Sm Hf Tl Y Yb

FIGURE I-12a

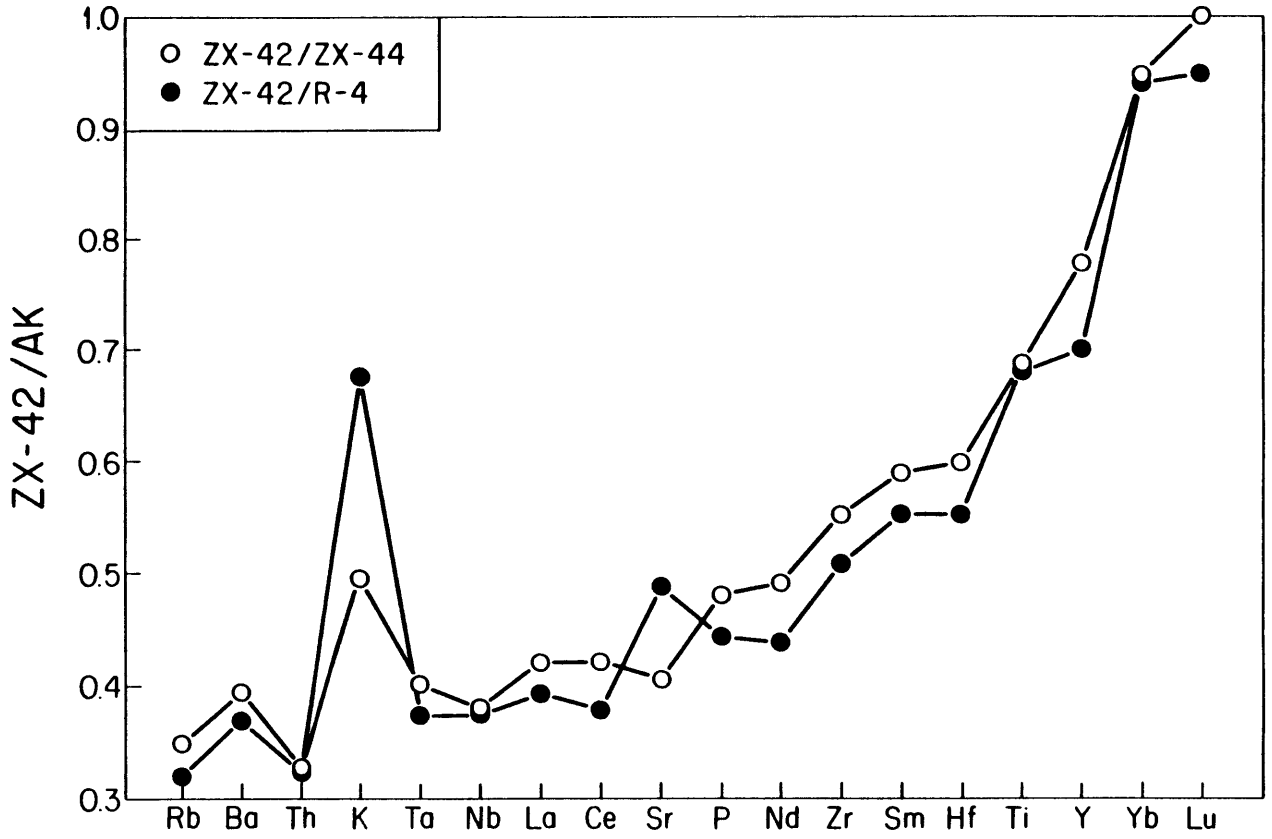
ZX-42/ZX-44
ZX-42/R-4
ZX-42/AK
1.0
0.9
0.8
0.7
0.6
0.5
0.4
0.3
Rb Ba Th K Ta Nb La Ce Sr P Nd Zr Sm Hf Ti Y Yb Lu

FIGURE 1-12b

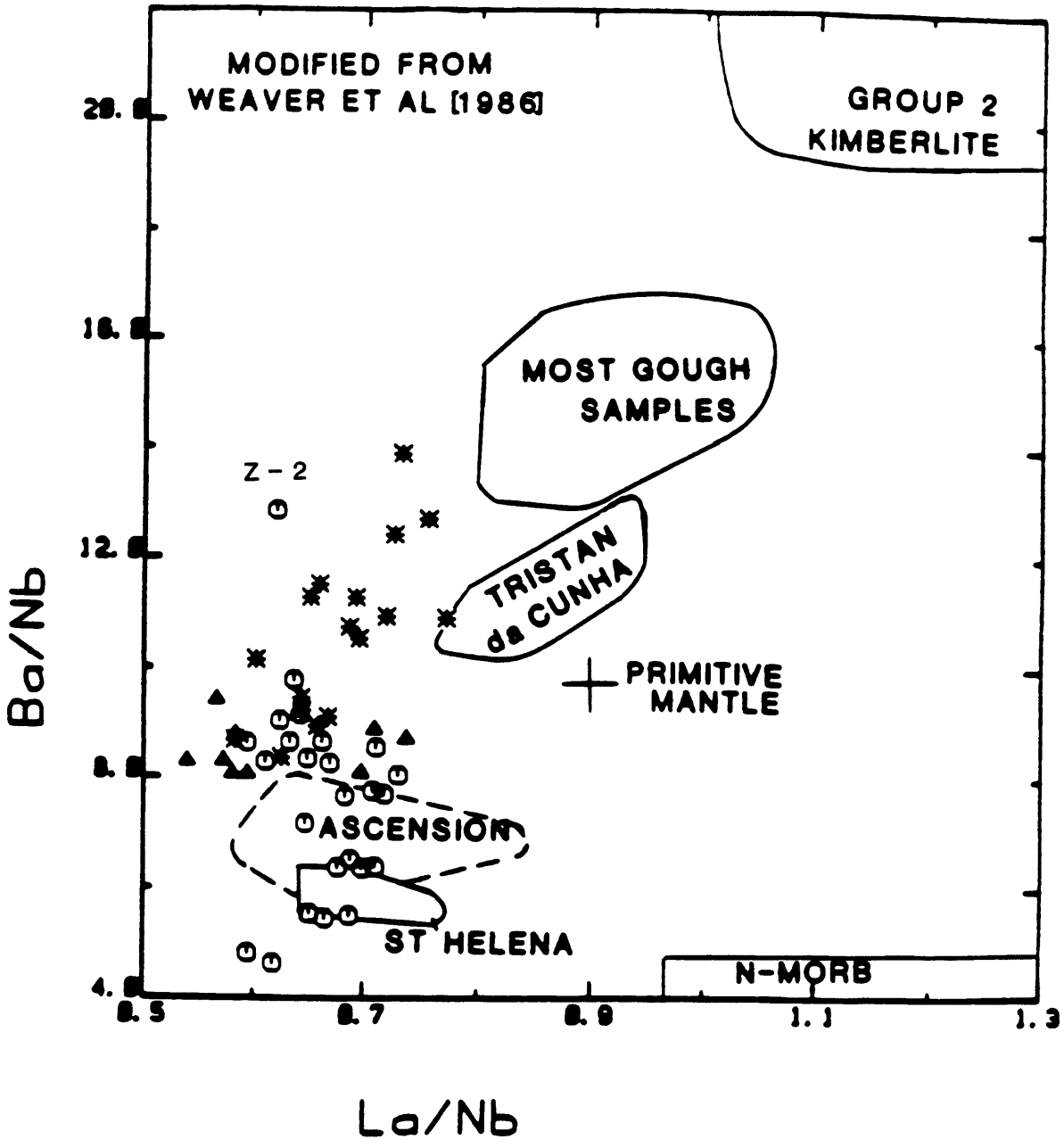
MODIFIED FROM
WEAVER ET AL [1986]
GROUP 2
KIMBERLITE
MOST GOUGH
SAMPLES
Z-2
TRISTAN
da CUNHA
PRIMITIVE
MANTLE
ASCENSION
ST HELENA
N-MORB
Ba/Nb
La/Nb
20.
16.
12.
8.
4.
0.5
0.7
0.9
1.1
1.3

FIGURE 1-13

CHAPTER 2: GEOCHEMISTRY OF MEGACRYSTS IN HANNUOBA ALKALI BASALTS: EVIDENCE FOR HIGH-PRESSURE FRACTIONAL CRYSTALLIZATION

2-1. INTRODUCTION

Compared with a group of primitive Hannuoba alkali basalts (MgO: 8-10%), an evolved group of alkali basalts have lower MgO, Sc, Ni, Cr, Co, V, Y, HREE and TiO_2 contents; however similar isotope compositions and highly incompatible element abundance ratios (Chapters 1 and 3), suggest that both groups were derived from the same mantle source. Zhi et al (1989) concluded that the more evolved alkali basalts were generated from the primary basanite magma by fractional crystallization of an eclogite mineral assemblage. A positive correlation between Ti/Zr vs. MgO (Fig. 1-11) suggests that magnetite/ilmenite is also a fractionating phase. The hypothesis of high pressure fractionation contrasts with the models previously proposed for the evolution of Hannuoba alkali basalts: i.e., the low pressure fractional crystallization model (fractionation of clinopyroxene, olivine, plagioclase and/or magnetite) proposed by Gan (1986); and the derivation of tholeiitic magmas from basanite magmas by fractionation of olivine and magnetite under high pressure (> 10Kb) (Zhai, 1984).

As indicated in Chapter 1 (see section 1-5.1), the Hannuoba alkalic basalts are fine-grained, dark grey and massive. Most have a low degree of crystallization with the total abundance of phenocrysts less than 5%. The phenocrysts are mainly olivine (0.03 - 0.1 mm), with rare plagioclase in a few samples. Opaque minerals are mainly magnetite. Most of

the olivine phenocrysts are not euhedral; the crystal forms are typically modified by corrosion or fragmentation, suggesting that they are not phenocrysts but rather xenocrysts. This is supported by the disequilibrium olivine "phenocryst" K_d data in basanite D-1 (for olivine compositions see Table 1-4). The smaller size of these olivine xenocrysts (0.03 - 1.5 mm) compared to the megacryst minerals (cm-size), and the similar chemical compositions of the of xenocryst core and olivines in the mantle xenoliths (Table 1-4) indicate that these xenocryst olivines are fragments from mantle xenoliths rather than megacrysts. Plagioclase phenocrysts occur in the center of thick flows of Hannuoba alkalic lavas (e.g., in basanite D-1). In flow margins or in thin flows of alkali basalts, plagioclase occurs only in the matrix. Therefore, there is no petrographic evidence in the Hannuoba alkali basalts for a low pressure fractionation assemblage, such as clinopyroxene, olivine and plagioclase (Gao, 1984). This assemblage is only observed in the Hannuoba transitional and tholeiitic basalts (see Chapter 1, section 1-5.2). If there was a low pressure fractionation process, the petrographic characteristics of the alkali basalts suggest that these low pressure crystallization phases have been segregated, while retaining the dense mantle xenoliths and xenocryst fragments (i.e., olivine) that were suspended in these magmas. This seems unlikely.

Zhai (1984) proposed that the basanite magmas evolved to tholeiitic magmas by fractionation of olivine and

magnetite under high pressure (> 10Kb). During this process, as the SiO_2 content increased, MgO, FeO and TiO_2 contents decreased, and Al_2O_3 contents increased. These trends proposed by Zhai are not supported by this study: i.e., the range of MgO and FeO abundances, and also the Mg numbers of the Hannuoba alkalic and tholeiitic basalts overlap, and MgO and FeO do not decrease as SiO_2 increases (Fig. 1-4 and Table 1-1). Furthermore, many geochemical variation trends (e.g., MgO vs. TiO_2, Ni, Zr/Y, La/Yb, and Ba/Th) show diverging trends from primitive alkali basalts to evolved alkali basalts, and from primitive alkali basalts to transitional and tholeiitic basalts (e.g., Figs. 1-5, 1-6, 1-8, 1-10a and 1-11). Therefore, there is not a continuous variation trend among the Hannuoba basalts. Two different evolutionary processes are required to explain these diverging trends.

Even within the alkalic basalt suite, fractionation of only olivine and magnetite is not reasonable. As indicated in Chapter 1, the trend between MgO and Ni/Co for the Hannuoba alkali basalts (Fig. 1-9a) could not be generated only by the fractionation of olivine, but could be generated by fractionation of clinopyroxene and olivine, and also by fractionation of clinopyroxene and garnet without olivine. The negative correlations between La/Yb vs. MgO and Zr/Y vs. MgO (Figs. 1-6 and 1-11) also cannot be interpreted by olivine plus magnetite fractionation.

Megacrysts, dominantly clinopyroxene (Cpx), lesser amounts of anorthoclase (Ano), and rare amounts of garnet (Gt) and titanomagnetite (Mt) occur in most Hannuoba alkali basalts, but are absent in Hannuoba tholeiites. Megacrysts in alkali basalts are generally divided into two groups (Irving, 1984; Schulze, 1987): Group A includes: Al-augite, Al-bronzite, olivine, kaersuitic amphibole, pyropic garnet, and plagioclase which may have crystallized from the host alkali basalts; Group B: anorthoclase, Ti-mica, Fe-Na-salite, apatite, magnetite, ilmenite, zircon, corundum, rutile and sphene are considered to be xenocrysts crystallized from a more evolved magma at shallow depths. Our objective is to evaluate the role of these megacrysts in creating the geochemical trends of the Hannuoba alkali basalts. In particular, we wish to evaluate the high pressure fractionation model of Zhi et al (1989).

2-2. MEGACRYST AND BASANITE DESCRIPTION

Clinopyroxene: The clinopyroxenes are obsidian-like, black to brown black in color with poor cleavage, conchoidal fractures and a glassy luster on broken surfaces. Dimensions are generally 1-2 cm, but range up to 12 cm. Clinopyroxene megacrysts generally have 0.5-2 mm gray reaction rims which are composed of radiating clinopyroxene.

Garnet: Garnet is purple red to orange red in color and generally altered along surfaces and fractures to form gray white reaction rims. Crystals are generally 0.5-1cm.

Anorthoclase: Anorthoclase is clear to white in color but some crystals are light brown-yellow due to alteration. There are well-developed crystal faces and cleavages. The crystals are generally about 2 cm, and range up to 13 cm in size.

Magnetite: Magnetite is black in color, the crystals are generally about 1 cm.

HOST BASANITE J-14 DESCRIPTION

The host basanite J-14 of megacrysts Cpx-1, -2 and Gt-1, -2 (Tables 2-1 and 2-2) contains abundant clinopyroxene and lesser amounts of garnet megacrysts plus rare garnet-clinopyroxene aggregates. This basanite is a very fine grained, black massive basalt. It contains less than 5% phenocrysts (~ 0.1 mm), most are olivine, with rare clinopyroxene. Most of these "phenocrysts" are probably xenocrysts. The groundmass is composed of plagioclase microlites plus clinopyroxene and granules of magnetite in roughly equal amounts, with subordinate quantities of granular olivine and apatite. One spinel fragment was observed in thin section.

BASANITE D-1 DESCRIPTION

D-1 is a thick lava flow in Damaping section which is the host lava of the largest xenolith accumulation zone (90m

X 56m X 20m), it also contains megacrysts (i.e., clinopyroxene No-18 and anorthoclase Ano-1 in Table 2-1 and 2-3). D-1 is unique in petrography. Compared with other alkali basalts, D-1 shows an unusual coarse grain size (0.5mm to less than 0.1mm) and abundant xenocrysts (10% olivine, ~5% augite, and rare spinel), and also rare coarse plagioclase (0.1 - 0.3 mm). There is a wide range in grain size suggesting a relatively slow cooling after eruption to the surface.

2-3. CHEMICAL COMPOSITIONS OF MEGACRYSTS and HOST BASANITE

Clinopyroxene:

The major element compositions of the Hannuoba clinopyroxene megacrysts (Table 2-1a) are similar to clinopyroxene megacrysts in other alkali basalts; i.e., they are titaniferous augites, rich in the Ca-Tschermak molecule, and poor in Cr (Table 2-4a). However, the Hannuoba clinopyroxene megacrysts are more Fe-rich than the clinopyroxene megacrysts from the Newer basalts, Australia (Irving, 1974), and poorer in Ca than the clinopyroxene megacrysts from Massif Central, France (Liotard et al., 1988), (Fig. 2-1). Also, the Hannuoba clinopyroxene megacrysts are more enriched in Na (jadeite molecule) content (Na_2O > 2%) than most clinopyroxene megacrysts worldwide (Na_2O < 2%).

The Hannuoba clinopyroxene megacrysts have different major element compositions than the phenocryst and matrix clinopyroxenes in the Hannuoba alkalic basalts (Table 2-1b). Also, clinopyroxene megacrysts generally contain less Na (reflected in the lower jadeite components), lower Cr, Mg number and higher Ti than clinopyroxene from the Group 1 mantle xenoliths (Binns et al., 1970). This is true for the Hannuoba megacrysts except that the Na content in the megacrysts is higher than in the Hannuoba xenolith clinopyroxenes (Table 2-1c). The Hannuoba clinopyroxene megacrysts have lower Mg number than the clinopyroxenes from two Group II xenoliths and similar Na content to the clinopyroxene from a garnet-pyroxenite TGZ (Table 2-1c).

The Hannuoba clinopyroxene megacrysts have chondrite normalized REE patterns similar to clinopyroxene megacrysts from other regions, i.e., convex upwards (Table 2-5b and Fig. 2-2a). The REE abundance ratios of megacryst/host are also similar to clinopyroxene megacrysts from other regions (Irving, 1980; Irving and Frey, 1984; Liotard, 1988).

Garnet:

Major element analyses (Table 2-2) are similar to pyrope megacrysts in kimberlites and alkali basalts worldwide (Irving and Frey, 1978); however, these Hannuoba garnet have a slight enrichment in Fe content (Fig. 2-3).

The Hannuoba garnet megacrysts have chondrite normalized REE pattern and a trace element abundance ratio of garnet/host (Table 2-5, Fig. 2-2b) well within the range

of pyrope megacrysts from other locations (Irving and Frey, 1978).

Anorthoclase:

The major element analyses are from Zhao (1983) (Table 2-3). The anorthoclase megacrysts also have similar compositions to the anorthoclase megacrysts worldwide (Fig. 2-4).

Host basanite:

A complex history for basanite D-1 can be inferred from the compositions of matrix, phenocryst and megacryst phases. The different Mg numbers and TiO_2 contents in two matrix clinopyroxenes (Table 2-1b) suggest that either these clinopyroxenes grew from different melt compositions formed during cooling, or possibly these fine-grain clinopyroxenes are xenocrysts. However, the latter interpretation is not consistent with the much lower Na_2O content of the matrix clinopyroxene (~ 0.6%) relative to the megacryst clinopyroxene (~ 2%). There are ~ 10% olivine xenocrysts in basanite D-1. The core to rim decrease in Mg number of the olivine xenocrysts, and the similar Mg numbers of the xenocryst core and the olivines from the mantle inclusions (Table 1-4) suggests that these olivine xenocrysts were derived from mantle inclusions and their rims equilibrated with the basaltic magma. In contrast to the olivine xenocrysts, the rims of the two clinopyroxene phenocrysts have higher Mg numbers than their cores (Table 2-1a) which suggests that these clinopyroxenes originally crystallized

from a more evolved magma and were mixed into a more mafic magma.

Except for basanite D-1, the olivine xenocryst content in most of the alkali basalts are lower than 5% (i.e., basanite J-14). A few brown spinel fragments have been observed in some of the alkali basalts (i.e., J-14, Z-2). Because of the very low REE and Sr contents in the olivine and spinel, this amount of olivine and spinel xenocrysts would not significantly change the REE and incompatible element abundances in the basalts, but it may modify the abundances of the olivine-compatible elements, i.e., Mg, Ni and Co, and also the Cr abundances may be modified by these spinel xenocrysts. Hence the REE and Sr abundances of the bulk basanite J-14 (without megacrysts), and other basanites with similar petrographic characteristics, can be interpreted to represent melt composition, however, this may not be true for the elements which are compatible in olivine or spinel: i.e., Ni, Co, and Cr. If 3-4% olivine xenocrysts are subtracted from the bulk compositions of basanite J-14, the resultant composition should be close to a melt composition, except for Cr which is compatible in spinel.

2-4. IMPLICATIONS OF THE MEGACRYST COMPOSITIONS

The enrichment in Ca-Tschermak and jadeite components in the Hannuoba clinopyroxene megacrysts, and the enrichment in pyrope of the Hannuoba garnet megacrysts suggest that both garnet and clinopyroxene crystallized in a high

pressure environment. Based on experimental studies, $K_d^{Gt/Cpx}$[1] (varies from 1.0 to 14.7) as a function of temperature, pressure and Ca contents of garnet (Raheim and Green, 1974; Thompson, 1974; Ellis and Green, 1979). Bulk chemical compositions do not perceptibly affect the K_d value for basaltic rocks in the range Mg number = 6.2 - 85 (Raheim and Green, 1974), and the different K_d values of eclogites from different geological environment are mainly due to different P, T conditions of formation (Ellis and Green, 1979). However, equilibrium between the Hannuoba megacrysts Gt-1 and Cpx-1 is suggested by their Kd value ($K_d^{Gt-1/Cpx-1}$ = 1.23[2]), and the $K_d^{Gt/Cpx}$ = 1.34 for garnet-lherzolite in eastern China, (Zhang and Cong, 1984), the $K_d^{Gt/Cpx}$ = 1.0 - 2.7 for garnet-clinopyroxene pairs in equilibrium with mafic liquids (figure 14 Irving, 1973; figure 7, Thompson, 1974). As indicated by Irving (1974), a trend of clinopyroxene megacrysts increasing in Ti, Al and Na with decreasing Si, Cr and Mg/(Mg+Fe) ratios (i.e., from No18 to No72 to No65 to Cpx-1) reflects crystallization at approximately constant pressure and falling temperature. Experimental melting studies (Cohen et al., 1967; Thompson, 1974; Arculus, 1975) of SiO_2 undersaturated basaltic magmas and subsolidus studies of garnet-clinopyroxene assemblages demonstrated

---

1. $K_d^{Gt/Cpx} = (Fe^{2+}/Mg^{2+})^{Gt}/(Fe^{2+}/Mg^{2+})^{Cpx}$.
2. Determination of $Fe^{2+}/(Fe^{2+} + Fe^{3+})$ ratios in garnets and clinopyroxenes in garnet lherzolites (Carswell and Dawson, 1970) indicates that Fe^{3+} contents are generally higher in clinopyroxenes than in coexisting garnets (Carswell and Gibb, 1980, 1987). Hence the $K_d^{Gt-1/Cpx-1}$, assuming all Fe as Fe^{2+}, is in effect minimum value.

that similar garnet and clinopyroxene compositions were crystallized at pressure from 15 to more than 30 kb. The reaction rims around both the clinopyroxene and garnet megacrysts suggest decreasing pressure during rapid ascent. The instability between the megacrysts and their host basalts at low pressures caused the rims to be partially melted. The reaction rim of the garnet megacryst is similar to septechlorite based on infra-red spectrogram analyses (Zhao, 1983). The rim of the clinopyroxene is augite with lower Al, Na, and higher Ca than the core. These rim compositions (Table 2-1a) are similar to that of the clinopyroxene phenocrysts (Zhai, 1984; and Zhao, 1983).

The major element compositions of the Hannuoba anorthoclase megacrysts are also similar to those in alkali basalts worldwide (Fig. 2-4) (Irving, 1974; Laughlin et al., 1974). However, unlike the garnet and clinopyroxene, the anorthoclase megacrysts do not have a reaction rim which may suggest that they were formed at more shallow depths than the garnet and clinopyroxene megacrysts. Plagioclase megacrysts could have crystallized from the alkali basalts, but anorthoclase megacrysts are believed to form in more evolved magmas at shallow depths (i.e., Irving and Frey, 1984; Schulze, 1987). However, Laughlin et al (1974) proposed that anorthoclase megacrysts could be phenocrysts in alkali basalts crystallized at high pressures. Experimental studies indicate that the An content of plagioclase decreases with increasing pressure (Cohen et

al., 1967; Green and Ringwood, 1967; Binns et al., 1970), and that sodic feldspar megacrysts could be near-liquidus phases of basaltic magma at moderate to high pressure: e.g., equivalent to a depth of 30 to 60 km (Aoki, 1970; Laughlin et al., 1974). The size of the positive Eu anomaly increases as the alkali content in feldspar increases (Schnetzler and Philpotts, 1970) and anorthoclase megacrysts have very large positive Eu anomalies (Figure 6, Irving and Frey, 1984). Consequently, the absence of negative Eu anomalies in Hannuoba alkali basalts (Fig. 1-5) excludes anorthoclase fractionation as a major process during the evolution of the Hannuoba alkali basalts. Furthermore, since Sr is compatible in anorthoclase[3], fractionation of anorthoclase would cause Sr to behave as a more compatible element which contrasts with the Sr-Th correlation in Fig. 1-8.

The enrichment of Fe in clinopyroxene and garnet megacrysts from eastern China relative to megacrysts from southern Australia (Figs. 2-1 and 2-3), and the similar Fe-enrichment between the clinopyroxene megacrysts from eastern China and the Massif Central, France, may suggest a relatively Fe-rich mantle source beneath eastern China and France. The significantly higher Na content in the clinopyroxene megacrysts from eastern China may suggest that they were formed at greater depths than most clinopyroxene megacrysts worldwide. The experimental studies by Thompson

3. The apparent anorthoclase-basalt partition coefficients are D^{Sr} = 5.6 (Laughlin et al., 1974), and D^{Sr} = 1.56-7.17 (Stuckless and Irving, 1976).

(1974) indicate that with rising temperature and pressure, "at high pressure, 28 to 31 Kb, ...elements Si, Ca, Mg and Fe cease to vary measurably while Na continues to rise". He concluded that the main chemical trend in clinopyroxene compositions is increased Al and Na content with rising pressure (and temperature), at the expense of the other elements.

The large variations in both major element (i.e., Mg#), and compatible element (i.e., Sc, Co, V and Ni) contents in the Hannuoba alkali basalts might be due to source heterogeneity, or more likely due to fractional crystallization. The latter process is evaluated in the next section.

2-5. EVALUATION OF FRACTIONAL CRYSTALLIZATION FOR THE HANNUOBA ALKALI BASALTS

The host basalts may not represent parental magmas for these megacrysts. However, a garnet megacryst in basanite J-14 has similar $^{143}Nd/^{144}Nd$ and $^{87}Sr/^{86}Sr$ ratios to the host (see Table 3-2 and Fig. 3-1). Also the REE abundance ratios of the garnet and clinopyroxene megacrysts over host lava J-14 (Table 2-5) are well within the range of megacrysts/host rock ratios from other locations (Irving and Frey, 1984). Because these ratios mimic trends of mineral/basaltic partition coefficients, the REE contents of the megacrysts are consistent with the megacrysts in J-14 being in

equilibrium with the host. Therefore, we estimated the degree of fractional crystallization for basanite J-14 based on major element data (Table 2-6b), and checked the results with trace element data.

2-5.1. Major Element Modelling:

Three parent-daughter pairs are chosen for major element modelling (R-4 to J-14, R-4 to R-2 and J-14 to Zh-20, Table 2-6). The similarity of isotope ratios and highly incompatible element abundance ratios suggest that the primitive and evolved alkali basalts could have been drived from the same mantle source. Therefore, the most primitive basanite R-4 is chosen as the parent, and basanite J-14 as the daughter magma because geochemical data are available for the megacrysts in basanite J-14. Then J-14 is chosen as an intermediate magma parental to the most evolved alkali basalt Zh-20. Primitive basalt R-4 and evolved basalt R-2 are also modelled because they are from the same cross-section (Fig. 1-2).

If the mole % of FeO equals to 0.9 times the total iron oxide in the Hannuoba basalts (see Chapter 1), and all the iron in high-pressure clinopyroxene is assumed to be Fe^{2+} (Thompson, 1974), the calculated K_d, $(FeO/MgO)_{cpx-1}/(FeO/MgO)_{J-14}$, value (0.46) is much higher than the average value of K_d (0.29) proposed for high-pressure clinopyroxene (Thompson, 1974), and also higher than the K_d range (0.20 -

0.40) which may correspond to clinopyroxenes in equilibrium with their host lavas (Liotard et al., 1988). However, the high Fe^{3+} in the clinopyroxenes analyzed in China (Table 2-1a) suggests equilibrium K_d values of 0.22-0.29 between these clinopyroxene megacrysts and the three evolved Hannuoba alkali basalts[4] (J-14, R-2 and Zh-20). Therefore, these clinopyroxene megacrysts may be cognate with the Hannuoba alkali basalts. In calculations 1 and 2 (Table 2-6), all Fe in the basalts and minerals are assumed to be Fe^{2+}, and the Fe/Mg ratios of the clinopyroxene and garnet megacrysts have been adjusted to be in equilibrium with the daughter basalts (K_d^{cpx}=0.29, K_d^{Gt}=0.35 which is based on $K_d^{Gt/Cpx}$=1.2). In calculations 3, 4 and 5 (Table 2-6), FeO = 0.9 the total FeO (mole %) is assumed for the basalts, and Fe^{2+} and Fe^{3+} are used as in measured minerals (Table 2-1). As stated in Chapter 1 (section 1-6.1), strong evidence for post-magmatic alkali metal mobility is illustrated by data for two alkalic basalt samples from the same flow Zh14-1 and 14-2 (Tables 1-1 and 1-2). They differ significantly in alkali metal and Ba contents, and all other major and trace element abundances in these two samples are less variable. Therefore, in calculations 1 and 2, K2O and Na2O are omitted.

Using a least-squares regression program an olivine-clinopyroxene-garnet-magnetite assemblage was evaluated for the major element modelling for the three parent-daughter

4. K_d = 0.32 - 0.36 between these clinopyroxene megacrysts and the most primitive basanite R-4.

pairs (calculation 1 in Table 2-6). Because olivine fractionation was not required, a clinopyroxene-garnet-magnetite assemblage was also evaluated (calculation 2 in Table 2-6). The required proportions of fractionated minerals are very similar to that in calculation 1. Furthermore, in calculation 3, an anorthoclase-olivine-clinopyroxene-garnet-magnetite assemblage was evaluated. Because anorthoclase fractionation was not required for the basalt pair R-4 and J-14 (Table 2-6a), an olivine-clinopyroxene-garnet-magnetite assemblage was evaluated in calculation 4, however, olivine fractionation was not required again as in calculations 1 and 2, this suggests that clinopyroxene-garnet-magnetite are the fractionation phases for basanite pair R-4 and J-14. Although minor amounts of anorthoclase fractionation is suggested by calculations 3 (F = 0.70) and calculation 4 (F = 0.66) for basalt pair J-14 and Zh-20 (Table 2-6b), the incompatible element abundance ratios (~1.35) for J-14 over Zh-20 suggest that the fractionation assemblage without anorthoclase and olivine (calculation 4, F = 0.74) is more reasonable. Based on above discussion, and as we indicated in Chapter 1, the variation trend between MgO and Ni/Co for the Hannuoba alkali basalts (Fig. 1-9a) could not be generated only by the fractionation of olivine, but could result from fractionation of clinopyroxene and olivine or clinopyroxene and garnet, without olivine. We conclude that olivine was not an important fractionating phase in the Hannuoba alkali

basalts as has been previously suggested (e.g., Zhai, 1984; Gao, 1986).

2-5.2. Trace Element Modelling:

Because REE and Sr (Table 2-7) are believed to have low abundances in magnetite, the REE and Sr abundances in the residual basalt (J-14) were calculated using the REE and Sr abundances in the parental liquid R-4 (Table 2-4), the degree of fractionation and the proportions of clinopyroxene and garnet megacrysts fractionated were determined from major element modelling (Table 2-6a), assuming equilibrium crystallization with the REE and Sr abundance ratios of megacryst/host (Table 2-5) as partition coefficients. The calculated results (Table 2-7) matches the major element modelling very well (Table 2-6a), which suggests that at least basanite J-14 could be related to the most primitive basaltic magma by undergoing high pressure fractionation of the observed megacryst assemblage. This model does not satisfactorily explain Cr and V abundances which is not a surprise because Cr is compatible in spinel and V is compatible in magnetite.

2-6. CONCLUSIONS

The crossing REE patterns in the Hannuoba alkali basalts could have been generated by different degrees ofmelting of a single source, by the mixing of two mantle sources/melts (Nakamura, 1986), or by high pressure garnet-clinopyroxene fractionation. High pressure garnet-clinopyroxene fractionation is supported by the petrography, the correlations between the major and compatible trace elements (i.e., MgO vs. Co/Ni, La/Yb, Zr/Y, and Ti/Zr), the major element, compatible element, and especially REE modelling, and by the similar isotope compositions and highly incompatible element abundance ratios among the alkali basalts. Furthermore, a high pressure fractionation model can explain the abundance of mantle xenoliths in the highly evolved alkali basalts (Mg#: 51 - 55), which suggests a short residence time for these magmas at shallow levels and an insufficient time for the fractional crystallization process in a low pressure environment. Therefore, an extensive fractional crystallization process under high to moderate pressure before the mantle-inclusions were captured is a reasonable model for the Hannuoba alkali basalts. There might even have been a subsequent low pressure fractional crystallization process (crystallization of olivine, clinopyroxene and plagioclase), but, it would have been a minor process.

TABLES

TABLE 2-1a. Chemical Analyses of Clinopyroxene (Cpx) Megacryst

	Clinopyroxene Megacryst					
	CPX-1	No18	No65	No72	AVG	STD
SiO_2	48.68	50.06	48.78	49.02	49.14	0.55
TiO_2	1.24	0.85	1.25	1.05	1.10	0.16
Al_2O_3	9.45	8.11	8.77	8.25	8.65	0.53
Cr_2O_3	0	0	0	0	0	
Fe_2O_3		2.26	3.06	3.84	3.05	0.65
FeO	8.27	5.86	5.38	5.09	6.15	1.25
MnO	0.11	0.15	0.15	0.14	0.14	0.02
MgO	13.18	16.23	13.43	13.55	14.10	1.24
CaO	16.08	14.44	16.19	14.06	15.19	0.95
Na_2O	2.11	1.54	2.16	2.00	1.95	0.25
Total	99.10	99.29	100.31	97.86	99.14	
Mg#	75.90	80.3	75.80	77.39		
		83.20*	81.64*	82.60*		
CaO	0.393	0.334	0.389	0.354	0.369	
MgO	0.449	0.523	0.449	0.475	0.477	
FeO	0.158	0.143	0.162	0.171	0.155	
Location:	in J-14	Damaping	Erdaobian	Daxigou		

1. Megacryst Cpx-1 in basanite J-14 was analysed using the electron probe at MIT. Data are the average of 5 points on a single Cpx grain.

2. Megacrysts with "No" prefix were analysed by wet chemistry in China (Zhao, 1984).

3. Mg# ($Mg/(Mg+Fe^{2+})$) were calculated assuming all Fe to be Fe^{2+} (same in Tables 2-1b and 2-1c), except for the Mg # with an asterisk which are calculated according to FeO and Fe_2O_3 for the Cpx analyzed in China.

4. AVG = average. STD = standard deviation.

TABLE 2-1a. Chemical Analyses of the Rim of Cpx Megacryst

	a	b	c
SiO_2	59.33	54.73	54.03
TiO_2	0.54	0.84	0.94
Al_2O_3	5.04	1.45	1.17
FeO	4.60	3.73	4.02
MgO	9.66	12.28	12.36
CaO	19.51	25.93	26.31
Na_2O	1.09	0.77	0.68
Total	99.77	99.73	99.51
Mg #	78.9	85.4	84.6

The rim compositions of Cpx megacrysts were analyzed by the electron probe in China (Zhai, 1984).
a - the part near the megacryst
b - the center of the rim
c - the outside part contacting the basalt.

2-1b. Chemical Analyses of Clinopyroxene (Cpx) in Basanite D-1

Cpx	Phenocryst 1		Phenocryst 2		Matrix	
	Core	Rim	Core	Rim	1	2
SiO_2	50.95	45.89	50.36	46.00	48.87	49.35
TiO_2	0.51	2.65	0.63	3.23	1.29	2.01
Al_2O_3	3.81	6.10	5.07	6.66	5.04	4.41
Cr_2O_3			0.03	0.05		
FeO	10.24	7.42	10.35	7.55	5.19	7.09
MnO	0.16	0.13	0.09	0.16	0.10	0.18
MgO	12.26	12.95	12.28	12.34	14.89	12.78
CaO	19.69	22.40	20.13	23.00	21.99	22.32
Na_2O	1.30	0.56	1.45	0.68	0.57	0.66
Total	99.10	98.19	100.40	99.68	98.62	98.86
Mg #	68.10	75.30	67.9	74.00	83.64	76.26

2-1c. Chemical Analyses of Clinopyroxene (Cpx) in Group I and Group II Xenoliths

	Clinopyroxene in lherzolites	Clinopyroxene in Group II Xenolith				
		TGZ		DM2-2		
		A	B	A	B	C
SiO_2	51.68 - 53.97	51.67	51.57	50.19	50.24	50.22
TiO_2	0.03 - 0.39	0.73	0.69	0.42	0.47	0.49
Al_2O_3	3.96 - 5.53	7.25	7.63	8.41	7.93	7.89
Cr_2O_3	2.20 - 2.69	0.13	0.16	0.00	0.07	0.12
FeO	2.20 - 2.69	3.99	4.01	3.35	3.50	3.46
MnO	0.03 - 0.14	0.08	0.09	0.09	0.02	0.00
MgO	15.77 - 17.35	15.13	14.98	14.35	14.40	14.43
CaO	19.86 - 21.41	18.21	18.37	22.69	22.92	22.63
Na_2O	0.91 - 1.58	2.16	2.18	0.90	0.87	0.85
Total		99.34	99.68	100.39	100.41	100.10
Mg #	91.3 - 92.7	86.9	86.9	88.3	88.2	88.1

All clinopyroxene data were analysed using the electron probe at MIT.

Data for clinopyroxene from the lherzolites are the range of clinopyroxenes from six Hannuoba spinel-lherzolites and three pyroxenite veins (Table 4-3c).

Each data set for Group II xenoliths is the average of 2 - 4 points on a single mineral grain.

Table 2-2. Chemical Analyses of Megacryst Garnet (Gt)

	HANNUOBA				
	GT-1	GT-2	GT-3*	AVG (HNB)	STD (HNB)
SiO_2	41.28	41.38	41.00	41.22	0.16
TiO_2	0.46	0.45	0.50	0.47	0.02
Al_2O_3	22.84	22.75	22.03	22.54	0.36
Fe_2O_3			0.68	0.68	0.00
FeO	12.96	12.94	11.79	12.56	0.55
MnO	0.30	0.30	0.34	0.31	0.02
MgO	17.16	16.99	15.93	16.69	0.54
CaO	5.62	5.31	5.06	5.33	0.23
Total	100.27	100.12	97.53	99.31	
Mg#	72.2	69.0	70.7*		

GT	EASTERN CHINA				AVG	STD
	GT-4*	GT-5*	GT-6	GT-7	(Total 7 Gt)	
SiO_2	41.70	42.78	40.85	41.24	41.46	0.60
TiO_2	0.51	0.53	0.35	0.43	0.47	0.06
Al_2O_3	21.75	23.68	22.51	22.41	22.51	0.57
Fe_2O_3	1.60	1.68	14.33	13.23	1.64	6.12
FeO	13.23	12.41			12.93	0.83
MnO	0.53	0.52	0.25	0.24	0.35	0.11
MgO	15.87	14.63	16.54	16.38	16.05	0.69
CaO	5.09	4.59	4.79	5.18	5.08	0.29
Total	100.28	100.83	99.62	99.11	100.49	

GT-1 and GT-2 are megacrysts from basanite J-14 and were analysed using the electron probe at T.Grove's labratory in MIT. GT-3 is megacryst from Hannuoba and was analysed in China (Zhao, 1984). The data of GT from eastern China are from Wang et al (1983). The data with an asterisk obtained by wet chemistry, others by electron probe.
STD = standard deviation.

Table 2-3. Chemical Analyses of Megacryst Anorthoclase (Ano) and Magnetite (MT)

ANO	Ano-1	Ano-2	AVG	STD	MT
SiO_2	65.16	66.34	65.75	0.59	0.17
TiO_2	0.03	0.04	0.04	0.00	21.84
Al_2O_3	19.18	19.42	19.30	0.12	4.07
Fe_2O_3	0.28	0.07	0.18		23.64
FeO	0.00	0.19	0.10	0.10	45.53
MnO	0.00	0.00	0.00	0.00	0.20
MgO	0.30	0.15	0.23	0.07	3.71
CaO	1.25	0.75	1.00	0.25	0.00
Na_2O	7.16	8.68	7.92	0.76	0.33
K_2O	5.32	3.36			0.00
P_2O_5	0.02	0.02			
Loss	0.27	0.32	0.30	0.02	
Total	98.97	99.34	99.16		99.49

Ano-1 is from Damaping sectino, Ano-2 is from Erdaobian section, both were analysed by wet chemistry in China (Zhao, 1984).
Magnetite (MT) was analyzed using electron probe in China (Gan, 1984).

Table 2-4a. Trace Element Abundances in Megacryst Garnet and Clinopyroxene

(ppm)	Sc	Ti	V	Cr	Sr	Zr	Ti/Zr
C1 (A&E)	5.76	436	56.70	2650	7.91	3.69	118.16
J-14	10.20	16306	151.50	119	1115.00	312.00	52.26
R-4	18.95	16066	180.30	186	820.10	252.10	63.73
<u>Garnet</u>							
Gt-1							
MEAN	80.77	3864	233.95	78.38	-	67.30	57.41
STD	3.30	141.5	30.93	2.93	-	5.45	25.95
<u>Clinopyroxene</u>							
Cpx-1							
MEAN	2.10	9145	418.38	88.30	80.93	48.45	188.75
STD	0.82	119	8.67	3.25	1.23	0.84	141.66
Cpx-2							
(ppm)	16.34		323.0	25.8	212.2	53.7	

Table 2-4b. REE abundances in garnet and clinopyroxene megacrysts

	Ce	Nd	Sm	Eu	Dy	Er	Yb
C1	0.616	0.457	0.149	0.056	0.245	0.160	0.159
J-14	101.60	48.50	9.97	3.10	-	-	1.00
R-4	79.10	28.20	7.80	2.55	-	-	1.34
Gt-1							
MEAN	0.197	1.043	1.487	0.894	7.701	5.094	4.769
STD	0.061	0.090	0.057	0.060	0.138	0.168	0.336
Cpx-1							
MEAN	6.706	6.376	2.476	0.937	1.886	0.731	0.685
STD	0.431	0.400	0.179	0.089	0.120	0.087	0.078

Cpx-2	La	Ce	Nd	Sm	Eu	Tb	Yb	Lu
(ppm)	3.0	9.94	8.83	2.80	1.05	0.50	0.30	0.05

1. C1 is the C1 Chondrite abundances from Anders and Ebihara (1982).
2. J-14 is the host basanite for Gt and Cpx megacrysts. R-4 is the most primitive alkali basalts. All basalt trace element data are from Table 1-2.
3. Gt-1 and Cpx-1 data were analyzed with the ion microprobe at N. Shimizu's laboratory by V. Salters. MEAN = mean concentrations based on 4 points analyzed from different portions of a single grain.
4. Cpx-1 and Cpx-2 are two different megacryst grains in basanite J-14. Cpx-2 data are based on the powder of one whole Cpx megacryst, its trace element data obtained by X-ray fluorescence at U. Mass Amherst (Song, this study) and by instrumental neutron activition analysis in R. Hon's laboratory at Boston College (Song, 1983).

Table 2-5a. TE Abundance Ratios of Megacryst Garnet and Clinopyroxene over chondrite and basalts

	Sc	Ti	V	Cr	Sr	Zr	Ti/Zr
Garnet (GT-1)							
MEAN/C1	14.02	8.86	4.13	0.03	-	18.24	0.49
MEAN/J-14	7.92	0.24	1.54	0.66	-	0.22	1.10
MEAN/R-4	4.26	0.24	1.30	0.42	-	0.27	0.90
Clinopyroxene (Cpx-1)							
MEAN/C1	0.36	20.97	7.38	0.03	10.23	13.13	1.60
MEAN/J-14	0.21	0.56	2.76	0.74	0.07	0.16	3.61
MEAN/R-4	0.11	0.57	2.32	0.47	0.10	0.19	2.96
Cpx-1							
Cpx/J-14	1.60		2.13	0.22	0.19	0.17	

Table 2-5b. REE Abundance Ratios of Clinopyroxene and Garnet Megacrysts over J-14

	Ce	Nd	Sm	Eu	Dy	Er	Yb
Gt							
MEAN	0.002	0.022	0.149	0.288	nd	nd	4.769
Cpx-1							
MEAN	0.066	0.131	0.248	0.302	nd	nd	0.685

	La	Ce	Nd	Sm	Eu	Tb	Yb	Lu
Cpx-2	0.70	0.098	0.18	0.28	0.34	0.45	0.30	0.36

Table 2-6a. Least-Square Estimates of the Amount of Fractionation Crystallization Based on Major Element Data

	Daughter J-14	Parent R-4	Calculation 1 Parent	r	Calculation 2 Parent	r
SiO_2	46.47	45.55	45.62	0.074	45.58	0.024
TiO_2	2.76	2.72	2.83	0.109	2.85	0.127
Al_2O_3	14.45	14.03	14.04	0.010	14.00	-0.035
FeO	12.74	12.64	12.62	-0.018	12.71	0.069
MgO	8.53	10.17	10.18	0.012	10.19	0.025
CaO	8.90	9.76	9.73	-0.027	9.68	-0.078
MnO	0.18	0.18	0.18	-0.001	0.18	-0.001
P_2O_5	0.92	0.80	0.68	-0.118	0.69	-0.113
			Σr^2 = 0.033		Σr^2 = 0.042	

Fractionated Mineral:

	Proportion	σ	Proportion	σ
Ol	-0.002	0.004		
Cpx	0.168	0.011	0.163	0.009
Gt	0.069	0.008	0.066	0.006
MT	0.024	0.002	0.025	0.002
Daughter: J-14	0.741	0.015	0.746	0.011
Minerals used for modelling:	Ol (B-5) Gt-a	Cpx-1 MT	Cpx-1 Gt-a	MT

	Calculation 3 Parent	r	Calculation 4 Parent	r	Calculation 5 Parent	r
SiO_2	45.51	-0.036	45.57	0.021	45.57	0.021
TiO_2	2.51	-0.207	2.54	-0.173	2.55	-0.167
Al_2O_3	14.06	0.035	14.03	-0.002	14.03	-0.003
Fe_2O_3	2.84	0.061	2.96	0.178	2.96	0.184
FeO	9.91	0.047	9.85	-0.006	9.87	0.007
MgO	10.18	0.010	10.14	-0.031	10.14	-0.029
CaO	9.77	0.012	9.71	-0.053	9.70	-0.056
Na_2O	3.08	0.474				
K_2O	0.88	-0.647				
MnO	0.20	0.015	0.19	0.012	0.19	0.012
P_2O_5	0.72	-0.078	0.64	-0.163	0.64	-0.163
	Σr^2 = 0.701		Σr^2 = 0.093		Σr^2 = 0.093	

Fractionated Mineral:

	Proportion	σ	Proportion	σ	Proportion	σ
Ano	-0.027	0.051				
Ol	0.002	0.015	-0.000	0.006		
Cpx	0.146	0.091	0.186	0.019	0.186	0.012
Gt	0.088	0.056	0.106	0.015	0.105	0.010
MT	0.005	0.021	0.016	0.003	0.016	0.003
Daughter: J-14	0.705	0.200	0.692	0.028	0.693	0.019

Minerals used for modelling:					
Ano-2 Cpx(No65)	Ol(B-5) Gt-3	MT	Ol (B-5) Gt-3	Cpx(No65) MT	Cpx (No65) Gt-3 MT

Table 2-6b. Least-Square Estimates of the Amount of Fractionation Crystallization Based on Major Element Data

	Daughter ZH-20	Parent J-14	Calculation 1 Parent	r	Calculation 2 Parent	r
SiO_2	47.42	46.47	46.30	-0.173	46.31	-0.163
TiO_2	2.44	2.76	2.61	-0.147	2.58	-0.176
Al_2O_3	15.06	14.45	14.45	-0.001	14.40	-0.049
FeO	11.99	12.74	12.74	-0.003	12.77	0.032
MgO	6.55	8.53	8.47	-0.058	8.53	0.000
CaO	8.43	8.90	9.01	0.111	8.84	-0.060
Na_2O	4.84	3.81	3.90	0.080	3.98	0.155
K_2O	1.93	1.24	1.46	0.216		
MnO	0.16	0.18	0.17	-0.006	0.17	-0.006
P_2O_5	1.19	0.92	0.98	-0.022	0.93	0.005
			$\Sigma r^2 = 0.121$		$\Sigma r^2 = 0.089$	

Fractionated Minerals:

	Proportion	σ	Proportion	σ
Ol	-0.010	0.007		
Cpx	0.155	0.017	0.133	0.009
Gt	0.074	0.011	0.065	0.008
MT	0.027	0.003	0.024	0.002
Daughter: ZH-20	0.755	0.019	0.777	0.011

Minerals used for modelling: Ol (B-6) Gt-b; Cpx (NO18) Mt; Cpx (NO18) Gt-b MT

	Calculation 3 Parent	r	Calculation 4 Parent	r	Calculation 5 Parent	r
SiO_2	46.06	-0.406	45.94	-0.532	46.13	-0.339
TiO_2	2.55	-0.212	2.59	-0.174	2.44	-0.318
Al_2O_3	14.47	0.018	14.45	0.004	14.61	0.156
Fe_2O_3	3.06	0.256	3.11	0.312	2.90	0.104
FeO	9.84	-0.098	9.85	-0.091	9.68	-0.260
MgO	8.47	-0.062	8.51	-0.023	8.40	-0.132
CaO	8.82	-0.080	8.98	0.083	9.08	0.184
Na_2O	3.91	0.095	3.81	-0.013	3.90	0.083
K_2O	1.43	0.187	1.36	0.121	1.43	0.188
MnO	0.17	-0.006	0.18	-0.005	0.18	-0.004
P_2O_5	0.84	-0.083	0.79	-0.130	0.88	-0.039
	$\Sigma r^2 = 0.347$		$\Sigma r^2 = 0.459$		$\Sigma r^2 = 0.414$	

Fractionated Mineral:

	Proportion	σ	Proportion	σ	Proportion	σ
Ano	0.021	0.034	0.024	0.032		
Ol	0.007	0.011				
Cpx	0.148	0.045	0.175	0.032	0.146	0.018
Gt	0.093	0.028	0.106	0.020	0.096	0.016
MT	0.027	0.012	0.032	0.010	0.018	0.004
Daughter: J-14	0.703	0.0102	0.663	0.082	0.740	0.023

Minerals used for modelling: Ano-2 Cpx(No65) Ol(B-5) Gt-3 MT; Ano-2 Cpx(No65) Gt-3 MT; Cpx(No65) Gt-3 MT

Table 2-6c. Least-Square Estimates of the Amount of Fractionation Crystallization Based on Major Element Data

	Daughter R-2	Parent R-4	Calculation 1 Parent	Calculation 1 r	Calculation 2 Parent	Calculation 2 r
SiO_2	45.92	45.55	45.57	0.018	45.56	0.008
TiO_2	2.92	2.72	2.84	0.120	2.83	0.107
Al_2O_3	14.16	14.03	14.01	-0.018	13.93	-0.100
FeO	12.60	12.64	12.42	-0.214	12.51	-0.129
MgO	8.29	10.17	10.17	-0.001	10.18	0.006
CaO	9.14	9.76	9.71	-0.053	9.53	-0.231
MnO	0.17	0.18	0.18	0.002	0.18	0.001
P_2O_5	0.95	0.80	0.71	-0.093	0.74	0.006
			Σr^2 = 0.073		Σr^2 = 0.009	

Fractionated Mineral:	Proportion	σ	Proportion	σ
Ol	-0.012	0.008		
Cpx	0.170	0.022	0.142	0.011
Gt	0.076	0.013	0.062	0.009
MT	0.021	0.004	0.018	0.002
Daughter: R-2	0.744	0.028	0.778	0.015

Minerals used for modelling:	Ol (B-5) Gt-a	Cpx (NO18) MT	Cpx (NO18) Gt-a	MT

1. Using least-squares regression program by Wright and Doherty (1970).
2. Σr^2 = residual sum of squares.
3. σ = standard error on parameter estimated.
4. The megacryst compositions are from Table 2-1, and olivines B-5 and B-6 are xenocrysts in basanite D-1 (Table 1-4).

The equilibrium Kd is assumed as: Kd^{Ol}=0.30, Kd^{Cpx}=0.29, Kd^{Gt}=0.35 which is based on $kd^{Gt/Cpx}$=1.2 (see footnote 3).

In calculations 1 and 2, all Fe in the basalts and minerals are assumed as Fe^{2+}, and the Fe/Mg ratios of the Cpx and Gt megacrysts have been adjusted to be in equilibrium with the daughter basalts. All mineral compositions were renormalized to 100% when computed for modelling.

In calculations 3, 4 and 5, FeO = 0.9 X FeO_{Total} (mole %), and the measured megacryst composition in Table 2-1 are used.

Table 2-7. Trace Element Modelling the Fractionation Model Based on Calculation 2 in Table 2-6b

(ppm)	Ce	Nd	Sm	Eu	Yb	Sr	Zr	Sc	Cr
Obs	101.6	48.5	9.97	3.10	1.00	1115	312	10.2	139
Calc*	107.9	51.3	10.10	3.22	1.04	1117	331	11.2	215
Calc**	107.4	50.8	10.03	3.20	1.12	1091	329	8.7	235
* d %	6.2	5.8	1.3	3.9	4.0	0.2	6.2	9.6	54.7
**d %	5.7	4.7	0.6	3.3	12.0	2.1	5.9	14.9	69.4

1. Obs - observed TE concentrations of basanite J-14 (Table 2-4).
2. Calc - calculated concentrations of basanite J-14. The calculation is using the TE abundance ratios of Gt and Cpx megacrysts over J-14 as partition coefficints, the TE abundances of primitive basanite R-4 (Table 2-4), and the fractionation proportions (calculation 2) from Table 2-6a. Rayleigh equilibrium fractionation equition was used for calculation.
3. * - Cpx-1 data are used in calculation.
   ** - Cpx-2 data are used in calculation.
4. d % = 100 X (Obs-Calc)/Obs.

FIGURES

FIGURE CAPTIONS

Figure 2-1. Ca-Mg-Fe components for clinopyroxene megacrysts (adopted from Fig. 2, Irving 1974). Triangles - Hannuoba clinopyroxene megacrysts (Table 1a). The field with solid line enclose 36 clinopyroxene megacrysts from the Newer basalts, Australia, two diamonds also are clinopyroxene megacrysts from the Newer basalts (from Fig. 2, Irving 1974). The field with dashed line are 11 clinopyroxene megacrysts from Massif Central, France, and the circle is also a clinopyroxene megacryst from Massif Central (Liotard et al., 1988).

Figure 2-2. Chondrite-normalized REE patterns for Hannuoba garnet and clinopyroxene megacrysts. The field for pyrope-rich garnet megacrysts from kimberlites and alkaline basalts is adopted from Irving and Frey (1978). The field for the clinopyroxene megacrysts from the alkali basalts is based on Irving and Frey (1984) and Liotard et al (1980).

Figure 2-3. Ternary plot of end-member proportions (mole %) for garnet megacrysts (adopted from Fig. 1, Irving and Frey, 1978). Triangles are garnet megacrysts from the Hannuoba basalts. Field I encloses pyrope-rich garnet megacrysts from the kimberlites and alkaline basalts, field II encloses almandine-rich garnet from calc - alkaline volcanics. Data sources see Irving and Frey, 1978.

Figure 2-4. Ternary plot for feldspar megacrysts in the alkaline basalts (adopted from Fig. 3, Irving, 1974). The diamond is Hannuoba anorthoclase megacryst Ano-2; the solid diamond is Hannuoba anorthoclase megacryst Ano-1. The field encloses the anorthoclase megacrysts from the Newer basalts, Australia; triangles are megacrysts from other localities in Australia. Data sources see Irving, 1974.

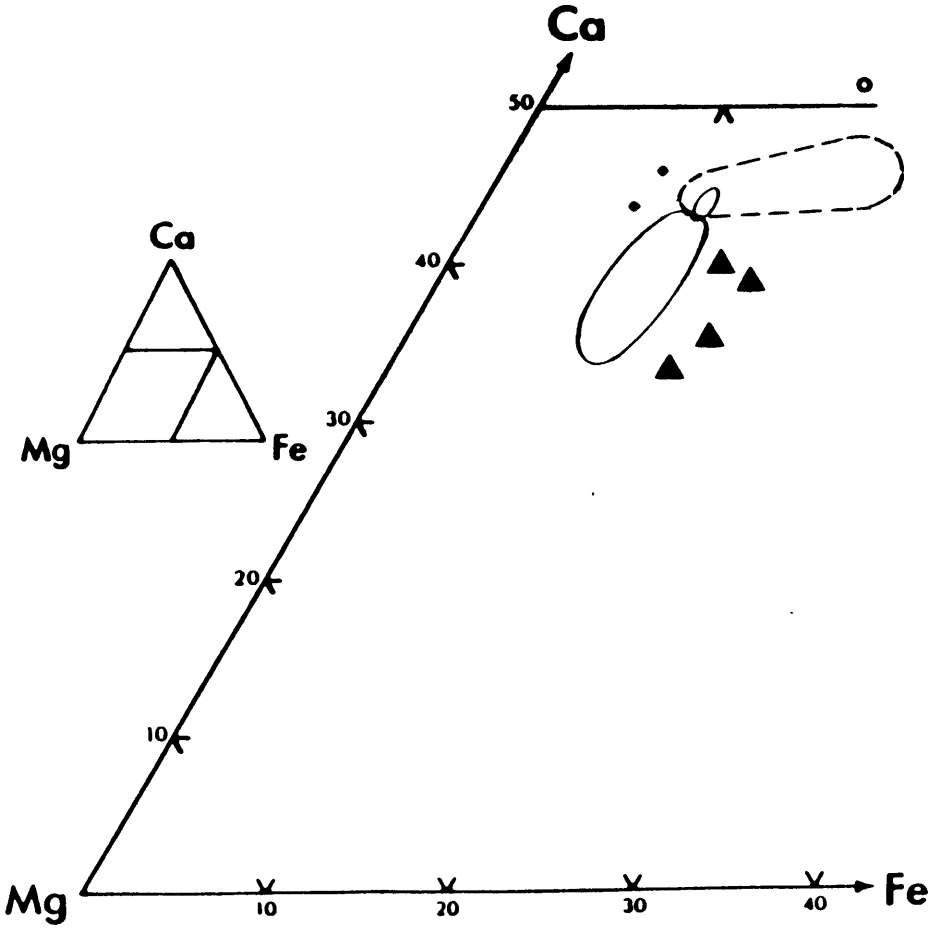

FIGURE 2-1

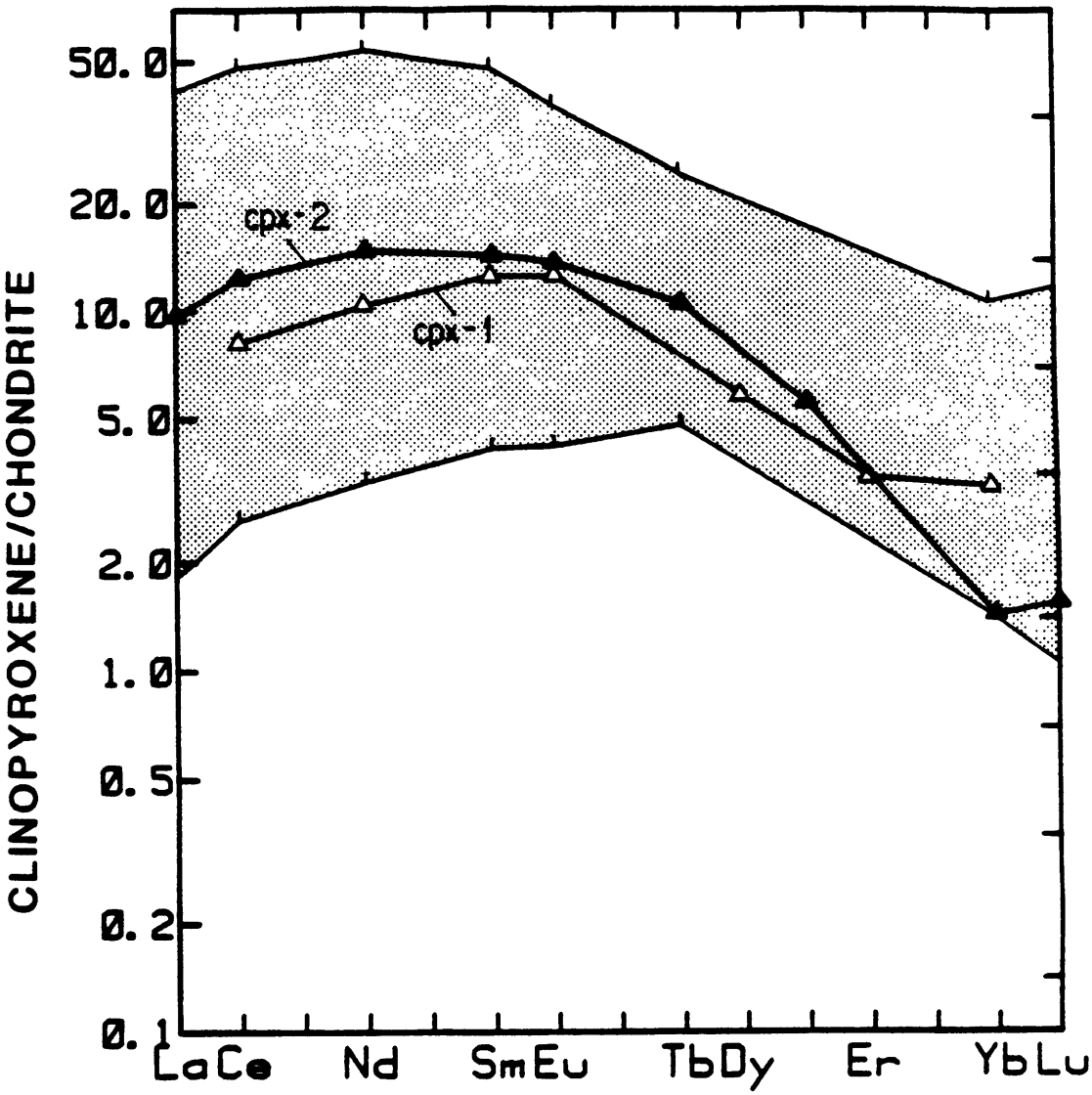
CLINOPYROXENE/CHONDRITE
50.0
20.0
10.0
5.0
2.0
1.0
0.5
0.2
0.1
cpx-2
cpx-1
LaCe
Nd
SmEu
TbDy
Er
YbLu

FIGURE 2-2a

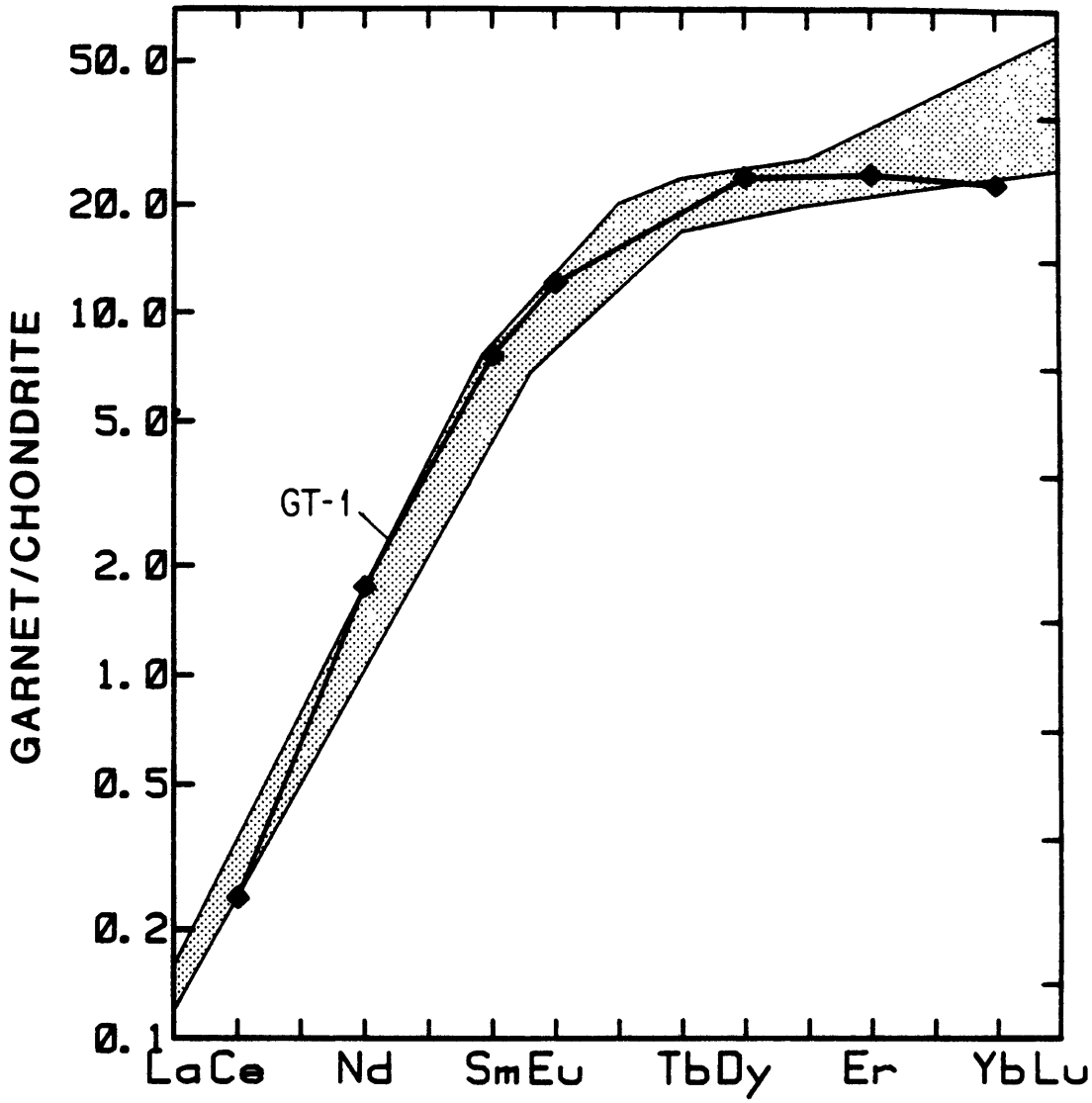
GARNET/CHONDRITE
50.0
20.0
10.0
5.0
2.0
1.0
0.5
0.2
0.1
GT-1
LaCe
Nd
SmEu
TbDy
Er
YbLu

FIGURE 2-2b

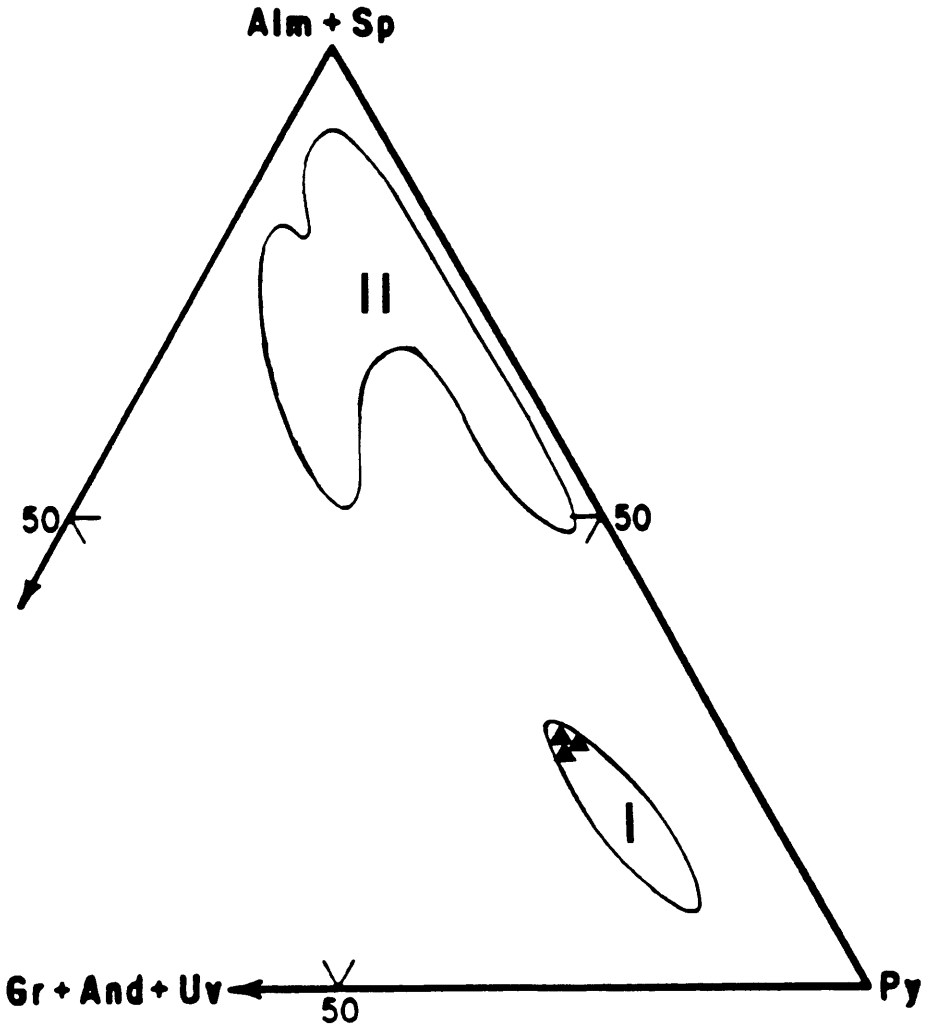

FIGURE 2-3

FIGURE 2-4

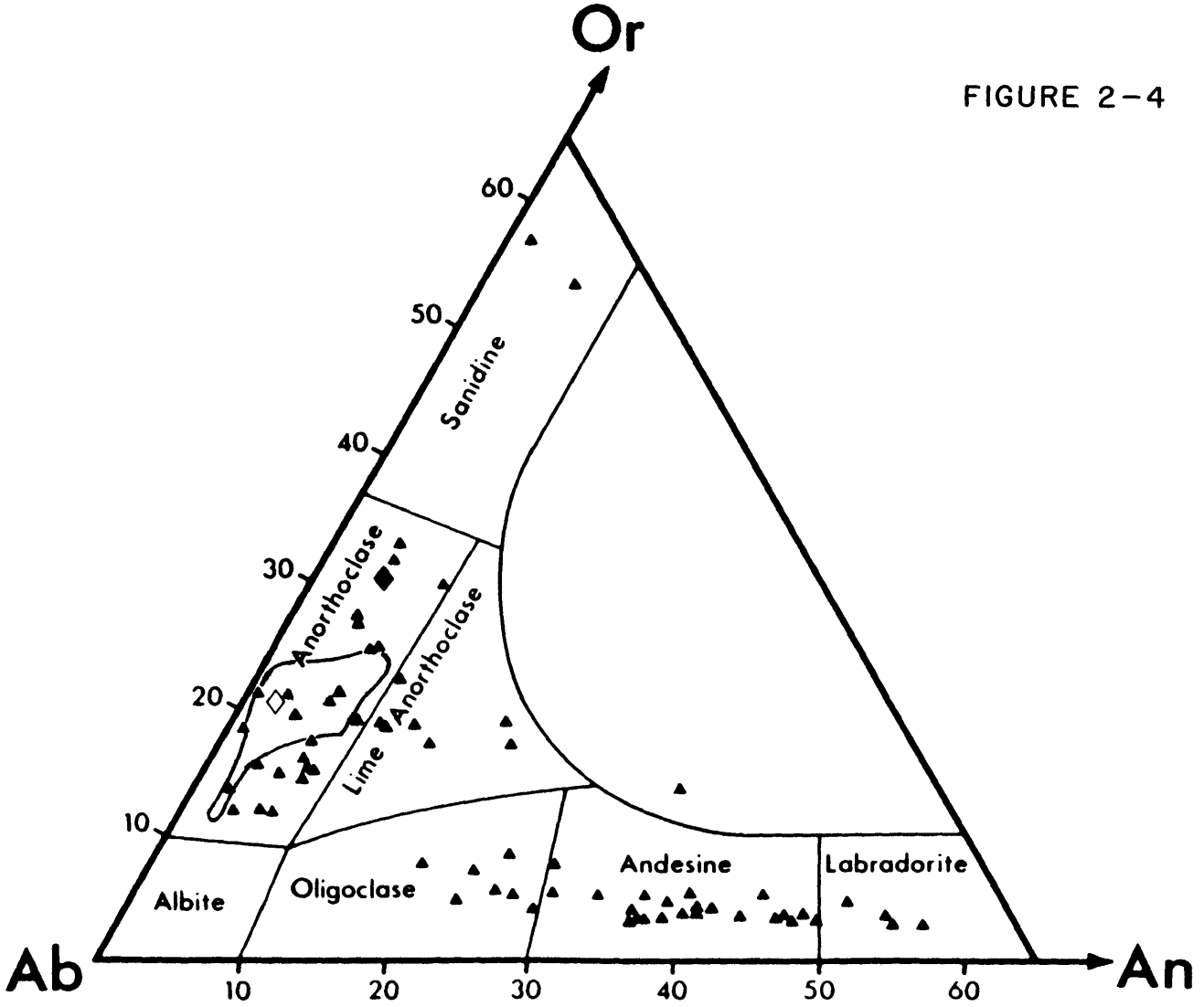
Or
Ab
An
10
20
30
40
50
60
Sanidine
Anorthoclase
Lime Anorthoclase
Albite
Oligoclase
Andesine
Labradorite

CHAPTER 3: ISOTOPIC CHARACTERISTICS OF HANNUOBA BASALTS: IMPLICATIONS FOR THEIR PETROGENESIS AND THE COMPOSITION OF SUBCONTINENTAL MANTLE

3-1. INTRODUCTION

The data base for isotopic ratios of Sr, Nd and Pb in oceanic basalts is now sufficient to discuss and possibly identify the end-member suboceanic mantle components required by the range of isotopic data (i.e., Zindler et al, 1982; Zindler and Hart, 1986; Hart et al., 1986; Hart, 1988). There is also a large isotopic data base for continental basalts. However, developing a comparable understanding of the subcontinental mantle is more complicated because: (a) mantle derived magmas in a continental setting may be contaminated during ascent through thick continental crust, and (b) the subcontinental mantle lithosphere is thicker and older than the suboceanic mantle lithosphere; therefore it is compositionally more diverse (e.g., Sun et al., 1989). For example, the relatively high $^{87}Sr/^{86}Sr$, and low $^{143}Nd/^{144}Nd$ ratios in most continental basalts could reflect crustal contamination (e.g., Carter et al., 1978; Carlson et al., 1981; Thirlwall and Jones, 1983; Carlson, 1984; Dickin et al., 1987; Perry et al., 1987) or enriched sub-continental lithosphere (e.g., Brooks et al, 1976; Carlson, 1984; Hawkesworth et al., 1984, 1986; Worner et al., 1986; Perry et al., 1987, 1988).

In an effort to understand mantle processes and to characterize subcontinental mantle beneath northeastern China, we determined the major and trace element compositions (Chapter 1, Zhi et al., 1989) and Sr, Nd and Pb

isotopic ratios (this Chapter) of intercalated tholeiitic and alkali Cenozoic basalts from Hannuoba, China. Also, Song and Frey (1989) (Chapter 4) studied the mantle xenoliths in these alkali basalts; therefore we can infer subcontinental mantle compositions in northeastern China from data for mantle xenoliths and mantle-derived basalts.

The contribution of subcrustal lithosphere and crust to the petrogenesis of continental basalts is a fundamental problem in geochemistry. The lack of information about the geochemical compositions of subcontinental mantle lithosphere and lower crust in many areas, including northeastern China, makes this problem more difficult to address. Previous geochemical studies of Cenozoic lavas from diverse areas of eastern China have shown that initial $^{87}Sr/^{86}Sr$ ratios correlate positively with crustal thickness in the region from the Bohai Sea to northeast Hebei Province (Zhou and Armstrong, 1982, Figure 11). In addition, the northeast-southwest trending Tan-Lu fault separates basalts with different Pb isotopic characteristics (Peng et al, 1986, Figure 8). These authors recognized that such geochemical trends might reflect crustal contamination; however, they favored differences in mantle compositions as an explanation for the isotopic trends defined by basalts from eastern China.

Hannuoba basalts, Hebei Province, are west of the Tan-lu fault (Fig. I-4) in a region with relatively thick crust (~40 km). These basalts are useful for evaluating the roles

of crustal contamination and compositional heterogeneties in the subcontinental mantle because:

(a) the intercalated Hannuoba alkali and tholeiitic basalts may have sampled the mantle at different depths;

(b) the abundant mantle-derived xenoliths in the alkali basalts require rapid magma ascent with little time for crustal contamination;

(c) studies of the mantle xenoliths provide direct constraints on upper mantle compositions in this region; and

(d) with a comprehensive geochemical data set we can use major and trace element compositional trends to constrain hypotheses for explaining variations in radiogenic isotope ratios.

3-2. ANALYTICAL TECHNIQUES

Clean fragments of most samples (150g) were powdered in an agate shatterbox at the Center of Geoalchemy, MIT; however powders of samples from the Xiliuling (ZX) and Damaping (ZB) sections are splits of samples prepared in China by Zhai (1983).

The high H_2O contents in some basalts (0.38 to 4.60%), the post-magmatic alkali metal mobility and the petrographic characteristics (Chapter 1) reflect surficial alteration. To evaluate the effects of alteration on isotopic ratios, several samples were analyzed for isotopic ratios before and after acid leaching (100^{o}C, 2.5N HCl, ~12 hours). In all

cases acid leached samples have lower $^{87}Sr/^{86}Sr$, with the largest decrease, 0.70430 to 0.70384, for sample D-3 (Table 3-1a). In contrast to the Sr isotopic system, Nd and Pb isotopic ratios were not markedly affected by acid leaching (Table 3-1a and 3-1b)). Typically, Rb and Sr contents were also lower in the leached residues (Table 3-1c). A second leaching step in more concentrated acid (6.2N HCL) did not cause a further decrease in $^{87}Sr/^{86}Sr$ (samples D-1 and J-1, Table 3-1a). We conclude that the easily removed 87Sr reflects surface alteration and secondary carbonate; therefore, $^{87}Sr/^{86}Sr$ ratios of acid-leached residues approximates the magmatic ratios.

In Table 3-2 all Sr and Nd isotopic data are for leached samples (100^{o}C, 2.5N HCl), but Pb data (Table 3-3) are for unleached samples. All isotopic ratios are reported as present-day values because the young age of the basalts (10-20 m.y.), leads to only small corrections for radioactive decay. Chemical and mass spectrometry techniques are indicated in Tables 3-2 and 3-3.

3-3. RESULTS

In a $^{143}Nd/^{144}Nd$ versus $^{87}Sr/^{86}Sr$ plot Hannuoba basalts lie within the main field defined by oceanic island basalts (OIB); specifically, the alkali basalts have relatively high $^{143}Nd/^{144}Nd$, low $^{87}Sr/^{86}Sr$ and overlap with the field for Hawaiian basalts whereas Hannuoba tholeiites range to near

bulk earth estimates (Fig. 3-1). Two tholeiitic laves (ZX-62 and Bai-17) are offset from the main trend to low $^{87}Sr/^{86}Sr$. Transitional basalts have Sr and Nd isotopic ratios filling the gap between alkalic and tholeiitic lavas (Fig. 3-1)[5].

In isochron plots there is an inverse trend between $^{143}Nd/^{144}Nd$ and Sm/Nd (Fig. 3-2) but there is no trend between Rb/Sr and $^{87}Sr/^{86}Sr$. Because the Rb and Sr data are for unleached altered basalts, the lack of a Rb/Sr-$^{87}Sr/^{86}Sr$ trend probably reflects mobility of Rb and Sr during alteration (e.g., see Table 3-1c). In a $^{206}Pb/^{204}Pb$ versus $^{207}Pb/^{204}Pb$ diagram (Fig. 3-3), the Hannuoba alkali basalts also lie within the field of oceanic island basalts, but the tholeiites extend to lower $^{207}Pb/^{204}Pb$ ratios and plot on the left side of the 4.55 b.y geochron. All of the Hannuoba basalt data define an elongated trend which has a steepr slope than the Northern Hemisphere reference line (Hart, 1984). The slope defined by Hannuoba basalts is also greater than that defined by Walvis Ridge basalts, but it is similar to the trend defined by Shandong basalts from eastern China which also extend to low $^{206}Pb/^{204}Pb$ (Peng et al, 1986). In a $^{206}Pb/^{204}Pb$ versus $^{208}Pb/^{204}Pb$ diagram Hannuoba basalts are also co-linear with the Shandong basalts, and they define a trend between the Walvis Ridge and oceanic regression line (Fig. 3-3b).

---

5. Transitional lavas (Chapter 1) have major element compositions intermediate to the tholeiitic and alkalic groups, they contain less than 50% SiO_2 but lack upper mantle xenoliths.

In summary, Hannuoba basalts have the distinctive isotopic characteristics that have been recognized in other Cenozoic basalts from eastern China, i.e., (1) alkali basalts have lower $^{87}Sr/^{86}Sr$ and higher $^{143}Nd/^{144}Nd$ than intercalated or nearby tholeiitic basalts, thereby creating an inverse trend between Sm/Nd and $^{143}Nd/^{144}Nd$ (Fig. 3-2 and Zhou and Carlson, 1982), and (2) the tholeiitic lavas trend to lower $^{206}Pb/^{204}Pb$ and $^{206}Pb/^{204}Pb$ than most oceanic lavas, thereby reflecting a time integrated low U/Pb ratio (Fig. 3-3 and Peng et al., 1986). Also, among the Hannuoba lavas the alkalic and tholeiitic fields define distinct isotopic fields with the transitional basalts filling the gap. Therefore, the Hannuoba suite as a whole defines elongated trends in isotopic plots (Figs. 3-1 to 3-3).

3-4. DISCUSSION

3-4.1. Summary of Geochemical Characteristics

Based on data in Chapter 1 and this Chapter, important geochemical characteristics of Hannuoba basalts are:

1) The alkalic basalts are compositionally similar to alkalic basalts from oceanic islands. Tholeiitic and alkalic Hannuoba basalts have similar abundance ratios of highly incompatible elements (such as La/Ce, Nb/Ta), and systematic differences in abundance ratios involving moderately incompatible elements. The latter could be explained by

different degrees of melting of a compositionally homogeneous source (Chapter 1, Figs. 1-10 and 1-12). However, 2) Evidence for different liquid lines of descent are reflected in the diverging trends in MgO variation diagrams, e.g., MgO vs. La/Yb, Ti/Zr and Zr/Y ratios (Figs. 1-6, 1-11), which cannot be interpreted by different degrees of melting of a compositionally homogeneous source. Compositional variations within the alkalic basalts, all containing upper mantle xenoliths, can be explained by high pressure fractionation of a garnet-clinopyroxene assemblage (Chapters 1 and 2).

3) Isotopic ratios of alkalic Hannuoba basalts overlap with those of OIB (Fig. 3-1 and 3-3) and Sr-Nd isotope compositions are near the PREMA field of Zindler and Hart (1986). Although isotopic ratios in alkalic Hannuoba lavas do not range widely, the most mafic, least evolved (MgO = 8-10 %) samples (R-6, Zh-3, Bai-9 and ZX-44) define the high $^{87}Sr/^{86}Sr$, low $^{143}Nd/^{144}Nd$ end of the field defined by the alkalic basalts (Figs. 3-1 and 3-4, Table 3-2).

4) Although relatively depleted in incompatible element contents, Hannuoba tholeiites have higher $^{87}Sr/^{86}Sr$ and lower $^{143}Nd/^{144}Nd$ than the intercalated alkali basalts. The tholeiites also trend to low $^{206}Pb/^{204}Pb$ - $^{207}Pb/^{204}Pb$ end of the northern hemisphere reference line (NHRL) of Hart (1984). They have lower $^{207}Pb/^{204}Pb$ than the enriched oceanic mantle component EMI of Zindler and Hart (1986) (Fig. 3-3). The lowest $^{206}Pb/^{204}Pb$ - $^{207}Pb/^{204}Pb$ ratios are

in two Hannuoba tholeiites (Bai-17 and Zx-62, Fig. 3-3) which also deviate from the $^{87}Sr/^{86}Sr$-$^{143}Nd/^{144}Nd$ trend to low $^{87}Sr/^{86}Sr$ ratios (Fig. 3-1).

5) The Nd, Sr, and Pb isotopic compositions of the Hannuoba basalts define coherent trends; specifically, the positive Nd-Pb correlation (Fig. 3-5a), and the negative Sr-Pb correlation (Fig. 3-5b) are opposite to the trend defined by MORB (Allegre et al., 1980; Cohen et al., 1980; Dupre and Allegre,1980), but they are similar to those of many continental basalts and some oceanic basalts.

In subsequent sections we use these geochemical characteristics to evaluate and constrain petrogenetic models for Hannuoba basalts.

3-4.2. Evidence For Mixing

The isotopic differences between Hannuoba alkalic and tholeiitic basalts require isotopically distinct mantle components or a significant role for assimilation of continental lithosphere, either mantle or crust. The elongated trends defined by all Hannuoba basalts in isotopic ratio plots (Figs. 3-1, 3-2 and 3-3) are consistent with a genetic relationship between alkalic, transitional and tholeiitic basalts. Based on the inverse correlation between $^{143}Nd/^{144}Nd$ and Sm/Nd in basalts from Hannuoba and other eastern China locations (Fig. 3-2) the simplest interpretation is that these trends reflect recent mixing of

isotopically distinct components. Near linear trends among abundances of highly incompatible elements (Th, Zr, La, Sr, and Nb, Fig. 1-6) are also consistent with mixing. Moreover, the elongated trends defined by Hannuoba basalts in plots of $^{143}Nd/^{144}Nd$ versus 1/Nd and $^{87}Sr/^{86}Sr$ versus 1/Sr (Fig. 3-6) are evidence for mixing of two isotopically distinct components. In each case the tholeiitic basalts with lower Sr and Nd contents than the alkalic basalts have isotopic ratios more similar to crustal rocks. However, the present Hannuoba lava compositions do not reflect simple mixing of two compositionally different components; for example, major and trace element abundances in the lavas define several complex, non-linear trends, such as MgO vs. P_2O_5, Th, and Ni-Th (Figs. 1-4 and 1-8). Evidence for different liquid lines of descent are the diverging trends in MgO variation diagrams, e.g., MgO vs. La/Yb Ti/Zr, Zr/Y (Figs. 1-6 and 1-11), and $^{143}Nd/^{144}Nd$ ratios (Fig. 3-4b). The mixing process reflected by isotopic variations and abundance variations of highly incompatible elements may precede mineral - melt segregation processes such as fractional crystallisation. Compositional variations within the alkalic basalts, all containing upper mantle xenoliths, can be explained by high pressure fractionation of a garnet-clinopyroxene assemblage. However, this high presssure fractionation can not explain the variation trends of MgO vs. Ba/La, Ba/Th and Ba/Nb (Fig.1-10a), these trends may indicate mixing of relatively primitive and evolved lavas for Hannuoba alkali basalts.

Therefore, there may be three sources/magmas mixing processes: mixing between the sources/magmas for primitive alkalic basalts and tholeiitic basalts, and mixing between the sources/magmas for the primitive and the very evolved (i.e., MgO = 5.7% in Zh-20) alkali basalts.

3-4.3. Endmember Components Represented in Hannuoba Alkalic Basalts

Alkalic basalts from Hannuoba have abundances of incompatible elements (Chapter 1) and isotopic ratios (Figs. 3-1, and 3-3) which overlap with OIB. Their Sr-Nd isotopic ratios are close to the PREMA component of Zindler and Hart (1986). This similarity extends to other continental alkalic basalts containing mantle xenoliths, e.g., the west African Shield (Allegre et al., 1981), eastern Australia (McDonough et al ., 1985), west Germany (Worner et al., 1986), western US (Perry et al., 1987, 1988) and the Cameroon line volcanics from oceanic and continental sectors (Halliday et al., 1988). Clearly, this type of OIB source material exists beneath oceanic and continental regions.

3-4.4. Endmember Components Represented in Hannuoba Tholeiitic Basalts

The components contributing to Hannuoba tholeiitic basalts are more difficult to define. In the following

discussion, we evaluate two alternative models. In Model A the geochemical trends defined by all Hannuoba lavas are interpreted as reflecting mixing of isotopically distinct components that are resident in the oceanic asthenosphere or below. In Model B the Hannuoba trends are interpreted as reflecting mixing of mantle-derived melts, formed by different degrees of melting of an oceanic mantle source, with subsequent and variable addition of a continental lithosphere, crust or mantle, component.

Evaluation of Model A: Derivation of all Hannuoba lavas from oceanic mantle sources.

Although distinct from Hannuoba alkali basalts, Sr and Nd isotopic ratios in Hannuoba tholeiites are also depleted relative to bulk earth estimates, and they are within the Sr and Nd isotopic field of oceanic basalts (Fig. 3-1). Hannuoba tholeiitic lavas also trend to low $^{206}Pb/^{204}Pb$ ratios (Fig. 3-3), define a positive $^{143}Nd/^{144}Nd$-$^{206}Pb/^{204}Pb$ trend and lie at high $^{87}Sr/^{86}Sr$, low $^{206}Pb/^{204}Pb$ end of the Hannuoba field (Fig. 3-5). Similar correlations between Sr, Nd and Pb isotopic ratios (Fig. 3-5) have been reported for many continental basalts, for instance,the Yellowstone Plateau Volcanic Field (Doe et al., 1982), and the Kenya Rift Valley of East Africa (Norry et al., 1980). Thus these correlations may represent a continental "flavor"; that is, a component with high $^{87}Sr/^{86}Sr$, low $^{143}Nd/^{144}Nd$ and $^{206}Pb/^{204}Pb$ as suggested by Peng et al (1986). However,

similar correlations also characterize the south Atlantic Walvis Ridge basalts (used to define the EMI component), Hawaiian basalts and mantle-derived alkaline magmas from the Quaternary East and West Eifel volcanics, West Germany (Worner et al., 1985, 1986). These similar Nd-Sr-Pb isotopic correlations in oceanic and continental regions may reflect similar mantle processes and components. Moreover, an unusual oceanic basalt from the western Indian Ocean (sample D-5, Hamelin and Allegre, 1985) lies along an extension of several isotopic trends defined by Hannuoba basalts (Figs. 3-3 and 3-4). Hart (1988) interpreted that this MORB sample reflects mixing of DMM with the EMI component. Thus, the isotopic trend of all Hannuoba basalts may reflect mixing between the PREMA and an EMI-like components (Figs. 3-1, 3-3 and 3-5).

However, the isotopically extreme tholeiites (ZX-62 and Bai-17) with the lowest $^{206}Pb/^{204}Pb$ ratios, and relatively low $^{87}Sr/^{86}Sr$ have $^{207}Pb/^{204}Pb$ and $^{208}Pb/^{204}Pb$ ratios lower than those for the EMI component defined by Hart (1988) (see Fig. 3-3). Compared to the other tholeiites, these two samples are also offset to lower $^{87}Sr/^{86}Sr$ (Fig. 3-1). A possible interpretation is heterogeneity in the EMI component.

Strong support for the role of an EMI-like component in Hannuoba tholeiites is provided by Ba/Nb-Pb isotopic trends (Fig. 3-7). Basalts from several oceanic islands, the Walvis Ridge and Indian Ocean sample D-5 define systematic trends

toward the Pb isotopic characteristics of the EMI component. Hannuoba samples fall within this trend with the tholeiitic lavas having higher Ba/Nb and more extreme Pb isotopic ratios (Fig. 3-7). Only a single broad trend is defined by Ba/Nb - delta 8/4 plot (Fig. 3-7a), but oceanic islands and MORB sample D-5 define two trends in the Ba/Nb - delta 7/4 plot. In this plot (Fig. 3-7b) Hannuoba tholeiites overlap with lavas from the Walvis Ridge, Tristan da Cunha and Kerguelen.

Evaluation of Model B: Derivation of all Hannuoba basalts from an oceanic mantle source with the addition of a continental-related component to the tholeiitic lavas.

Abundance ratios of incompatible elements in Hannuoba alkalic and tholeiitic basalts could be explained by varying degrees of melting of a compositionally homogeneous source (see Chapter 1). In this case, the intersecting chondrite-normalized REE patterns of tholeiitic and alkalic lavas (Fig. 1-5) requires that the alkalic lavas equilibrated with residual garnet. The absence of residual garnet during generation of the tholeiitic lavas may reflect melting at lower pressure or elimination of garnet by high degrees of melting. Thus, the major and trace element data are consistent with derivations of Hannuoba alkalic and tholeiitic basalts from compositionally similar mantle. However, the isotopic differences between the basalt types require isotopically different components. Therefore a main

question is: was the enriched isotopic component (EMI-like) in the tholeiitic basalts from mantle or from continental crust? This is a classic and also modern question: how important was the crustal contamination for the petrogenesis of continental basalts?

Because alkali basalts from oceanic and continental regions are geochemically similar, and because of the abundance of dense, mantle-derived inclusions in Hannuoba alkali basalts, we infer that crustal contamination did not affect these alkali basalts. However, the tholeiitic lavas do not contain mantle inclusions. Moreover, if the tholeiitic magmas were derived by relatively higher degrees of melting, they would be more susceptible to crustal contamination because of their lower incompatible element content and their lower dissolved volatile contents may have caused lower ascent rates. Country rocks in the Hannuoba region are Archean metamorphic rocks, Jurassic sediments and granites, Cretaceous to Quaternary sediments (BHTHED, 1978). Clearly, possible crustal contaminants are melts/fluids derived from the siliceous upper crust or the acid to ultramafic Archean granulites (lower crust?).

There is no evidence that the tholeiitic lavas evolved in a shallow magma system where assimilation of crustal wallrock accompanied fractional crystallization. That is, the more evolved tholeiitic lavas do not have isotopic ratios closer to typical upper crust; in fact, the lowest $^{87}Sr/^{86}Sr$ ratios are in tholeiites with the lowest

Mg/(Mg+Fe) (Fig. 3-4). Also most upper crustal rocks do not have the Sm/Nd-$^{143}Nd/^{144}Nd$ ratios required by the Hannuoba mixing trend (Fig. 3-8a).

In an effort to further constrain the possible continental component in Hannuoba tholeiites we used geochemical data for Archean granulites exposed ~250 km east of Hannuoba region (Jahn and Zhang, 1984). Based on these data the Hannuoba basalt trend is not consistent with contamination by the acid or intermediate granulites (Figs. 3-8 and 3-9). However, the mafic granulites and Hannuoba tholeiites have geochemical similarities. For example, they have similar SiO_2 and Sm/Nd (Fig. 3-9). Moreover, two ultrabasic granulites lie along the inverse $^{143}Nd/^{144}Nd$ - Sm/Nd defined by Hannuoba lavas (Fig. 3-8a). However, in detail none of these granulites (or samples in a world-wide survey of granulites) have all the geochemical characteristics required to explain the Hannuoba basalt trend. For example, neither the granulites or partial melts from the granulites lie along the $^{143}Nd/^{144}Nd$ - $^{87}Sr/^{86}Sr$ trend of the Hannuoba lavas (Fig. 3-8b).

Pb isotopic data are useful in identifying crustal contamination because of relatively high Pb contents in crustal rocks, and the general trend for upper crustal rocks to have higher radiogenic Pb isotope ratios than lower crustal rocks (e.g., Zartman and Doe, 1981; Zartman and Haines, 1988). However, continental mantle lithosphere may have a Pb isotopic signature similar to the lower crust

(e.g., Halliday et al., 1985, 1988; Menzies et al., 1987). Examples of subcontinental mantle lithosphere with isotopic characteristics similar to Hannuoba tholeiites are mantle xenoliths, interpreted as samples of enriched lithosphere, below Scotland (Menzies et al., 1987). Also, a spinel lherzolite xenolith (DM1-7, see Chapter 4) from Hannuoba is offset to $^{143}Nd/^{144}Nd$ along the trend formed by the Hannuoba tholeiites with low $^{87}Sr/^{86}Sr$ (Fig. 3-1). Therefore, the relatively low $^{143}Nd/^{144}Nd$ coupled with low $^{206}Pb/^{204}PPb$ in Hannuoba tholeiites (Fig. 3-5a) reflecting time integrated low U/Pb and Sm/Nd, may be characteristic of enriched subcontinental mantle lithosphere (e.g., Fraser at al., 1985/86, Hawkesworth et al., 1986) or lower crustal granulites (e.g., Othman et al., 1984).

Supporting evidence for a crustal component in Hannuoba tholeiites are provided by Pb/Ce abundance ratios (Table 3-3). Consistent with an oceanic mantle composition for the source of Hannuoba alkali basalts, the Hannuoba alkali basalts have the same Ce/Pb range (25±5) as oceanic basalts (Hofmann et al., 1986; Newsom et al., 1986). However, the Hannuoba tholeiites have lower Ce/Pb values (18.9 to 15.6). This difference in Pb/Ce ratios and the Pb isotopic ratios of tholeiite Bai-17 (the sample with the lowest $^{206}Pb/^{204}Pb$ ratio) are consistent with mixing at least 90% mantle-derived melt with up to 10% melt derived from the lower crust. This mass balance result is based on an uncontaminated mantle with $^{206}Pb/^{204}Pb$ = 18.0 (typical of

Hannuoba alkali basalt), Pb/Ce = 0.036 (typical OIB ratio, Hofmann et al., 1986; Newsom et al., 1986) and a Pb content of 1 ppm (chosen to be representative of maximum value in uncontaminated tholeiitic basalts), and a lower crust with Pb/Ce = 0.30, $^{206}Pb/^{204}Pb$ = 15.96 (Table 3-4, Newsom et al., 1986), and a minimum Pb concentration of 10 ppm. Therefore, the Hannuoba tholeiites may have formed from the same mantle source as the alkali basalts by higher degrees of partial melting, and then assimilated up to 10% of lower crust or an old subcrustal mantle lithosphere.

It is also possible that low Ce/Pb ratios occur in oceanic basalts. In particular, the enriched oceanic component EMI may be characterized by low Ce/Pb; e.g., based on limited data (3 samples), Ce/Pb ratios are ~18 in Indian Ocean basalts with $^{206}Pb/^{204}Pb$ = 17.3 (Hofmann et al., 1986; Ito et al., 1987).

At this point we conclude that the distinctive geochemical characteristics of the Hannuoba tholeiites <u>are not</u> consistent with control by a upper crust component, <u>but we can not</u> distinguish between components from enriched oceanic mantle (EMI-like, Model A) or continental components residing in the lower crust or upper mantle. However, the small isotopic variations within the alkalic, xenolith-bearing, Hannuoba basalts may lead us to eliminate the lower continental crust as an important component. Specifically, the Hannuoba alkali basalts were divided into two groups based on major and trace element abundances (see Chapter 1).

Although the isotopic variations are small, the primitive alkali basalts (R-6, Zh-3, Zx-44 and Bai-9) have slightly higher radiogenic Sr, and lower radiogenic Nd than the more evolved alkali basalts (Table 3-2). Therefore, the more primitive alkali basalts have isotopic ratios closest to the field defined by the tholeiites, i.e., the least evolved alkalic lavas may have experienced a larger amount of contamination than more evolved alkali basalts. Similar results have been observed in other continental basalts, for example, the Paleocene magmas in Skye, Northwest Scotland (Thirlwall and Jones, 1983; Dickin et al., 1987), and the Deccan Traps flood basalts in the Western Ghats area of western India (Devey and Cox, 1987). This observation has been interpreted as reflecting contamination during magma ascent rather than in a magma chamber (Huppert and Sparks 1985; Devey and Cox, 1987). The more primitive compositions are more contaminated because of their higher temperature and lower incompatible element content (Huppert and Sparks 1985; Dickin et al., 1987). However, the presence of mantle xenoliths in Hannuoba alkali basalts suggests that crustal contamination was not important for these basalts. The primitive alkali basalts were contaminated by an EMI-like composition (the source for Hannuoba tholeiites) from a mantle component rather than from lower crust. Therefore, lower crust is an unlikely source of the enriched component present in the tholeiitic basalts and to a lesser extent in the primitive alkalic basalts. However, an exception may be,

the alkali basalts containing mantle xenoliths also could be contaminated by crust due to the rapid heat transfer from a turbulently convecting magma (Huppert and Sparks, 1985; Campbell, 1985; Rutter, 1987). If this is true, the isotopic difference between alkalic and tholeiitic basalts may reflect up to 10% of lower crustal contamination for tholeiitic basalts (i.e., Bai-17), and slightly crustal contamination for primitive alkali basalts.

3-4.5. Proposed Petrogenetic Model for Hannuoba Lavas

We conclude that Hannuoba alkalic basalts were generated from garnet-bearing asthenosphere by small degrees of melting. Their mantle source had depleted Sr and Nd isotopic characteristics but enriched Pb isotope characteristics; i.e., isotopic characteristics similar to the PREMA component of Zindler and Hart (1986). This is a world-wide source for alkali basalts erupted on oceanic islands and continents. During ascent in the mantle, some of the alkalic basalts fractionated clinopyroxene and garnet (Chapter 1 and 2). However, the small amount of isotopic variation among the Hannuoba alkalic basalts (Figs. 3-1 and 3-3) shows that the least evolved samples are slightly offset towards the isotopic field defined by the tholeiitic lavas. This suggests that the most primitive alkalic basalts (MgO = 8-10 %) assimilated material from a mantle component that was the source of Hannuoba tholeiitic basalts.

Hannuoba tholeiitic basalts are isotopically more diverse than the alkalic basalts and they define trends to higher $^{87}Sr/^{86}Sr$, lower $^{143}Nd/^{144}Nd$ and less radiogenic Pb isotopic ratios (Figs. 3-1 and 3-3). Although it is unlikely that the tholeiites ascended through continental crust without contamination, we discern no obvious geochemical effects resulting from assimilation of upper crustal components. In isotopic space the tholeiites trend towards the enriched EMI-like component expressed in oceanic basalts. However, in detail Hannuoba tholeiites may define two distinct trends (e.g., Fig. 3-1) reflecting heterogeneity in this enriched component, or one trend represented by ZX-62 and Bai-17 was due to ~10% lower crust contamination. The relatively low Ce/Pb and high Ba/Nb abundance ratios in Hannuoba tholeiites (Table 3-3, Fig. 3-7) may also be characteristic of this enriched component.

Although we can define the geochemical characteristics of the enriched component expressed in Hannuoba tholeiites, we cannot determine whether this enriched component was originally in or below the asthenosphere beneath eastern China or if it was part of a remobilized continental lithosphere mantle or lower crust created by continental extension. Our studies (see Chapter 4) of spinel peridotite xenoliths from the continental mantle lithosphere beneath Hannuoba, document extreme compositional and isotopic heterogeneity in this lithosphere. Moreover, one of these peridotites, DM1-7, deviates from the main Sr-Nd isotopic

trend to low $^{143}Nd/^{144}Nd$ along a trajectory defined by some Hannuoba tholeiites (Fig. 3-1). Therefore, it is likely that the isotopic features of Hannuoba tholeiites exist in the ancient subcontinental lithosphere beneath the Sino-Korean craton.

An additional constraint on the petrogenesis of Hannuoba lavas are the linear trends formed by all Hannuoba lavas (i.e., alkalic, transitional and tholeiitic) in plots involving radiogenic isotope ratios and/or incompatible element abundances (e.g., Figs. 3-1, 3-2, 3-3, 3-5 and 3-6). These trends provide evidence for a mixing process. Because compatible element trends do not form linear trends, it is evident that crystal fractionation postdated the mixing process.

Another important petrogenetic constraint is provided by field observations; i.e., the intercalation of tholeiitic and alkali lavas. As shown in Fig. 1-2 alkali lavas occur early in the stratigraphic sequence and tholeiitic lavas dominate in the uppermost levels at three of five stratigraphic sections; however, all stratigraphic sections have intercalated tholeiitic and alkali flows. Although melt-residual matrix segregation processes are likely to be complex, it is unlikely that partial melting of a single source would lead to intercalated lavas formed by very different degrees of melting. Therefore, we reject model B which envisioned alkalic and tholeiitic lavas forming from same source with the slower ascending tholeiitic lavas,

formed by higher degrees of melting, subsequently interacting with continental lithosphere. However, we cannot reject alkalic and tholeiitic basalts derived from different sources, and the tholeiitic magmas were assimilated by subcrustal lithosphere (with or without lower crusts).

Our favored model (Fig 3-10) is that alkali and tholeiitic lavas from Hannuoba formed from different mantle sources. The alkali basalts were generated by small degrees of partial melting of asthenosphere, perhaps a PREMA component, whereas the tholeiites were generated by partial melting of an enriched component (EMI-like) in the oceanic mantle. This enriched component may have resided in the upwelling asthenosphere or subcontinental lithosphere (top of lithosphere or lower crust). Hart (1988) noted that an EMI signature is not seen in continental alkalic basalts. Perhaps this is because the EMI component is stored in continental lithosphere and sampled by tholeiitic basalts whereas oceanic and continental alkali basalts are derived from compositionally similar sources.

We propose that mixing between the PREMA and an EMI-like components created the linear trends of radiogenic isotopic ratios defined by Hannuoba lavas. It is likely that this mixing between mantle components occurred during the rifting event that caused extension in northeast China ~40my ago. (Zhang and Huang, 1982). For example, Perry et al (1987, 1988) proposed that the tholeiitic volcanism on the Rio Grande rift resulted from partial melting of continental

lithosphere that was heated by the ascending asthenosphere. This proposal is consistent with the transition from dominantly alkalic to dominantly tholeiitic volcanism at Hannuoba. Moreover, the proximity of upwelling asthenosphere and heated, former continental lithosphere enable mixing of isotopically diverse components (Fig. 3-10).

3-4.6. Plate Tectonic Interpretations of the Origin of the Hannuoba Basalts

As defined by Huang (1978), eastern China belongs to the Marginal Pacific Tectonic Domain. Its tectono-magmatic evolution was a result of the interactions among the Eurasian, Pacific and Indian plates. Uyeda and Miyashiro (1974) proposed that the mid-oceanic Kula-Pacific Ridge began to subduct about 150 m.y. ago, and in the late Cretaceous (80-90 m.y. ago) probably collided with the East Asian continent (Japan) and descended beneath it. During that time, the Pacific coast of the Eurasian continent was subjected to an intense orogenic activity, and the igneous activity occurred in an unusually wide zone, about 2000-3000 km, as continental rifting began. After subduction of the Kula-Pacific Ridge the area on the continental side of the subduction zone was probably subjected to great tension, and the Sea of Japan began to open by initiation of ocean-floor spreading. The main episode of the spreading occured between 20 and 60 m.y. Similar extension took place in the Bohai

Sea, China, but there it never developed into a full scale ocean-floor spreading activity (Li and Cong, 1980).

Somewhat later, between 40 to 60 m.y. (Molnar and Tapponier, 1977), the Indian continent began to collide with the Eurasian plate on the south. The collision, presently still in progress, undoubtedly caused the development of large tectonic disturbances by large lateral movements along existing or newly formed geofractures (lithospheric fracture zones) in northeastern China. These deep fractures, as well as the rifting associated with the formation of the Bohai Sea, provide numerous ascent routes for basaltic magmas to reach the surface.

In addition, the Pacific, the Philippine and the Indoaustralian plates all have their subduction zones sliding under the Eurasian plate. The resulting complex interaction among all the plates must affect the thermal regime within the mantle, beneath the southeastern part of the Eurasian continent, including northeastern China. Also about 40 m.y. ago, the relative motion of the Pacific plate with respect to the Eurasian plate abruptly changed NNW to WNW (Uyeda and Miyashiro, 1974), further modifying the thermal regime in the mantle beneath China. The late Tertiary and Quaternary basalts in eastern China are scattered, often occurring near major active faults, which were reactivated largely as a result of the collision of the Indian and Eurasian plates (Molnar and Tapponier, 1977). The crustal extension in northeastern China is linked to the

uplift of the mantle material (Li and Cong, 1980; Lui et al., 1983). This extension is still underway as documented by the persistence of seismic activity.

The petrogenetic model we proposed for Hannuoba basalts in section 3-4.6 (Fig 3-10) is consistent with this rifting event in northeastern China.

TABLES

Table 3-1.a Leaching experiment on Sr-Nd isotopic compositions

Sample	$^{87}Sr/^{86}Sr$ unleached	leached residue	leachate
D-1	0.704234±30	0.703791±24	0.704516±26
		0.703831±28	
		0.703796±26*	
D-3	0.704560±26	0.704108±24	-
D-5	0.704891±28	0.704791±30	-
J-1	0.704929±30	0.704733±26	-
		0.704719±25*	
J-14	0.704062±24	0.703929±27	
Z-2	0.703915±30	0.703891±30	0.703964±32

Sample	$^{143}Nd/^{144}Nd$ unleached	leached residue	leachate
D-1	0.512913±21	0.512955±18	0.512909±19
		-	
		0.512941±21*	
Z-2	-	0.512951±29	0.512948±20

- All samples were leached in 100°C 2.5N HCl overnight, except * indicates that the samples were leached in cool 2.5N HCl overnight, then in 100°C 6.2N HCl for one hour.

Table 3-1.b Leaching experiment on Pb isotopic compositions

		$^{206}Pb/^{204}Pb$	$^{207}Pb/^{204}Pb$	$^{208}Pb/^{204}Pb$
R-6	U	17.811	15.476	37.829
	L	17.807	15.488	37.846
D-1	U	17.834	15.477	37.883
	L	17.848	15.485	37.936
D-3	U	17.745	15.469	37.533
	L	17.706	15.450	37.671
D-5	U	17.563	15.456	37.619
	L	17.565	15.458	37.626
Zh-9	U	17.511	15.444	37.835
	L	17.535	15.434	37.931

U - unleached.
L - samples were leached in 100°C 2.5N HCl overnight.
All ratios have been corrected for NBS standards.
Based on repeated runs of NBS-981 common Pb standards, the reproducibility is better than 0.05% per AMU, and the Pb isotopic ratios were corrected relative to the average standard Pb isotopic compositions of Todt (1983) and Hamelin (1985). The in-run 2ĺ errors are less than 0.012%.

Table 3-1.c Leaching experiment on Sr-Rb concentrations

Sample (ppm)	unleached Sr	unleached Rb	leached residue Sr	leached residue Rb	leachate Sr	leachate Rb
D-1	1124.9	62.2	1066.9	23.5	565.4	54.9
D-3	843.5	17.3	522.1	-		
D-5	529.8	15.6	419.8	14.7		
J-1	467.6	10.2	466.6	10.6		
Z-2	1208.1	45.9	443.8	15.5		

Rb, Sr concentrations were determined by isotope dilution.
Weigth of leachate = weight of basalt before leaching
- weight of basalt after leaching.

Table 3-2. Sr and Nd Isotope Compositions of Hannuoba Basalts

	$^{87}Sr/^{86}Sr$	$^{143}Nd/^{144}Nd$
Alkali Basalts		
PRIMITIVE GROUP		
Zx-44	0.703928±29	0.512872±22
R-6	0.703973±27	0.512902±18
Zh-3	0.703987±25	0.512928±20
EVOLVED GROUP		
ZX-36	0.703965±30	0.512921±18
R-9	0.703886±30	0.512952±13
Bai-1	0.703863±27	0.512910±19
Bai-3	0.703781±25	--
Bai-9	0.703970±30	0.512912±19
D-1	0.703791±24	0.512955±18
ZB-53	0.703948±28	0.512937±17
ZB-83	0.703803±28	0.512974±20
Zh-6	0.703853±28	0.512966±20
Zh-14	0.703794±29	0.512957±19
Z-2	0.703891±27	0.512951±30
	--	0.512977±31
J-14	0.703929±27	0.512929±24
	--	0.512905±12
Garnet megacryst in basanite J-14		
Gt-1	0.703651±20	0.512992±16

(continue)

	$^{87}Sr/^{86}Sr$	$^{143}Nd/^{144}Nd$
Transitional Basalts		
R-19	0.704094±31	0.512948±19
Bai-10	0.704054±30	0.512869±18
Bai-22	0.703997±26	0.512891±19
D-3	0.704108±24	0.512924±17
ZB-77	0.704289±28	0.512857±20
Tholeiites		
ZX-48	0.704753±27	0.512680±17
ZX-62	0.704183±27	0.512692±35
Bai-6-2	0.704757±32	0.512785±17
Bai-17	0.704299±33	0.512684±19
D-5	0.704791±30	0.512806±17
Zh-4	0.704792±24	0.512769±20
Zh-9	0.704666±27	0.512772±17
Zh-17	0.704679±31	--
Zh-18	0.704617±23	0.512803±19
Zh-21	0.704385±26	0.512830±20
	0.704426±25	0.512825±22
Zh-22	0.704403±25	0.512832±23
J-1	0.704733±26	0.512798±19
	0.704619±25	--

The chemical and mass spectrometric techniques used to determine the isotopic composition of Sr and Nd were described by Hart and Brooks (1977), Zindler et al (1979).

The $^{87}Sr/^{86}Sr$ values are corrected relative to 0.70800 for E & A standard and are normalized to $^{86}Sr/^{88}Sr=0.11940$.

The $^{143}Nd/^{144}Nd$ values are corrected relative to $^{143}Nd/^{144}Nd=0.512640$ for BCR-1 and are normalized to $^{146}Nd/^{144}Nd=0.721900$.

Table 3-3. Pb Isotope Ratios for Hannuoba Basalts

	$^{206}Pb/^{204}Pb$	$^{207}Pb/^{204}Pb$	$^{208}Pb/^{204}Pb$	△7/4	△8/4	Pb (ppm)	Ce/Pb
Alkali Basalts							
PRIMITIVE GROUP							
R-6	17.811	15.476	37.829	5.4	65.3	3.23	26.1
EVOLVED GROUP							
ZX-36	17.916	15.496	37.939	6.3	65.2		
R-9	17.910	15.503	38.014	7.1	71.9	4.28	28.5
Bai-1	17.805	15.469	37.868	4.8	71.5		
	17.808	15.472	37.878				
Bai-9	17.783	15.478	37.824	5.9	69.7		
Bai-3	17.806	15.461	37.838	4.0	68.4		
D-1	17.834	15.477	37.883	5.3	69.5	4.14	22.9
ZB-53	17.860	15.502	37.874	7.5	65.4		
ZB-83	17.936	15.505	37.936	7.0	62.4		
Zh-6	17.917	15.511	37.989	7.8	70.0		
	17.934	15.517	38.024				
Zh-14	17.920	15.486	37.889	5.3	59.6		
Z-2	17.923	15.516	38.047	8.2	73.5	4.78	24.8
J-14	17.864	15.494	37.985	6.6	75.1	5.19	19.6
Transitional Basalts							
R-19	17.820	15.506	37.963	8.3	79.7	3.28	24.4
Bai-10	17.612	15.455	37.726	7.2	80.6		
Bai-22	17.726	15.473	37.802	6.1	74.4		
	17.723	15.470	37.792				
D-3	17.745	15.469	37.533	4.0	63.4		
ZB-77	17.643	15.458	37.651	5.3	69.5		
	17.642	15.457	37.718				

(continued)

	$^{206}Pb/^{204}Pb$	$^{207}Pb/^{204}Pb$	$^{208}Pb/^{204}Pb$	△7/4	△8/4	Pb (ppm)	Ce/Pb
Tholeiites							
ZX-48	17.100	15.395	37.371	5.0	107.0		
ZX-62	17.107	15.360	37.195	1.5	88.6		
Bai-6-2	17.431	15.415	37.440	3.5	73.9	2.29	18.9
	17.437	15.422	37.475				
Bai-17	17.153	15.366	37.201	1.6	83.6	1.87	16.1
	17.160	15.376	37.231				
D-5	17.563	15.456	37.619	6.1	75.9	2.49	16.6
Zh-4	17.494	15.446	37.812	5.9	103.7		
Zh-9	17.511	15.444	37.835	5.5	103.7	2.39	15.6
Zh-17	17.507	15.468	37.933	7.9	114.0		
Zh-21	17.389	15.426	37.778	5.5	112.2		
Zh-22	17.484	15.449	37.794	4.3	104.7		
J-1	17.543	15.443	37.650	5.0	89.1		

1. The chemical and mass spectrometer techniques used to determine the isotopic composition and concentration of Pb were described by Cameron et al(1969), Manhes et al (1978) and Pegram (1986).

2.Based on repeated runs of NBS-981 common Pb standards, the reproducibility is better than 0.05% per AMU, and the Pb isotopic ratios were corrected relative to the average standard Pb isotopic compositions of Todt et al (1983) and Hamelin et al (1985). The in-run statistics are better than 0.012% AMU^{-1}.

FIGURES

FIGURE CAPTIONS

Figure 3-1 Sr-Nd isotope correlation plot for Hannuoba basalts: circle = alkali basalts, asterisks = tholeiitic basalts and triangle = transitional basalts. A field is drawn for oceanic basalts based on data from Zindler et al (1982), Hart (1984) and Hart et al (1986). The mantle components DMM, PREMA, EMI and EMII (Zindler and Hart, 1986) are indicated. The LoNd array line of Hart et al (1986) is shown. DM1-7 is clinopyroxene from a spinel-lherzolite which is the most isotopically enriched (highest $^{87}Sr/^{86}Sr$, lowest $^{143}Nd/^{144}Nd$) lherzolite among the six Hannuoba spinel-lherzolites, and solid triangle is a megacryst garnet Gt-2 from basanite J-14 (Table 3-2). D-5 is an unusual oceanic basalt from the western Indian Ocean (Hamelin and Allegre, 1985). Field with diagonal lines encloses high Ti-P (HPT) basalt group from Parana of south Brazil (Hawkesworth et al., 1986). The same symbols are used in the following figures.

Figure 3-2 $^{143}Nd/^{144}Nd$ versus Sm/Nd for Hannuoba basalts. The field for EM end-member is based on the Lowest $^{143}Nd/^{144}Nd$ and Sm/Nd ratios in lavas from the Walvis Ridge basalts (Richardson et al., 1982) and Parana HPT group basalts (Hawkesworth et al., 1986).

Figure 3-3 Pb isotope correlation plots for Hannuoba basalts. Basalts of Shandong, eastern China are from Peng et al (1986). Lamproite field encloses six lamproites from Smoky Butte, Montana (Fraser et al, 1986). North Hemisphere reference line (NHRL) and two Dupal anomaly Pb reference lines (delta 7/4 Pb = 15, delta 8/4 Pb = 150) are from Hart (1984, 1988). Field for oceanic basalts is drawn based on Hart (1988). EMI field is defined by Walvis Ridge lavas. Field with diagonal lines encloses high Ti-P (HPT) basalt group from Parana of south Brazil (Hawkesworth et al., 1986). Other symbols as in Fig. 3-1.

Figure 3-4 Mg number (Mg/(Mg+Fe)) versus Nd and Sr isotopes for Hannuoba basalts. The lines indicate the general correlations between Mg numbers and isotopic compositions. Basanite D-1 is special, its Mg # has been modified by the accumulated olivine xenocrysts.

Figure 3-5 a) Nd-Pb and b) Sr-Pb isotope correlation plots for Hannuoba basalts. Enclosed fields are from Zindler and Hart (1986). Other symbols as in Fig. 3-1.

Figure 3-6 $^{143}Nd/^{144}Nd$ versus 1/Nd and $^{87}Sr/^{86}Sr$ versus 1/Sr variations for Hannuoba basalts.

Figure 3-7 Ba/Nb versus a) delta 8/4 and b) delta 7/4 for Hannuoba basalts. Figures and oceanic data are adopted from figure 12 of Roex et al (1988). Solid circle represents the average composition of an oceanic basalt province: K = Kerguelen, W = Walvis Ridge, T = Tristan da Cunha, G = Gough, D = Discovery, As = Ascension, B = Bouvet, M = Marion, S = Shona, SW = Central Southwest Indian Ridge (D-5). Hannuoba basalts indicated by asterisk (tholeiitic), triangle (transitional) and open circle (alkalic).

Figure 3-8 $^{143}Nd/^{144}Nd$ versus Sm/Nd and $^{87}Sr/^{86}Sr$. Enclosed fields are for Hannuoba basalts. Ak represents alkali basalts, TH represents tholeiitic basalts. Diamond = Archean granulites (filled symbol represents ultramafic compositions) from Qianxi area, ~250 km east of Hannuoba region (Jahn and Zhang, 1984). Triangle = world-wide granulites (Othman et al, 1984). Solid star represents average upper crustal composition, and open circle represents average lower crust composition: Sm/Nd ratios from Taylor and McLennan (1985), $^{143}Nd/^{144}Nd$ values from Zartman and Haines (1988). Open star represent crust (upper and lower crust) composition of Allegre et al (1983).

Figure 3-9 SiO_2 versus Sm/Nd for Hannuoba basalts. Fields for Qianxi granulites are based on Jahn and Zhang (1984). Field A represents acid, field I - intermediate, field B - mafic, and field UB - ultramafic granulites respectively. Solid star = average upper crustal composition, open star = average lower crust composition (Taylor and McLenna, 1985).

Figure 3-10 Sketched diagram for model A and model B. In basaltic lava flows, the black layers represent alkalic basalts (AK), the blank layers represent transitional basalts (TR) and tholeiitic basalts (TH).

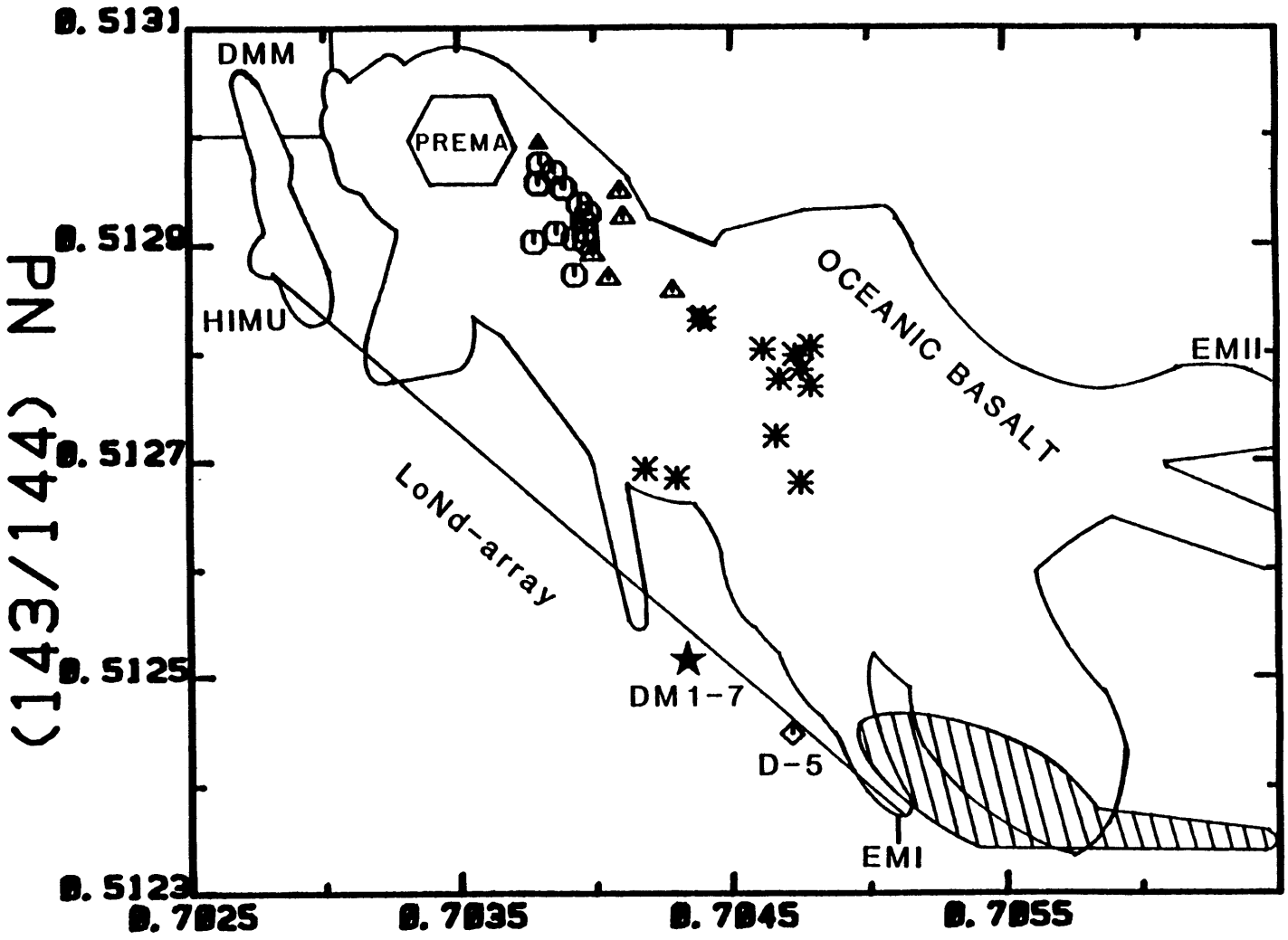
0.5131
0.5129
0.5127
0.5125
0.5123
(143/144) Nd
0.7025
0.7035
0.7045
0.7055
(87/86) Sr
DMM
PREMA
HIMU
OCEANIC BASALT
EMII
EMI
LoNd-array
DM1-7
D-5

FIGURE 3-1

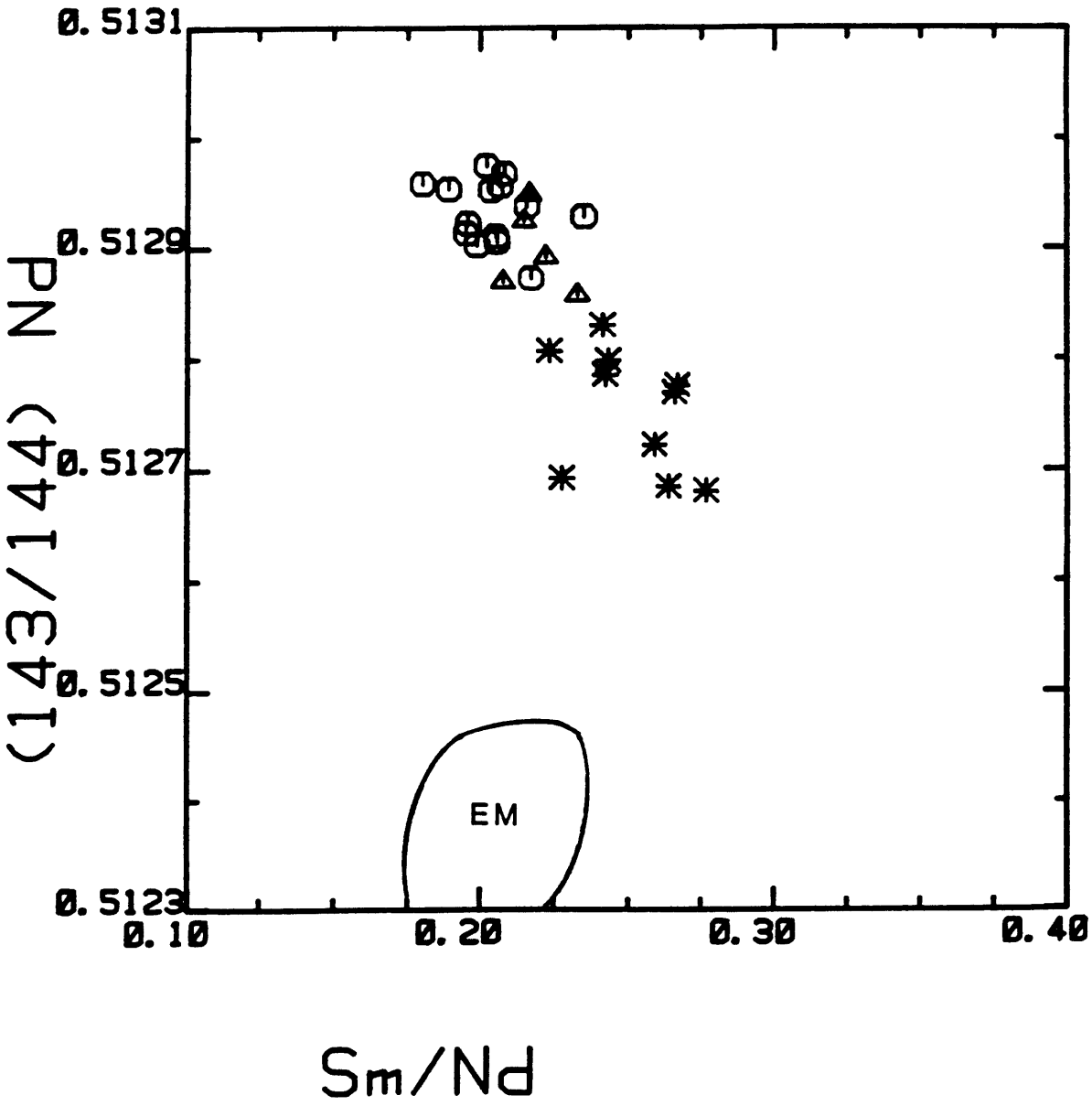
0.5131
0.5129
0.5127
0.5125
0.5123
(143/144) Nd
EM
0.10
0.20
0.30
0.40
Sm/Nd

FIGURE 3-2

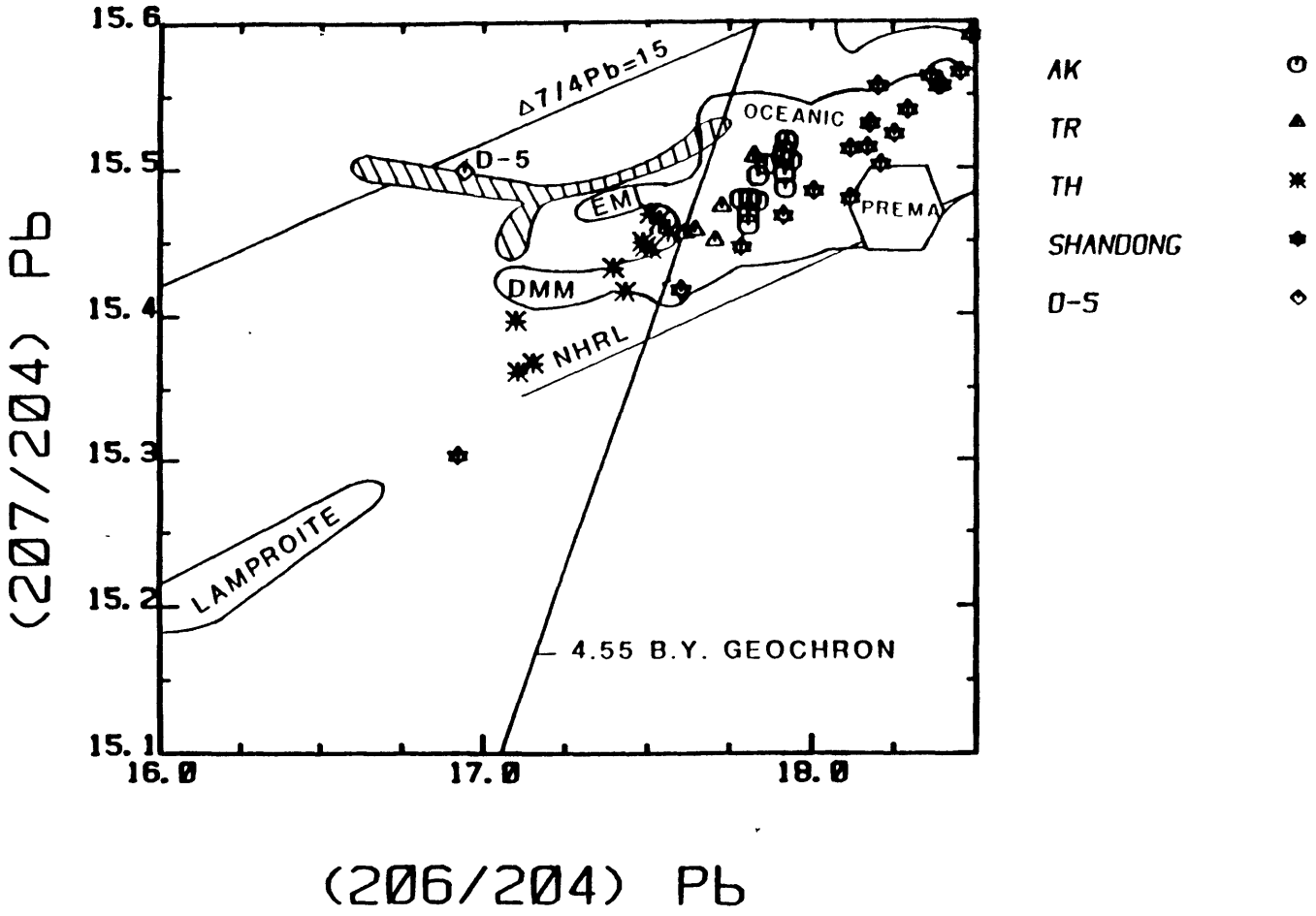
15.6
15.5
15.4
15.3
15.2
15.1
16.0
17.0
18.0
(207/204) Pb
(206/204) Pb
Δ7/4Pb=15
OCEANIC
D-5
EM
PREMA
DMM
NHRL
LAMPROITE
4.55 B.Y. GEOCHRON
AK
TR
TH
SHANDONG
D-5

FIGURE 3-3

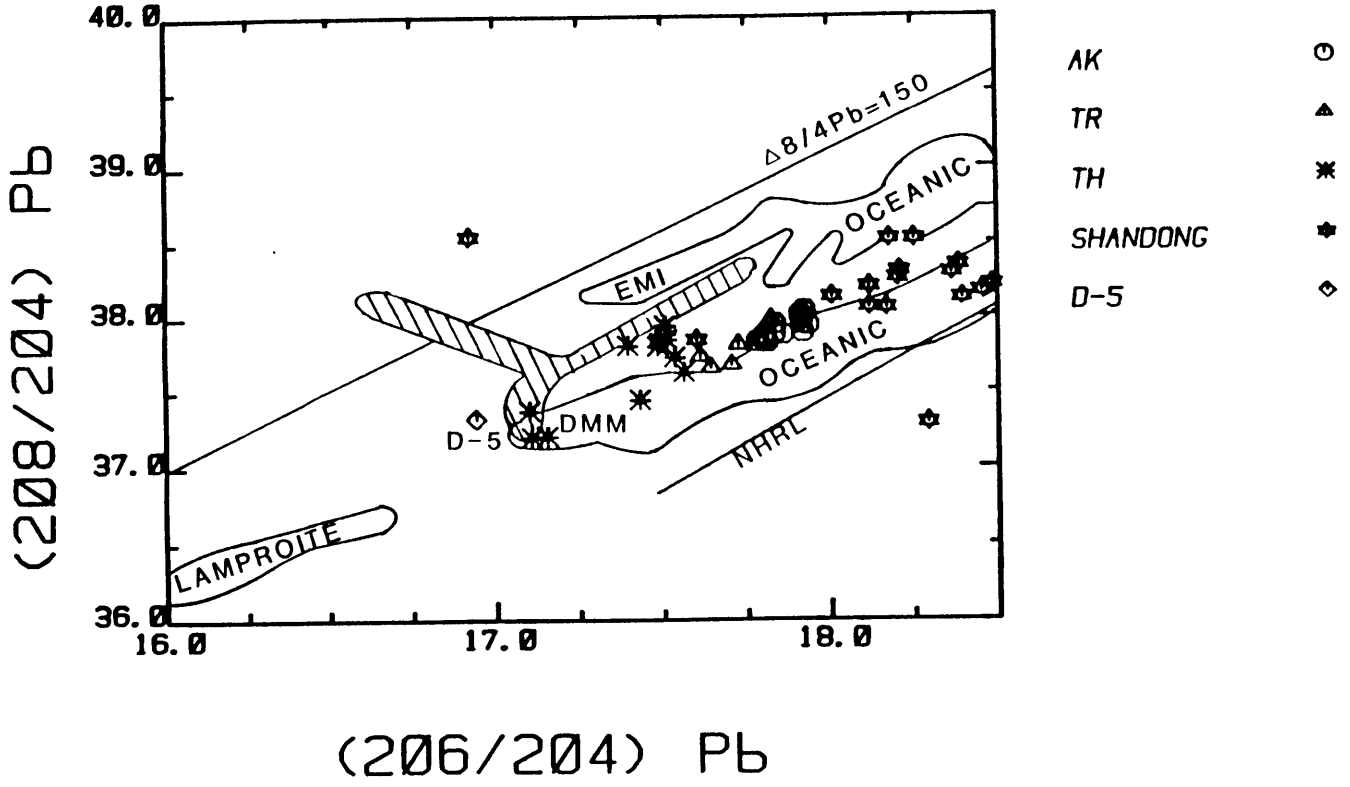
40.0
39.0
38.0
37.0
36.0
16.0
17.0
18.0
(208/204) Pb
(206/204) Pb
Δ8/4Pb=150
OCEANIC
EMI
OCEANIC
NHRL
DMM
D-5
LAMPROITE
AK
TR
TH
SHANDONG
D-5

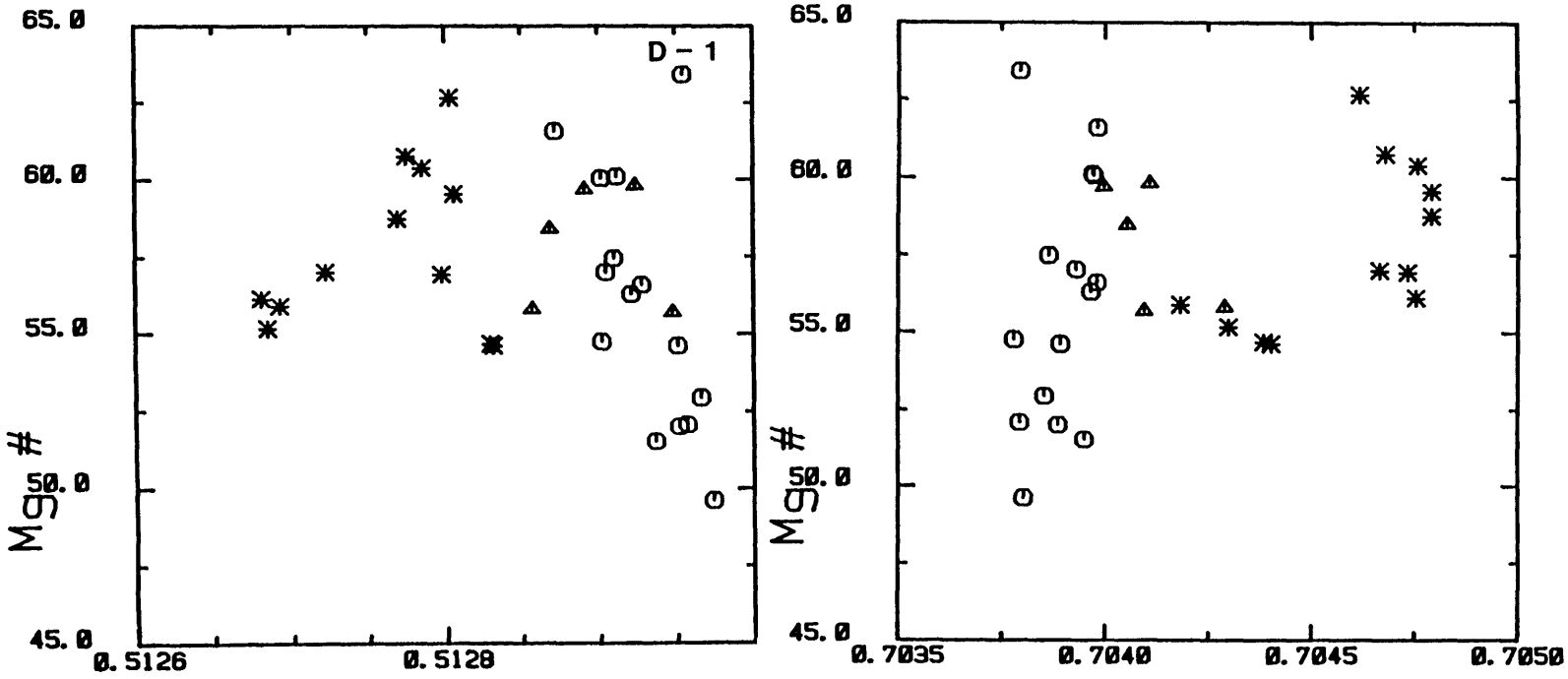
65.0
60.0
55.0
50.0
45.0
Mg#
D-1
0.5126
0.5128
(143/144)Nd
65.0
60.0
55.0
50.0
45.0
Mg#
0.7035
0.7040
0.7045
0.7050
(87/86)Sr

FIGURE 3-4

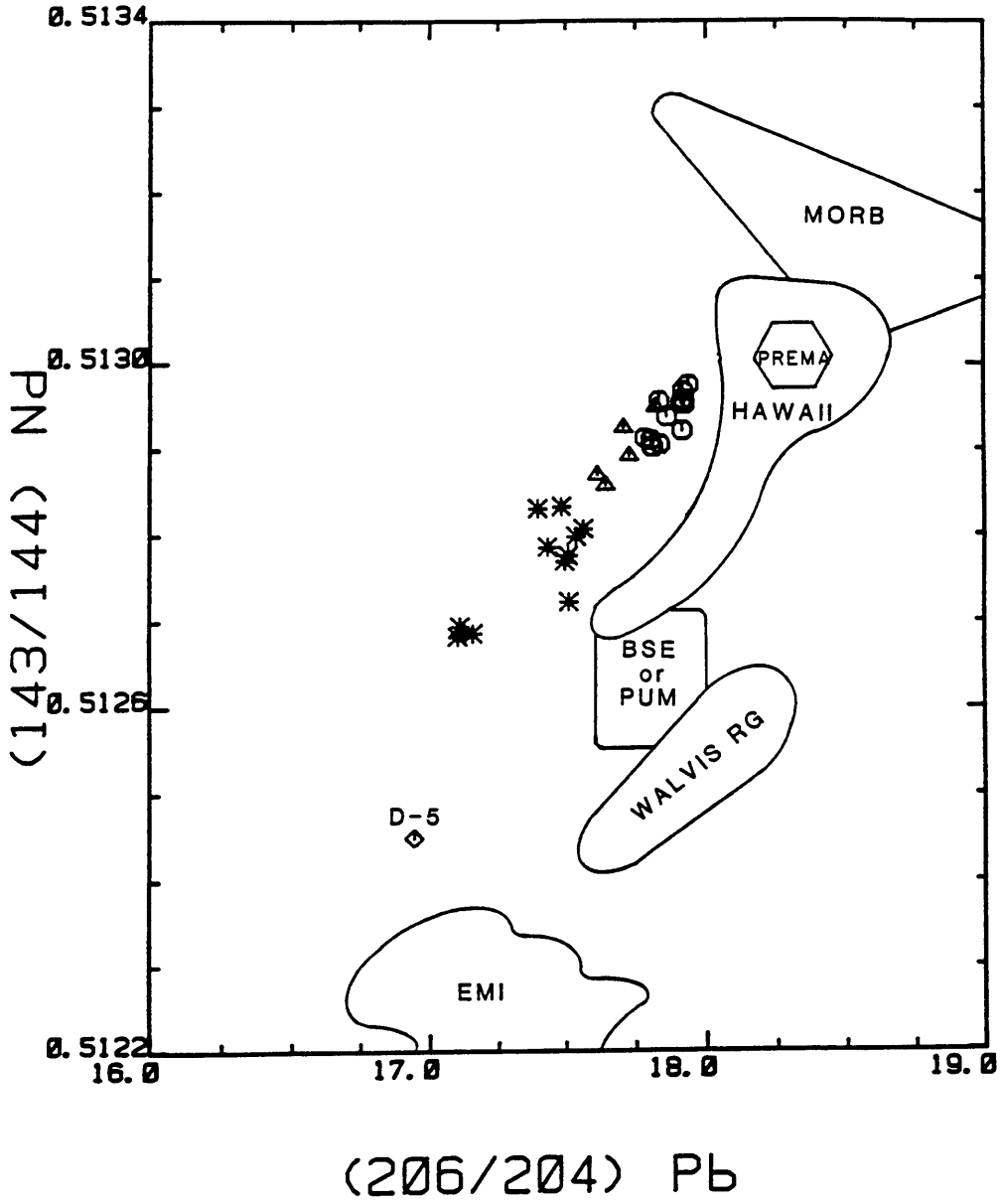
0.5134
0.5130
0.5126
0.5122
(143/144) Nd
16.0
17.0
18.0
19.0
(206/204) Pb
MORB
PREMA
HAWAII
BSE
or
PUM
WALVIS RG
D-5
EMI

FIGURE 3-5

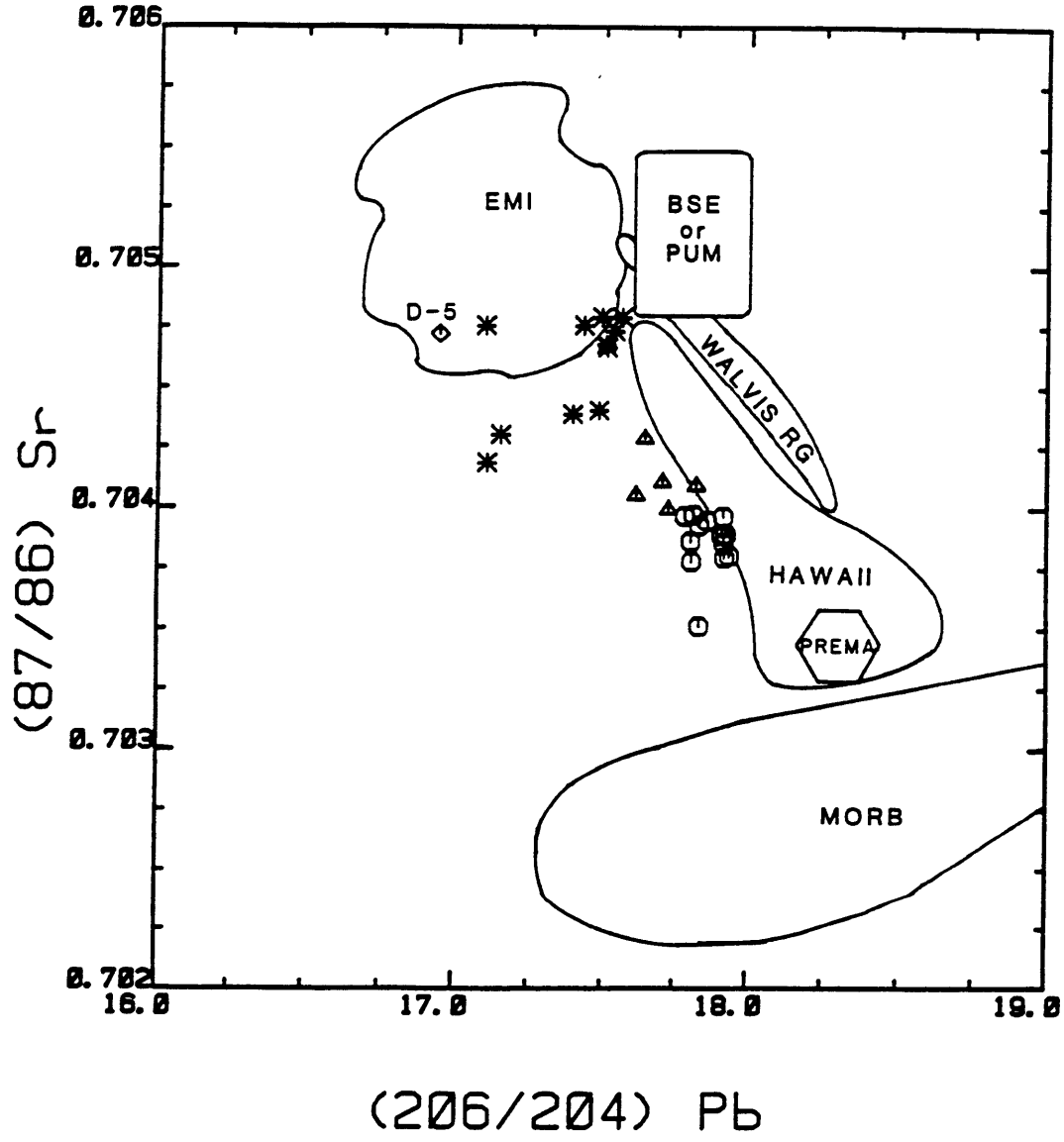
0.706
0.705
0.704
0.703
0.702
(87/86) Sr
16.0
17.0
18.0
19.0
(206/204) Pb
EMI
BSE
or
PUM
D-5
WALVIS RG
HAWAII
PREMA
MORB

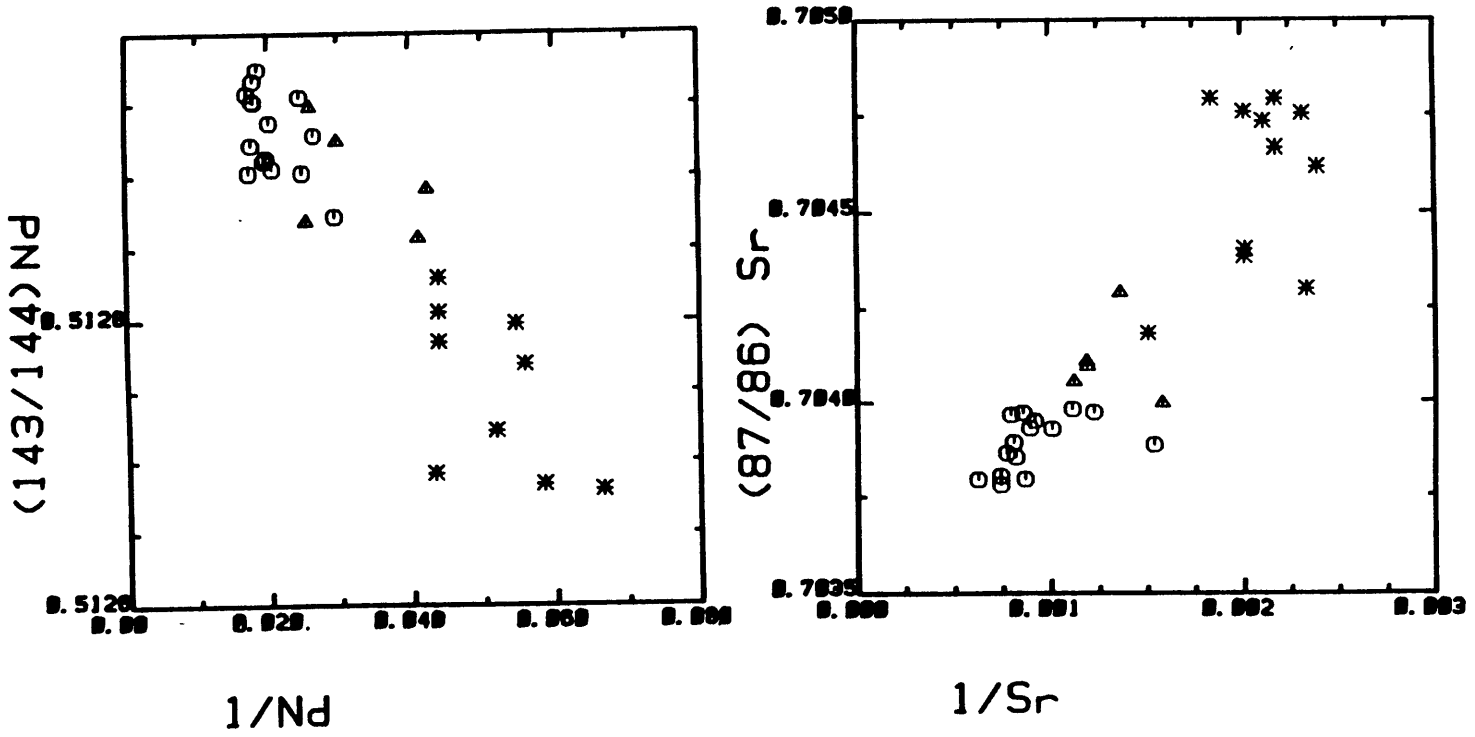
(143/144)Nd
0.5128
0.5126
0.020
0.040
0.060
1/Nd
(87/86) Sr
0.7045
0.7035
0.001
0.002
0.003
1/Sr

FIGURE 3-6

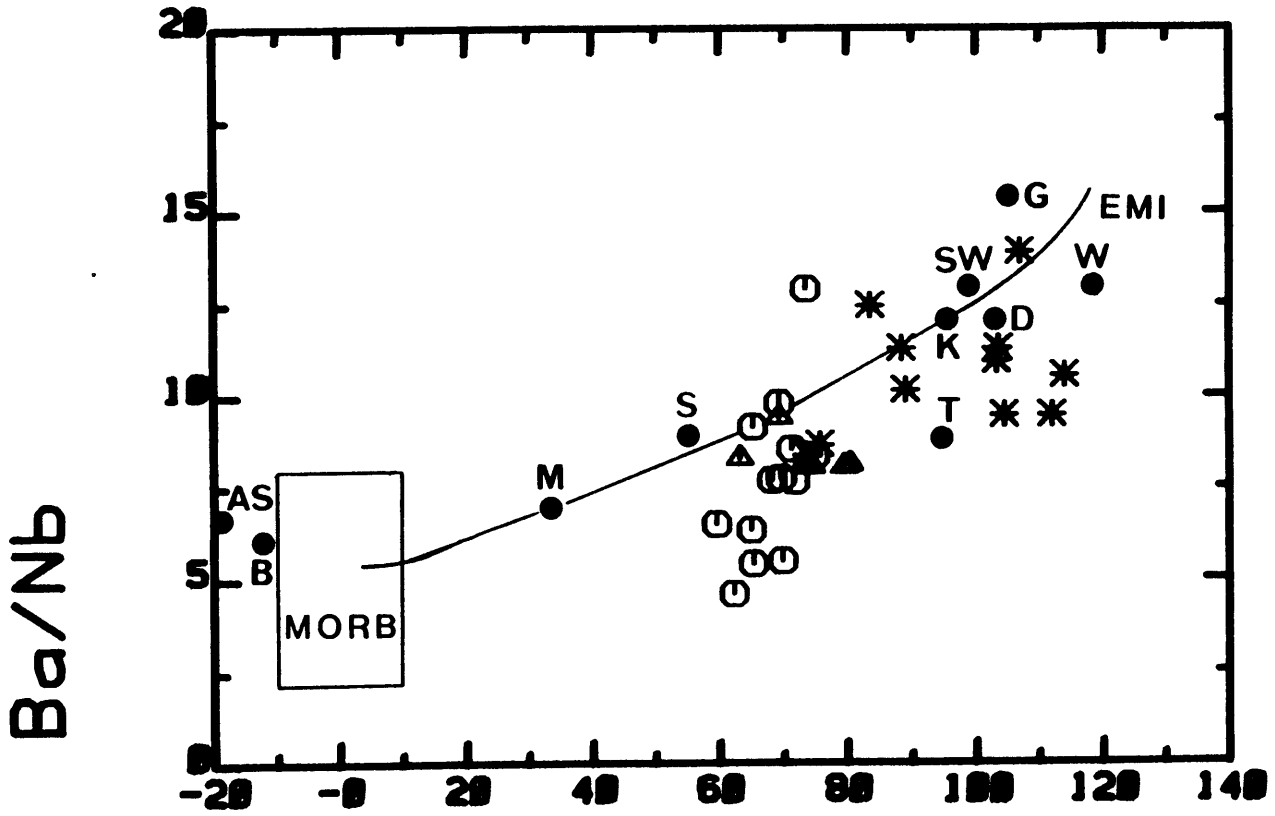

FIGURE 3-7a

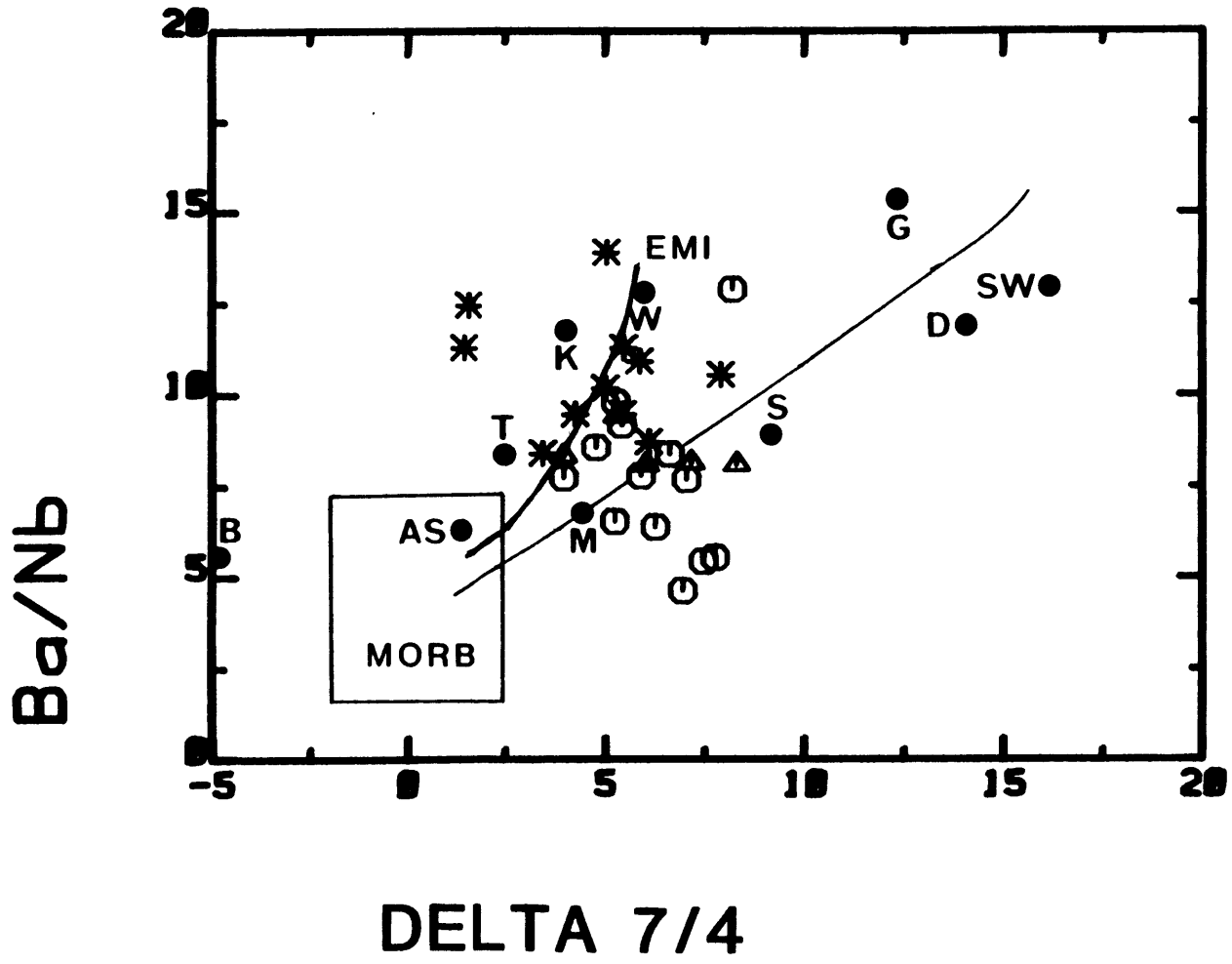

FIGURE 3-7b

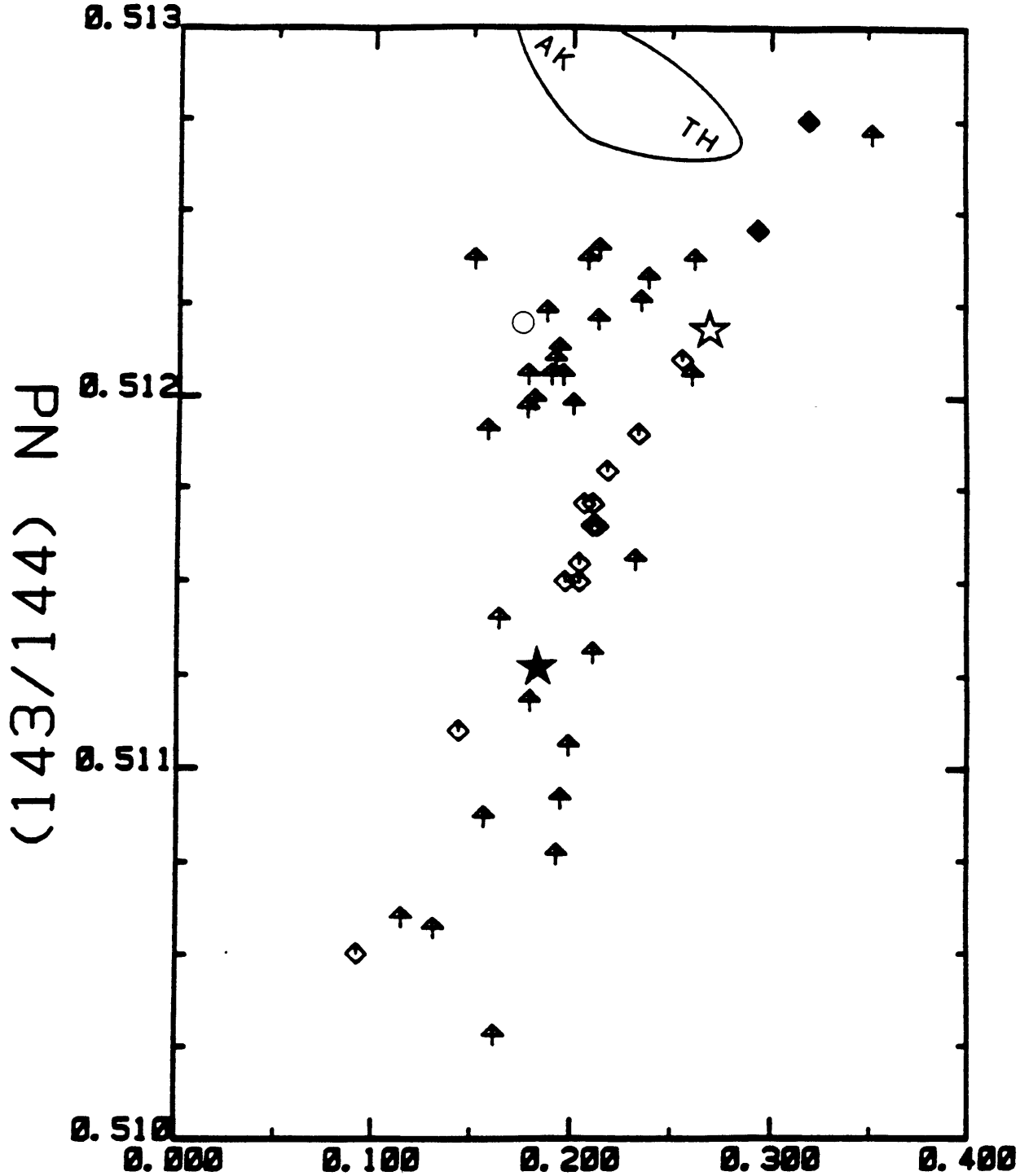
0.513
0.512
0.511
0.510
(143/144) Nd
AK
TH
0.000
0.100
0.200
0.300
0.400
Sm/Nd

FIGURE 3-8a

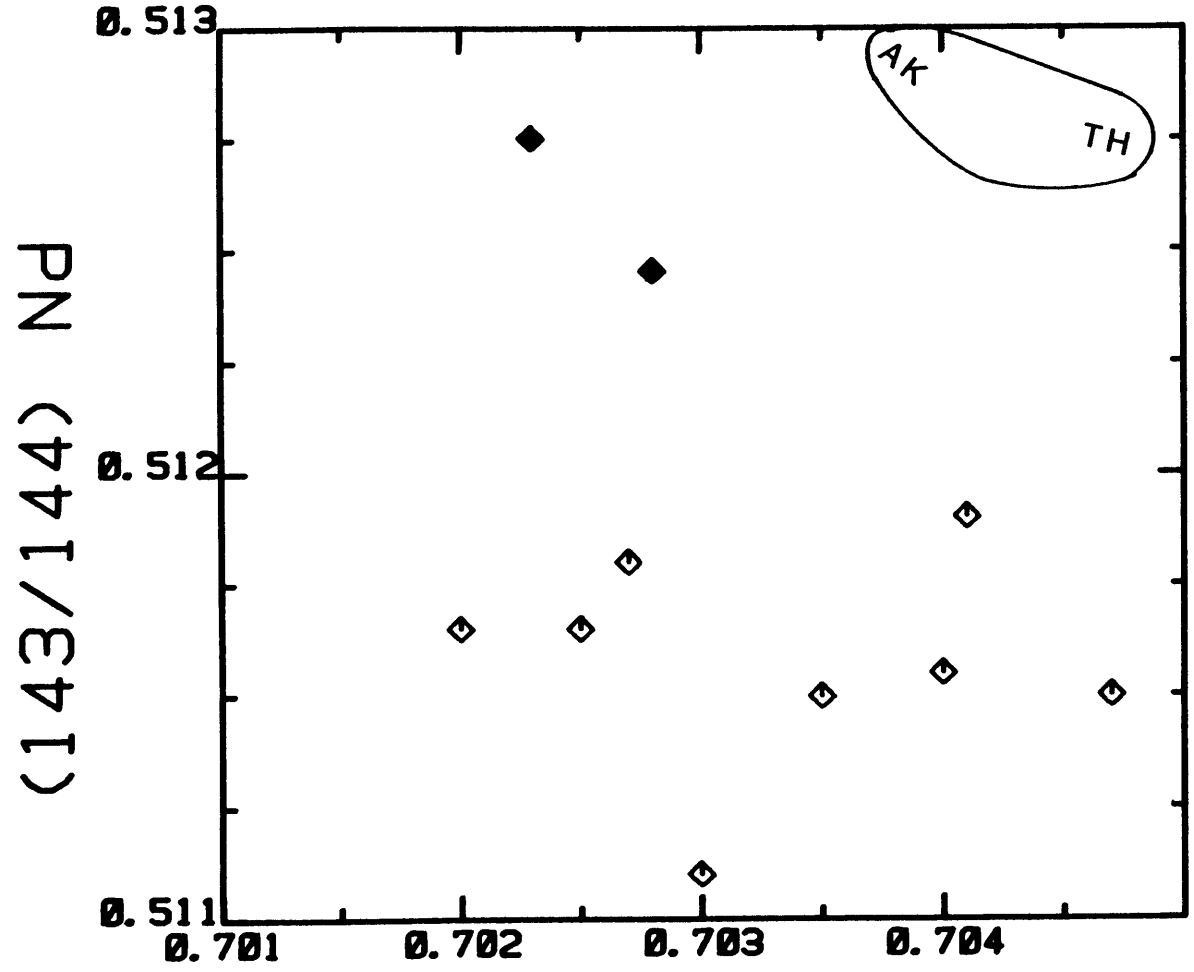
0.513
0.512
0.511
0.701
0.702
0.703
0.704
(143/144) Nd
(87/86) Sr
AK
TH
QIANXI-GRN

FIGURE 3-8b

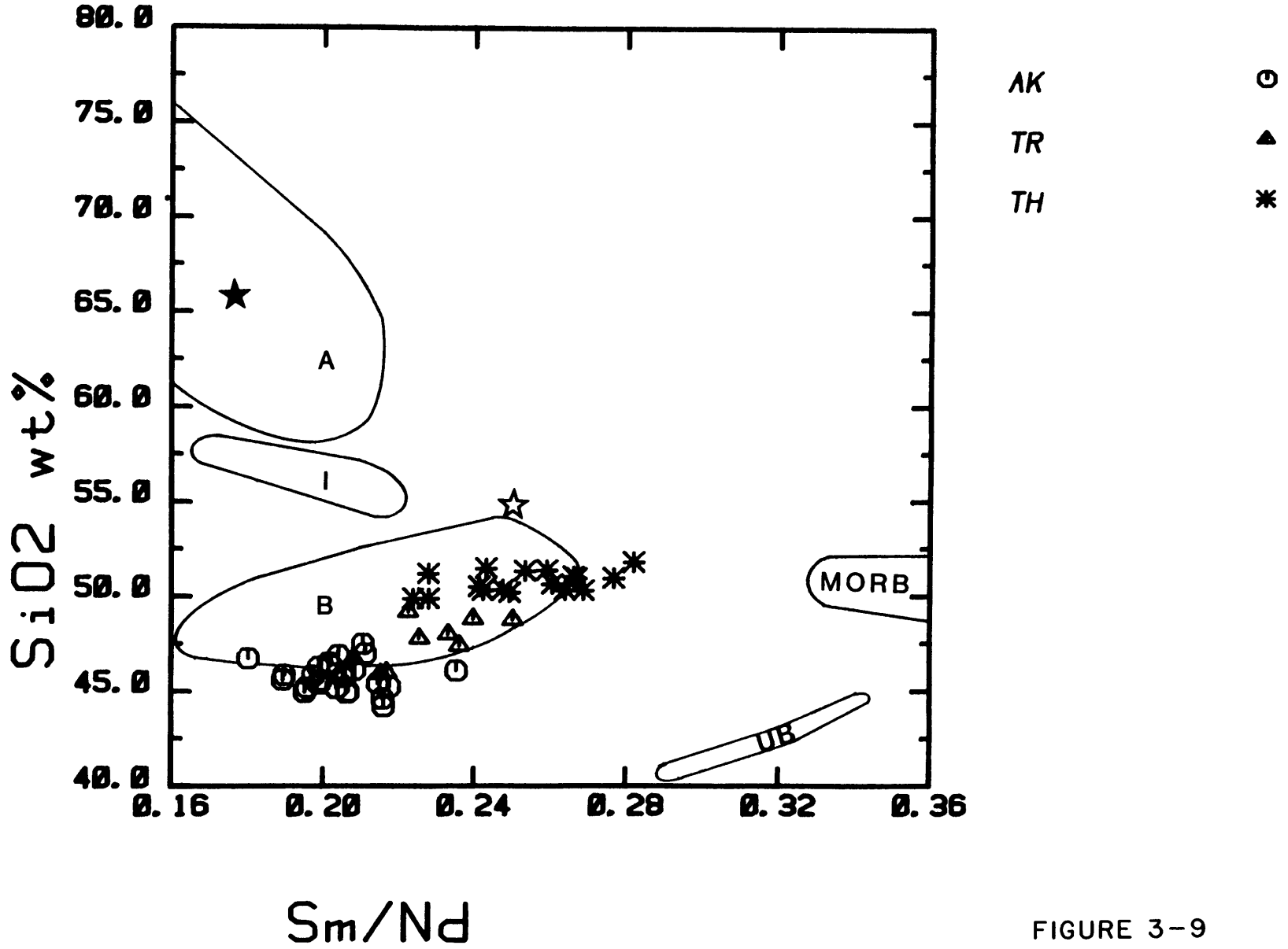
80.0
75.0
70.0
65.0
60.0
55.0
50.0
45.0
40.0
SiO2 wt%
0.16
0.20
0.24
0.28
0.32
0.36
Sm/Nd
A
I
B
MORB
UB
AK
TR
TH

FIGURE 3-9

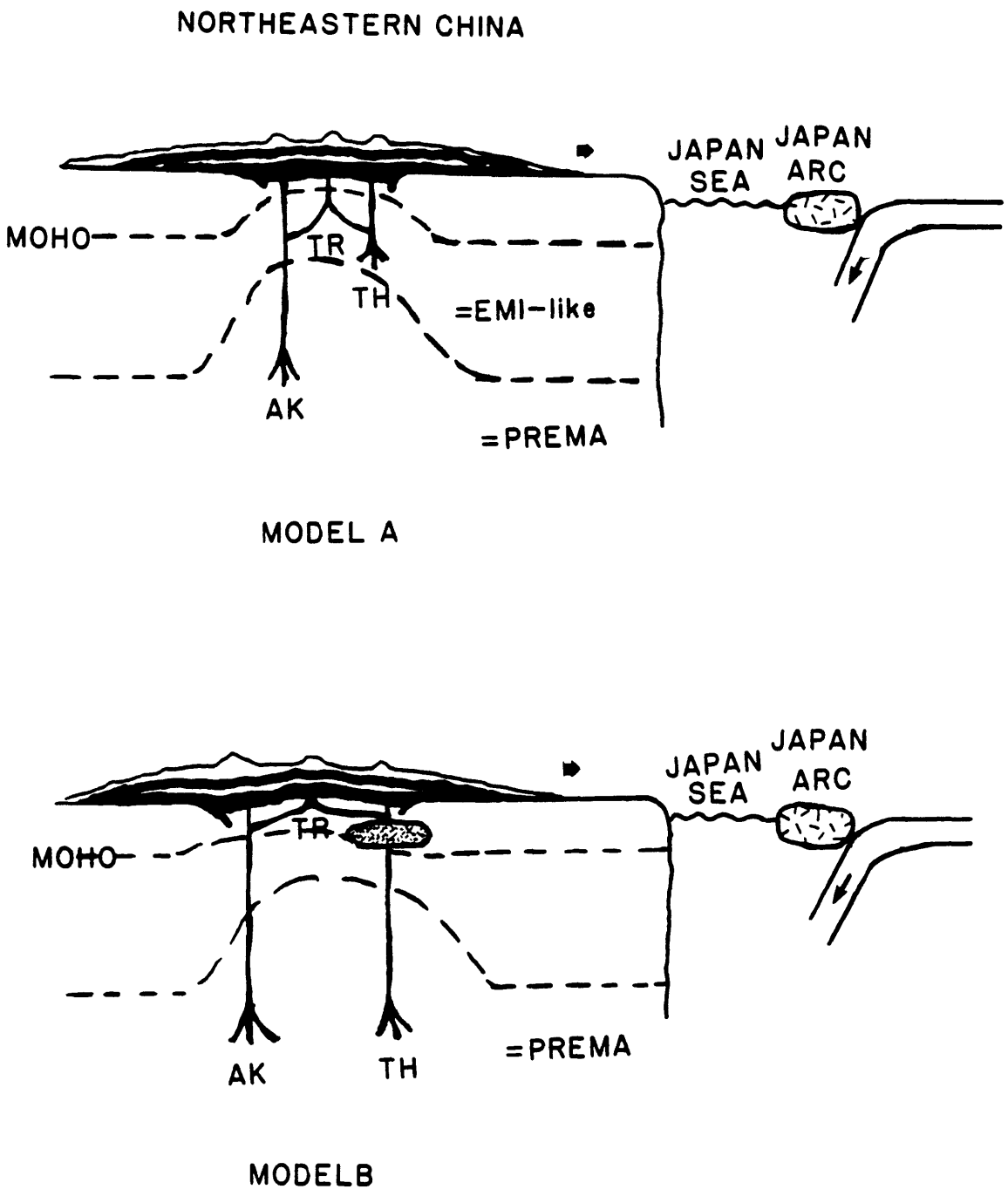
NORTHEASTERN CHINA
JAPAN SEA
JAPAN ARC
MOHO
IR
TH
=EMI-like
AK
=PREMA
MODEL A
JAPAN SEA
JAPAN ARC
MOHO
TR
AK
TH
=PREMA
MODELB

FIGURE 3-10

CHAPTER 4: GEOCHEMISTRY OF PERIDOTITES IN BASALT FROM HANNUOBA: IMPLICATIONS FOR SUBCONTINENTAL MANTLE HETEROGENEITY

4-1. INTRODUCTION

In order to characterize and understand mantle evolution beneath northeast China, we studied Cenozoic alkalic basalts from Hannuoba (Chapters 1, 2 and 3) and their abundant mantle inclusions. Petrographic and mineralogic data on Hannuoba ultramafic inclusions are available (Feng, 1980; Feng et al., 1982; Feng and Han, 1982; Zhai, 1983, 1984), but geochemical studies have focussed on major elements (Zheng, 1980; Liu et al., 1981) with only limited emphasis on radiogenic isotopes (Zhou and O'Nions, 1986), and trace elements (Cong and Zhang, 1982, 1983; Cong et al., 1983). In this chapter we report major and trace element abundances and isotopic ratios (Sr and Nd) for six anhydrous spinel peridotite xenoliths. We find that the upper sub-continental mantle beneath northeast China is compositionally and isotopically heterogeneous: the six xenoliths show larger isotopic variation range than the Hannuoba basalts. This diversity is similar to that beneath other continents; e.g., southwest USA (Menzies et al., 1985; Roden et al., 1988), southeast Australia (McDonough and McCulloch, 1987; Griffin et al., 1988; O'Reilly and Griffin, 1988; Chen et al., 1988), Europe (Stosch and Lugmair, 1986; Downes and Dupuy, 1987), and Ethiopia (Ottonello, 1980). These heterogeneties reflect multiple events accompanied by depletion and enrichment of incompatible elements. Characterizing and understanding these events is the major objective of this chapter.

4-2. GEOLOGICAL SETTING

Cenozoic continental basalts are widely distributed in eastern China. Hannuoba basalts in northwest Hebei province (Fig. I-4) form a basaltic plateau which is part of the Inner Mongolian plateau (Feng and Han, 1982). These basalts are widespread (1700 km^2), and consist of interlayered alkali basalt and subalkali basalt. The southern margin of the Hannuoba plateau is very steep with a thickness of about 100 to 300 m (Barbour, 1929; Feng et al., 1982). Along this margin there are about forty xenolith-rich zones which may have been the result of gravitational accumulation in ancient geographic depressions (Feng, 1980).

A xenolith-rich zone at Damaping (90m x 56m x 20m) is particularly noteworthy for its abundant xenoliths (approximately 85% of the outcrop), their large size (the largest is 800mm x 600mm x 450mm; the diameters of most xenoliths are about 100 to 500mm), and for the coarse grain size resulting in a gem-quality peridot deposit (Koivula and Fryer, 1986). The large gem-peridot fragments are 2 cm in diameter and up to 25 ct in weight; more than one million grains of gem-peridotitic were mined from Damaping during 1980-1981 (Feng, 1980; Feng et al., 1982; Keller and Wang, 1980; Koivula and Fryer, 1986). Most (>95%) xenoliths at this locality are Group I peridotites (Feng, 1980). All

xenolixths studied in this Chapter were collected at Damaping by the author in the summer of 1984.

4-3. PETROGRAPHY

Ultramafic xenoliths in basalts were classified as Group I and Group II by Frey and Prinz (1978). For a recent summary of terminology see Wilshire (1987). Group I Hannuoba xenoliths are mainly spinel-lherzolites, but clinopyroxene-rich zones interlayered with olivine-rich zones occur in some inclusions. Group II inclusions are much less common at Hannuoba, and are mainly Fe-Al-Ti-rich websterites. Both groups occur in the basanites, but only Group II inclusions occur in the alkali olivine basalts. (Cong and Zhang, 1982).

The interior portions (central 200mm) of six large (>300mm) Group I peridotites were selected for geochemical analyses. Three of these, DM1-3, DM1-5 and DM1-7, have 10 to 20 mm Cr diopside-rich veins in the olivine-rich host lherzolite. These xenoliths consist of olivine (ol), orthopyroxene (opx), clinopyroxene (cpx), and spinel (sp). Because of the mineral size and inhomogeneous mineral distribution, modes of the peridotites (Table 4-1) are not based on the mineral point counting on thin sections, but were calculated from bulk rock (Table 4-2), and mineral compositions (Table 4-3). The samples have variable amounts of serpentinization along grain boundaries and partings of olivine. DM1-4 has almost no serpentine, DM1-9 less than 2%,

DM1-2 and DM1-3 about 2-3%, and DM1-5 about 5%. Harzbugite DM1-7 is the most strongly serpentinized sample (<15%) with serpentine veinlets along olivine grain boundaries. Both the peridotites and Cr-diopside rich veins contain fluid inclusion trains within minerals and along subgrain boundaries of olivines and pyroxenes; however, fluid inclusions are less abundant in the harzburgite, DM1-7, than in lherzolite DM1-4.

Grain size and textural characteristics are summarized in Table 4-4. Spinels have the most complex morphology. Most spinels have vermicular shapes and are located between pyroxene grains forming opx-cpx-sp clusters. Some rounded spinels are included in orthopyroxene, or rarely in clinopyroxene grains; very few spinels are disseminated between olivine crystals.

Deformation features indicative of high temperature plastic flow are observed in all the xenoliths; e.g., kink banding in olivine, undulose extinction in orthopyroxenes or olivine, and faint foliation defined by weakly elongated olivines and pyroxenes in three xenoliths (DM1-4, DM1-7 and DM1-9). Only sample DM1-7 has foliation visible in handsample, and a Cr-diopside rich vein cuts this foliation at a small angle. According to the classification of Harte (1977), these shear features are characteristic of coarse-equant, coarse-tabular to tabular mosaic-porphyroclastic textures (Table 4-4).

4-4. SAMPLE PREPARATION AND ANALYTICAL TECHNIQUES

4-4.1. Sample Preparation

The peridotite xenoliths (more than one kg for each sample) were sawn to remove weathering surfaces and hammer marks. The pyroxene veins were separated from the host spinel-lherzolites by sawing. The saw marks were ground away with silicon carbide, then samples were cleaned ultrasonically in distiled water. The remaining samples were reduced to small pieces (~ 1cm) by hammer. The fragments of peridotite xenoliths were shaken to homogenize the rock chips, then approximately half (~500g) of samples were split from each sample by coning and quartering. The half of xenolith fragments for major and trace element analyses were further powdered in an agate shatterbox. The another half of xenolith fragments for isotope analysis were further crushed by hammer to the sizes < 5mm. To avoid metal contamination the samples were wrapped in clean plastic plates surrouded by cotton towels during all hammering procedures. All handling of the samples in all processes were with a gloved (poly) hand. The fragments of xenoliths for isotope analysis were sieved through plastic sieves, and the minerals less than 200 mesh size range were separated by a Frantz isodynamic magnetic separator (Model L-1). A garnet megacryst (Gt-1) from basanite J-14 was crushed in a C-Co mortar immersed in methanol. The separated clinopyroxenes and garnets were ultrasonically cleaned in 2.5 N HCl, and

were then hand-picked in ethanol under a binocular microscope following the method described by Zindler and Jagoutz (1988). The picked minerals were than ultrasonically cleaned in 2.5 N HCl again to improve surface quality, and re-examined under a binocular microscope to insure the quality of each grain and resulting in 100% pure separates with no inclusions, no fractures, and homogeneous in color. Prior to disslution, the picked clinopyroxenes and garnet were leached in hot (125^{o}C) 2.5 N HCl for 1.5hr, in cold 5% HF for 15 min, and ultrasonically cleaned in 2.5 N HCl for 40 min. After each step, mineral separates were ultrasonically cleaned in water. All reagent used in leaching were 2-bottle distilled.

The first leached, hot 2.5 N HCl, leachates from clinopyroxenes DM1-3, DM1-7 and DM2-2 were poured into 10 ml beakers, and the first washed waters were added to the leachates. The leachates were evaporated and used for isotope analyses. The clinopyroxenes were dried and weighted to determine weight loss during leaching and which was assumed to be the weight of the leachate.

4-4.2. Analytical Techniques

Whole-rocks and minerals were analyzed by several techniques. For precision estimates, details of techniques and analytical references see footnotes in tables. Major and trace elements (except Sc, Cr, Co, and rare earth elements)

abundances were obtained by X-ray fluorescence at the University of Massachusetts; Sc, Cr, and Co abundances by instrumental neutron activation analysis at MIT; rare earth elements (REE) by radiochemical neutron activation analysis at MIT. Mineral compositions were determined with a JEOl 733 electron microprobe at MIT. REE abundances in single clinopyroxene crystals were analyzed with a Cameca IMS 3f ion microprobe at MIT.

Isotopic ratios of Sr and Nd, and the concentrations of Sr, Nd, Sm, and Rb were obtained for the six bulk xenoliths, acid leached clinopyroxenes separated from the six spinel peridotites and the three Cr-diopside rich veins, and two HCl leachates of clinopyroxenes. The chemical and mass spectrometric techniques used to determine the isotopic composition of Sr and Nd, and the concentrations of Sr, Nd, Sm, and Rb were described by Hart and Brooks (1977) and Zindler et al (1979). The $^{87}Sr/^{86}Sr$ values are relative to 0.70800 for E & A $SrCO_3$ standard and are normalized to $^{86}Sr/^{88}Sr=0.11940$. The $^{143}Nd/^{144}Nd$ values are corrected relative to $^{143}Nd/^{144}Nd=0.512640$ for BCR-1 and are normalized to $^{146}Nd/^{144}Nd=0.721900$. The concentrations of Sr, Nd Sm and Rb obtained by isotope dilution (ID) have estimated precisions of less than 0.5%. Contributions from blanks are negligible.

4-5. RESULTS

4-5.1. Major Elements

Cong and Zhang (1983) found high CaO contents (3-4%) in Group I Hannuoba spinel lherzolites, and they proposed that these lherzolites were undepleted mantle samples. The six spinel peridotites studied in this Chapter range widely in composition (e.g., 1.2 to 2.5% CaO, Table 4-2), and the major element abundance trends are similar to those defined by lherzolite xenoliths from worldwide occurrences (Maaloe and Aoki, 1977) and peridotite massifs (Fig. 4-1). A significant exception is the systematically higher Fe contents in the four samples obtained from Cong and Zhang. These samples were powdered in China, a possible reason for higher Fe contents is contamination during sample preparation. For comparison, the four samples were reanalyzed by the author in U. Mass. The reanalyzed data (Table 4-2b) show major element trends consistent with those of the six spinel peridotites studied in this thesis.

Minerals within the olivine-rich (lherzolite) portion of these Hannuoba peridotites are compositionally homogeneous (Table 4-3) and reflect equilibrium partitioning. Specifically, compositional variations within single mineral grains and between different grains in a sample are generally within counting statistics, except that there are small variations between different clinopyroxene grains in sample DM1-3, and ion probe data show that the

clinopyroxene from DM1-3 vein is zoned in Sr concentration (unpublished data).

In sample DM1-7 minerals from the pyroxene-rich and olivine-rich portions are compositionally similar (Table 4-3); however, minerals, especially clinopyroxene and spinel, from diopside-rich layers in samples DM1-3 and DM1-5 are compositionally distinct from mineral compositions in the olivine-rich hosts. These differences are complex. That is, in sample DM1-3 clinopyroxene and spinel from the vein have lower TiO_2 and lower Al/Cr, respectively, than the corresponding minerals from the host; in contrast, clinopyroxene and spinel from sample DM1-5 show the opposite trends (Table 4-3). In order to thoroughly document these complexities, detailed ion and electron microprobe analyses of host-vein transects are planed in the future.

4-5.2. Trace Elements

Abundances of most compatible to moderately incompatible trace elements (Table 4-5) form well defined trends. For example, Ni abundances are positively correlated with MgO contents, whereas Sc, V, Ga, Y are inversely correlated (Fig. 4-2). Cr and MgO are not positively correlated (Fig. 4-2), and this is typical in peridotites (e.g., Frey et al, 1985).

The highly incompatible trace elements (e.g., La and Sr, Tables 4-6, 4-7 and 4-8) are not correlated with MgO or

CaO (Fig. 4-3). In particular, two samples (DM1-3 and DM1-7) with higher La contents, and DM1-7 with high Sr content plot far away from the Ronda peridotite field in Fig. 4-3. The three samples (DM1-9, DM1-4 and DM1-5) within the Ronda peridotite La-CaO field have light REE (LREE) depleted patterns (Fig. 4-4); sample DM1-2 is not in the Ronda field (Fig. 4-3) and it has a slightly LREE enriched pattern (Fig. 4-4). The other two samples have U-shaped REE patterns (Fig. 4-4). With the exception of xenoliths DM1-2 and DM1-3, the REE patterns of clinopyroxenes (Fig. 4-4) are similar to those of the bulk rocks. Also, clinopyroxenes from the host lherzolites and clinopyroxene-rich veins in sample DM1-5 and DM1-7 have similar REE contents (Fig. 4-4). The very similar REE contents of clinopyroxene from DM1-7 host and vein are consistent with similar mineral compositions in the host and vein (Table 4-3). However, in sample DM1-3, clinopyroxene from the host peridotite and clinopyroxene-rich vein differ significantly in abundances of TiO2 and in REE patterns (Fig. 4-4b).

4-5.3. Radiogenic Isotopes (Sr and Nd)

The bulk peridotites and constituent clinopyroxenes have similar $^{143}Nd/^{144}Nd$ ratios but four of six bulk rocks have significantly higher $^{87}Sr/^{86}Sr$. Based on the clinopyroxene Sr-Nd isotope ratios (Table 4-8, Fig 4-5), the six peridotites show three distinctive components:

1. The strongly LREE depleted discrete xenoliths DM1-4 and DM1-9 have isotopic compositions similar to the depleted mantle end member composition of Zindler and Hart (1986).

2. The discrete xenolith DM1-2, and two composite xenoliths, DM1-5 and DM1-3, have isotopic composition similar to the PREMA (prevalent mantle) composition of Zindler and Hart (1986), and similar or more isotopically depleted than the Hannuoba alkali basalts (Fig. 4-5).

3. The composite xenolith DM1-7 has Sr-Nd isotopic composition similar to the low-Nd (LoNd) array composition of Hart et al (1986).

4-5.4. GROUP II xenoliths

Relative to Group I inclusions Group II inclusions are much less common at Hannuoba. They are mainly Fe-Al-Ti-rich websterites. Both groups occur in the basanites, but only Group II inclusions occur in the alkali olivine basalts. (Cong and Zhang, 1982).

Six Group II xenoliths have been analyzed for bulk rock major and trace elements (Table 4-10); and major element (Tabels 2-1c) and Sr-Nd isotopes have been analyzed in two clinopyroxenes (from DM2-2 and TGZ) (Table 4-8). The six Group II xenoliths are Al-spinel websterite (DM2-2 and Bd10), garnet-clinopyroxenite (TGZ), phlogopite-amphibole-pyroxenite (d10-10), spinel (magnalumoxide)-lherzolite(d1-z1), and gabbro (d2-51)).

The Group II xenoliths are more enriched in Al, Ti, Fe/Mg, and Ca than the Group I xenoliths (Fig. 4-6). Because the Group II xenoliths are clinopyroxene-rich and olivine-poor compared to the Group I xenoliths, some are more enriched in Sc, but poorer in Ni and Co than Group I xenoliths (Fig. 4-7). Also, the Cr-poor and Fe-Al-Ti rich Group II minerals (clinopyroxene and spinel, i.e., Table 2-2c) lead to a lower Cr content in the Group II xenoliths (Fig. 4-7). The Ni abundances in the Group II xenoliths show a larger variation range (24 to 988 ppm) than that in the Group I xenoliths (2150 to 2460 ppm, Fig. 4-7), which suggests a cumulative origin from basic magma for Group II but not for Group I xenoliths (Frey and Prinz, 1978; Frey et al., 1985). REE abundances in bulk Group II xenoliths are higher than in the Group I xenoliths. The gabbro has a Eu positive anomaly (Fig. 4-8).

Group II xenoliths generally are believed to have originated as high pressure segregations (< 25-30 kb) from basaltic melts (Frey and Prinz, 1978; Frey, 1980; Kempton, 1987). However, a similar cognate relationship is not supported by the isotopic data of the clinopyroxenes from two Group II xenoliths. Although the Nd isotopic data are very poor, the clinopyroxene and garnet from garnet-pyroxenite (TGZ) have Sr-Nd characteristics similar to clinopyroxenes from the Group I xenoliths with PREMA compositions, and clearly more depleted in Sr and Ns isotope compositions than the Hannuoba alkalic basalts (Table 4-8,

Fig. 4-5). In contrast, clinopyroxene from an Al-spinel websterite DM2-2 has extremely high $^{87}Sr/^{86}Sr$ and low $^{143}Nd/^{144}Nd$ ratios, which also do not overlap with the Hannuoba basalts. The enriched isotopic characteristics of clinopyroxenes from DM2-2 may reflect an end member for the Hannuoba tholeiitic basalts (however, Pb isotope data are needed to evaluate this suggestion). The Sr-Nd isotope ratios of the leachates from DM2-2 clinopyroxenes show similar isotopic characteristics to the host basanite D-1 (Table 4-8), which suggests that the leachate materials are mainly infiltrated host basaltic magma. The very much larger Sr-Nd isotope variations in the two Group II inclusions may suggest that they were derived from different mantle sources (i.e., different depths), the garnet-pyroxenite was from a depleted mantle, and the isotope compositions of DM2-2 clinopyroxenes suggest a very enriched composition either in the subcontinental lithosphere mantle, or in the lower crust (if DM2-2 is a lower crust granulite).

Further work (i.e, mineralogy, isotope geochemistry etc) for the Group II xenoliths will be conducted by the author in the near future, and therefore the Group II xenoliths are not discussed in further.

4-6. DISCUSSION OF MANTLE PROCESSES

4-6.1. Constraints from Whole-Rock Major Element Chemistry

Although mantle-derived lherzolites from diverse tectonic settings range significantly in major element content, CaO, Al_2O_3, Na_2O, and TiO_2 contents are nearly linear inverse functions of MgO abundance (e.g., Kuno and Aoki, 1970; Maaloe and Aoki, 1977). Early studies (Harris et al., 1967; Chen, 1971) interpreted these trends as resulting from segregation of varying amounts of melt from a compositionally homogeneous source. This interpretation is now generally accepted (Frey et al., 1985; Palme and Nickel, 1985; Hart and Zindler, 1986). There are no systematic major element differences between the oceanic and continental spinel lherzolites. (Kuno and Aoki, 1970; Maaloe and Aoki, 1977). Hannuoba Group I peridotites define similar major element trends (Fig. 4-1). We like others (e.g., Harris et al., 1967; and Chen, 1971), interpret that they formed as residues from different degrees of partial melting. Cong and Zhang (1982) indicate that the CaO content (3-4%) of some Group I Hannuoba spinel lherzolites is among the highest reported from all over the world. On this basis they propose that these lherzolites may be fertile mantle samples. In contrast, the majoe element data of this study show larger depletions in the low temperature melting components (Ca, Al, Na) for the six spinel peridotites than those studied by Cong and Zhang. The peridotites from both studies show an inverse linear correlation between CaO and MgO content. The wide variation range suggests that the Hannuoba Group I peridotites may represent residues after

different degrees of partial melting. Apparently the upper mantle beneath the Hannuoba area is composed of peridotites ranging from relatively fertile to very depleted in basaltic components. Major element variations in these Hannuoba peridotites are similar to those defined by lherzolite xenoliths from worldwide occurences and peridotite massifs such as Ronda, Spain and Horomon, Japan and show approximately similar linear major element variation trends, except SiO_2 vs MgO. Possibly, the Hannuoba suite is slightly higher in SiO_2 abundances. Therefore the primitive source composition of the Hannuoba peridotites was similar to the source composition of Ronda and Horoman peridotites, but perhaps higher in silica content. Similar silica enrichment also was observed for garnet lherzolites relative to spinel lherzolites worldwide (Maaloe and Aoki, 1977, Figure. 4).

If the Hannuoba spinel peridotites are assumed to have been generated as partial melting residues from a relatively homogeneous source, then the degrees of melting can be calculated by assuming a primitive source composition. The small range of major element variation for the estimated primitive source compositions of peridotites from Ronda, Spain; Horoman, Japan; Victoria, Australia and Tariat, Mongolia (Frey et al., 1985; Leinbach, 1987; Nickel and Green, 1984; Preß et al., 1986), and the silicate mantle composition (Table 4-2 G, Zindler and Hart, 1986) in Fig. 4-1 define a range of possible primitive upper mantle compositions. In order to estimate the melting range for the

six Hannuoba peridotites, the silicate mantle composition of Zindler and Hart (1986) was assumed as the initial composition because its SiO2 content is similar to the least depleted Hannuoba peridotites. The calculation is based on mass balance (for details, see Frey et al., 1985) and Fe/Mg Kd for olivine = 0.3. We assume that the peridotites represent residues without trapped melt. The calculated results indicate that the peridotites DM1-4 and DM1-9 with relatively lower Mg number are residues generated by lower degrees of partial melting (<5%); the peridotites DM1-2, DM1-3, DM1-5 and DM1-7 with relatively higher Mg number are residues generated by higher degree of melting (15-20%).

4-6.2. Constraints from Mineral Composition

The compositions of residual phases in peridotites change continuously during partial melting, e.g., as the degree of melting increases, Fe, Al, Ti, and Na in silicate minerals and Al in spinel decrease, whereas Mg in silicate minerals, Cr in spinel, and Ni in olivine, generally increase (e.g., Dick and Fisher, 1984). Therefore, the Mg/Fe of silicate minerals, the Al_2O_3, TiO_2, Na_2O contents of pyroxene, and Cr/Al of spinel are indices of the degree of melting. These correlations exist in the Hannuoba peridotites.

Mg/Fe ratios in minerals and bulk rocks are positively correlated with bulk rock Mg/Fe, and decrease in the order

of clinopyroxene, orthopyroxene, and olivine, with ratios of Fo content over bulk rock Mg# close to unity (Fig. 4-9). These trends are consistent with equilibrium Fe/Mg partitioning. Ratios of $(Na_2O/CaO)_{cpx}$ over $(Na_2O/CaO)_{whole\ rock}$ are near unity except DM1-5 (Fig. 4-10), thereby indicating that clinopyroxene is the major host phase for CaO and Na_2O. Although the correlations of Na_2O, Al_2O_3, and TiO2 with Mg# of pyroxenes are poor, in the Hannuoba peridotites samples with lower bulk rock Mg/Fe (DM1-4 and DM1-9) contain minerals with relatively low Mg/Fe, pyroxenes with relatively high Na_2O, $Al2O_3$, and TiO_2, and high Al/Cr spinels (Table 4-3). Therefore, both whole rock major element contents and mineral compositions are consistent with the interpretation that the xenoliths represent residues formed by varying degrees of melting.

Based on the studies of Carswell and Gibb (1980, 1987) Wells's geothermometer (1977) is judged to be currently the best calibration of two-pyroxene solvus for assemblages equilibrated at less than 37 kb. Temperatures calculated assuming all Fe as Fe^{2+} are closer to experimental temperatures than those for which Fe^{3+} contents were calculated by stoichiometric charge balance, since the calculated Fe^{3+}/Fe^{2+} ratios are highly susceptible to any analytical errors (especially in SiO_2). Therefore, the Wells's geothermometer was used for the Hannuoba spinel-peridotites, and all Fe in pyroxenes were assumed as Fe^{2+} (Table 4-3b). For comparison, the geothermometer of Wood and

Banno (1973) also has been used, showing ~ 100°C higher than the temperatures calculated based on Wells's method (Fig. 4-11). Temperatures based on the two pyroxene geothermometers are mainly controlled by Ca^{2+} - Mg^{2+} exchange reaction and by the presence of other elements (notably Fe) occupying M1 and M2 sites. Temperatures show positive correlation with LnK[6] (Fig. 4-11). The clinopyroxenes with lower Mg/Fe (DM1-4 and DM1-9) are lower in CaO content than the clinopyroxenes with higher Mg/Fe (DM1-2, DM1-3, DM1-5 and DM1-7) (Table 4-3). The broad inverse trend of CaO in orthopyroxene and CaO in coexisting clinopyroxene can be interpreted as a result of different equilibrium temperatures (~914°C to 1083°C for host peridotites, Table 4-3b). These temperatures do not represent temperatures during partial melting but are subsolidus equilibration temperatures.

In a plot of Al_2O_3 contents between orthopyroxene and spinel the Hannuoba peridotites are within or slightly lower than the alpine type peridotites (Fig. 4-12). That is, similar to alpine peridotites the Hannuoba peridotites have a lower Al orthopyroxene/spinel partition coefficient than abyssal peridotites. This may reflect the compositional difference between the continental and abyssal peridotites (Dick and Fisher, 1984), or more likely reflects a higher equilibrium temperature of abyssal peridotites relative to continental peridotites (Henry and Medaris, 1980; Dick and Fisher, 1984).

---

6. $Lnk = a^{cxp}/a^{opx}$.

4-6.3. Constraints from Trace Element Geochemistry

The relative order of decreasing bulk solid/melt partition coefficients for olivine dominated four phase (olivine, orthopyroxene, clinopyroxene, and spinel) mantle peridotites is Ni > Co > Cr > Sc > V > Ga > Zr ~ Sr> LREE (Frey et al 1985). Highly incompatible elements, such as K, Rb, Cs, Ba, Sr, Th, LREE and Ta, are almost completely rejected by these four phases. The moderately incompatible elements Sc, V, HREE, Zr, Hf, Na, and Ti are incorporated into clinopyroxene; Cr is mainly accepted by spinel, and to a lesser degree by clinopyroxene. The highly compatible elements Ni and Co are primarily in olivine.

a. Highly Compatible to Moderatly Incompatible Trace Elements:

The highly compatible to moderately incompatible elements of the six Hannuoba peridotites (Table 4-5) follow the ME variation trends of most continental peridotites (Fig. 4-2). The bulk solid/melt partition coefficient of the most compatible element, Ni, is much higher than unity (Hart and Davis, 1978), and Ni is positively correlated with MgO (Fig. 4-2). The Ni variation range of the six Group I peridotites is very small (2150 ppm to 2460 ppm, Table 4-5) compared to the range for six Group II Hannuoba xenoliths (24 ppm to 988 ppm) (Fig. 4-6). The small Ni variation range is consistent with derivation as partial melting residues

rather than as olivine-rich accumulates from basic magma (Frey and Prinz, 1978; Frey et al., 1985). In contrast to Ni, Cr is not positively correlated with MgO (Fig. 4-2). In general, Cr and MgO contents are poorly correlated in mantle peridotites (e.g., Frey et al., 1985). The negative near-linear correlations of the moderately incompatible elements (Sc, V, Ga and Y) with MgO (Fig. 4-2) are expected in residues formed by less than 30% partial melting (Frey et al, 1985). Therefore, abundance variations of Ni, Sc, V, Ga and Y are consistent with inferences based on major element contents.

b. Highly Incompatible Trace Elements:

In contrast to compatible and moderately incompatible elements, abundances of highly incompatible trace elements, such as LREE, in peridotites are often decoupled from the major element trends (e.g., Frey and Green, 1974; Frey 1984; Kempton, 1987). Variations in Sr and La content with MgO and CaO for peridotites, DM1-9 and DM1-4 are consistent with small degrees of partial melting (<5%), but peridotites (DM1-7 and DM1-3) whose major elements reflect generation by a relatively higher degree of partial melting (16-20%) have unexpectedly high La and Sr contents (Fig. 4-3). Frey and Green (1974) suggested that high abundances of incompatible elements in residual peridotites reflects addition of an enriched component, fluid or melt, to partial melting residues.

c. Bulk Rock REE Geochemistry

LREE depleted xenoliths:

Lherzolites DM1-4 and DM1-9 are the most depleted in LREE (La about 0.3 x chondrite) of the Hannuoba peridotites; DM1-5 is slightly depleted in LREE (La=0.7 x chondrite). These samples have relatively constant HREE abundances (Lu about 1.1 to 1.4 x chondrite)(Fig. 4-4). This wide range in LREE abundance with relatively constant HREE abundance is expected in residues from different degrees of partial melting of a compositionally homogeneous garnet peridotite source (Loubet et al., 1975; Loubet and Allegre, 1982; Frey, 1984). Sample DM1-5 has the least depleted LREE pattern (La = 0.7 x chondrite, Lu = 1.4 x chondrite), and the highest CaO and Al_2O_3 contents (Table 4-2). Hence, it may represent a more "fertile" xenolith. However, DM1-5 has a higher bulk-rock Mg number and olivine Fo content, and hence a higher calculated partial melting degree (20%) than DM1-4 and DM1-9. These discrepancies are inconsistent with a simple model. Sample DM1-5 was either modified by an enriched component or perhaps, it is not simply related to DM1-4 and DM1-9. Similar discrepancies are observed in xenoliths from other locations; for example, the high CaO and Al_2O_3 concentrations in DM1-5 may be similar to some xenoliths in Tariat Mongolia, where enrichment of clinopyroxene and

spinel resulted from a process different from liquid/crystal fractionation (Preß et al, 1986).

LREE enriched xenoliths:

Lherzolite DM1-2 has a nearly flat REE pattern with only slight enrichment in LREE content; in contrast, samples DM1-7 and DM1-3 have U-shaped REE patterns (Fig. 4-4). Compared to LREE depleted samples, samples DM1-7 and DM1-3 are relatively enriched in LREE (La = 0.9 to 1.5 x chondrite), depleted in heavy REE (HREE) (0.6 to 0.8 x chondrite), and strongly depleted in middle REE (MREE). The LREE enrichment and U-shaped REE patterns reflect a complicated evolution. The low HREE and MREE content of samples DM1-7 and DM1-3, and their lower Al_2O_3, CaO and Na_2O contents (Table 4-2) suggest that they were more extensively depleted by partial melting than the LREE depleted samples, DM1-4 and DM1-9. Apparently sample DM1-7 and DM1-3 were subsequently enriched in highly incompatible trace element, such as LREE, and this enrichment created the U-shaped REE patterns.

This enrichment of anhydrous peridotites requires a mantle enrichment or crustal contamination process. The interpretation of LREE enrichment in whole rock peridotites is complicated because whole-rock LREE contents can not always be mass balanced with the major minerals. However, clinopyroxene from the most strongly serpentinized sample DM1-7 is identical in REE pattern to its host peridotite

(Fig. 4-4), and clinopyroxene accounts for the total amount of Nd and Sm in the bulk rock. In contrast, clinopyroxene from the less serpentinized sample DM1-3 has a very different REE pattern than its host peridotite, and the clinopyroxene contains only 50% and 70% of the bulk rock Nd and Sm respectively. These results suggest that the LREE enrichment in these peridotites was not controlled by serpentinization.

Based on analyses of acid leached minerals, large proportions of the whole rock budget of alkaline earths and alkaline metals, and to a lesser extent LREE , are present in leachable phases of presumed secondary origin (Zindler et al., 1983; Stosch et al., 1986; Nielson and Noller, 1987; and Zindler and Jagoutz, 1988). Therefore, based on bulk peridotite analyses it is difficult to interpret REE abundances, the Rb/Sr isotopic system, and to a lesser extent the Sm/Nd isotopic system. The primary mantle characteristics can only be interpreted after the secondary contamination is recognized and removed, e.g., by analysis of unaltered minerals.

d. Clinopyroxene REE Geochemistry:

In anhydrous spinel lherzolite, clinopyroxene is the major carrier for REE. Consequently, relative REE abundances are usually similar in clinopyroxene and the bulk rock (e.g., Frey and Green, 1974; Stosch and Seck, 1980). However, in some samples REE are concentrated on grain

boundaries and in poorly characterized minor phases. In such samples REE abundance patterns in clinopyroxene and the bulk rock may be very different (e.g., Stosch et al., 1986).

The REE contents of Hannuoba clinopyroxenes were analyzed by ion microprobe on carefully handpicked and well-polished clinopyroxene grains (Table 4-7), these analyzed spots are belived to be free of surface contamination.

Peridotites are subdivided into subgroups based on their cpx REE signature. As defined by Kmepton, 1987. Type Ia cpx has chondrite normalized LREE/HREE < 1. Type Ib cpx with chondrite normalized LREE/HREE > 1, and is generally lower in HREE content. There is no distinction in terms of major element composition between Type Ia and Type Ib, but generally there is a positive correlation between the degree of LREE enrichment and Cr/Al ratios. This positive correlation is mainly due to the lower alumina content of Type Ib minerals. The Al_2O_3 contents of most Type Ia cpx is greater than 5 wt%, while Type Ib cpx has less than 6 wt %. (Kempton, 1987). For easier comparison, the average whole rock compositions of Type Ia and Type Ib from other locations (Kempton, 1987) are also listed in Table 4-2c. Based on the above criterions, the six Hanoba peridotites are subdivided into:

<u>Discrete xenolith:</u>

Type Ia xenolith: DM1-4, DM1-9 and DM1-2

<u>Composite xenolith</u>

(As the relaiton between the host lherzolite/vein):

Type Ia/Type Ia xenolith: DM1-5;

Type Ia/Type Ib xenolith: DM1-3; and

Type Ib/Type Ib xenolith: DM1-7.

All whole rocks have higher La/Sm than their constituent clinopyroxene (Fig. 4-4). The higher bulk rock La/Sm may result in part from olivine, grain boundary material or fluid inclusions (e.g., Nielson and Noller, 1987). However, Sm/Nd ratios in clinopyroxene and whole rocks are very similar (within 10%) in all xenoliths (Table 4-8) except DM1-3 which contains compositionally heterogeneous clinopyroxene. In samples DM1-5 and DM1-7 clinopyroxenes from the host lherzolites and clinopyroxenite veins have similar REE patterns and in sample DM1-7 the clinopyroxene patterns are very similar to that of the bulk peridotite (Fig. 4-4). The similar REE patterns of the whole rock and clinopyroxene imply that the LREE enrichment feature in the U-shaped pattern of the whole rock xenolith DM1-7 was not caused by a crustal alteration process, but is an intrinsic mantle signature.

Clinopyroxene-rich veins in peridotites, are commonly accepted as evidence for a migratory mantle fluid/melt. Such fluids can enrich peridotite wall rocks in incompatible elements (e.g., Stosch and Seck, 1980; Roden et al., 1984; Schneider and Eggler, 1984; Menzies et al., 1985; Kempton, 1987; Menzies and Hawkesworth, 1987; Nielson and Noller, 1987; Wilshire, 1987; Bodinier., et al., 1988; Roden et al.,

1988; O'Reilly and Griffin, 1988). In the Hannuoba composite xenoliths, clinopyroxenes from two veins (DM1-3 and DM1-7) are markedly enriched in LREE. Therefore, the LREE enrichment in the peridotite host of these pyroxenites may be due to interaction with the fluids that formed the veins. Differences in the REE patterns of the host bulk rocks, the clinopyroxenes from the host lherzolites, and the clinopyroxenes from the veins may reflect variable extents of fluid-peridotite interaction (Neilson and Noller, 1987).

e. Clinopyroxene Sr/Nd Ratios:

In spinel peridotite systems Sr and Nd are concentrated in clinopyroxene. Therefore Sr/Nd ratios of clinopyroxenes are usually similar to Sr/Nd ratios of their host peridotites (e.g., McDonough and McCulloch, 1987). However, in some xenoliths Sr and LREE, including Nd, are concentrated on grain boundaries or minor phases (Zindler et al., 1983; Stosch et al., 1986; Nielson and Noller, 1987; Zindler and Jagoutz, 1988). In such samples Sr/Nd ratios in clinopyroxenes and in host peridotites might be very different. Except for the two peridotites with U-shaped REE patterns (DM1-3 and DM 1-7) the Sr/Nd ratios of Hannuoba peridotites are similar (within 20%) to that of their clinopyroxenes (Table 4-8). The Sr/Nd ratio of DM1-3 whole rock (15.0) is significantly lower than the ratio of its clinopyroxene (20.7), and the Sr/Nd ratio of DM1-7 whole rock (39.5) is much higher than the ratio of its

clinopyroxene (16.5). This decoupling between clinopyroxene and bulk rock can be explained by the widely different Sr/Nd ratios in leachates from samples DM 1-3 and DM 1-7 (Table 4-8). The high Sr contents and Sr/Nd ratios of DM1-7 are similar to some LREE enriched lherzolites (e.g., Nunivak Island, Roden et al., 1984).

The Sr/Nd ratios of clinopyroxenes from the host peridotites and veins of DM1-5 and DM1-7 are similar (Table 4-8). The discrepancy in Sr/Nd ratio (20.7 and 27.2, Table 4-8) between clinopyroxenes from vein and host lherzolite of DM1-3 is consistent with other geochemical differences such as REE content (Fig. 4-4).

The Sr/Nd range of Hannuoba peridotites and their clinopyroxenes (whole rocks: 14.2 to 23.7, except for DM1-7=39.5; clinopyroxenes: 10.6 to 27.2) extends to lower values than the Sr/Nd range of the Hannuoba basalts (20 to 30) (Fig. 4-13), and is same as the Sr/Nd range (~9-28) of clinopyroxene from other peridotite xenoliths, e.g., San Carlos, Eifel and the Tariat Depression (Stosch and Lugmair, 1986; Stosch et al., 1986; Zindler and Jagoutz, 1988). Thus, Hannuoba peridotites have Sr/Nd similar to the range of MORB and intraplate basalts, but lower than the Sr/Nd range of basalts from convergent plate margins (e.g., McDonough and McCulloch, 1987). Formation of the North China Basin may be related to subduction of the Kula Pacific Ridge (Li and Cong, 1980; Zhang and Huang, 1982, Capter 3: 3-4.6). However, the Sr/Nd range of Hannuoba peridotites and basalts

and the enrichment of Nb and Ta in Hannuoba basalts (Chapter 1) indicate that the mantle composition represented by these peridotites and basalts beneath the northeastern China has not been affected by subduction of the western Pacific margin.

4-6.4. Constraints from Isotope Geochemistry:

a. Peridotites:

In general $^{143}Nd/^{144}Nd$ ratios are similar in the whole rocks and clinopyroxenes although four of the six samples have slightly higher $^{143}Nd/^{144}Nd$ in the clinopyroxene. In contrast, in four samples clinopyroxene has significantly lower $^{87}Sr/^{86}Sr$ than the whole rocks (Table 4-8). Because whole rock ratios may have been affected by secondary processes.

Based on the Sr-Nd isotopic ratios of nine clinopyroxenes from the peridotites (Table 4-8), the upper mantle beneath the Hannuoba area contains three distinctive components (Fig. 4-5).

1. Depleted Mantle (DMM): The LREE depleted xenoliths, DM1-4 and DM1-9, represent the most depleted compositions. Their $^{143}Nd/^{144}Nd$ ratios are higher than MORB (Fig. 4-5). Although DM1-4 and DM1-9 are the most depleted in LREE (Fig. 4-4), they are the least depleted in basaltic components based on major element criteria (Fig. 4-1). Therefore, relative depletion in a basaltic component is not coupled

with the depleted characteristics reflected by REE and isotopic data.

2. Prevalent Mantle (PREMA): The discrete xenolith DM1-2 and composite xenoliths DM1-5 and DM1-3, have isotopic compositions similar to the PREMA composition of Zindler and Hart (1986). Clinopyroxenes from these xenoliths have $^{87}Sr/^{86}Sr$ slightly lower and $^{143}Nd/^{144}Nd$ slightly higher than the host alkali basalts (Fig. 4-5). This isotopic range overlaps with many ocean island basalts which suggests that the material with an isotopic signature identical to PREMA occurs in the oceanic and continental upper mantle.

3. LoNd-like mantle: A composite xenolith DM1-7, plots below the "mantle array" and along the low-Nd (loNd) array defined by Hart et al (1986). This requires a component with a time-integrated Sm/Nd ratio < bulk earth and Rb/Sr < bulk earth in the subcontinental mantle beneath northeast China.

b. Clinopyroxenite Veins:

Comparisons of the geochemical characteristics of clinopyroxene from the clinopyroxene-rich veins and host peridotite (Table 4-8) provide important data for evaluating mantle metasomatism. The isotopic and REE characteristics of clinopyroxene from DM1-7 clinopyroxene-rich vein and host peridotite are nearly identical. Clinopyroxenes from DM1-5 clinopyroxene-rich vein and host peridotite are slightly more discrepant in $^{87}Sr/^{86}Sr$ and $^{143}Nd/^{144}Nd$, and in sample DM1-3 the isotopic differences are significantly larger than

analytical precision. In DM1-3 the clinopyroxenes also have different REE contents (Fig 4-4). Apparently fluids forming the veins were isotopically distinct from the wallrock peridotite, and enrichment/metasomatism occurred by diffusion or melt/fluid infiltration along cracks and grain/subgrain boundaries. Enrichment effects would be enhanced by large amounts of vein magma, high H_2O or CO_2 contents in the magma, small temperature contrasts between magma and wall rock, and small grain size in the wall rock. Since these parameters are likely to vary with time and from vein to vein, it is possible that some veins have extensively modified their wallrocks converting them to an equilibrium composition (e.g., DM1-7) while other veins have only partially reequilibrated their wallrocks (DM1-3 and DM1-5). The low Ce/Sm of clinopyroxene from the DM1-5 vein (Fig. 4-4) may reflect a lower Ce/Sm in the vein material or that this vein equilibrated with a large volume of host peridotite.

Other studies of clinopyroxene from Group I lherzolites and their associated pyroxenite veins have yielded similar results. That is, clinopyroxene from the lherzolite host and vein may be isotopically identical (e.g., KH73-1 in Roden et al., 1988), but more commonly the vein clinopyroxene has lower $^{143}Nd/^{144}Nd$ and higher $^{87}Sr/^{86}Sr$, typically overlapping with the oceanic island basalt field. Also the vein clinopyroxene may be more enriched in LREE contents (Menzies et al., 1985 and Fig. 4-4).

c. Leachate:

Since a complex history is suggested by the major element, trace element and isotopic features of the peridotites with U-shaped REE patterns, isotopic ratios were measured for the acid (2.5N HCl) leachate of clinopyroxene from host lherzolites DM1-3 and DM1-7. The materials leached by 2.5N HCl acid are believed to be mainly grain boundary materials, perhaps with small amounts dissolved from mineral edges. Possible sources for such materials include the continental crust, glasses from penetration of the host magma or forming in situ from decompression melting along grain boundaries, and mantle derived elements which were not incorporated into the major minerals (Noller, 1986; Stosch et al., 1986; Zindler and Jagoutz, 1988).

In sample DM1-7, $^{143}Nd/^{144}Nd$ ratios of the whole rock, clinopyroxene from the peridotite and clinopyroxene from the clinopyroxene-rich vein span a small range, 0.51249 to 0.51254, that is within the relatively large uncertainty of the leachate data (Table 4-8). In contrast, the leachate has a slightly lower $^{87}Sr/^{86}Sr$ (0.70422) than the clinopyroxenes (0.70430 to 0.70434). This lower value is identical to the bulk-rock ratio. Because the leachate has a high Sr content (49 ppm), the leachable component accounts for the lower bulk-rock $^{87}Sr/^{86}Sr$. Therefore, there is no evidence in this xenolith for contamination from crustal material with high $^{87}Sr/^{86}Sr$. Apparently, this sample interacted with a fluid

having a higher Sr/Nd but lower $^{87}Sr/^{86}Sr$ than its clinopyroxene.

In sample DM1-3 the bulk rock, leachate and clinopyroxenes from the peridotite and clinopyroxene-rich vein also have similar $^{143}Nd/^{144}Nd$ (0.51282 to 0.51300), but in contrast the leachate has a higher $^{87}Sr/^{86}Sr$ (0.70433) than the clinopyroxenes (0.70372 to 0.70386) or the bulk peridotite (0.70380). Moreover, in five samples (Sm/Nd)cpx/(Sm/Nd)wr is near unity, but in DM1-3 the whole-rock has significantly lower Sm/Nd (0.276) than clinopyroxene from the peridotite (0.371) (Table 4-8). The clinopyroxene leachate has an even lower Sm/Nd (0.146) which is similar to Sm/Nd (0.166) in clinopyroxene from the clinopyroxene-rich vein. Thus, the leachate may have a LREE enriched pattern similar to clinopyroxene from the vein, and REE differences between the host peridotite and its clinopyroxene (Fig. 4-4) probably reflects the leachate contribution to the bulk peridotite composition.

The leachates also have high Rb/Sr ratios. There are large differences in Rb/Sr between the clinopyroxene and the leachates (Table 4-8); e.g., factors of 2 and 100 for DM1-7 and DM1-3 respectively. These Rb/Sr variations and the higher $^{87}Sr/^{86}Sr$ ratios of the bulk peridotites and acid leachate relative to clinopyroxene (except DM1-7) lead us to conclude that the Rb/Sr isotopic systematics are more complex than the Sm/Nd isotopic systematics.

An notable point is: the clinopyroxenes from the GroupII, an Al-spinel websterite DM2-2 show extremely high $^{87}Sr/^{86}Sr$ and low $^{143}Nd/^{144}Nd$ ratios, which clearly is not related to the host basaltic magma, but its Sr-Nd isotope ratios of the leachates show identical isotopic characteristics to the host basanite (Table 4-8), which suggests that the leachate materials are mainly the infiltrated host basaltic magma.

d. Rb/Sr isotope:

There is an inverse correlation between the whole rock Rb/Sr and $^{87}Sr/^{86}Sr$ ratios (Fig. 4-14), and a positive correlation between Mg numbers and the $^{87}Sr/^{86}Sr$ ratios (Fig. 4-15). Similar characteristics have been found in some xenoliths from other locations. For instance, xenolith SL1 from southeast Australia has the highest $^{87}Sr/^{86}Sr$ ratio, but a very low Rb/Sr ratio compared with other xenoliths from the same location (Chen et al., 1989); the most depleted xenoliths, MO103 and MO102, from the Tariat depression Mongolia (Stosch et al, 1986), and the very depleted Sc-23 from Peridot Mesa, San Carlos, Arizona (Zindler and Jagoutz, 1987) have relatively high $^{87}Sr/^{86}Sr$ ratios. These features may be caused by mixing with a late-stage alteration component, or alternatively, by mixing with a mantle fluid/melt with low Rb content but high $^{87}Sr/^{86}Sr$ ratios and high Sr and LREE contents. If the first assumption is true, these correlations are the result of

mixing with secondary alteration material, e.g., the lower Rb/Sr in the bulk peridotites may be produced by ground water removing the Rb from the whole rocks. However, the inverse correlation between Mg numbers and Rb/Sr ratios (Fig. 4-16) is difficult to explain by this effect. Because the positive correlation between La and Sr is an intrinsic property of clinopyroxenes (Fig. 4-17), and the Rb/Sr ratios are likely increased when contaminated by crustal material (Zindler and Jagoutz, 1987), these Rb/Sr-$^{87}Sr/^{86}Sr$-Mg# trends may reflect mantle processes. Therefore, a possible model for the inverse correlation between Rb/Sr and $^{87}Sr/^{86}Sr$ is that ancient, depleted upper mantle was metasomatized by a fluid/melt with low Rb, but high Sr and LREE contents. If this enrichment event occurred a long time ago, a relatively low $^{143}Nd/^{144}Nd$ would have resulted; e.g., sample DM1-7 in Fig. 4-5. If the enrichment event occurred recently, the isotopic signature of depleted upper mantle would remain unchanged, but the incompatible element abundances would have been enriched; e.g., xenoliths DM1-3. However, the inability to mass balance Rb contents of ultramafic rocks with unaltered minerals makes such interpretations tenuous. The possibility that the inverse correlation between $^{87}Sr/^{86}Sr$ and Rb/Sr ratios was caused by some unknown alteration phases cannot be excluded.

e. Summary:

Comparisons of geochemical characteristics of the bulk peridotite and clinopyroxenes from the veins and host peridotite lead us to conclude that:

(1) initially the veins were compositionally distinct from the host-rock (e.g., in sample DM1-3 the vein clinopyroxene has different $^{87}Sr/^{86}Sr$ and $^{143}Nd/^{144}Nd$ ratios and normalized-REE patterns than the host clinopyroxene; and

(2) the host rock was affected by the veins and in some cases (sample DM1-7) the vein and host rock have equilibrated. Therefore, contamination by fluids derived from the veins can explain the anomalous REE abundances in samples like DM1-7. However, this relatively simple explanation does not account for all the geochemical characteristics of the peridotites. The higher La/Sm and $^{87}Sr/^{86}Sr$ of the bulk rocks relative to the constituent clinopyroxenes, and the compositional characteristics of leachates, especially Sr/Nd and $^{87}Sr/^{86}Sr$ which differ from the bulk rock and clinopyroxene ratios, provide evidence for a contamination process distinct from that caused by the clinopyroxene-rich veins. However, there is no strong evidence that any of these contamination events were caused by crustal components.

4-6.5. Timing of Depletion and Enrichment Events in the Subcontinental Mantle

At upper mantle temperatures, diffusive equilibrium is faster than evolution of Sr and Nd radiogenic isotopes (Zindler and Jagoutz, 1988.) Therefore, the assumption of intermineral isotopic equilibrium in the upper mantle is generally accepted. Since clinopyroxene is the major carrier of REE and Sr in spinel lherzolite, the clinopyroxene Nd and Sr isotopic composition should be close to the isotopic composition of the whole rocks.

The higher $^{87}Sr/^{86}Sr$ ratios for whole rocks (except DM1-7) and DM1-3 acid leachate relative to clinopyroxenes indicates that the Sr isotopic ratio was affected by a secondary process. Therefore, model age calculations based on Rb/Sr systematics are not as reliable as those based on Sm/Nd systematics. The depleted nature of the DMM xenoliths DM1-4 and DM1-9 (Figs. 4-4, 4-5) suggest a simple history such as ancient melt extractions. The more complicated REE patterns and isotopic signatures of the PREMA and LoNd xenoliths suggest two-stage (depletion and enrichment) processes. Therefore the calculation of the model ages based on clinopyroxene may only be reasonable for DMM xenoliths.

For the two DMM xenoliths the bulk rock Sm/Nd and Rb/Sr bulk earth model ages are similar (Table 4-9). The inferred age of about 2 Ga is similar to the depletion age of the peridotites from the Tariat depression, central

Mongolia (Stosch et al., 1986). Therefore, these depleted lherzolites were derived from a bulk earth composition about 2 Ga ago, or an already depleted (e.g., MORB) source at some more recent time. However bulk rock model ages for another xenolith with a slightly LREE depleted pattern, DM1-5, are not consistent. This supports previous conclusions based on major and trace element data that DM1-5, unlike DM1-4 and DM1-9, was not generated by a single depletion event.

The isotopic and REE characteristics of PREMA and LoNd xenoliths suggest two enrichment events in the upper mantle beneath Hannuoba area. PREMA xenoliths were derived from a long term depleted mantle that has been enriched recently; thus radiogenic isotope ratios do not yet reflect this enrichment. The LoNd xenolith DM1-7 may reflect an ancient mantle enrichment event in which depleted upper mantle was enriched by LREE enriched, Rb-poor fluids (Hart et al, 1986). In the Sm/Nd system an isochron exhibited (Fig. 4-18) by the six peridotites defines a 1.08 Ga age, which may indicate an enrichment event about 1 Ga ago. However, this line also may represent a mixing line.

4-7. DEVELOPMENT OF A METASOMATIC MODEL

Several geochemical features of the Hannuoba peridotite xenoliths must be explained by an enrichment/metasomatic model.

1). The peridotites show positive correlations between HREE abundance and CaO or Al_2O_3 contents, and negative correlations between LREE/HREE, (or LREE/MREE), and CaO or Al_2O_3 contents (Fig. 4-19). This is a general feature of peridotite xenoliths in basalts (Frey 1984; Kempton, 1987; Nielson and Noller, 1987; O'Reilly and Griffin, 1988).

2). Two anhydrous peridotites have U-shaped REE patterns, a characteristic which has also been found in many peridotites, especially harzburgites worldwide (e.g., Stosch et al., 1980; Frey 1984; Roden et al., 1984; Prinzhofer and Allegre, 1985; Bodinier et al, 1988).

3). Among the anhydrous peridotites, the most depleted in "basaltic" components (e.g. Ca, Al, or Na) are the most isotopically enriched, i.e., highest $^{87}Sr/^{86}Sr$ and lowest $^{143}Nd/^{144}Nd$ (Fig. 4-15). A few xenoliths depleted in basaltic components from other locations follow this trend; e.g., samples Mo103 and Mo102, from the Tariat depression, Mongolia (Stosch et al, 1986), the very depleted Sc-23 from Peridot Mesa, San Carlos, Arizona (Zindler and Jagoutz, 1988), and highly deformed samples from the Massif Central, France (Downes and Dupuy, 1987).

These trends indicate that the amount of basalt in a peridotite as measured by CaO, Al_2O_3, TiO_2 and Na_2O, is inversely proportional to incompatible element content and the degree of depletion as reflected by Sr and Nd isotopic ratios. The major element-isotopic correlation is based on few data but where present this trend precludes LREE

enrichment as resulting from varying degrees of melting of a homogeneous source.

Important questions to be resolved are:

1). What causes U-shaped REE patterns in peridotites?

2). What causes decoupling of major elements and incompatible elements in peridotite? Especially, why is La/Yb inversely related to CaO and Al_2O_3 contents?

The causes of U-shaped REE patterns in peridotites have been discussed by several authors (e.g., Stosch et al., 1980; Roden et al., 1984; Prinzhofer and Allegre, 1985; Navon and Stolper, 1987; O'Reilly and Griffin, 1988). Proposed models include:

a). LREE enrichment of cpx-poor, anhydrous peridotites caused by residual spinel or olivine which have solid/melt partition coefficients of LREE > MREE. Spinels are not a likely source of LREE enrichment (Frey, 1984; Prinzhofer and Allegre, 1985), but relatively high partition coefficients for LREE in olivine may reflect inclusions highly enriched in LREE contents (Kurat et al 1980; Roden et al., 1984; Nielson and Noller, 1987; Zindler and Jagoutz, 1988).

b). LREE enrichment as a result of a two-stage process. Formation of a partial melting residue with $(LREE/HREE)_N < 1$ followed by a secondary process, such as alteration, metasomatism, or trapping of melt/fluid which causes LREE enrichment (Frey and Green, 1974; Stosch et al., 1980; Prinzhofer and Allegre, 1985; O'Reilly and Griffin, 1988).

Due to both the extremely low partition coefficients of spinel, and the fact that spinel is a minor phase (< 1% in Hannuoba peridotites), its contribution to the LREE enrichment in bulk peridotites is neglected. Olivine dominates the bulk rock REE pattern only when clinopyroxene is a minor phase as in the case of harzbugite or dunite. Hannuoba peridotites have clinopyroxene contents higher than 5% (Table 4-1), and except for sample DM1-3, clinopyroxene accounts for more than 80% of the bulk-rock REE contents. Therefore, a two-stage process is a more reasonable explanation for the U-shaped REE pattern of Hannuoba peridotites. The isotopic heterogeneity among the Hannuoba peridotites suggest that depleted mantle, such as DMM xenoliths, mixed with a component having relatively high $^{87}Sr/^{86}Sr$ and low $^{143}Nd/^{144}Nd$.

Only two quantitative models for the generation of U-shaped REE patterns have been proposed; the "disequilibrium melting model" of Prinzhofer and Allegre (1985), (abbreviated as "P & A" model in this paper), and the "mantle as a chromatographic column model" of Navon and Stolper (1987), (abbreviated as "N & S" model in this paper).

In the P & A model, disequilibrium melting proceeds as the mantle rises from the garnet lherzolite facies to plagioclase lherzolite facies. Initially relative LREE enrichment is created in residues by disequilibrium melting of garnet. Subsequent disequilibrium melting of plagioclase

at lower pressure preferentialy removes LREE and Eu thereby creating a residue with a U shaped REE patten and a negative Eu anomaly. Although the P & A model may produce decoupling between major element and incompatible elements, it is very difficult to generate U-shaped REE pattern unless the residues are dunites, especially, if the peridotite was relatively depleted in LREE prior to enrichment (Leinbach, 1987). Also this model cannot generate a residue with a LREE content greater than the source. We conclude that the P & A model cannot explain the LREE enriched Hannuoba peridotites.

The N & S model considers the interaction between depleted mantle and a melt highly enriched in incompatible elements as an ion-exchange process similar to a chromatographic column. The ascending enriched melt is not in equilibrium with the overlying residual mantle, spinel or garnet peridotite, and during ascent equilibrium is reached by enriching the depleted peridotite in incompatible elements. Highly incompatible elements, such as LREE, move more rapidly through the column (depleted peridotite) than more compatible elements; therefore, LREE abundances in the peridotite increase more rapidly than HREE abundances. During passage of an incompatible element rich melt through a depleted peridotite the N&S model generates a wide variety of REE patterns (Fig. 4-20). Such a process could explain the REE patterns in Hannuoba peridotites. However, the inverse correlation between the major element, CaO and Al_2O_3, and incompatible element abundances in the

peridotites (Fig. 4-19) was not considered in the N & S model. An important aspect of this model is that before the matrix reaches equilibrium with the ascending melt it develops a wide range of REE patterns which vary systematically as a function of depth (Fig. 4-21). Because we can not accurately infer the relative mantle location of individual spinel peridotite xenoliths, alpine peridotites are more appropriate for testing the relevance of this model; e.g., the zoned Horoman peridotite in Japan (Obata and Nagahara, 1987; Leinbach, 1987).

We propose a different model which we prefer for explaining the U-shaped REE patterns in Hannuoba peridotites. This model is a quantitative form of the two component mixing model proposed by Frey and Green (1974).

Peridotite melting in the upper mantle can be initiated by pressure decrease, or a zone of anomalously high temperature. In either case, a gradient in pressure or temperature exists from a partially melted region to a deeper unmelted region. Consequently, there will be a gradient in degree of melting. We postulate that there is a minimum degree of melting necessary for melt extraction, (e.g., permeability threshold of Maaloe, 1982). Therefore, near the relatively cool wall-rock boundaries, the degree of melting might be insufficient for melt segregation. However in the hotter interior, melts may ascend through a porous solid and eventually accumulate and migrate as dikes in fractures (Spera, 1987). When melt is extracted from the

hotter interior there is the possibility that incipient melts penetrate upwards from the deeper regions of the melting zone into the newly created residual peridotite. Penetration of the residue by incipient melts depends upon many factors including density and viscosity which will change during melt extraction. Important factors to consider are the degree of melting as a function of depth and the amount of the melt extracted from the upper residual peridotite zone. These two factors affect the density and viscosity contrast between the upper residual zone and melts from deeper region. As the degree of melting and the amount of melt extracted from the upper melting zone increase, the density and viscosity contrast increases, thereby facilitating compaction of the partially molten matrix of the deeper region. Consequently, melt formed by small degrees of melting becomes easier to expel upwards.

The essence of this model, migration of incipient melts highly enriched in incompatible elements into depleted peridotite, is an expected consequence of the melt extraction model discussed by McKenzie (1985), and O'Hara's (1985) evaluation of the geochemical effects of the "shape" of the partial melting regime. The geochemical models of Galer and O'Nions (1986) invoke such a process. Perhaps, similar to melting process in a spreading ridge environment, melting in the upper mantle beneath large continental faults leads to a melting regime where only a small region

experiences a large (>1%) degree of melting whereas much larger regions are melted to a very small degree.

The REE patterns of the peridotites depend on the degree of melting and mineralogy involved when the initial residue was formed and when the enriched melt was formed. If these processes occur in the spinel stability field, LREE enriched patterns are developed; U-shaped REE patterns require melting in the garnet stability field (Fig. 4-21). If melts generated by small degrees of melting (<1%), were extracted from large volumes of primitive mantle at a pressure corresponding to the garnet stability field, the melts would be strongly LREE enriched. Mixing of these melts with overlying residues could explain the relative LREE enrichment of the depleted peridotites (cf. Figs. 4-5 and 4-21).

We postulate that the residues from high degrees of melting had DMM isotopic characteristics; i.e., an isotopic signature similar to MORB. Mixing of these residues with incipient melts having higher $^{87}Sr/^{86}Sr$ and lower $^{143}Nd/^{144}Nd$ could explain the relatively higher $^{87}Sr/^{86}Sr$ and lower $^{143}Nd/^{144}Nd$ in the most depleted (high Mg number) peridotites (Fig. 4-15). However, the inverse correlation between the basaltic components (e.g., CaO and Al_2O_3) and incompatible element abundances, and the lower $^{87}Sr/^{8}6Sr$, higher $^{143}Nd/^{144}Nd$ in the lower Mg-number peridotites requires that the largest amounts of incipient melt

penetrated the most depleted peridotites. We propose two alternative explanations for this result:

(1) Incipient melts flowed more readily through olivine-rich, i.e., more depleted peridotites (Toramaru and Fujii, 1986);

(2) The harzburgites and lherzolites were physically separated in ascending mantle with the harzburgites formed by high degrees of melting overlying the less depleted lherzolites. In this case, incipient melts derived from the lherzolites will ascend and interact with the overlying harzburgites. Conceptually, this model is similar to that of Richter (1986, figures 3 and 8) who calculated the incompatible element content of melts as a function of time and position in a deforming matrix which has a decreasing melt fraction with increasing depth.

A similarity of the P & A model and the simple mixing model (Fig. 4-21) is that the peridotites are initially melted in the garnet stability field, and re-equilibrated in the spinel or plagioclase stability fields before incorporation by basaltic magma. Textural evidence for the earlier presence of garnet in the Hannuoba peridotites are spinel - orthopyroxene - clinopyroxene clusters. Similar clusters have been interpreted as forming during the transition from garnet to spinel peridotites (Smith, 1977; Nicolas, 1986; Nicolas et al, 1987).

We are uncertain how the clinopyroxenite veins in samples DM1-3, 1-5 and 1-7 relate to our proposed mixing

model. Certainly, at some point upwelling melts can be accumulated and continue ascent in fractures. The relative LREE enrichment of clinopyroxenes from veins in DM1-3 and DM1-7 (Fig. 4-4) are consistent with melts formed by small degrees of melting. Also, the clinopyroxenes from DM1-3 and DM1-5 have higher $^{87}Sr/^{86}Sr$ and lower $^{143}Nd/^{144}Nd$ than clinopyroxenes in the respective host rocks. However, the clinopyroxenites do not have major element compositions consistent with a genetic relationship to incipient melts; i.e., they have high Mg/Fe and hydrous minerals are absent. Perhaps these characteristics were eliminated by equilibration with the surrounding peridotite. The similarity of clinopyroxenes from the host and vein in sample DM1-7 may represent a totally equilibrated example.

4-8. SUMMARY OF CONCLUSIONS

Anhydrous Hannuoba spinel peridotites in basanites indicate the heterogeneous nature of the upper mantle beneath this part of eastern China. Specifically:

a) Hannuoba spinel peridotites are variable in major element composition ranging from relatively fertile to very depleted in basaltic components.

b) Hannuoba peridotites show a positive correlation between basaltic components (e.g., CaO and Al_2O_3) and HREE content, and poor correlation between basaltic components and LREE contents. Relative to chondrites three of the six

Hannuoba peridotites are relatively depleted in LREE; the others have slightly LREE enriched or U-shaped REE patterns.

c) Sr and Nd isotopic ratios in the six Hannuoba peridotites are variable. In terms of isotopically distinct mantle components (Zindler and Hart, 1986; Hart et al., 1986) these xenoliths range from "depleted" (DMM) to prevalent mantle (PREMA) to LoNd-like types. The more complicated REE patterns and isotopic signatures of the PREMA and LoNd xenoliths suggest that parts of the long term depleted mantle beneath Hannuoba area were enriched at different times, an ancient LREE enrichment event (about 1 Ga ago) with the strongst enrichment for the LoNd-like xenolith (DM1-7), and a recent enrichment event for PREMA xenoliths.

Possible models explaining the U-shaped REE pattern of Hannuoba peridotites are a "chromatographic column model" proposed by Navon and Stolper (1987), or the "simple mixing metasomatism model" proposed in this paper. The latter model is preferred for Hannuoba peridotites. We postulate an upper mantle that is vertically zoned in radiogenic isotopic ratios. As this zoned mantle experiences partial melting, the shallower mantle (but within the garnet stability field) with relatively low $^{87}Sr/^{86}Sr$ and high $^{143}Nd/^{144}Nd$ melts to a higher degree than the underlying enriched mantle which undergoes only incipient melting. As the degree of melting and melt segregation increase in the upper regions, increasing amounts of incipient melts are able to ascend and

interact with the overlying residual peridotites. This model can explain the range of REE patterns from LREE depleted to LREE enriched to U-shaped REE patterns. The inverse correlations of incompatible element abundances with CaO and Al_2O_3 contents plus the higher $^{87}Sr/^{86}Sr$, lower $^{143}Nd/^{144}Nd$ in xenoliths with the highest Mg/Fe require that incipient melts preferentially interacted with the most depleted peridotites. Subsequently, these enriched garnet peridotites re-equilibrated in the spinel stability field and were incorporated into the host basanite magma.

TABLE

Table 4-1. Modal proportions (vol%) of Hannuoba peridotites

	OL	OPX	CPX	SP	Opaque	Rock Group
DM1-2	62.3	30.3	6.6	0.8	tr	Sp-Lher
DM1-3	64.1	26.7	8.3	0.9	tr	Sp-Lher
DM1-4	59.4	29.4	9.8	1.4	tr	Sp-Lher
DM1-5	55.3	32.0	11.5	1.2	tr	Sp-Lher
DM1-7	77.4	17.1	4.8	0.7	tr	Sp-Harz
DM1-9	71.3	19.1	7.9	1.7	tr	Sp-Lher

Abbreviations: Lher = lherzolite Harz = harzburgite
OPX = orthopyroxene OL = olivine SP = spinel
CPX = clinopyroxene tr = trace

Table 4-2a. Major Element Abundances (volatile-free) of Hannuoba Group I peridotites

	DM1-4	DM1-9	DM1-5	DM1-2	DM1-3	DM1-7
SiO_2	44.75	43.46	45.41	44.81	45.40	44.06
TiO_2	0.06	0.06	0.09	0.07	0.05	0.02
Al_2O_3	2.68	2.27	2.71	1.91	1.70	1.27
Fe_2O_3	8.76	9.41	8.31	8.27	8.24	8.48
MnO	0.14	0.14	0.13	0.13	0.13	0.13
MgO	40.39	42.12	40.04	42.11	41.70	44.01
CaO	2.19	1.83	2.52	1.54	1.93	1.23
Na_2O	0.17	0.14	0.17	0.11	0.11	0.06
K_2O	0.005	0.008	0.007	0.007	0.003	0.004
P_2O_5	0.003	0.005	0.007	0.007	0.007	0.009
Cr_2O_3	0.50	0.47	0.39	0.38	0.44	0.35
NiO	0.27	0.31	0.28	0.29	0.30	0.31
Total	99.84	100.31	100.01	99.54	99.91	99.86
LOI	0.2	0.7	0.3	0.2	0.5	0.3
Mg #	90.13	89.86	90.52	90.98	90.93	91.14
CaO/Al_2O_3	0.82	0.81	0.93	0.81	1.14	0.97

1. Samples in tables are listed in order of increasing La/Yb ratios which approximately corresponds to increasing Mg #.

2. ME data obtained by X-ray fluorescence at U.Mass. Amherst in laboratory of J.M. Rhodes. Na_2O abundances analyzed by instrumental neutron activation analysis at MIT. Relative deviations of duplicate analyses are: SiO_2:0-0.4%, TiO_2:0-16%, Al_2O_3:0-1.7%, Fe_2O_3:0-0.9%, MnO:0.4-1.2%, MgO:0.1-0.5%, CaO:0-1.0%, K_2O:8.4-29.8%, P_2O_5:1.7-21.0%.

3. LOI=loss on ignition, analyzed in J. Dostal's laboratory at St. Marys University, Halifax, Canada.

4. Mg#=Mg/(Mg+Fe). All Fe as Fe^{+2}.

Table 4-2b. Comparison of Major Element Analyses of Hannuoba Group I peridotites

	Analyses I				Analyses II			
	H-1	H-2	H-3	H-6	H-1	H-2	H-3	H-6
SiO_2	43.38	43.57	43.33	44.56	43.02	44.51	44.66	44.82
TiO_2	tr	0.29	0.19	0.19	0.04	0.12	0.04	0.04
Al_2O_3	2.52	2.74	2.06	1.55	2.24	3.64	2.64	1.97
Fe_2O_3	3.98	2.72	1.74	4.42	9.36	9.94	10.12	9.85
FeO	10.39	7.74	8.12	8.19				
MnO	0.16	0.16	0.16	0.15	0.14	0.15	0.15	0.14
MgO	35.08	36.49	38.86	36.28	42.76	37.97	39.91	41.60
CaO	3.51	2.94	2.35	1.32	1.64	2.93	1.92	1.17
Na_2O	0.29	0.75	1.20	0.70	0.22	0.30	0.15	0.14
K_2O	0.05	0.02	0.10	0.02	0.02	0.02	0.01	0.02
P_2O_5					0.01	0.01	0.01	0.01
Cr_2O_3	-	0.38	0.20	0.26				
H_2O^{+3}	tr	1.12	1.18	1.16				
H_2O^-	-	0.35	0.19	0.42				
Total	99.36	98.89	99.48	99.01	99.45	99.59	99.61	99.76
Mg #	85.8	88.9	89.5	88.8	90.05	88.33	88.65	89.32

Analyses I-- Data analyzed by wet chemical analyses in chemical labratory of Institute of Geology, Academia Sinica (Cong and Zhang, 1982).

Analyses II-- Data analyzed by X-ray fluoraescence at Univ. of Mass. Amherst in labratory of J.M. Rhodes.

Table 4-2c. Major Element Abundances of Average Group I Peridotites Worldwide

	Total Average Group IA	Group IB
SiO_2	44.34 ± 1.03	43.74 ± 0.82
TiO_2	0.10 ± 0.04	0.07 ± 0.06
Al_2O_3	3.19 ± 0.73	1.99 ± 0.82
FeO*	8.46 ± 1.14	8.69 ± 1.56
MnO	0.13 ± 0.01	0.14 ± 0.03
MgO	39.94 ± 2.05	42.43 ± 2.55
CaO	2.81 ± 0.62	1.80 ± 0.92
Na_2O	0.24 ± 0.07	0.21 ± 0.11
K_2O	0.02 ± 0.01	0.05 ± 0.05
Cr_2O_3	0.43 ± 0.06	0.38 ± 0.11
NiO		
Tatol	99.66	99.45
Mg #	89.4	89.7

Average Group IA data based on 31 peridotites, and Average Group IB data based on 20 peridotites (P. D. Kempton, 1987).

Table 4-3a. Chemical Analyses of Olivines

	DM1-4	DM1-9	DM1-5H	DM1-5V	DM1-2	DM1-3H	DM1-3V	DM1-7H	DM1-7V
SiO_2	40.65	40.48	40.87	40.83	40.37	40.89	41.19	41.65	40.37
TiO_2	0	0	0.03	0.02	0.01	0.01	0.03	0	0
Al_2O_3	0	0.04	0.04	0.04	0.01	0	0.05	0.04	0
Cr_2O_3	0.04	0.04	0.03	0	0.02	0.01	0.03	0.02	0
FeO	9.68	9.38	8.66	9.26	8.94	9.45	8.55	8.28	8.60
MnO	0.16	0.09	0.10	0.12	0.18	0.14	0.11	0.10	0
MgO	48.73	49.02	49.87	49.27	50.03	48.92	49.47	48.84	50.95
CaO	0.05	0.05	0.09	0.05	0.04	0.04	0.06	0.09	0.09
NiO	0.30	0.37	0.32	0.37	-	0.33	0.39	0.25	0.3
Total	99.61	99.47	100.02	99.96	99.63	99.80	99.90	99.27	100.32
Fo	89.9	90.2	91.1	90.5	91.0	90.2	91.1	91.3	91.3

Table 4-3b. Chemical Analyses of Orthopyroxene

	DM1-4	DM1-9	DM1-5H	DM1-5V	DM1-2	DM1-3H	DM1-3V	DM1-7H	DM1-7v
SiO_2	55.39	55.62	56.13	55.83	55.83	55.55	55.38	56.34	55.94
TiO_2	0.07	0	0.06	0.08	0.06	0.09	0.02	0.05	0.07
Al_2O_3	4.07	4.07	3.46	3.31	3.68	3.56	3.62	3.57	3.42
Cr_2O_3	0.46	0.52	0.25	0.34	0.42	0.40	0.60	0.56	0.53
FeO	6.09	5.91	6.01	5.65	5.56	5.84	5.45	4.93	5.20
MnO	0.12	0.16	0.04	0.13	0.14	0.13	0.14	0.14	0.10
MgO	33.64	33.31	34.20	34.33	34.12	34.12	33.71	33.22	34.22
Cao	0.74	0.76	0.45	0.45	0.63	0.51	0.88	0.79	0.88
Na_2O	0.10	0.09	0.07	0.03	0.06	0.04	0.08	0.10	0.08
Total	100.68	100.44	100.67	100.15	100.50	100.24	99.89	99.70	100.49
Mg#	90.7	90.8	91.1	91.5	91.6	91.1	91.6	92.3	92.2
T^oC	962	947	1009	961	970	914	980	1033	1083

1. H=Host Peridotite V=Vein
2. Temperature based on geothermometer by Wells (1977).

Table 4-3c. Chemical Analyses of Clinopyroxene

	DM1-4	DM1-9	DM1-5H	DM1-5V	DM1-2	DM1-3H	DM1-3V	DM1-7H	DM1-7V
SiO_2	52.36	51.68	52.66	52.25	53.97	52.55	52.73	52.56	52.78
TiO_2	0.30	0.36	0.12	0.39	0.39	0.34	0.03	0.14	0.14
Al_2O_3	5.53	5.60	4.71	5.25	4.98	5.09	3.96	4.15	4.34
Cr_2O_3	0.93	1.04	1.03	0.91	1.01	1.08	1.01	1.05	1.13
FeO	2.69	2.70	2.46	2.23	2.29	2.20	2.53	2.48	2.38
MnO	0.09	0.04	0.08	0.08	0.14	0.09	0.03	0.05	0.03
MgO	16.08	15.94	17.19	15.77	15.98	15.99	17.22	17.35	17.34
Cao	20.51	20.40	21.15	20.21	21.02	21.34	21.41	20.82	19.86
Na_2O	1.48	1.58	0.91	1.51	1.33	1.34	0.98	0.92	0.94
Total	99.97	99.34	100.31	98.60	101.22	99.86	99.90	99.51	98.97
Mg#	91.4	91.3	92.5	92.6	92.6	92.7	92.4	92.6	92.7

Table 4-3d. Chemical Analyses of Spinel

	DM1-4	DM1-9	DM1-5H	DM1-5V	DM1-2	DM1-3H	DM1-3V	DM1-7H	DM1-7V
SiO_2	0.11	0.06	0.11	0.04	0.02	0.07	0.07	0	0.06
TiO_2	0.13	0.17	0.13	0.09	0.13	0.13	0.05	0.10	0.13
Al_2O_3	52.28	51.96	45.19	54.20	50.09	49.75	44.87	45.19	45.25
Cr_2O_3	16.29	16.35	24.89	14.40	19.02	19.16	23.24	24.67	24.87
FeO*	11.30	11.36	11.09	10.72	10.96	11.04	12.13	10.80	11.26
MnO	0.12	0.13	0.12	0.08	0.37	0.12	0.12	0	0.13
MgO	19.95	19.84	19.56	19.96	20.25	19.44	18.97	18.53	19.28
CaO	0	0	0	0	0.01	0	0.01	0.01	0
NiO	0.25	0.17	0.29	0.21	0.25	0.24	0.17	0.23	0.20
Total	100.25	100.10	101.38	99.70	100.89	99.83	99.63	99.53	101.18
FeO	10.00	9.98	9.77	9.99	9.08	10.18	9.98	10.70	10.09
Fe_2O_3	1.44	1.53	1.46	0.81	2.08	0.95	2.39	0.11	1.30
Al_2O_3/Cr_2O_3	3.21	3.18	1.82	3.76	2.63	2.60	1.93	1.83	1.82

1. H=Host Peridotite V=Vein
2. Fe_2O_3 was calculated assuming spinel stoichiometry.

Table 4-4. Petrography

Sample	Grain size	Texture
DM1-2	OL: most > 3mm, and can be up to 8mm Px and Sp: most < 2mm, with some Opx up to 4mm	The weak bimodal grain size distribution shows a transitional texture between coarse and porphyroclastic.
DM1-3 and DM1-5	OL and Opx: most > 2mm, and can be up to 6mm Cpx: most 2-3mm Sp: most 1-2mm, down to 0.5mm	Coarse-equant texture: curvilinear grain boundaries with a few minerals showing straight boundaries. The Opx, Cpx, and Sp are often connected to form Opx-Cpx-Sp aggregates.
DM1-4	OL and Opx: most 1-3mm with some Ol up to 4mm Cpx and Sp: most < 1mm	OL and Px are very slightly elongated to form very weak foliation. Px and Sp neoblasts are around large OL aggregates forming a tabular mosaic-porphyroclastic texture.
DM1-9	Grain sizes are slightly smaller than DM1-4. most OL and pyroxenes are about 2 X 1mm. a few OL: 2 x 4mm to 6mm most elongated Sp with length<2mm, and rounded Sp < 1mm. one large Sp grain: 7 x 7 mm.	Minerals are elongated to form weak foliation. Large OL are strongly kinked. Tabular mosaic-porphyroclastic texture.
DM1-7	OL and Px: most > 2mm Sp: most < 2mm	Ol and Px are slightly elongated to form a coarse-tabular texture.

Table 4-5. Trace Element Abundances in Hannuoba Peridotites

ppm	DM1-4	DM1-9	DM1-5	DM1-2	DM1-3	DM1-7
Sc	13.4	10.3	12.2	9.7	11.0	9.2
V	58.3	48.0	59.1	42.8	44.0	32.3
Cr	3400	3259	2647	2572	3055	2377
Co	115	121	109	110	109	114
Ni	2146	2457	2223	2284	2333	2452
Zn	55.3	59.4	52.4	58.4	51.0	54.4
Ga	3.2	3.5	2.9	3.1	2.8	2.1
Rb	0.2	0.4	0.1	0.4	0.1	0.4
Y	1.7	1.5	2.2	1.1	1.2	0.5
Zr	2.4	2.8	4.0	3.7	1.8	2.6
Nb	0.1	0.2	0.8	0.6	0.5	1.2

1. Sc, Cr and Co abundances by instrumental neutron activation analysis at MIT, according to the methods described by Ila and Frey (1984).

2. other TE abundances by XRF at U. Mass. Amherst. The relative deviations of most trace elements are less than 10%, except that of Ga and Nb (up to 30% for Ga and up to 87% for Nb).

Table 4-6a. Rare-Earth Element Abundances in Hannuoba Peridotites (ppm)

	DM1-4	DM1-9	DM1-5	DM1-2	DM1-3	DM1-7	Pre(%)
La	0.082 ±.007	0.116 ±.002	0.239 ±.003	0.290 ±.008	0.505 ±.007	0.400 ±.008	10
Ce	-	0.319 ±.14	0.717 ±.11	0.475 ±.075	0.876 ±.12	0.954 ±.14	14
Nd	0.224 ±.080	0.287 ±.087	0.587 ±.084	0.350 ±.087	0.523 ±.100	0.523 ±.110	6
Sm	0.105 ±.003	0.116 ±.003	0.210 ±.003	0.117 ±.002	0.124 ±.002	0.100 ±.004	8
Eu	0.048 ±.002	0.052 ±.002	0.083 ±.002	-	0.046 ±.002	0.035 ±.008	11
Tb	0.037 ±.002	0.030 ±.004	0.052 ±.001	-	0.021 ±.003	0.009 ±.003	13
Yb	0.207 ±.009	0.176 ±.021	0.250 ±.003	0.169 ±.002	0.130 ±.003	0.081 ±.003	7
Lu	0.045 ±.008	0.038 ±.001	0.043 ±.004	0.033 ±.001	0.027 ±.001	0.020 ±.001	9
Nd*(%)	3.9	0.0	3.9	2.3	4.1	3.3	
Sm*(%)	2.3	0.4	2.3	2.2	3.5	0.5	

1) Data were d etermined by radiochemical neutron activation (RNAA) procedure described by Hickey and Frey (1981) at MIT in laboratory of F.A. Frey. Errors based on counting statistics.

2) Pre = Relative precision based on mean and standard deviation from five repeat analyses of Horoman peridotite 62210 which were analyzed during the same RNAA procedures as the Hannuoba peridotites.

3) *: Relative deviation of Nd and Sm abundances determined by RNAA and isotope dilution (ID) (see Table 4-8).

Table 4-6b Rare-Earth Element Abundances in Hannuoba Peridotites (ppm)

	DM1-2	**(%)	DM1-7	**(%)
La	0.228	(12.0)	0.359	(5.4)
Ce	0.479	(0.4)	0.799	(8.8)
Nd	0.342	(1.2)	0.453	(7.2)
Sm	0.113	(1.7)	0.096	(2.0)
Eu	0.044	-	0.031	(6.1)
Gd	0.160		0.100	
Dy	0.170		-	
Er	0.116		0.057	
Yb	0.117	(18.1)	0.067	(9.5)

1) Data obtained by isotope dilution by D.C. Gerlach at Leeds University, U.K.

2) **: Relative deviation of REE abundances determined by RNAA and isotope delution.

Table 4-7. Rare Earth Element Abundance in Clinopyroxene (ppm)

	DM1-4	DM1-9	DM1-5H	DM1-5V	DM1-2	DM1-3H	DM1-3V	DM1-7H	DM1-7V
La	0.44 (7)	0.56 (5)	2.00 (4)	2.07 (6)	0.81 (6)	2.02 (3)	10.11 (6)	6.61 (3)	6.26 (4)
Ce	1.32 (4)	1.66 (5)	5.05 (2)	6.86 (7)	2.07 (6)	2.84 (3)	13.68 (6)	12.23 (2)	11.75 (2)
Pr	0.27 (8)	0.39 (1)	0.96 (5)	1.22 (9)	0.47 (4)	0.50 (6)	1.48 (6)	1.92 (3)	1.95 (7)
Nd	2.18 (6)	2.69 (8)	5.42 (4)	7.36 (4)	3.62 (4)	2.91 (5)	6.52 (6)	9.69 (3)	9.56 (8)
Sm	0.98 (6)	1.37 (8)	2.35 (3)	3.03 (9)	1.49 (6)	1.18 (4)	1.19 (11)	2.19 (6)	2.10 (4)
Eu	0.42 (7)	0.64 (5)	1.03 (3)	1.10 (5)	0.65 (3)	0.47 (4)	0.45 (2)	0.69 (3)	0.73 (4)
Dy	1.99 (6)	2.57 (4)	3.74 (1)	2.69(10)	2.29(12)	1.84 (3)	1.70 (5)	1.36 (2)	1.15 (4)
Er	1.39 (7)	1.68 (3)	2.44 (1)	1.59 (8)	1.60 (7)	1.17 (6)	1.40 (4)	1.02 (5)	0.96 (7)
Sm*	0.5%	6.6%	10.6%	11.0 %	8.4%	4.4%	4.8%	5.5%	3.7%

1. Data were analyzed with the ion microprobe in N. Shimizu's labratory at MIT by D. Hickmott.

2. Data in parentheses are percent of mean deviation based on counting statistics.

3. Nd data were obtained by isotope dilution (ID). Nd is the most intense REE peak. The Nd/Si ion probe measured intensity versus Nd concentration measured by ID was used as a working curve. The other REE were normalized to Nd.

4. Sm*: Relative deviation (R.D) of Sm abundances in Cpx based on ion probe and ID (Table 8) methods. The high R.D in some samples may due to inhomogeneous Sm concentrations among different Cpx grains, probe data were collected on single grains. However, (Sm/Nd) ratios obtained by ion probe and ID are similar.

Table 4-8. Isotope Ratios and Trace Element Concentrations (ppm) for Hannuoba Group I peridotites

	$^{87}Sr/^{86}Sr$	$^{143}Nd/^{144}Nd$	Rb	Sr	Sm	Nd	Sm/Nd	Sr/Nd
CPX (Discrete xenolith)								
DM1-4	0.702215±25	0.513585±13	<0.002	47.2	0.99	2.18	0.454	21.7
DM1-9	0.702156±26	0.513483±20	<0.008	52.0	1.20	2.70	0.444	19.2
DM1-2	0.703768±23	0.512944±44	-	45.3	1.26	3.62	0.348	12.5
CPX (Composite xenolith)								
DM1-5 (host)	0.703133±29	0.513072±17	<0.002	68.3	1.90	5.42	0.351	12.6
DM1-5 (vein)	0.703229±24	0.513017±15	<0.006	77.9	2.42	7.36	0.329	10.6
DM1-3 (host)	0.703724±36	0.513004±17	<0.002	60.3	1.08	2.91	0.371	20.7
DM1-3 (vein)	0.703864±36	0.512902±20	<0.003	177.3	1.08	6.52	0.166	27.2
DM1-7 (host)	0.704300±21	0.512491±24	<0.008	159.7	1.96	9.69	0.202	16.5
DM1-7 (vein)	0.704340±27	0.512515±46	<0.008	156.6	1.95	9.56	0.204	16.4
Bulk Host Peridotite								
DM1-4	0.702609±25	0.513495±18	0.286	5.74	0.110	0.242	0.450	23.7
DM1-9	0.702684±25	0.513363±77	0.409	5.25	0.115	0.287	0.401	18.3
DM1-5	0.703583±27	0.512960±93	0.265	9.60	0.22	0.635	0.346	14.2
DM1-2	0.703965±33	0.513023±38	0.251	4.75	0.112	0.334	0.335	15.1
DM1-3	0.703801±21	0.512991±17	0.101	7.22	0.133	0.482	0.276	15.0
DM1-7	0.704217±29	0.512538±20	0.204	19.35	0.101	0.490	0.206	39.5

(continued)

	$^{87}Sr/^{86}Sr$	$^{143}Nd/^{144}Nd$	Rb	Sr	Sm	Nd	Sm/Nd	Sr/Nd
2.5N HCl Leachate of CPX from Host Peridotite								
DM1-3	0.704332±22	0.51282±18	3.68	55.9	1.03	7.05	0.146	7.9
DM1-7	0.704223±23	0.512562±87	0.005	49.2	-	0.69	-	71.3
GROUP II Xenolith								
DM2-2 (Websterite)								
Cpx	0.711872±25	0.51152±14						
Whole Rock	0.711242±29	0.51149±14						
HCl Leachate	0.703841±24	-						
TGZ (Garnet pyroxinite)								
Cpx	0.702658±24	0.51320±43	0.004	45.3	1.40	3.30	0.424	13.7
Garnet	-	0.51334±19				0.29		

1. host = Host Peridotite. vein = Pyroxenite Vein

2. The chemical and mass spectrometric techniques used to determine the isotopic composition of Sr and Nd, and the concentrations of Sr, Nd, Sm, and Rb were described by Hart and Brooks (1977), Zindler et al (1979). The $^{87}Sr/^{86}Sr$ values are relative to 0.70800 for E & A standard and are normalized to $^{86}Sr/^{88}Sr=0.11940$. The $^{143}Nd/^{144}Nd$ values are corrected relative to $^{143}Nd/^{144}Nd=0.512640$ for BCR-1 and are normalized to $^{146}Nd/^{144}Nd=0.721900$.

3. The concentrations (ppm) obtained by isotope dilution (ID) have estimated precisions of less than 0.5%. Contributions from blanks are negligible. The large uncertainties for the ID data of acid leachates are mainly due to the very small amounts of mass leached out and difficulties in weighing and spiking, especially for Rb/Sr system.

Table 4-9. Model Age Calculation

	$^{143}Nd/^{144}Nd$	$^{147}Sm/^{144}Nd$	$^{87}Sr/^{86}Sr$	$^{87}Rb/^{86}Sr$	Model Age (10x9 yr) Sm/Nd	Rb/Sr
DM1-4	0.513585	0.273	0.702215	0.000115	1.93	1.99
DM1-9	0.513483	0.270	0.702156	0.00319	1.79	2.11
DM1-5	0.513072	0.212	0.703133	0.00009	4.38	1.28
DM1-2	0.512944	0.210	0.703768	-	3.66	-
DM1-3	0.513004	0.224	0.703724	0.000103	2.0	0.82
DM1-7	0.512491	0.123	0.743000	0.000133	0.27	0.37

1. Sm-Nd ages calculated using $\lambda_{Sm}=6.54X10^{-12}$, present-day bulk earth: $^{147}Sm/^{144}Nd = 0.1967$ and $^{143}Nd/^{144}Nd = 0.51262$.

2. Rb-Sr ages calculated using $\lambda_{Rb}=1.42X10^{-11}$, present-day bulk earth: $^{87}Rb/^{86}Sr=0.089$ and $^{87}Sr/^{86}Sr=0.7046$.

Table 4-10. Major and Trace Element Abundances (volatile-free) of Hannuoba Group II Xenoliths

	DM2-2	D1-Z1	B-D-10	D10-10	T-G-Z	D2-51
SiO_2	47.29	50.06	50.65	45.02	49.18	53.81
TiO_2	0.55	0.46	0.33	0.88	0.48	0.81
Al_2O_3	11.17	10.29	6.76	13.68	11.81	18.44
Fe_2O_3	4.21	6.44	7.42	5.61	7.09	7.85
MnO	0.06	0.15	0.15	0.06	0.18	0.11
MgO	14.91	20.30	19.51	14.53	18.34	5.39
CaO	20.99	10.79	14.22	18.48	11.67	8.36
Na_2O	0.75	0.94	0.58	0.54	1.21	3.69
K_2O	0.02	0.34	0.02	1.22	0.14	1.56
P_2O_5	0.019	0.03	0.011	0.007	0.019	0.135
Cr_2O_3	0.002	0.222	0.367	0.004	0.131	0.012
NiO	-	0.119	0.126	0.006	0.036	0.006
Tatol	99.95	100.14	100.01	100.03	100.28	100.16
Mg #	88.62	87.41	85.27	85.08	85.07	60.18
Rb	10	16	5	56	14	20
Sr	128	184.4	48.8	126	109.2	1272.6
Ba	20.4	13.6	4.7	945.6	19.7	848
Sc	8.22	42.4	38.8	9.23	43.2	19.2
V	54.54	214.5	232	79.7	284	150.3
Cr	11.40	29	896	1520	2514	83
Co	10.49	47.2	61.4	0.4	42.7	28.1
Ni	23.7	935.8	988.4	46.2	605.1	48.8
Zn	106.2	48.8	49.2	123.5	30.2	75.9
Zr	207.6	31.9	10.9	415.7	29.3	49.5
Nb	2.9	3	1.5	10.1	1	2.2
Hf	5.6	0.61	0.29	7.9	0.77	0.878
Ta	0.383	0.15	0.09	0.4	0.08	0.139
Th	0.59	-	-	0.46	-	0.18
La	10.15	1.6	0.836	8	0.658	9.15
Ce	28.64	4.8	2.69	23.53	2.3	19.65
Nd	20.08	3.76	3.03	14.9	2.41	8.98
Sm	3.62	1.296	0.881	3.39	1.08	1.96
Eu	0.89	0.54	0.324	0.85	0.49	1.37
Tb	0.375	0.43	0.159	0.35	0.35	0.26
Yb	0.99	2.52	0.607	0.88	2.27	0.67
Lu	0.15	0.403	0.1	0.136	0.358	0.106

ME and TE data analyzed by X-ray fluorescence at Univ. of Mass. Amherst, except Sc, Cr, Co,Ba and REE abundances analyzed by INAA at MIT.

FIGURES

FIGURE CAPTIONS

Figure 4-1 Variation diagrams of MgO versus CaO, Al2O3, Na2O, TiO2, FeO and SiO2 in Hannuoba peridotites. Total oxides are normalized to 100% anhydrous with all Fe as FeO. For comparison, Ronda peridotite data (Frey et al., 1985) are plotted on the figure of MgO vs. CaO. In other panels the Ronda data (except two low MgO samples) are shown as a field. Cong and Zhang (1983) studied four different Hannuoba peridotite xenoliths. Our analyses of powder aliquots supplied by Cong lie along the same trends, except for FeO which may have been added during sample preparation in China.

PMC are estimates of primitive mantle compositions based on peridotites from Ronda (Frey et al., 1985), Horoman (Leinbach,1987), Victoria (Nickel and Green, 1984), Tariat (Preß et al., 1986) and the bulk silicate mantle composition (Table 4-2 G, Zindler and Hart, 1986).

Figure 4-2 MgO abundances versus Ni, Cr, Sc, V, Ga and Y contents in six Hannuoba peridotites. Field encloses Ronda data as in Figure 4-2.

Figure 4-3 MgO and CaO abundances versus Sr and La contents in six Hannuoba peridotites. Numbers are sample numbers without "DM1-" prefix. Field encloses Ronda data as in Figure 4-1.

Figure 4-4 Chondrite-normalized REE (Evensen et al., 1978) diagrams for a) bulk peridotites, b) clinopyroxenes and host peridotites. CPX-H = clinopyroxene from host peridotites ; CPX-V = clinopyroxene from vein; BR = host bulk peridotites.

Figure 4-5 $^{143}Nd/^{144}Nd$ versus $^{87}Sr/^{86}Sr$ for clinopyroxenes from six Hannuoba peridotites. Diamonds designate cpx from host peridotite; triangles designate cpx from clinopyroxene-rich vein. Numbers in Figure 4-6 and 7 are sample numbers without DM1- prefix. Solid diamond represents clinopyroxene from a Group II garnet-pyroxenite TGZ. Unlabeled field with diagonal lines encloses the range of 14 Hannuoba alkali basalts (Chapter 3). Lines at 0.7047 and 0.51262 are bulk earth estimates. Field for oceanic basalts based on data in White and Hofmann (1982); Zindler et al (1984); Hart et al (1986), and Frey and Roden (1987).

Figure 4-6 Comparison diagrams of MgO versus CaO, Al_2O_3, Na_2O, TiO_2, FeO and SiO_2 in Hannuoba GroupI and Group II xenoliths. Total oxides are normalized to 100% anhydrous with all Fe as FeO.

Figure 4-7 Comparison diagrams of MgO abundances versus Ni, Cr, Sc, and Co contents in Hannuoba Group I and Group II inclusions.

Figure 4-8 Chondrite-normalized REE (Evensen et al., 1978) diagrams for Group II inclusions.

Figure 4-9 Variation diagram of whole rock Mg# versus mineral Mg#.

Figure 4-10 Variation diagram of Na_2O/CaO cpx versus Na_2O/CaO whole rock.

Figure 4-11 Variation diagram of LnK versus $1/TC^O$ for clinoperoxenes from host peridotites and veins. +: calculation based on geothermometer by Wells (1977), square: calculation based on geothermometer by Wood and Banno (1973). $Lnk = a^{cxp}/a^{opx}$.

Figure 4-12 Al_2O_3 contents of coexisting orthopyroxenes and spinels in Hannuoba peridotites. The enclosed fields of abyssal peridotites (I) and alpine type peridotites (II) are from Dick and Fisher (Figure 7, 1984).

Figure 4-13 Variation diagram of Sr/Nd versus $^{87}Sr/^{86}Sr$ in Clinopyroxenes and Hannuoba basalts.

Figure 4-14 Variation diagram of Rb/Sr versus $^{87}Sr/^{86}Sr$ in bulk peridotites.

Figure 4-15 $^{143}Nd/^{144}Nd$ and $^{87}Sr/^{86}Sr$ of clinopyroxene versus (Mg/(Mg+Fe)) of bulk peridotites. Error bar is smaller than data points.

Figure 4-16 Variation diagram of Rb/Sr versus Mg # in bulk peridotites.

Figure 4-17 Variation diagram of La versus Sr in clinopyroxene.

Figure 4-18 $^{143}Nd/^{144}Nd$ versus $^{147}Sm/^{144}Nd$ in clinopyroxenes (cpx) from host peridotites, cpx from clinopyroxene veins and an acid leachate from cpx in host DM1-3. A one b.y. reference isochron is drawn through the samples. Error bar is smaller than data points.

Figure 4-19 Correlation of whole-rock CaO in anhydrous peridotite xenoliths with chondrite-normalized Yb abundances and La/Yb ratios. The positive Yb - CaO correlation for Hannuoba samples (squares) is typical of spinel peridotite xenoliths as shown by the field. A similar correlation between LREE and CaO is absent. In fact there is a broad inverse trend between La/Yb and CaO (see also Kempton, 1987; Nielson and Noller, 1987). The X indicates sample 5 from

Sardinia (Dupuy et al., 1987) and it is atypical in having high CaO and La/Yb. The fields enclose data for 120 anhydrous peridotites from diverse locations. Data sources: Bonatti et al., 1986; BVSP, 1981; Chen et al., 1988; Dautria and Girod 1987; Dupuy et al., 1986, 1987; Frey and Green, 1974; Jagoutz et al., 1979; Kurat et al., 1980; Morten, 1987; Ottonello, 1980; Ottonello et al., 1984; Roden et al., 1988; Stosch and Seck, 1980; Stosch et al., 1986.

Figure 4-20 Evolution of REE abundance patterns in a 1km section of porous mantle using the chromatographic column model proposed by Navon and Stolper (1987). Ascending melt composition is that produced by 0.1% batch melting of a source with two times chondritic abundance contaning 5% garnet, 10% Cpx, 20% Opx, and 65% Ol. The melt is composed of 40% garnet, 40% Cpx, and 20% Opx. Column matrix composition is that of a residue after 13% non-modal batch melting of the same source, and is composed of 6% Cpx, 20% Opx, 74% Ol, similar to Hannuoba xenolith DM1-7.

The calculation was done with a computer program provided by Navon. The parameters used in this calculation are (from Navon and Stolper, 1987):

a = 0.5cm (radius of grains in the column matrix)
Ds = 10^{-14}cm^2/Sec (diffusivities in the solid)
ϕ = 0.01 (volume fluid fraction in the column)
Vf = 3.2cm/yr (melt velocity relative to the column)
Kd = Cs/Cf The partition coefficient Set 1 of Frey et al (1978) was used.
L = column length (the total column length is 1 km in this calculation, and 0 is the top of the column)
Cs = REE concentration in the solid matrix
Co = REE concentration in the source = 2 x chondrite
tc = L/Vf (time it takes for the fluid to pass through the Column)

In panel (a), t = 0.5t_c, the ascending melt has modified the REE pattern of the matrix at depths from L = 1000 to 350 m. The varying REE patterns with column height (e.g., L = 1000m, 750m and 500m as indicated) result because the highly incompatible LREE ascend more rapidly than HREE. From 350m to the top of the matrix the REE pattern equals that of the initial matrix (labelled "Original Residue") because the melt has not yet ascended to these levels.

At later times when t equals or is greater than t_c (panels b, c, and d), all of the matrix has reacted with the ascending melt. Eventually, the ascending melt converts the column matrix into an equilibrium composition. Note, that the lower parts of the column equilibrate with the input melt before the upper parts of the column. In panel d the entire matrix is very similar to that in equilibrium with the 0.1% batch melt entering the bottom of the column.

Figure 4-21 Mixing models, residue plus partial melt, proposed to explain U-shaped REE patterns. Melt composition is produced by 1% fractional melting of a primitive mantle source (REE = 2 X chondrites) with 5% garnet, 10% cpx, 20% opx, and 65% ol. Residue composition is formed by varying degrees (1 to 13%, see legend) of nonmodal fractional melting of the same source, and removing a melt composed of 40% garnet, 40% cpx, and 20% opx. The partition coefficients in panels a and b are from Prinzhofer and Allegre (1985), and in panels c and d are set 1 of Frey et al (1978). Batch nonmodal melting can generate similar REE patterns but the U-shape would not be as well developed.

a) and c): Lines represent the sum of adding 1 % mass of melt formed by 1 % melting to 99% mass of residues formed by degrees of melting varying from 3 to 13%. Several mixtures have U-shaped REE patterns but all have LREE contents less than the assumed primitive source.

b) and d): Lines represent the sum of adding 3% (mass) melt formed by 1% melting to 97% (mass) residue formed by degrees of melting varying from 3 to 13%. U-shaped REE patterns occur in all mixtures and LREE contents exceed those in the assumed source.

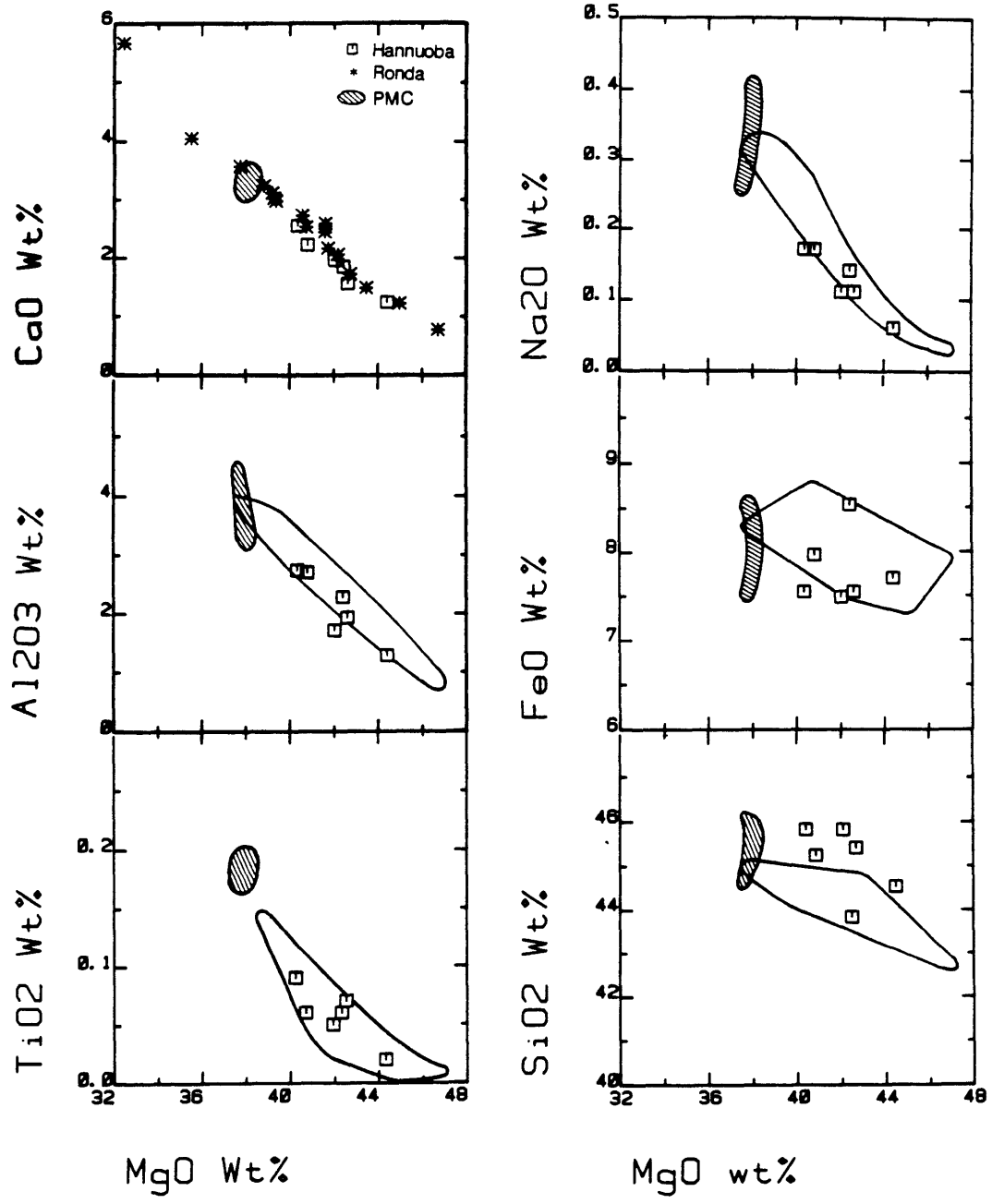
Hannuoba
Ronda
PMC
CaO Wt%
Al2O3 Wt%
TiO2 Wt%
MgO Wt%
Na2O Wt%
FeO Wt%
SiO2 Wt%
MgO wt%

FIGURE 4-1

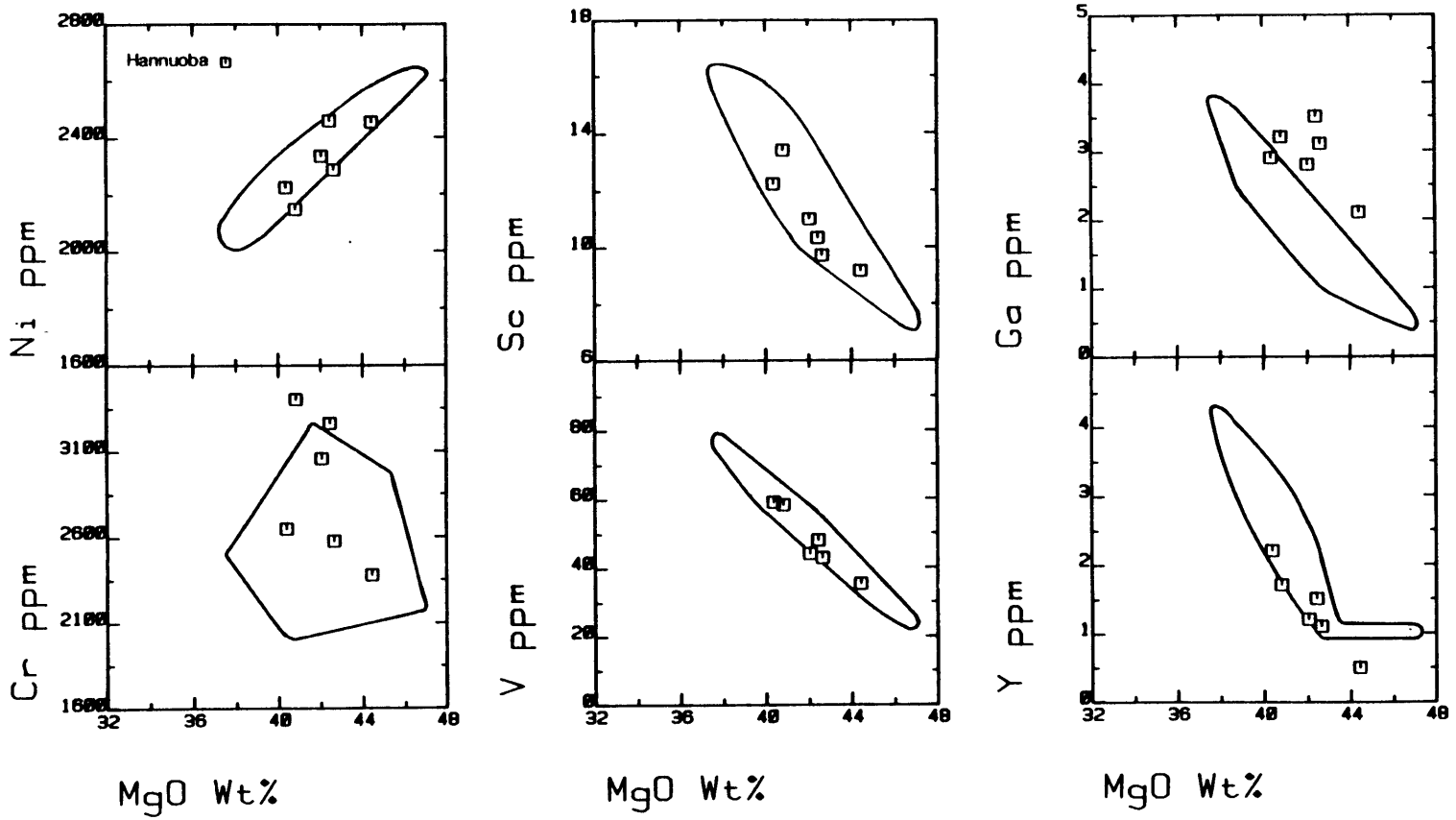
Hannuoba
Ni ppm
Cr ppm
Sc ppm
V ppm
Ga ppm
Y ppm
MgO Wt%
MgO Wt%
MgO Wt%

FIGURE 4-2

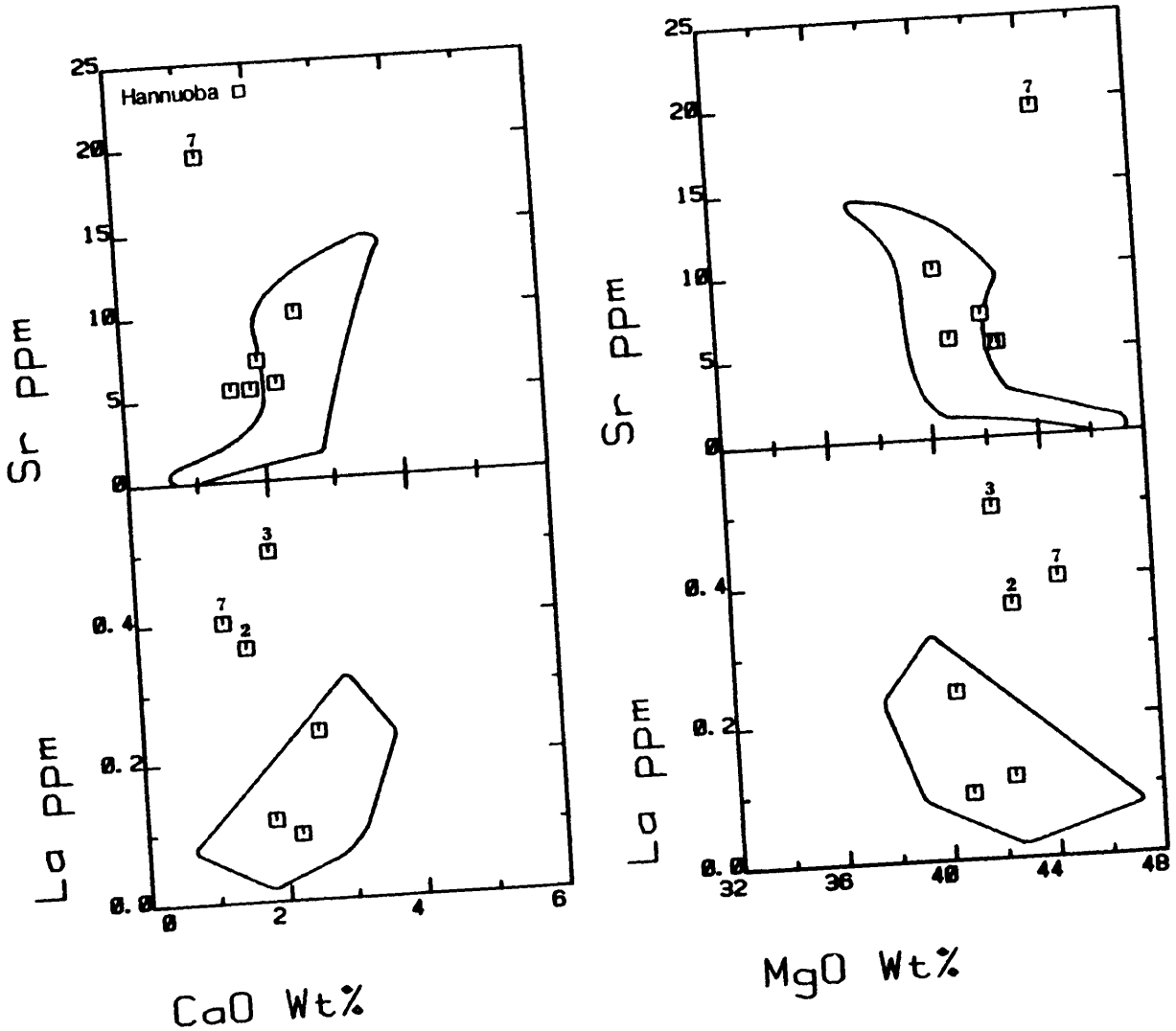
Hannuoba
Sr PPM
La PPM
CaO Wt%
MgO Wt%
25
20
15
10
5
0
0.4
0.2
0.0
2
4
6
32
36
40
44
48

FIGURE 4-3

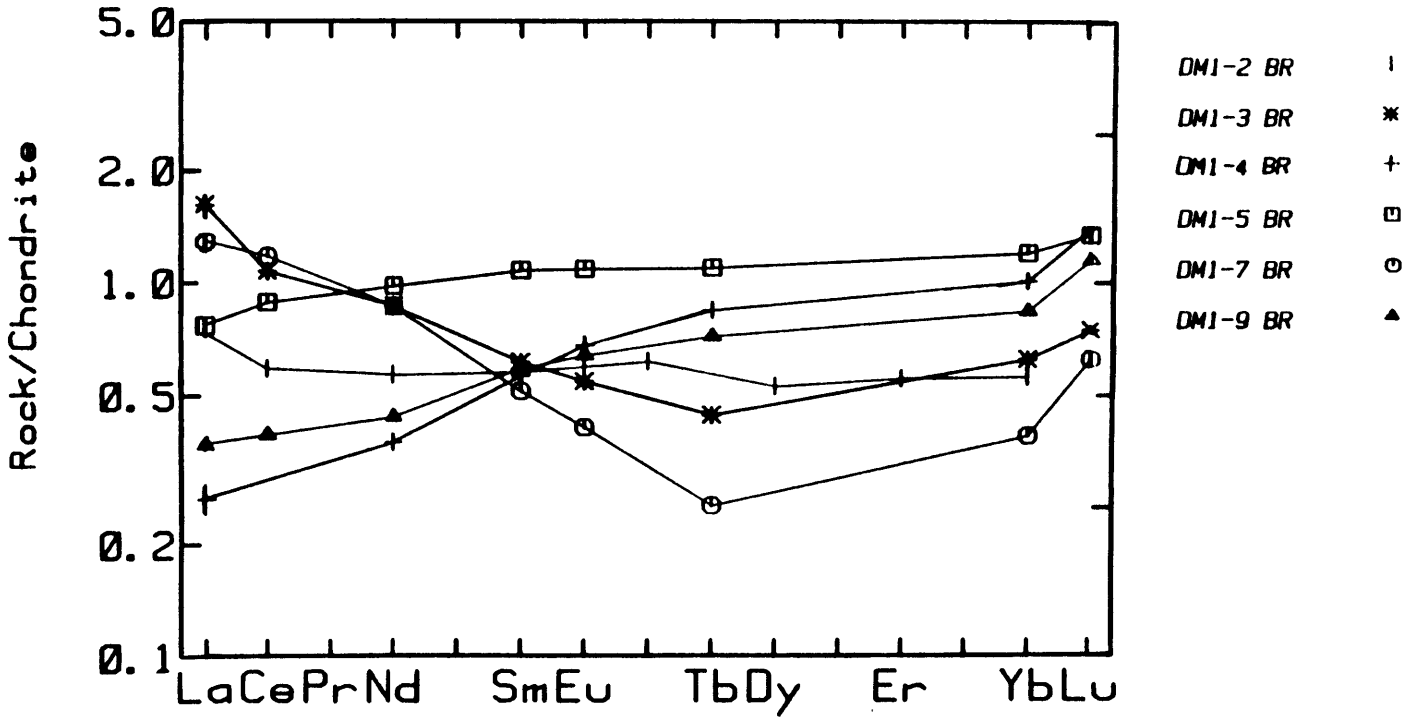
5.0
2.0
1.0
0.5
0.2
0.1
Rock/Chondrite
LaCePrNd
SmEu
TbDy
Er
YbLu
DM1-2 BR
DM1-3 BR
DM1-4 BR
DM1-5 BR
DM1-7 BR
DM1-9 BR

FIGURE 4-4a

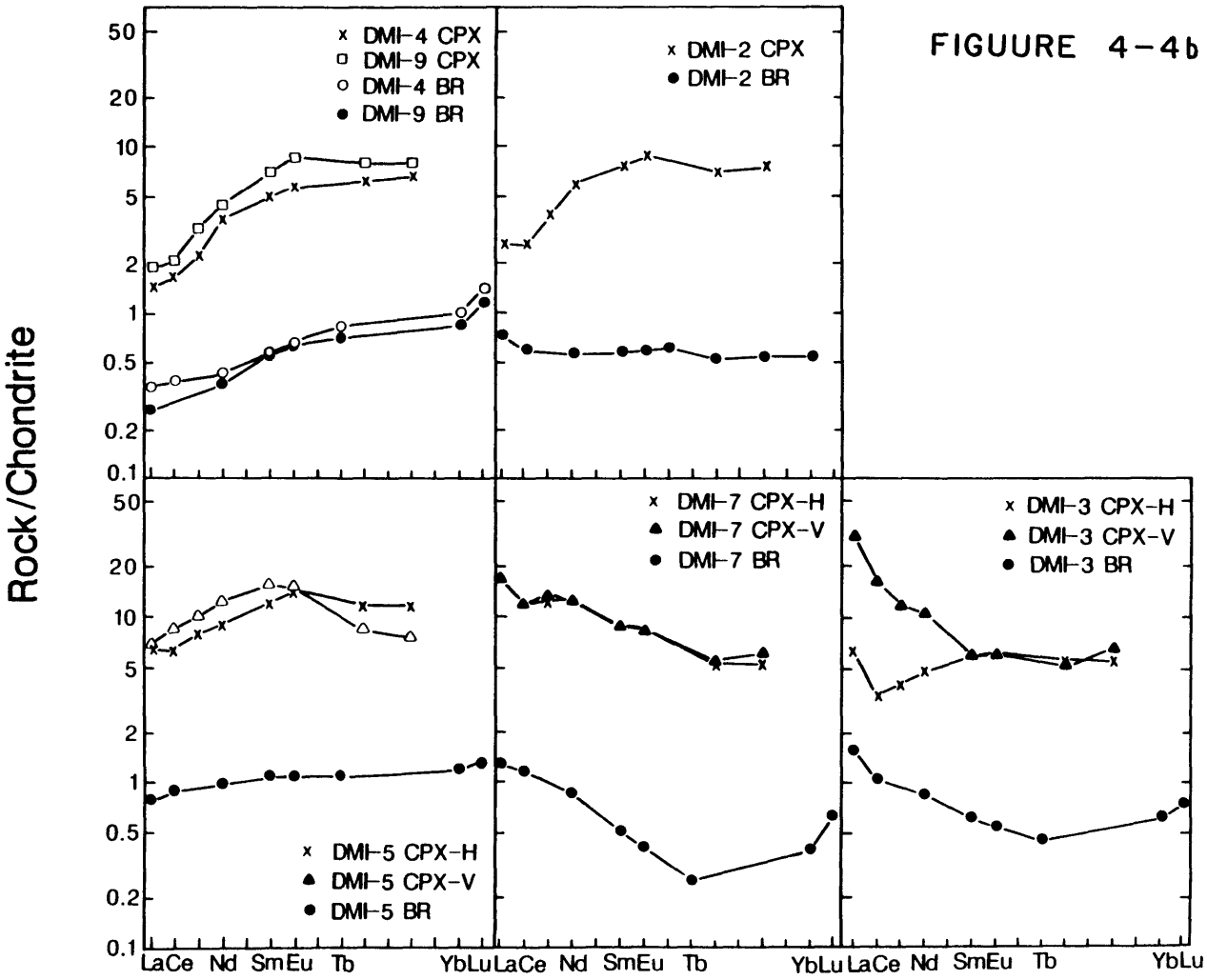
Rock/Chondrite
50
20
10
5
2
1
0.5
0.2
0.1
x DMI-4 CPX
□ DMI-9 CPX
○ DMI-4 BR
● DMI-9 BR
x DMI-2 CPX
● DMI-2 BR
x DMI-7 CPX-H
▲ DMI-7 CPX-V
● DMI-7 BR
x DMI-3 CPX-H
▲ DMI-3 CPX-V
● DMI-3 BR
x DMI-5 CPX-H
▲ DMI-5 CPX-V
● DMI-5 BR
LaCe Nd SmEu Tb YbLu

FIGUURE 4-4b

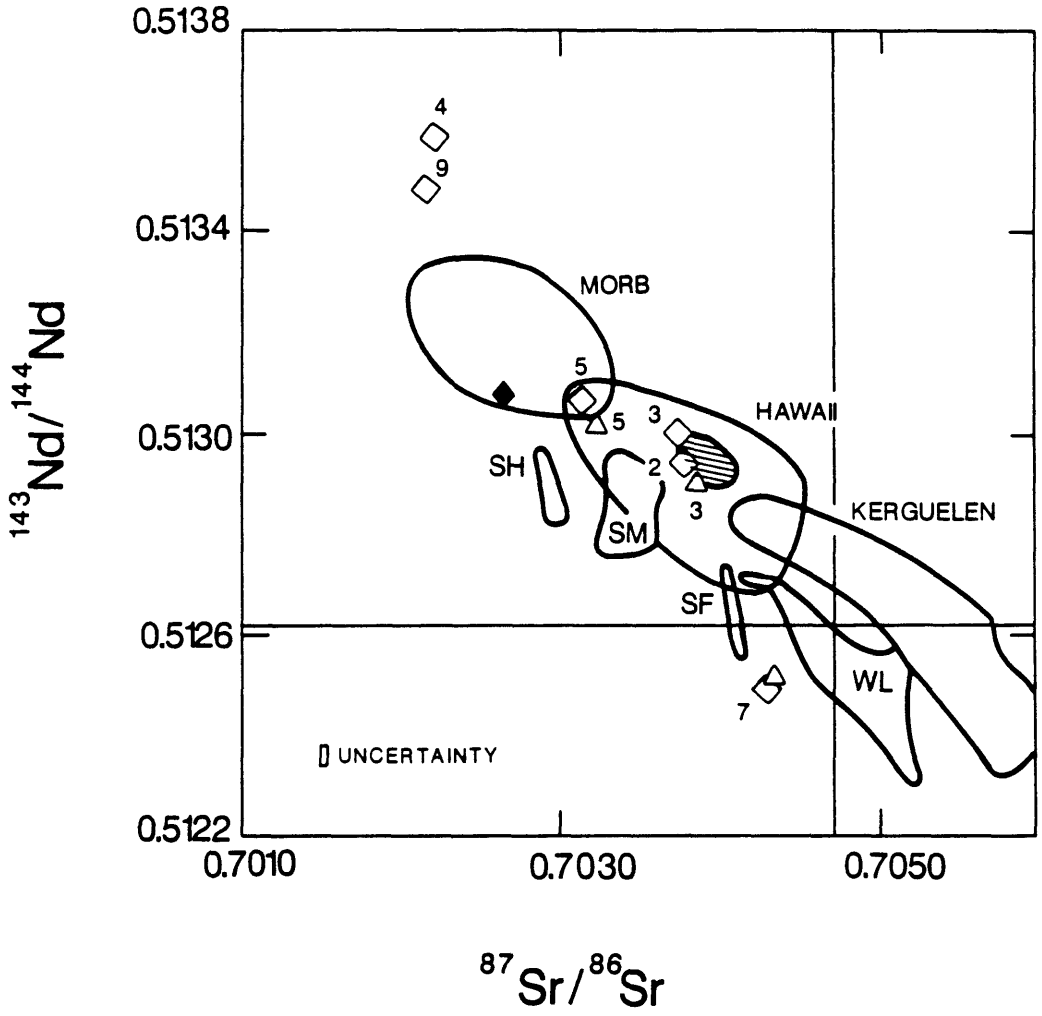
0.5138
0.5134
0.5130
0.5126
0.5122
0.7010
0.7030
0.7050
$^{143}Nd/^{144}Nd$
$^{87}Sr/^{86}Sr$
MORB
HAWAII
KERGUELEN
SH
SM
SF
WL
UNCERTAINTY
4
9
5
5
3
2
3
7

FIGURE 4-5

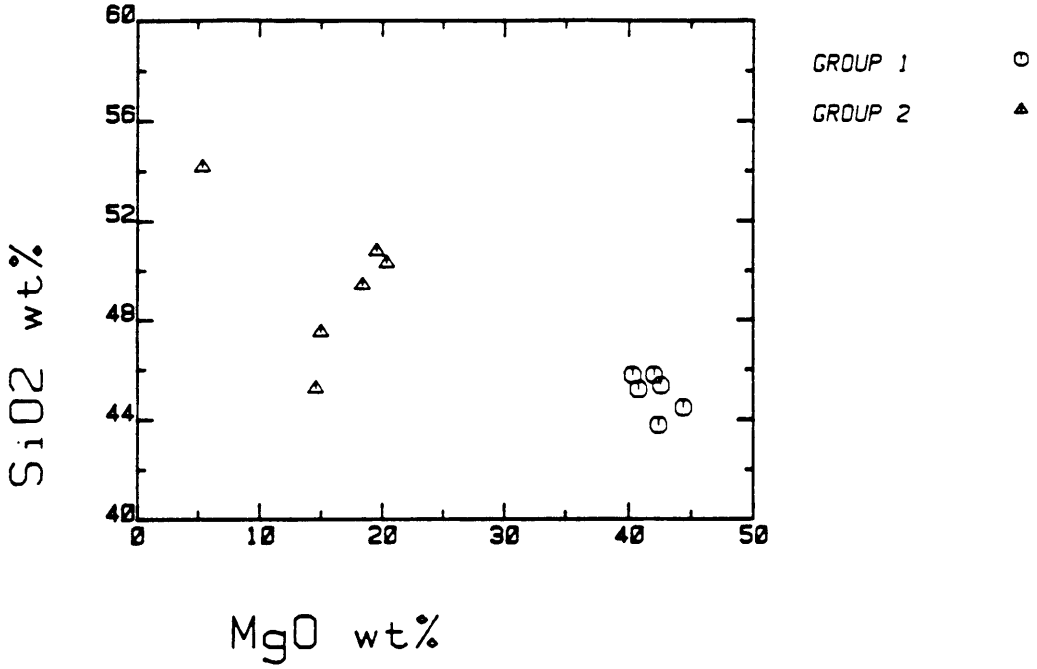
60
56
52
48
44
40
0
10
20
30
40
50
SiO2 wt%
MgO wt%
GROUP 1
GROUP 2

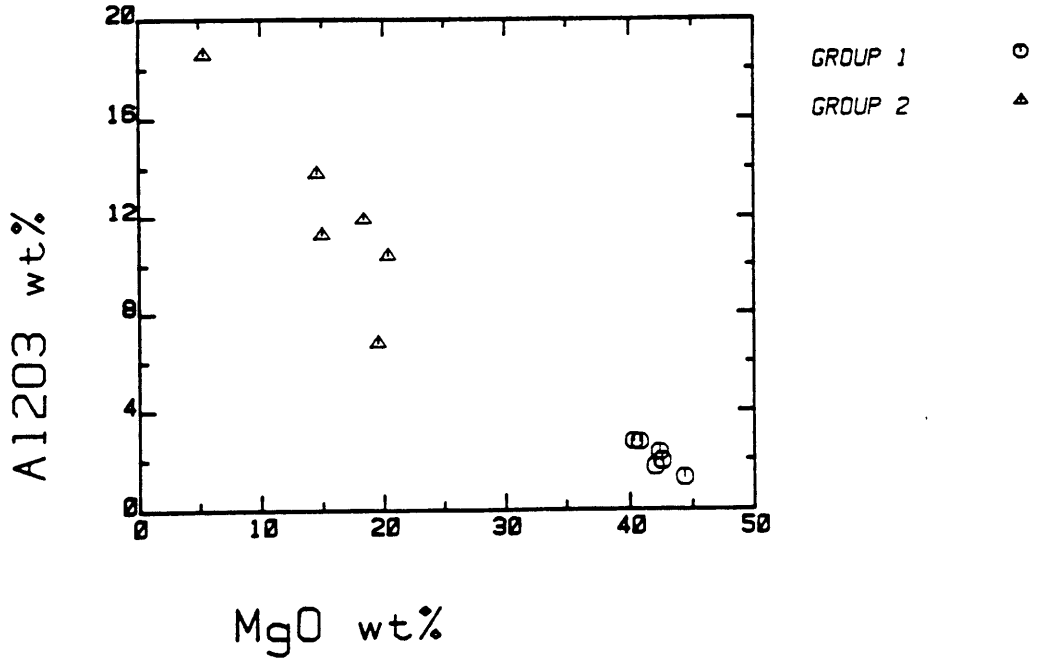
20
16
12
8
4
0
0
10
20
30
40
50
Al2O3 wt%
MgO wt%
GROUP 1
GROUP 2

FIGURE 4-6

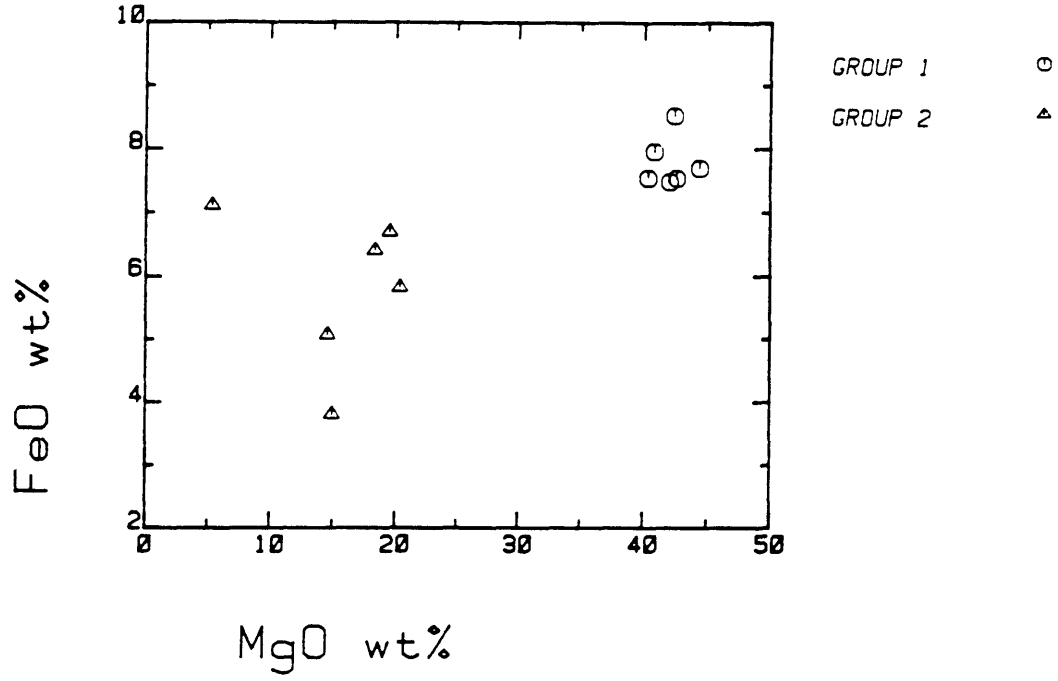
10
8
6
4
2
0
10
20
30
40
50
FeO wt%
MgO wt%
GROUP 1
GROUP 2

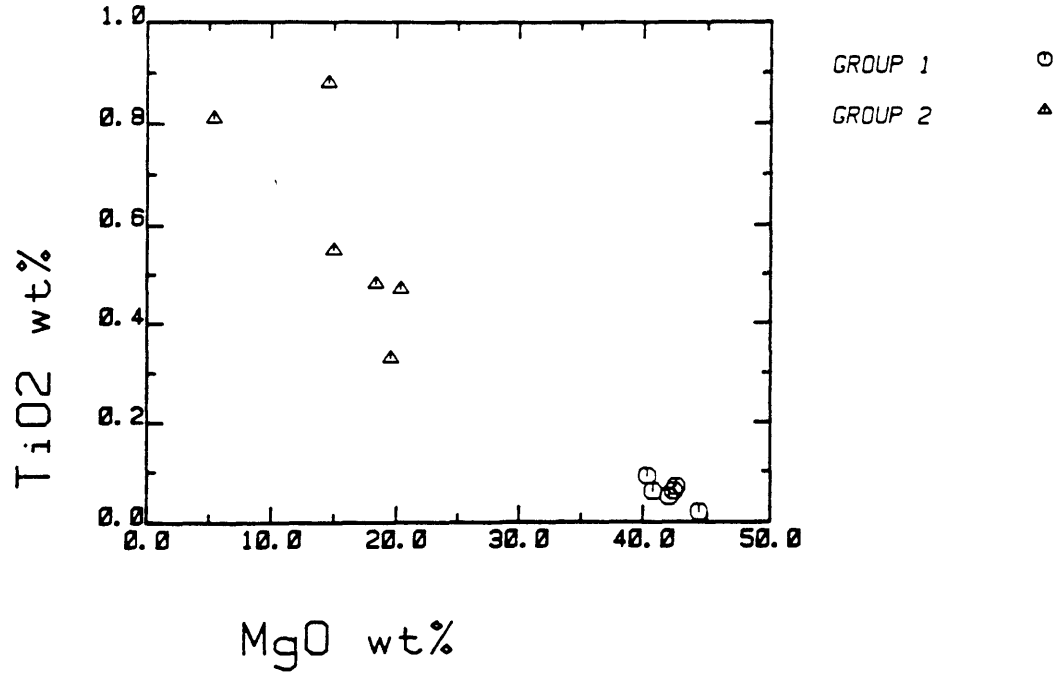
1.0
0.8
0.6
0.4
0.2
0.0
0.0
10.0
20.0
30.0
40.0
50.0
TiO2 wt%
MgO wt%
GROUP 1
GROUP 2

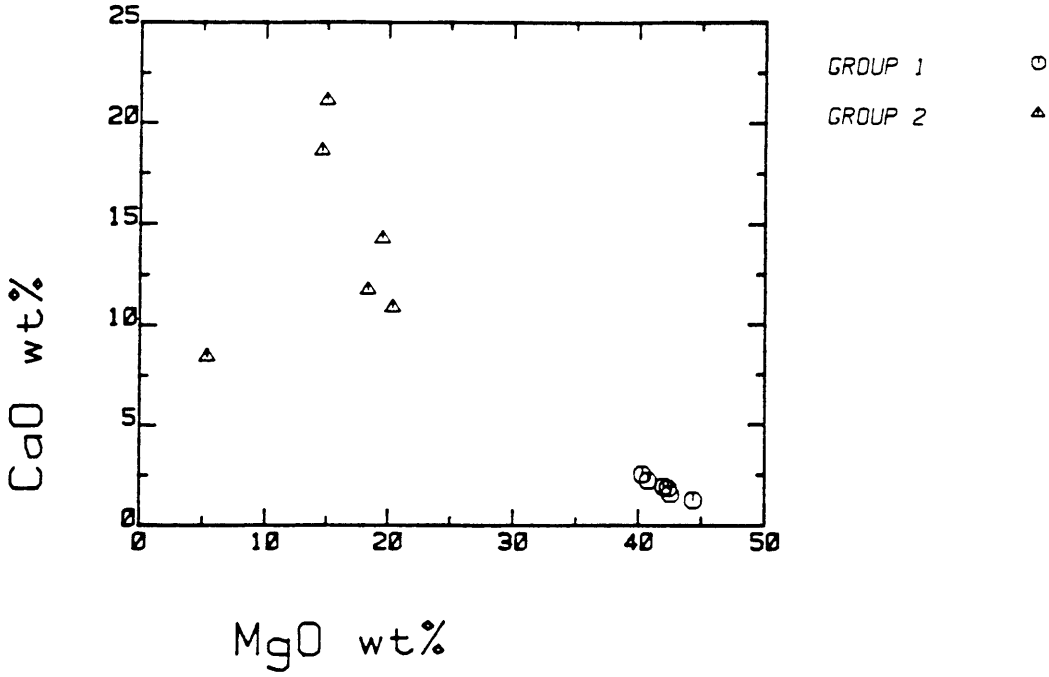
25
20
15
10
5
0
0
10
20
30
40
50
CaO wt%
MgO wt%
GROUP 1
GROUP 2

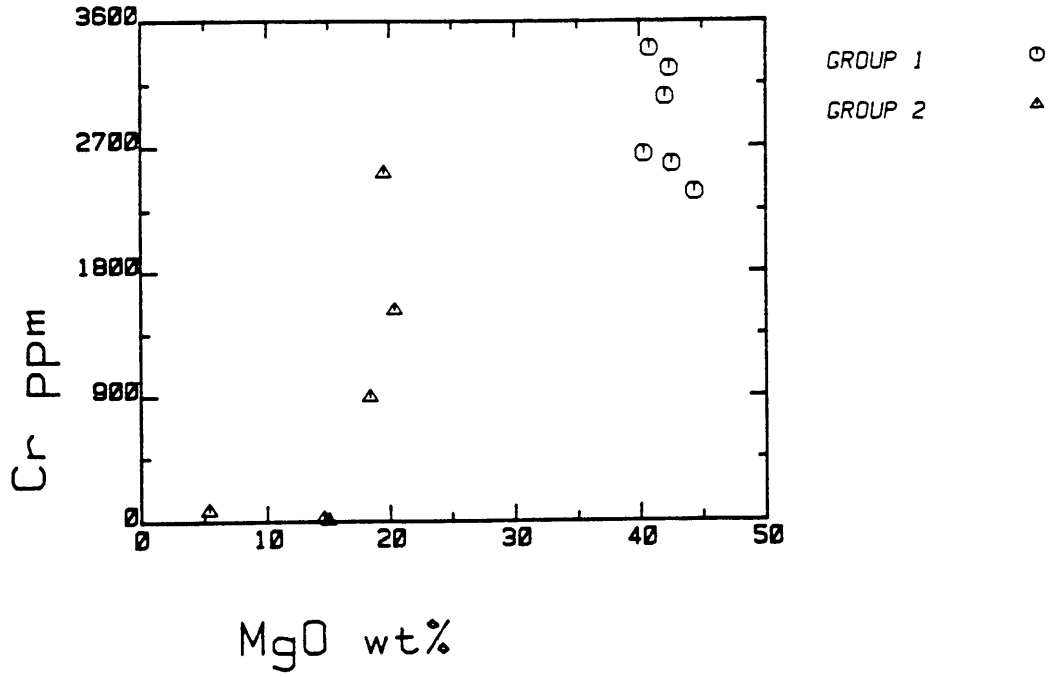
3600
2700
1800
900
0
0
10
20
30
40
50
Cr PPm
MgO wt%
GROUP 1
GROUP 2

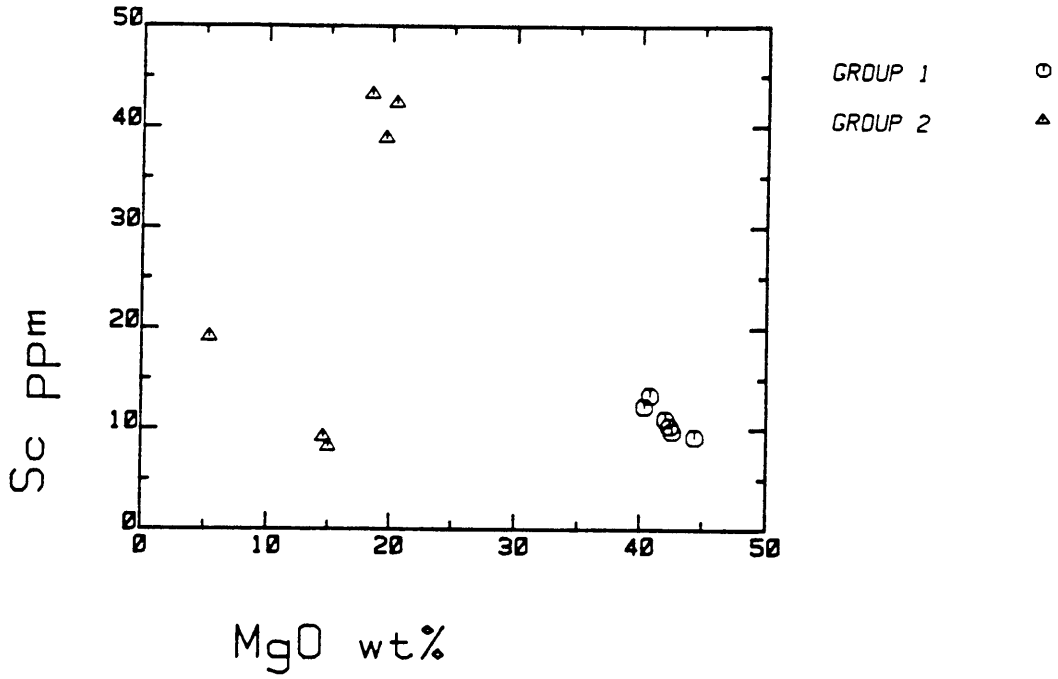
Sc PPm
MgO wt%
GROUP 1
GROUP 2
0
10
20
30
40
50

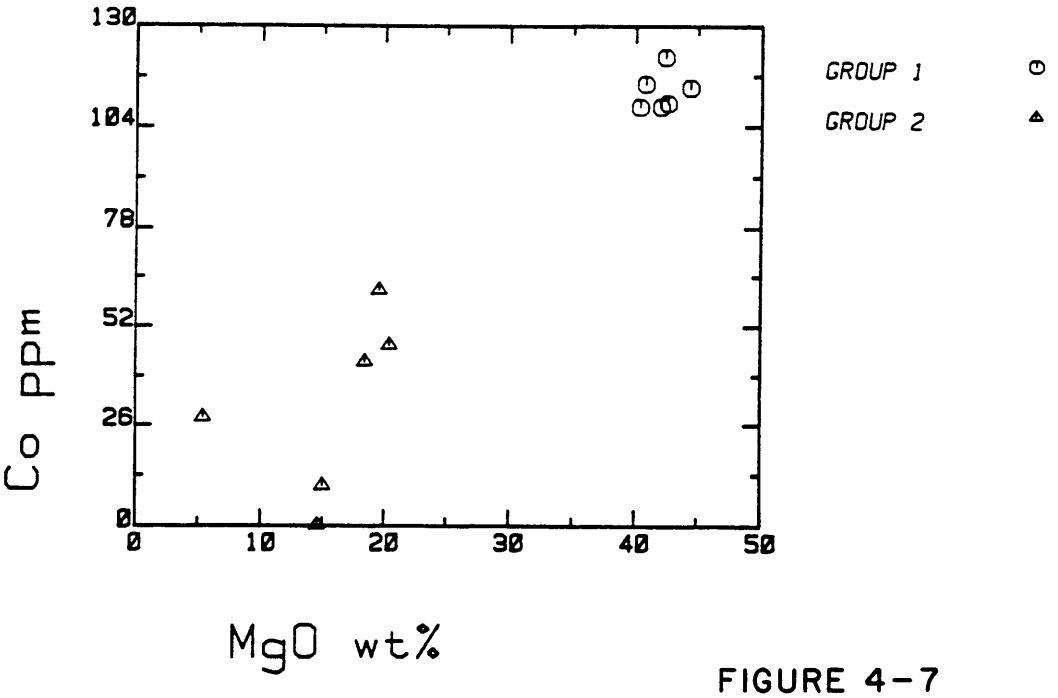
Co PPm
MgO wt%
GROUP 1
GROUP 2
0
26
52
78
104
130
10
20
30
40
50

FIGURE 4-7

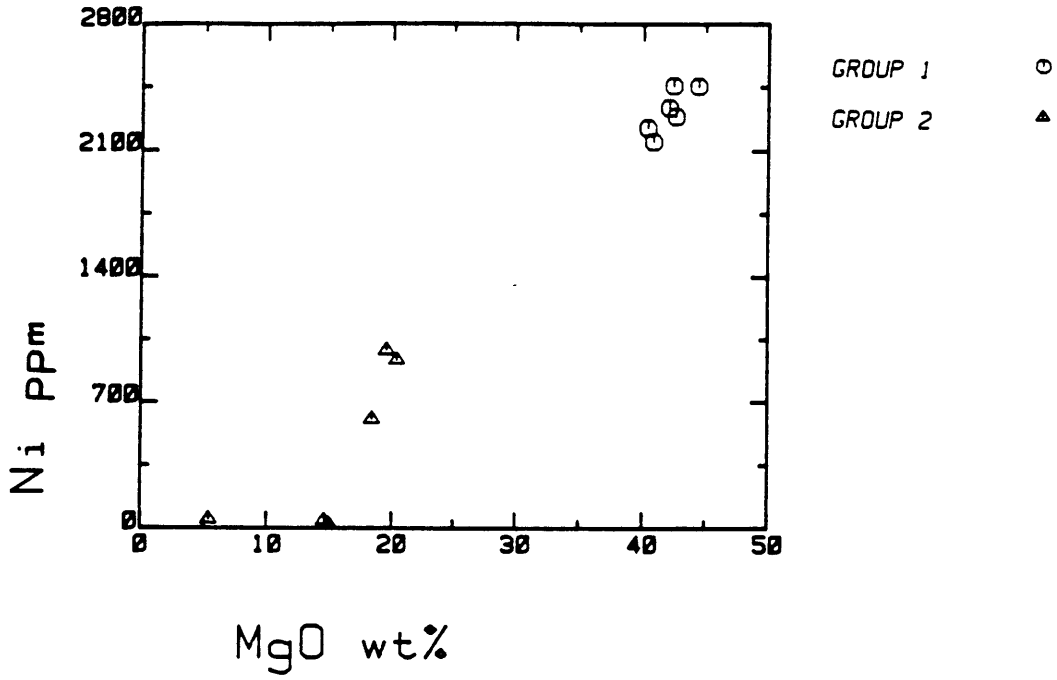
2800
2100
1400
700
0
Ni ppm
0
10
20
30
40
50
MgO wt%
GROUP 1
GROUP 2

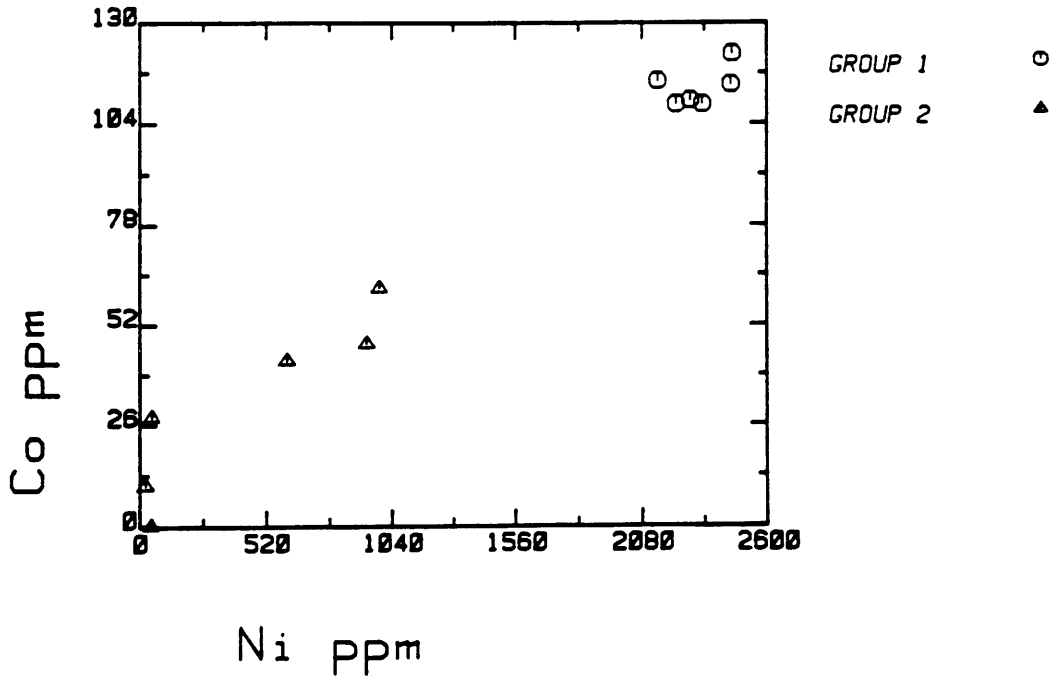
130
104
78
52
26
0
Co ppm
0
520
1040
1560
2080
2600
Ni ppm
GROUP 1
GROUP 2

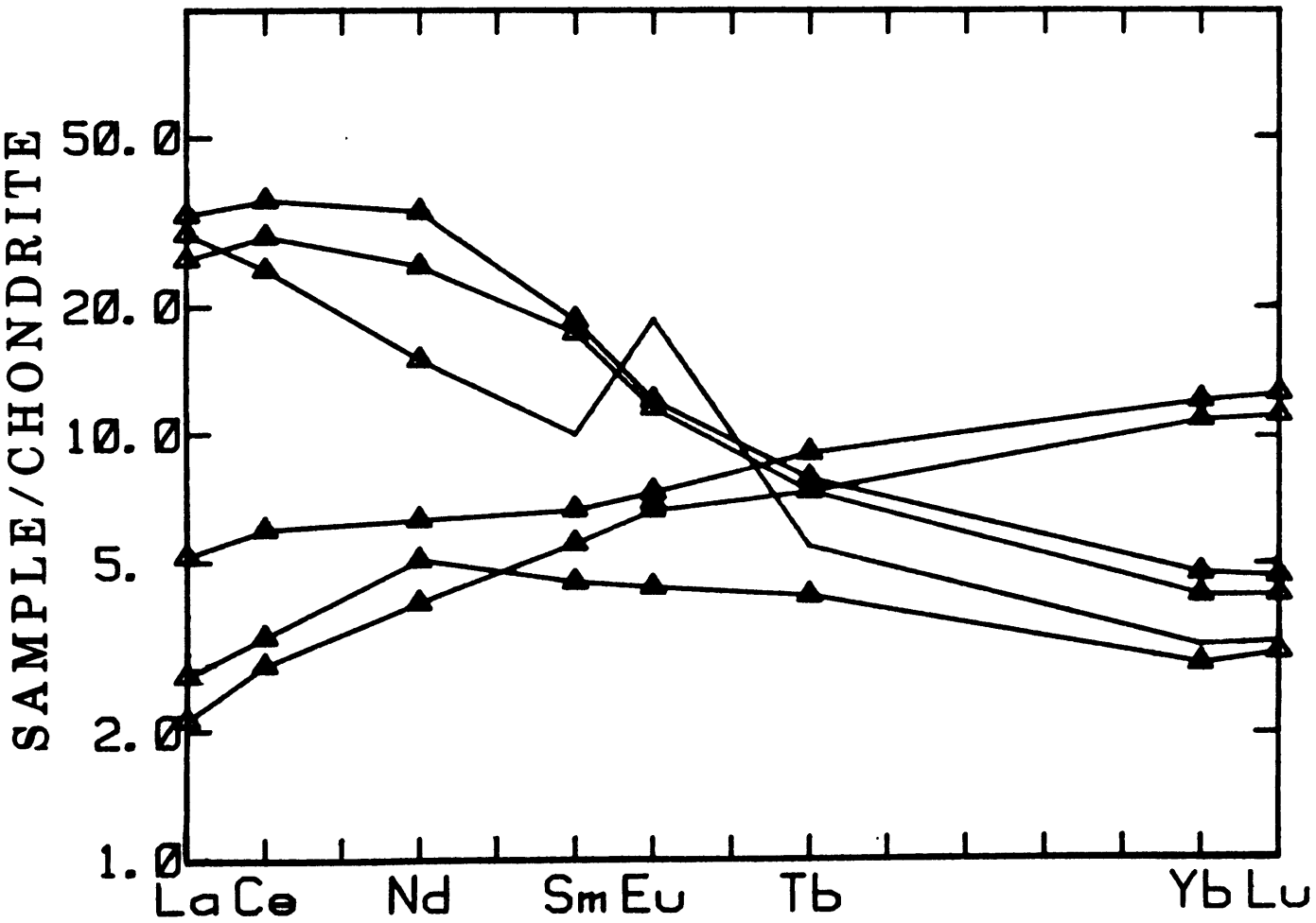

GROUP 2

FIGURE 4-8

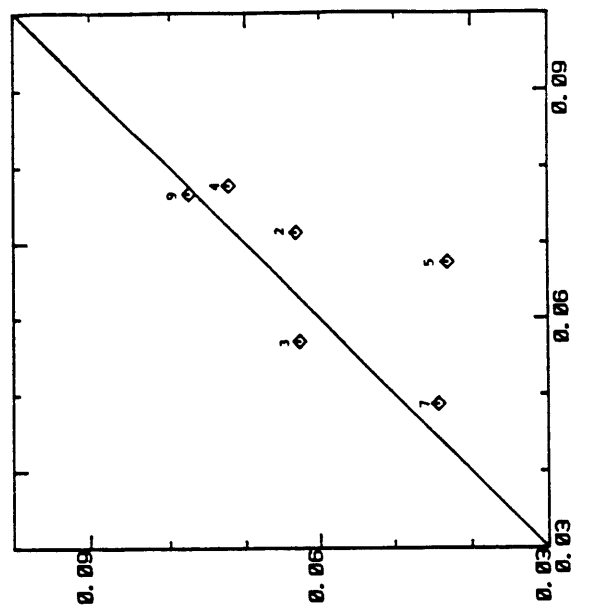

FIGURE 4-10

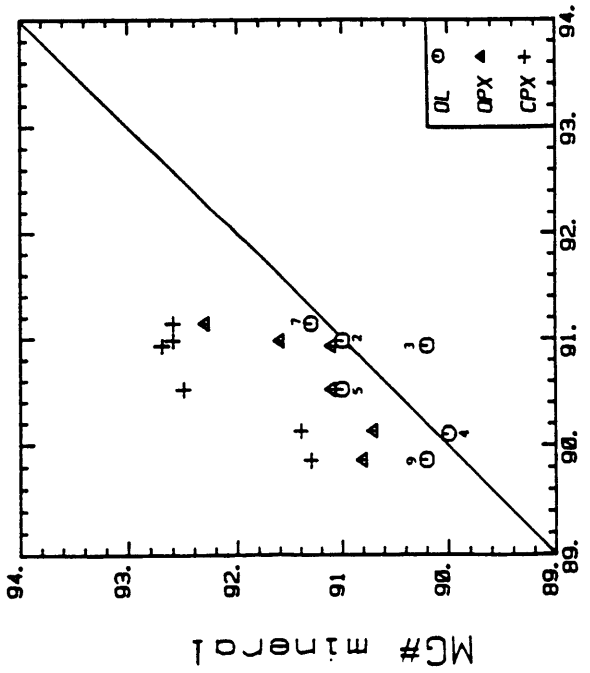

FIGURE 4-9

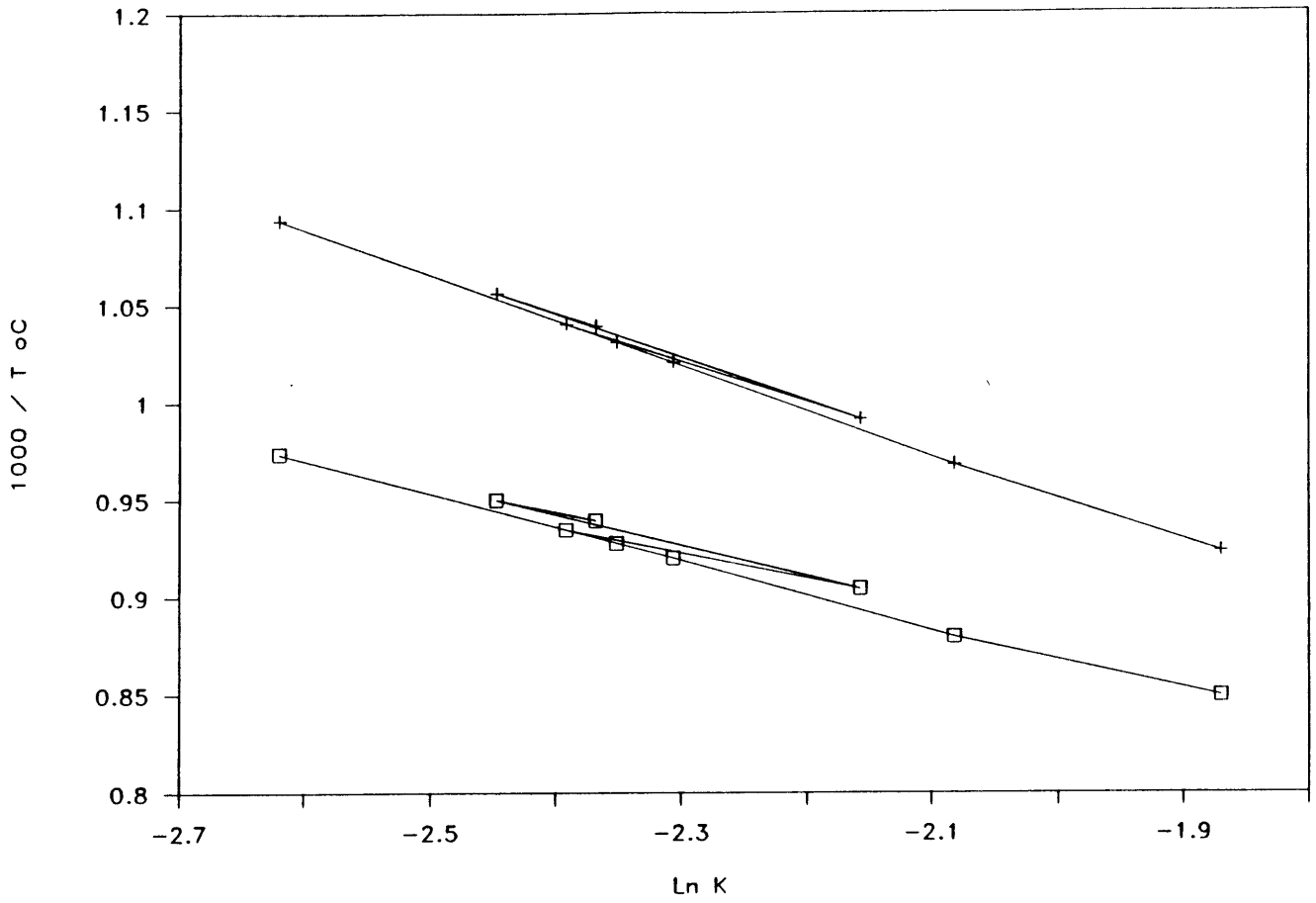

FIGURE 4-11

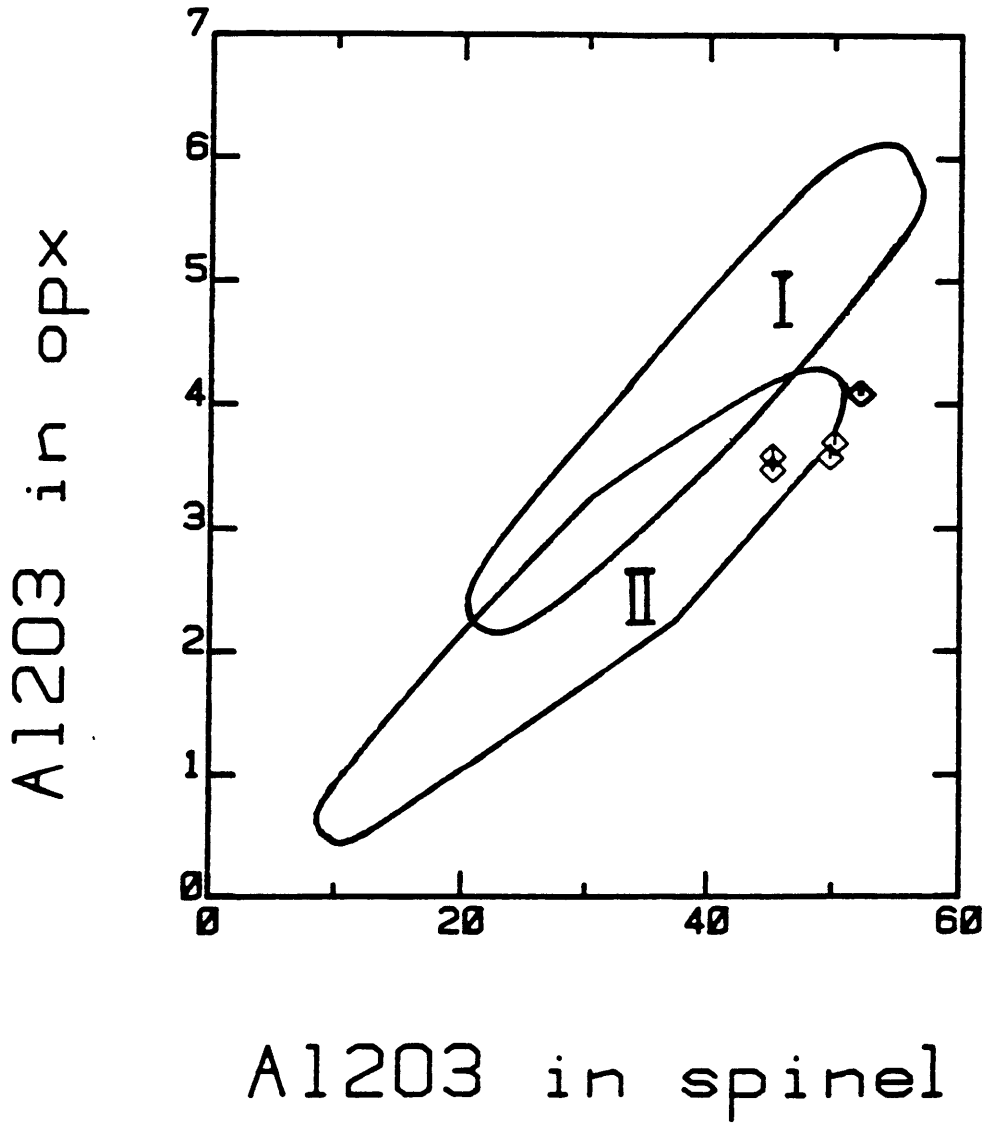

FIGURE 4-12

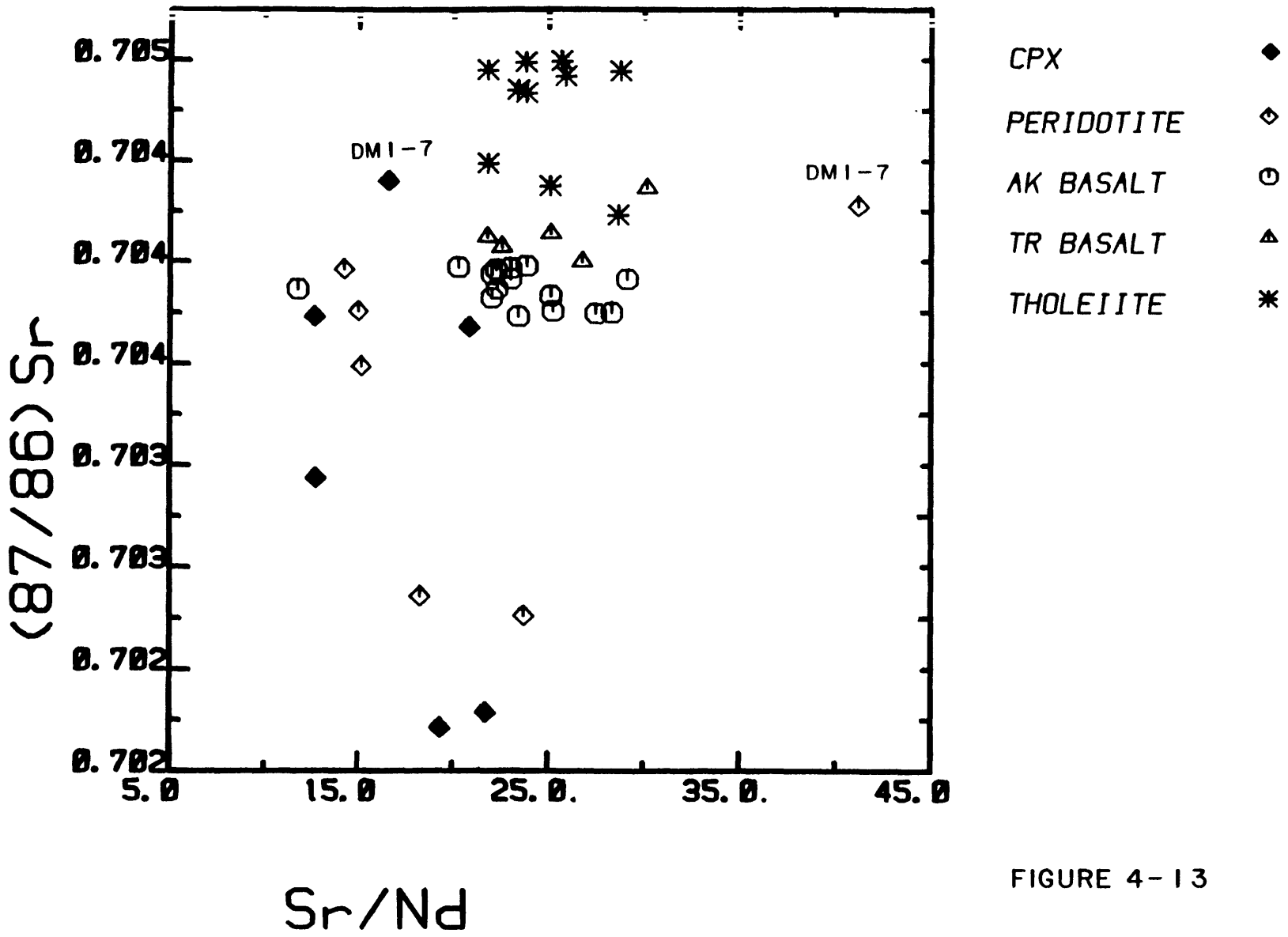
0.705
0.704
0.704
0.704
0.703
0.703
0.702
0.702
(87/86) Sr
DMI-7
DMI-7
5.0
15.0
25.0.
35.0.
45.0
Sr/Nd
CPX
PERIDOTITE
AK BASALT
TR BASALT
THOLEIITE

FIGURE 4-13

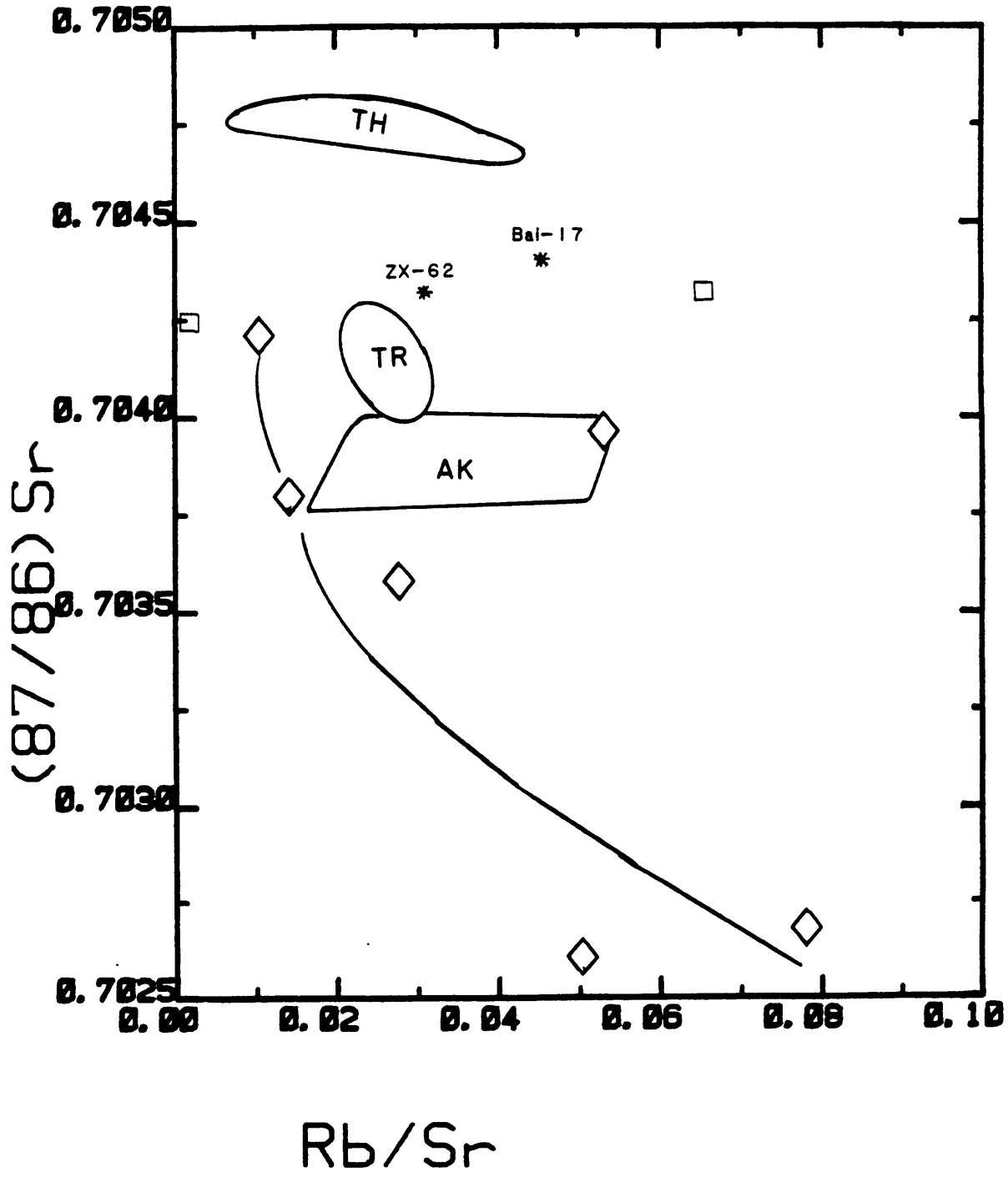
0.7050
0.7045
0.7040
0.7035
0.7030
0.7025
(87/86) Sr
TH
TR
AK
Bai-17
ZX-62
0.00
0.02
0.04
0.06
0.08
0.10
Rb/Sr

FIGURE 4-14

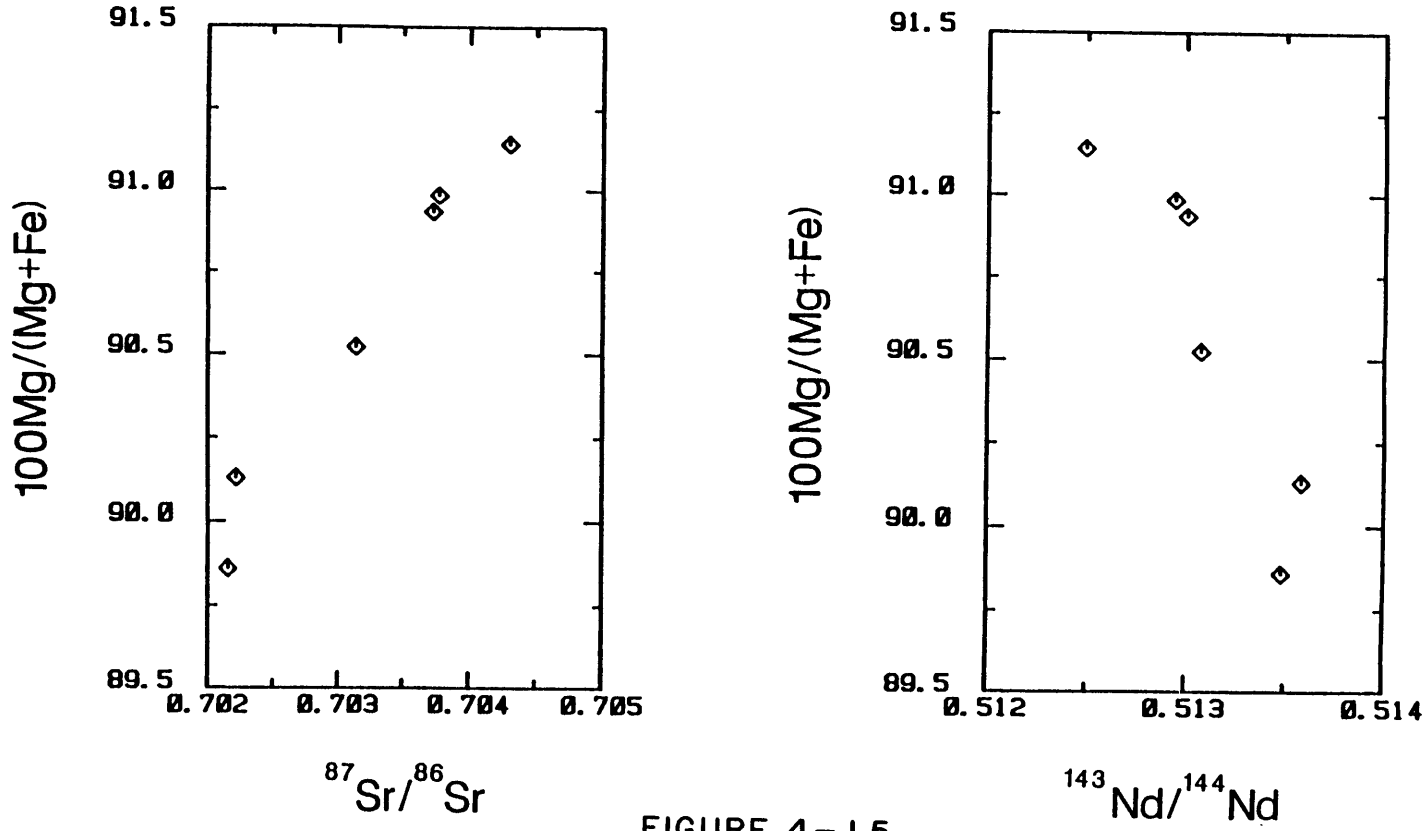
91.5
91.0
90.5
90.0
89.5
100Mg/(Mg+Fe)
0.702
0.703
0.704
0.705
87Sr/86Sr
91.5
91.0
90.5
90.0
89.5
100Mg/(Mg+Fe)
0.512
0.513
0.514
143Nd/144Nd

FIGURE 4-15

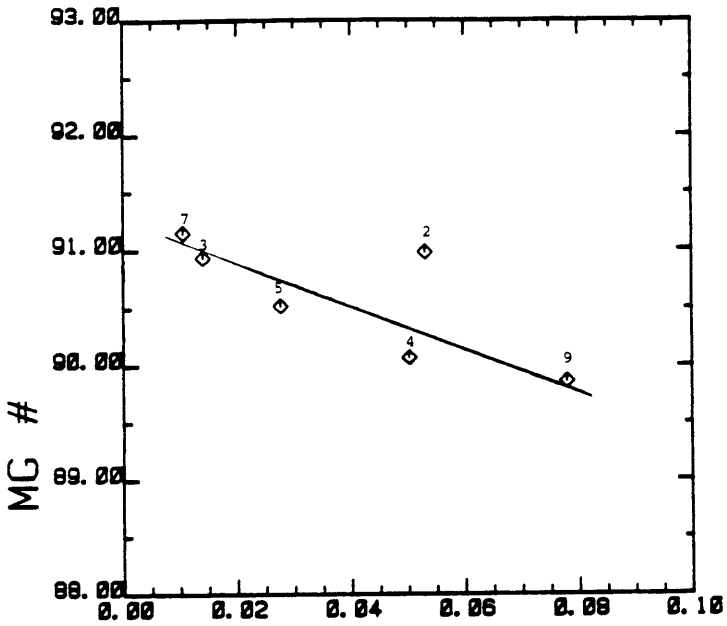

FIGURE 4-16

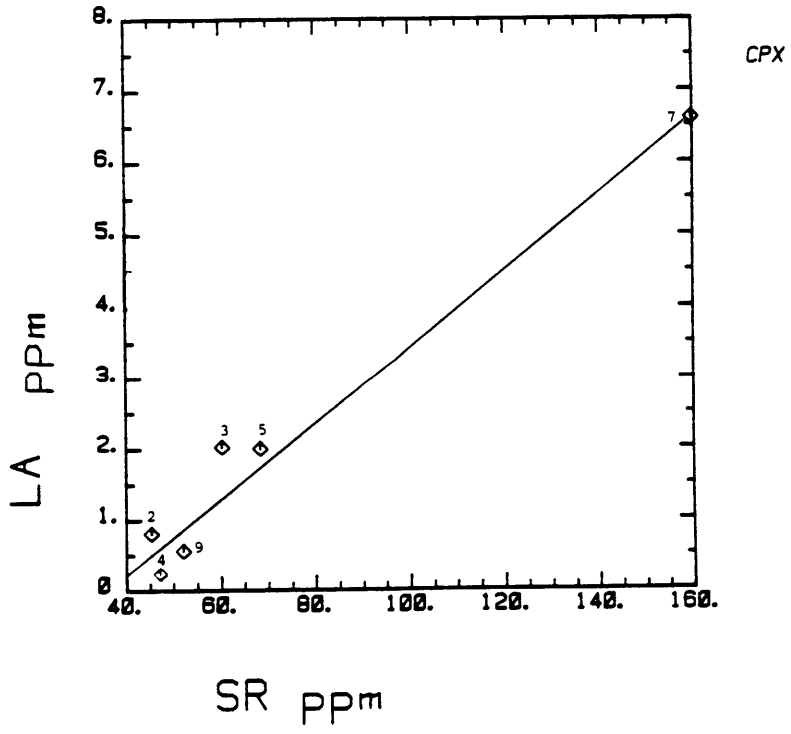

FIGUURE 4-17

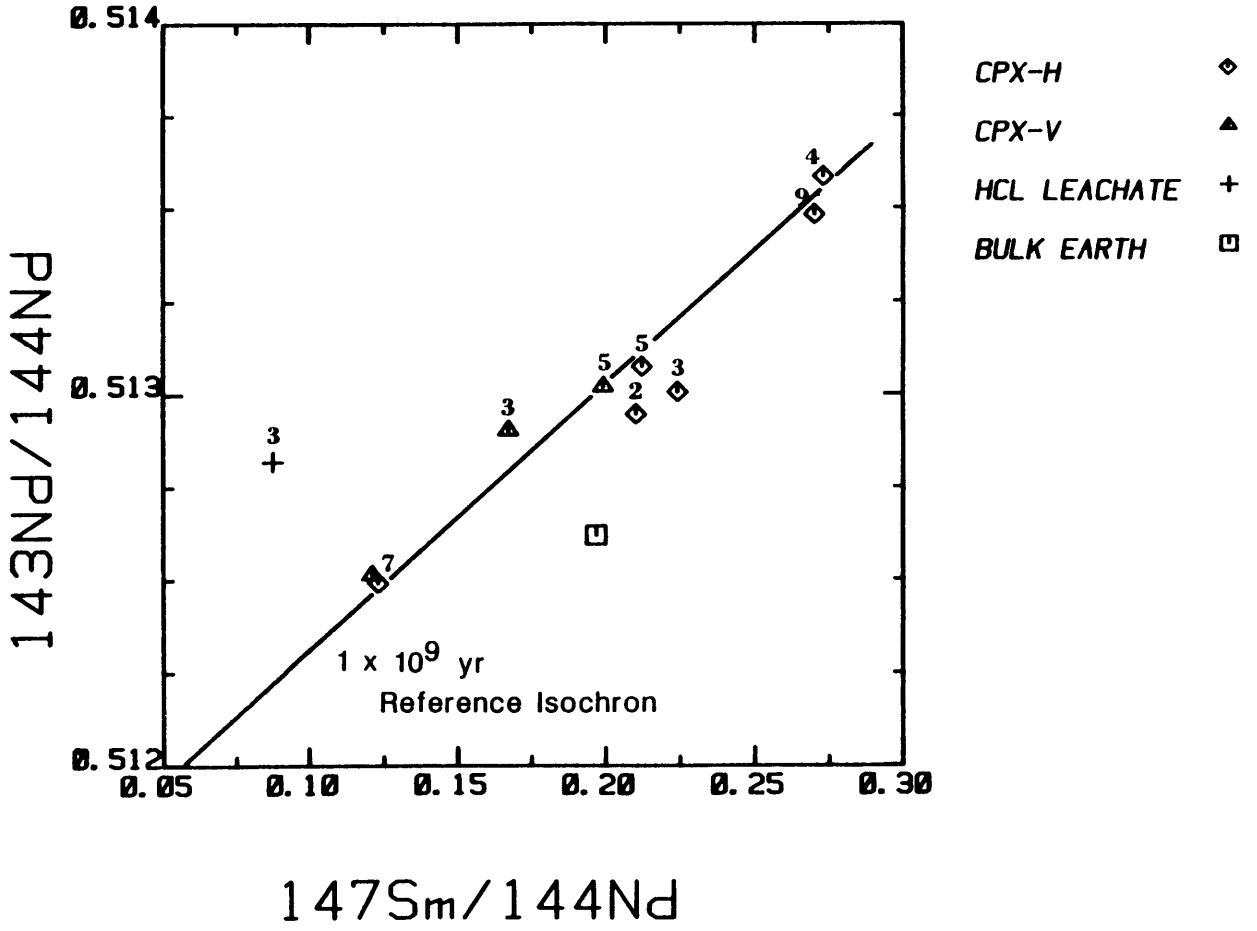
0.514
0.513
0.512
143Nd/144Nd
0.05
0.10
0.15
0.20
0.25
0.30
147Sm/144Nd
1 x 10^9 yr
Reference Isochron
CPX-H
CPX-V
HCL LEACHATE
BULK EARTH

FIGURE 4-18

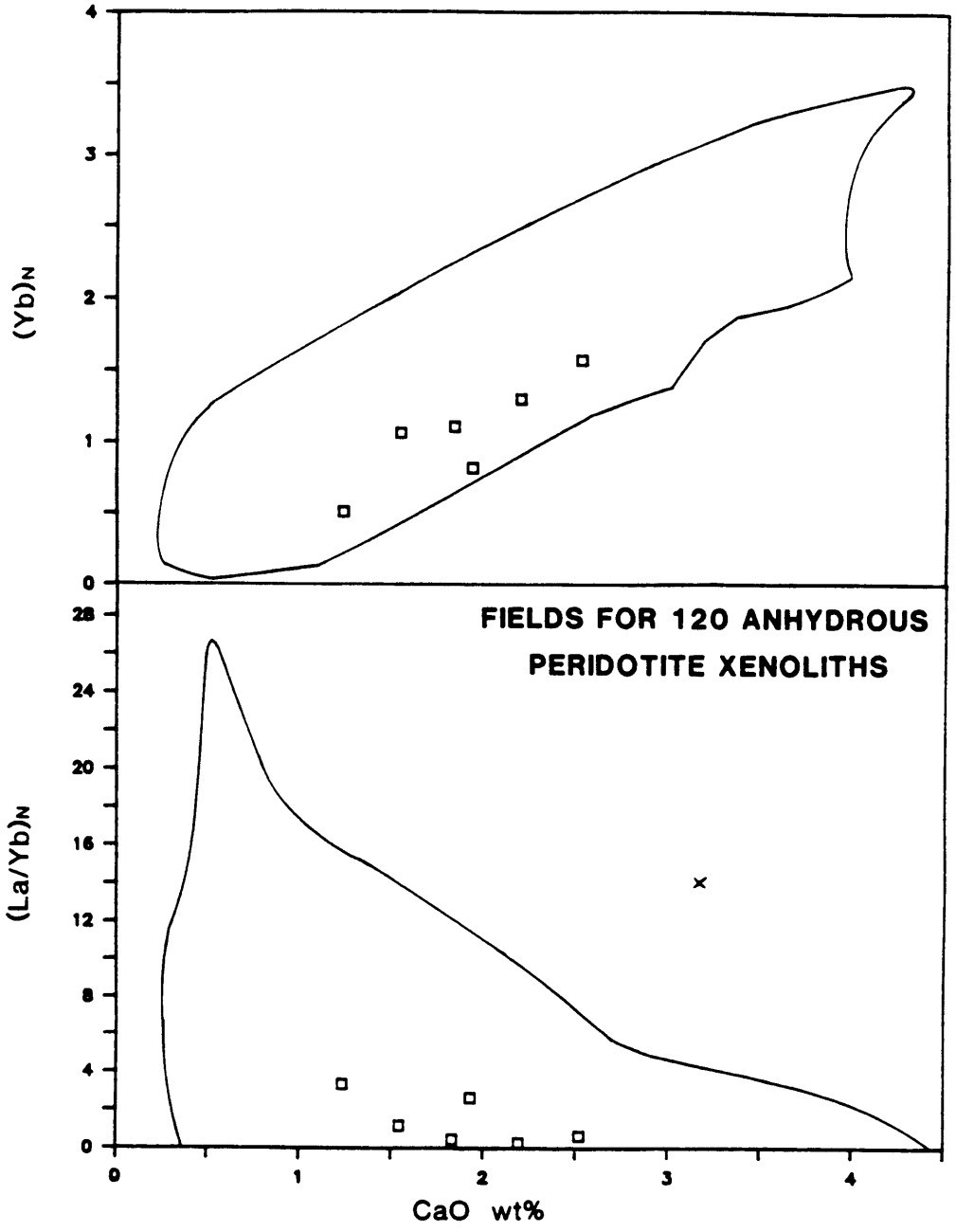
FIELDS FOR 120 ANHYDROUS
PERIDOTITE XENOLITHS
(Yb)N
(La/Yb)N
CaO wt%
0
1
2
3
4
0
4
8
12
16
20
24
28

FIGURE 4-19

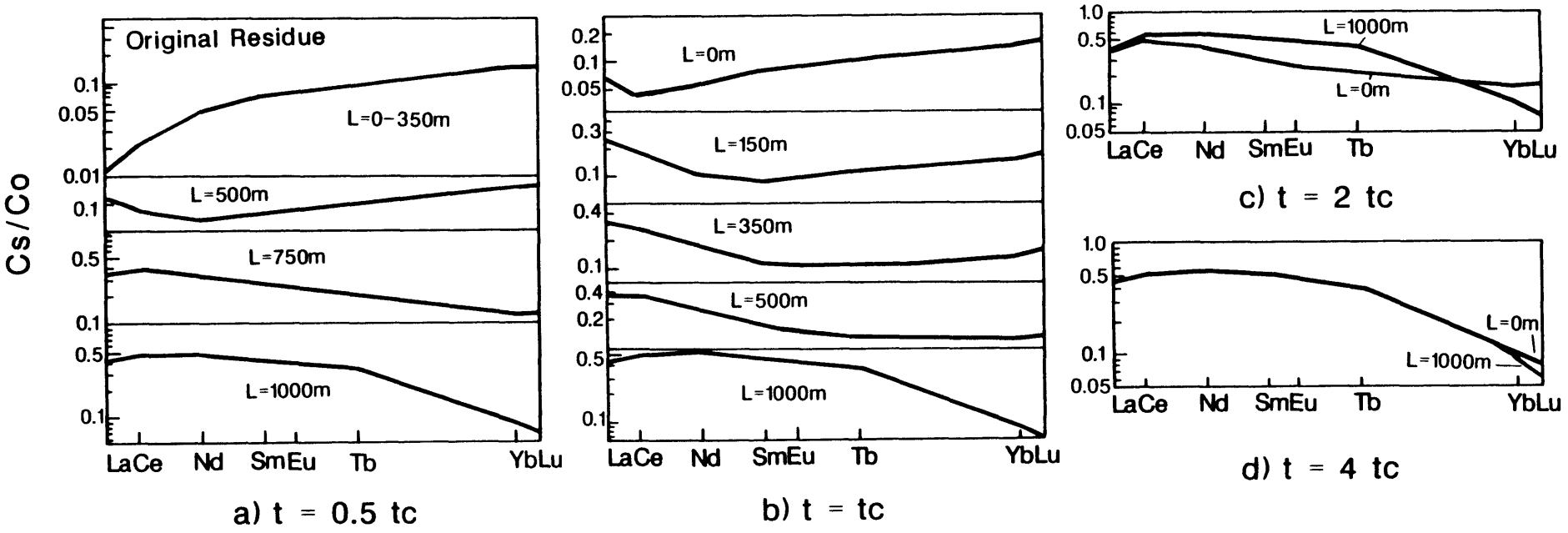
Cs/Co
Original Residue
L=0-350m
L=500m
L=750m
L=1000m
LaCe
Nd
SmEu
Tb
YbLu
a) t = 0.5 tc
L=0m
L=150m
L=350m
L=500m
L=1000m
b) t = tc
L=1000m
L=0m
c) t = 2 tc
L=0m
L=1000m
d) t = 4 tc

FIGURE 4-20

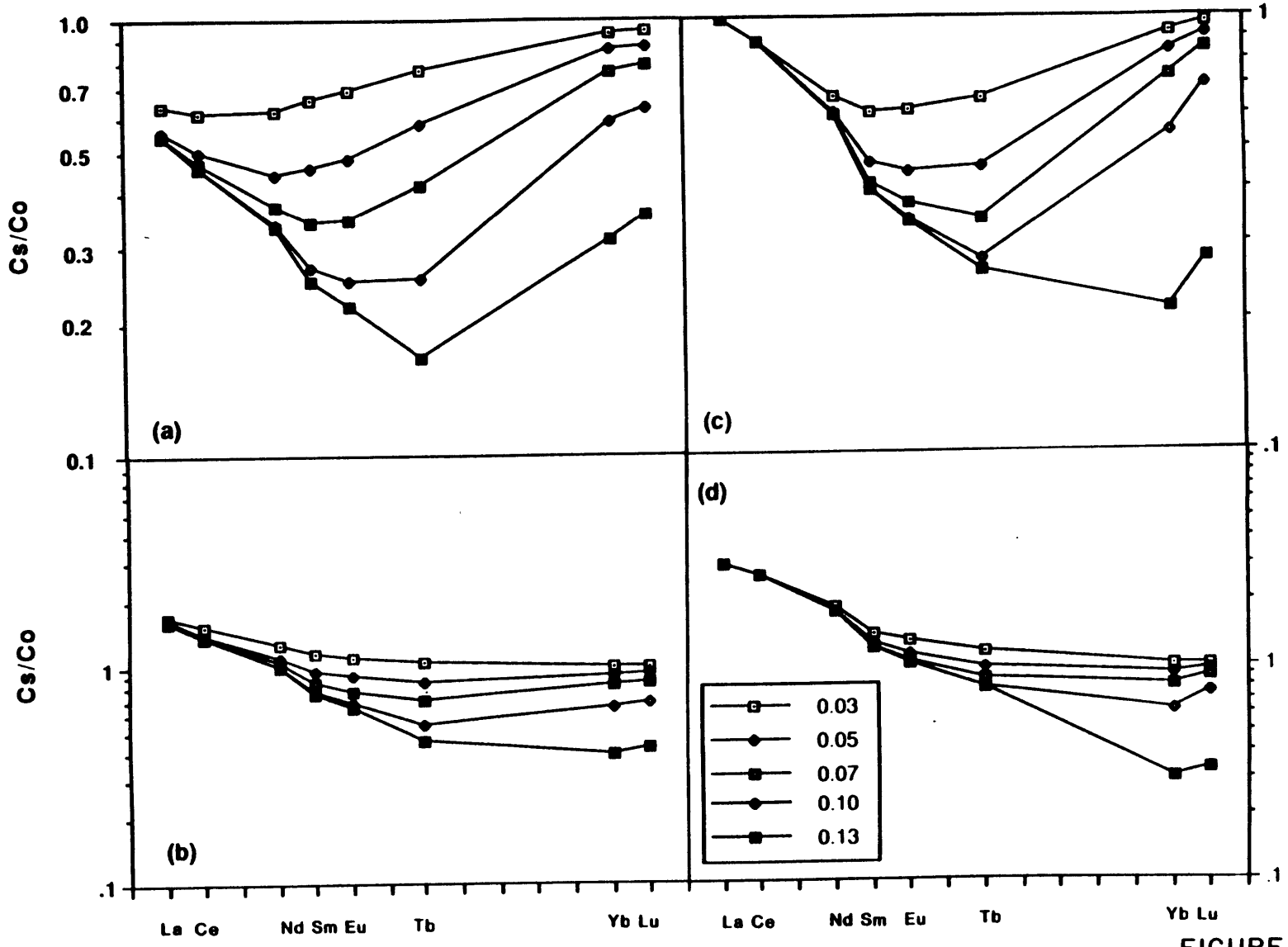
1.0
0.7
0.5
0.3
0.2
0.1
Cs/Co
(a)
(c)
(b)
(d)
1
.1
0.03
0.05
0.07
0.10
0.13
La Ce
Nd Sm Eu
Tb
Yb Lu

FIGURE 4-21

REFERENCES

Allegre C.J., Brevart O., Dupre B. and Minster J.-F., 1980. Isotopic and chemical effects produced in a continuously differentiating convecting earth mantle. Philos. Trans. R. Soc. London, Ser A. 297, 447-477.

Allegre C.J., Dupre B., Lambret B. and Richard P., 1981. The subcontinental versus suboceanic debate. I. Lead-neodymium-strontium isotopes in primary alkali basalts from a shield area: the Ahaggar volcanic suite. Earth Planet. Sci. Lett. 52, 85-92.

Allegre C.J., Hart S.R. and Minster J.-F., 1983. Chemical structure and evolution of the mantle and continents determined by inversion of Nd and Sr isotopic data, II. Numerical experiments and discussion. Earth Planet. Sci. Lett. 66, 191-213.

Anders E. and Ebihara M., 1982. Solar-system abundances of the elements. Geochem. Cosmochim. Acta 46, 2363-2380.

Aoki K.-I., 1970. Andesine megacrysts in alkali basalts from Japan. Contrib. Mineral Petrol. 25, 284-288.

Arculus R.J., 1975. Melting behavior of two basanites in the range 10 to 35 kbar and the effect of TiO_2 on the olivine-diopside reactions at high pressure. (abstr). Geol. Soc. Am., Abstr. Programs 7, 979-980.

Barbour G.B., 1929. The geology of the Kalgan Area. Mem. Geol. Surv. China., (A) 6, 54-61.

Basaltic Volcanism Study Project (BVSP). 1981. Basaltic Volcanism on the Terrestrial Planets (eds. R.B.MERRILL and R. RIDINGS). Pergamon Press. 1286p.

BHTHED (Baishang Hydrographic Team of Hydrographic Engineering Department). 1978. Geological period of Hannuoba basalts. Bulletin of Hebei Geological College. 2, 32-46. (in Chinese)

Binns R.A., Duggan M.B. and Wilkinson J.F.G., 1970. High pressure megacrysts in alkaline lavas from northeastern New South Wales. Amer. J. Sci. 269, 132-168.

Bodinier J.L., Dupuy C. and Dostal J., 1988. Geochemistry and petrogenesis of eastern Pyrenean peridotites. Geochim. Cosmochim. Acta 52, 2893-2907.

Bonatti E., Ottonello G. and Hamlyn P.R., 1986. Peridotites from Zabargad (ST. Jehn), Red Sea: Petrology and geochemistry. J. Geophys. Res. 91, 599-631.

Brooks C., James D.E. and Hart S.R., 1976. Ancient lithosphere: Its role on young continental volcanism. Science, 193, 1086-1094.

Cameron A.E., Smith D.N. and Walker R.L., 1969. Mass spectrometry of nanogram-size samples of lead. Anal. Chem. 41, 525-526.

Campbell I.H., 1985. The differences between oceanic and continental tholeiites: a fluid dynamic explanation. Contrib. Mineral Petrol. 91, 37-43.

Carlson R.W., 1984. Isotopic constraints on Columbia River flood basalt genesis and the nature of the subcontinental mantle. Geochim. Cosmochim. Acta 48, 2357-2372.

Carlson R.W., Lugmair G.W. and Macdougall J.D., 1981. Columbia River volcanism: the question of mantle heterogeneity or crustal contamination. Geochem. Cosmochim. Acta 45, 2483-2499.

Carswell D.A. and Dawson J.B., 1970. Garnet peridotite xenoliths in South African kimberlite pipes and their petrogenesis. Contrib. Mineral Petrol. 25, 163-184.

Carswell D.A. and Gibbs F.G.F., 1980. Geothermometry of garnet lherzolite nodules with spinel reference to those from the kimberlites of Northern Lesotho. Contrib. Mineral Petrol. 74, 403-416.

Carswell D.A. and Gibb F.G.F., 1987. Evaluation of mineral thermometers and barometers applicable to garnet lherzolite assemblages. Contrib. Mineral Petrol. 95, 499-511.

Carter S.R., Evensen N.M., Hamilton P.J. and O'Nions R.K., 1978. Neodymium and strontium isotope evidence for crustal assimilation of continental volcanics. Science 202, 743-747.

Chen C.Y. and Frey F.A., 1985. Trace element and isotopic geochemistry of Haleakala volcano, East Maui, Hawaii: Implications for the origin of Hawaiian basalts. J. Geophys. Res. 90. B10, 8743-8768.

Chen C.Y., Frey F.A. and Song Y., 1989. Evolution of the upper mantle beneath Southeast Australia: Geochemical evidence from peridotite xenoliths in Mount Leura basanite. submitted to Earth Planet. Sci. Lett.

Chen J.C., 1971. Petrology and chemistry of garnet lherzolite nodules in kimberlite from Africa. Amer. Mineral. 56, 2098-2110.

Clague D.A. and Frey, F.A., 1982. Petrology and trace element geochemistry of the Honolulu volcanics, Oahu: Implications for the oceanic mantle below Hawaii. J. Petrol. 23 447-504.

Cohen L.H., Ito K. and Kennedy G.C., 1967. Melting and phase relations in anhydrous basalts to 40 kilobars. Am. Jour. Sci. 265, 475-518.

Cohen R.S., Evensen N.M., Hamilton P.J. and O'Nions R.K., 1980. U-Pb, Sm-Nd, and Rb-Sr systematics of mid-oceanic ridge basalt glasses. Nature 283, 149-153.

Cong B. and Zhang R., 1982. Transition metal geochemistry of Hannuoba basalts and their ultramafic inclusions. IGAS. Research on Geology, 44-53.

Cong B. and Zhang R., 1983. Petrogenesis of Hannuoba basalts and their ultramafic inclusions. Scientia Sinica. (Foreign language edition). 26, 308-315.

Cong B., Zhang W. and Ye D., 1979. The study of the Cenozoic basalts in North China Fault Block. Acta Geol. Sin., 2, 112-123 (in Chinese).

Cong B., Zhang R., Yang R., Luo S., Guo Y., Wang Z., Zhao C., Jiang Y. and Feng X., 1983. Rare earth element geochemistry of basalts and their ultramafic inclusions from Damaping, Wanquan, North China. Kexue Tongbao. Scientia Sinica. (Foreign language edition). 28, 792-797.

Daudria J.M. and Girod M., 1987. Cenozoic volcanism associated with swells and rifts. In Mantle Xenoliths (ed. P.M.Nixon), pp 195-124. Wiley, London.

Devey C.W. and Cox K.G., 1987. Relationships between crustal contamination and crystallisation in continental flood basalt magmas with special reference to the Deccan Traps of the Western Ghats, India. Earth Planet. Sci. Lett. 84, 59-68.

Dick H.J.B, and Fisher R.L., 1984. Mineralogic studies of the residues of mantle melting, abyssal and alpine type peridotites. In Kimberlites II: The Mantle and Crust-Mantle Relationships (ed. J.KORNPROBST), pp295-308. Elsevier Sci. Publ.

Dickin A.P., Jones N.W., Thirlwall M.F. and Thompson R.N., 1987. A Ce/Nd isotope study of crustal contamination processes affecting Palaeocene magmas in Skye, Northwest Scotland. Contrib. Mineral Petrol. 96, 455-464.

Doe B.R., Leeman W.P., Christiansen R.L. and Hedge C.E., 1982. Lead and strontium isotopes and related trace elements

as genetic tracers in the Upper Cenozoic rhyolite-basalt association of the Yellowstone Plateau Volcanic Field. J. Geophys. Res. 87, 4785-4806.

Dostal J., Dupuy, C. and Liotard J.M., 1982. Geochemistry and origin of basaltic lavas from Society Islands, French Polynesia (South Central Pacific Ocean). Bull. Volcanol. 45-1, 51-62.

Downes H. and Dupuy C., 1987. Textural, isotopic and REE variations in spinel peridotite xenoliths, Massif Central, France. Earth Planet. Sci. Lett. 82, 121-135.

Duda A. and Schmincke H-U., 1985. Polybaric differentiation of alkali basaltic magmas: evidence from green-core clinopyroxenes (Eifel, FRG). Contrib. Mineral. Petrol. 91, 340-353.

Dupre B. and Allegre C.J., 1980. Pb-Sr-Nd isotope correlation and the chemistry on the North Atlantic mantle. Nature 286,17-22.

Dupuy C., Dostal J., Liotard J.M. and Leyreloup A., 1980. Partitioning of transition elements between clinopyroxene and garnet. Earth Planet. Sci. Lett. 48, 303-310.

Dupuy C., Dostal J. and Girod M., 1986. Geochemistry of spinel peridotite inclusions in basalts from Hoggar, Algeria. J. African Earth Sci. 5, 209-215.

Dupuy C., Dostal J. and Bodinier J.L., 1987. Geochemistry of spinel peridotite inclusions in basalts from Sardinia. Mineral. Mag. 51, 561-568.

Ellis D.J. and Green D.H., 1979. An experimental study of the effect of Ca upon garnet-clinopyroxene Fe-Mg exchange equilibria. Contrib. Mineral Petrol. 71, 13-22.

Evensen N.M., Hamilton, P.J. and O'Nions R.K., 1978. Rare-earth abundances in chondritic meteorites. Geochim. Cosmochim. Acta 42, 1199-1212.

Fan S., Wang H. and Yang X., 1983. K-Ar dating of Cenozoic basalts from the area of Tengchong in Yunnan, Hannuoba in Hebei and Datong in Shanxi, China. Annual Reports Institute of Geochemistry, Academia Sinica, Guizhou People's Publishing House. 45-47. (in Chinese with English abstract).

Feng J., 1980. The ultramafic-mafic xenolith accumulation zones in Wanquan, Hebei. Bulletin of Hebei Geological College. No 1, 27-33. (in Chinese).

Feng J. and Han Z., 1982. Inclusions of phlogopite spinel lherzolite discovered in the Hannuoba basalt. Review of Geology. 29, 570-572. (in Chinese with English abstract).

Feng J., Xie M., Zhang H. ang Li W., 1982. Hannuoba basalt and its deep source xenoliths. Bulletin of Hebei Geological college. 1-2, 45-63. (in Chinese).

Feng J., Xie M. and Zheng H., 1986. Geochemical characteristics of rare earth elements in Hannuoba basalts. Bulletin of Hebei Geological College. 9, 217-232. (in Chinese with English abstract).

Fitton J.G.and Dunlop H.M., 1985. The Cameroon line, West Africa, and its bearing on the origin of oceanic and continental alkali basalts. Earth Planet. Sci. Lett. 72, 23-38.

Francis D. and Ludden J., 1988. The mantle source for Quaternary olivine nephelinites, basanites, and transitional alkaline basalts in the northern Canadian Cordillera. EOS 69, 1480P.

Fraser K.J., Hawkesworth C.J., Erlank A.J. and Mitchell R.H., 1985/86. Sr, Nd and Pb isotope and minor element geochemistry of lamproites and kimberlites. Earth Planet. Sci. Lett. 76, 57-70.

Frey F.A., 1980. The origin of pyroxenites and garnet pyroxenites from salt lake crater, Oahu, Hawaii: trace element evidence. Am. Jour. Sci. 280-A, 427-449.

Frey F.A., 1984. Rare earth element abundances in upper mantle rocks. In Rare earth element geochemistry (ed. P.HENDERSON), pp153-203. Elsevier, Amsterdam.

Frey F.A. and Green D.H., 1974. The mineralogy, geochemistry and origin of lherzolite inclusions in Victorian basanites. Geochim. Cosmochim. Acta 38, 1023-1059.

Frey F.A. and Prinz M., 1978. Ultramafic inclusions from San Carlos, Arizona, petrologic and geochemical data bearing on their petrogenesis. Earth Planet. Sci. Lett. 38, 139-176.

Frey F.A. and Roden M.F., 1987. The mantle source for the Hawaiian islands, constraints from the lavas and ultramafic inclusions. In Mantle Metasomatism (eds. M.A.MENZIES and C.J.HAWKESWORTH), pp423-464. Academic Press.

Frey F.A., Green D.H. and Roy S.D., 1978. Integrated models of basalt petrogenesis: A study of quartz tholeiites to olivine melilitites from South Eastern Australia utilizing geochemical and experimental petrological data. J. Petrology. 19, 463-513.

Frey F.A., Suen C.J. and Stockman H.W., 1985. The Ronda high temperature peridotite: Geochemistry and Petrogenesis. Geochim. Cosmochim Acta 49, 2469-2491.

Galer S.J.G. and O'Nions R.K., 1986. Magmagenesis and the mapping of chemical and isotopic variation in the mantle. Chemical Geol. 56, 45-61.

Gan H., 1986. The geochemical studies of the petrogenesis of the Hannuoba basalts. M.S. dissertation (in Chinese).

Gladney E.S. and Roelandts I., 1988. 1987 Compilation of elemental concentration data for USGS BHVO-1, MAG-1, QLO-1, RGM-1, SCo-1, SDC-1, SGR-1 and STM-1. Geostandards Newsletter 12, 253-362.

Govindaraju K., 1984. 1984 Compilation of working values and sample description for 170 international reference samples of mainly silicate rocks and minerals. Geostandards Newsletter, Special Issue, Vol. 8.

Green D.H. and Ringwood A.E., 1967. The genesis of basaltic magma. Contri. Mineral. Petrol. 15, 103-190.

Green D.H. and Hibberson W.O., 1970. Experimental duplication of conditions of precipitation of high-pressure phenocrysts in a basaltic magma. Phys. Earth Planet. Interiors 3, 247-254.

Griffin W.L., O'Reilly S.Y. and Stabel A., 1988. Mantle metasomatism beneath western Victoria, Australia, II: Isotopic geochemistry of Cr-diopside lherzolites and Al-augite pyroxenites. Geochim. Cosmochim Acta 52, 449-460.

Halliday A.N., Stephens W.E., Hunter R.H., Menzies M.A., Dickin, A.P. and Hamilton P.J., 1985. Isotopic and chemical constraints on the building of the deep Scottish lithosphere. Scott. J. Geol. 21, 465-491.

Halliday A.N., Dickin A.P., Fallick A.E. and Fitton J.G., 1988. Mantle dynamics: A Nd, Sr, Pb and O isotopic study of the Cameroon line volcanic chain. J. Petrol. 29, 181-211.

Hamelin B. and Allegre C.J., 1985. Large scale regional units in the depleted upper mantle revealed by an isotopic study of the Southwest Indian Ridge. Nature 315, 196-199.

Hamelin B., Marches G., Albarede F. and Allegre C.J., 1985. Precise lead isotope measurements by the double spike technique: A reconsideration. Geochim. Cosmochim Acta 49, 173-182.

Harris P.G., Reay A. and White I.G., 1967. Chemical composition of the upper mantle. J. Geophys. Res. 72, 6359-6369.

Hart S.R., 1984. A large-scale isotope anomaly in the Southern Hemisphere mantle. Nature. 309, 753-757.

Hart S.R., 1988. Heterogeneous mantle domains: signatures, genesis and mixing chronologies. Earth Planet. Sci. Lett. 90, 273-296.

Hart S.R. and Brooks C., 1977. The geochemistry and evolution of the early Precambrian mantle. Contrib. Mineral. Petrol. 61, 109-128.

Hart S.R. and Davis, K.E., 1978. Nickel partitioning between olivine and silicate melt. Earth Planet. Sci. Lett. 40, 203-219.

Hart S.R. and Allegre C.J., 1980. Trace element constraints on magma genesis. in: R.B. Hargraves (Editor), Physics of magmatic processes. Princeton University Press., 121-139.

Hart S.R., Gerlach D.C. and White W.M. 1986. A possible new Sr-Nd-Pb mantle array and consequences for mantle mixing. Geochemica et Cosmochim. Acta 50, 1551-1557.

Harte B., 1977. Rock nomenclature with particular relation to deformation and recrystallization textures in olivine-bearing xenoliths. J. Geol. 85, 279-288.

Hawkesworth C.J., Rogers N.W., Calsteren P.W.C. and Menaies M.A., 1984. Mantle enrichment processes. Nature 311, 331-335.

Hawkesworth C.J., Mantovani M.S.M., Taylor P.N. and Palacz Z., 1986. Evidence from the Parana of south Brazil for a continental contribution to Dupal basalts. Nature, 322, 356-359.

Henderson P., 1982. Inorganic geochemisty. Oxford, Pergamon Press. 353pp.

Henry D.J. and Medaris L.G., Jr., 1980. Application of pyroxene and olivine-spinel geothermometers to spinel peridotites in southwestern Oregon. Am. Jour. Sci. 280A, 211-231.

Hickey R. and Frey F.A., 1981. Rare-earth element geochemistry of Mariana fore-arc volcanics: Deep-Sea Drilling Project Site 458 and Hole 4596. In Initial Reports of the Deep-Sea Drilling Project (eds. D.M.HUSSONG and S.UYEDA), Vol.60, pp735-741. U.S. Government Printing Office.

Hofmann A.W., Jochum K.P., Seufert M. and White W.M., 1986. Nd and Pb in oceanic basalts: new constraints on mantle evolution. Earth Planet. Sci. Lett. 79, 33-45.

Huang W., Xu J., Gao Z. and Nan J., 1982. Mineralogical study of spinel-lherzolite xenoliths from basalts in southern and eastern China. Acta Mineralogica Sinica. 3, 175-187. (in Chinese with English abstract).

Huppert H.E.and Sparks R.S., 1985. Cooling and contamination of mafic and ultramafic magmas during ascent through continental crust. Earth Planet. Sci. Lett. 74, 371-386.

Ila, P. and Frey, F.A., 1984. Utilization of neutron activation analysis in the study of geologic materials, in use and development of low and medium flux research reactors. In: O.K. Harling, L. Clark and P. von der Hardt (Editors), Suppl. Atomkernenergie Kerntechnik. 44, 710-716.

Irvine T.N. and Baragar W.R.A., 1971. A guide to the chemical classification of the common volcanic rocks. Canadian J. Earth Sci. 8, 523-548.

Irving J.A., 1974. Geochemical and high-pressure experimental studies of garnet pyroxenite and pyroxene granulite xenoliths from the delegate basaltic pipes, Australia. J. Petrol. 15, 1-40.

Irving J.A., 1974. Megacryst from the Newer basalts and other basalts of Southeastern Australia. Geol. Soci. Amer. Bull. 85, 1503-1514.

Irving J.A. and Price C.J., 1981. Geochemistry and evolution of lherzolite-bearing phonolitic lavas from Nigeria, Australia, East Germany and New Zealand. Geochim. Cosmochim. Acta 45, 1309-1320.

Irving J.A. and Frey F.A., 1984. Trace element abundances in megacrysts and their host basalts: Constraints on partition coefficients and megacrysts genesis. Geochem. Cosmochim. Acta 48, 1201-122.

Ito E., White W.M. and Gopel C., 1987. The O, Sr, Nd, and Pb isotope geochemistry of MORB. Chem. Geol. 62, 157-176.

Jagoutz E., Palme H., Baddenhausen H., Blum, K., Cendales M., Dreibus G., Spettel B., Lorenz V. and Wanke H., 1979. The abundances of major, minor and trace elements in the earth's mantle as derived from primitive ultramafic nodules. Proc. 10th Lunar Planet. Sci. Conf. 2, 2031-2050.

Jahn B.M. and Zhang Z.Q., 1984. Archean granulite gneisses from eastern Hebei Province, China: rare earth geochemistry

and tectonic implications. Contrib. Mineral Petrol. 85, 224-243.

Kempton P.D., 1987. Mineralogic and Geochemical evidence for differing styles of metasomatism in spinel lherzolite xenoliths: enriched mantle source of basalts? In Mantle Metasomatism (eds. M.A.Menzies and C.J.Hawkesworth), pp45-90. Academic Press.

Koivula J.I. and Fryer C.W., 1986. The gemological characteristics of Chinese peridot. Gem & Gemology. 22, 38-40.

Kuno H. and Aoki K., 1970. Chemistry of ultramafic nodules and their bearing on the origin of basaltic magmas. Phys. Earth Planet. Interiors 3, 273-301.

Kurat G., Palme H., Spettel B., Baddenhausen H., Hofmeister H., Palme C. and Wanke H., 1980. Geochemistry of ultramafic xenoliths from Kapfenstein, Austria: evidence for a variety of upper mantle processes. Geochim. Cosmochim. Acta 44, 45-60.

Lacroix, M.A., 1928. La composition mineralogique et chimique des rockes eruptives et particulievencent des laves Mesozoique et plus Recentes de la Chine orientale. Bull. Geol. Soc. China. 7 No.1.

Laughlin A.W., Manzer G.K. and Carden J.R., 1974. Feldspar megacrysts in alkali basalts. Geol. Soci. Amer. Bull. 85, 413-416.

Leinbach A.E., 1987. A geochemical study of a layered portion of the Horoman Peridotite, Southern Hokkaido, Japan. M.S. dissertation, Mass. Inst. Tech., 307p.

Li J.L and Cong B.L., 1980. A preliminary research on the origin and evolution of the Bohai Sea. In Formation and development of the North China Fault Block Region. (in Chinese). Institute of Geology, Academia Sinica and National Bureau of Seismology, 206-220.

Liotard J.M., Barsczus H.G., Dupuy C. and Dostal J., 1986. Geochemistry and origin of basaltic lavas from Marquesas Archipelago, French Polynesia. Contrib. Minersal Petrol. 92 260-268.

Liotard J.M., Briot D. and Boivin P., 1988. Petrological and geochemical relationship between pyroxene megacrysts and associated alkali-basalts from Massif Central (France). Contrib. Mineral Petrol. 98, 81-90.

Liu R., Yang M., Xu H., Guo J. and Wang W., 1981. Preliminary study of ultramafic xenoliths from Cenozoic

alkaline basalts in north China. Seismology and Geology. 3, 1-16, 39-48. (in Chinese with English abstract).

Liu R., Sun J. and Chen W., 1983. Cenozoic basalts in North China-their distribution, geochemical characteristics and tectonic implications. Geochemistry 2, 17-33.

Loubet M. and Allegre C.J., 1982. Trace elements in orogenic lherzolites reveal the complex history of the upper mantle. Nature. 298, 809-814.

Loubet M., Shimizu N. and Allegre C.J., 1975. Rare earth elements in Alpine peridotites. Contrib. Mineral. Petrol. 53, 1-12.

Maaloe S., 1982. Geochemical aspects of permeability controlled partial melting and fractional crystallization. Geochim. Cosmochim. Acta 46, 43-57.

Maaloe S. and Aoki, K-I., 1977. The major element composition of the upper mantle estimated from the composition of lherzolites. Contrib. Mineral. Petrol. 63, 161-173.

Macdonald G.A. and Katsura T., 1964. Chemical composition of Hawaiian lavas. J. Petrol. 5, 82-133.

Macdonald G.A. and Powers H.A., 1968. A further contribution to the petrology of Haleakala volcano, Hawaii. Bull. Geol. Soc. Amer. 79, 877-888.

Manhes G., Minster J.-F., and Allegre C.J. 1978. Comparative uranium-thorium-lead and rubidium-strontium study of the St. Severin amphoterite: consequences for early solar system chronology. Earth Planet. Sci. Lett. 39, 14-24.

Mattinson J.M. 1972. Preparation of hydrofluoric, hydrochloric, and nitric acids at ultra-low lead levels. Anal. Chem. 44, 1715-1716.

McDonough W.F. and McCulloch M.T., 1987. The Southeast Australia lithospheric mantle: isotopic and geochemical constraints on its growth and evolution. Earth Planet. Sci. Lett. 86, 327-340.

McDonough W.F., McCulloch M.T. and Sun S.S., 1985. Isotopic and geochemical systematics in Tertiary-Recent basalts from southeastern Australia and implications for the evolution of the sub-continental lithosphere. Geochem. Cosmochim. Acta 49, 2051-2067.

McKenzie D., 1985. The extraction of magma from the crust and mantle. Earth Planet. Sci. Lett. 74, 81-91.

Menzies M.A. and Murthy, V.R., 1980. Mantle metasomatism as a precursor to the genesis of alkaline magmas-isotopic evidence. Am. J. Sci. 280A, 622-638.

Menzies M.A. and Hawkesworth C.J., 1987. Preface, In Mantle Metasomatism (eds. M.A.Menzies and C.J.Hawkesworth) Academic Press.

Menzies M.A., Kempton P. and Dungan M., 1985. Interaction of continental lithosphere and asthenospheric melts below the Geronimo volcanic field, Arizona, U.S.A. J. Petrol. 26, 663-693.

Menzies M.A., Halliday A.N., Palacz Z., Hunter R.H., Upton G.J., Aspen P. and Hawkesworth C.J., 1987. Evidence from mantle xenoliths for an enriched lithospheric keel under the Outer Hebrides. Nature. 325, 44-47.

Morten L., 1987. Italy: a review of xenolithic occurrences and their comparison with Alpine peridotites. In Mantle Xenoliths (ed. P.M.NIXON), pp 135-148. Wiley, London.

Nakamura E., 1986. The geochronology and geochemistry of Cenozoic alkaline basalts from Japan, Korea and China. Univ. Toronto, Ph.D. dissertation.

Nakamura E., Campbell H.I. and Sun S.S., 1985. The influence of subduction processes on the geochemistry of Japanese alkaline basalts. Nature. 316, 55-58.

Navon O. and Stolper E., 1987. Geochemical Consequences of melt percolation: The upper mantle as a chromatographic column. Jour. Geol. 95, 285-307.

Newsom H.E., White W.M., Jochun K.P. and Hofmann A.W., 1986. Siderophile and chalcophile element abundances in oceanic basalts, Pb isotope evolution and growth of the Earth's core. Earth Planet. Sci. Lett. 80, 299-313.

Nickel K.G. and Green, D.H., 1984. The nature of the upper-most mantle beneath Victoria, Australia as deduced from ultramafic xenoliths. In Kimberlites II: The Mantle and Crust-Mantle Relationship (ed. J.KORNPROBST), pp161-178. Elsevier. Sci. Publ.

Nicolas A., 1986. A melt extraction model based on structural studies in mantle peridotites. J. Petrol. 27, 999-1022.

Nicolas A., Lucazeau F. and Bayer R., 1987. Peridotite xenoliths in Massif central basalts: Textural and geophysical evidence for asthenospheric diapirism. In Mantle Xenoliths (ed. P.M.NIXON), pp563-574. J. Wiley Publ.

Nielson J.E. and Noller J.S., 1987. Processes of mantle metasomatism: Constraints from observation of composite peridotite xenoliths. In Mantle Metasomatism and Alkaline Magmatism (eds. E.M.MORRIS and J.D. PASTERIS), pp 61-76. Geol. Society of America, Inc Publ.

Noller J.S., 1986. Solid and fluid inclusions in mantle xenoliths: An analytical dilemma? Geology. 14, 437-440.

Norry M.J., Truckle P.H., Lippard S.J., Hawkesworth S.D.W and Marriner G.F., 1980. Isotopic and trace element evidence from lavas bearing on mantle heterogeneity beneath Kenya. R. Soc. London Philos. Trans., Ser. A 297, 259-271.

O'Hara M.J., 1968. The bearing of phase equilibria studies on the origin and evolution of basic and ultrabasic rocks. Earth Sci. Rev. 4, 69-133.

O'Hara M.J., 1985. Importance of the "shape" of the melting regime during partial melting of the mantle. Nature. 314, 58-62.

O'Hara M.J., Saunders M.J. and Mercy E.L.P., 1975. Garnet-peridotite, primary ultrabasic magma and eclogite: Interpretation of upper mantle processes in kimberlite. Physics Chemistry Earth 9, 571-604.

O'Hara M.J. and Yoder, H.S., 1967. Formation and fractionation of basic magmas at high pressures. Scott. J. Geol. 3, 67-117.

O'Reilly S.Y. and Griffin W.L., 1988. Mantle metasomatism beneath western Victoria, Australia: I. Metasomatic processes in Cr-diopside lherzolites. Geochim. Cosmochim Acta 52, 433-448.

Obata M. and Nagahara N., 1987. Layering of alpine-type peridotite and the segregation of partial melt in the upper mantle. J. Geophys. Res. 92, 3467-3474.

Othman D.B., Polve M. and Allegre C.J., 1984. Nd-Sr isotopic composition of granulites and constraints on the evolution of the lower continental crust. Nature 307, 510-515.

Ottonello G., 1980. Rare earth abundances and distribution in some spinel peridotite xenoliths from Assab (Ethiopia). Geochim. Cosmochim. Acta 44, 1885-1901.

Ottonello G., Joron J.L. and Piccardo B.G., 1984. Rare Earth and 3d transition element geochemistry of peridotitic rocks: II. Ligurian peridotites and associated basalts. J. Petrol. 25, 373-393.

Pagram W.J., 1986. The isotope, trace element, and major element geochemistry of the Mesozoic Appalachian tholeiitic province. Ph.D dissertation, Mass. Inst. Tech., 622p.

Palacz Z.A. and Saunders, A.D., 1986. Coupled trace element and isotope enrichment in the Cook-Austral-Samoa islands, southwest Pacific. Earth Planet. Sci. Letter. 79, 270-280.

Palme H. and Nickel K.G., 1985. Ca/Al ratio and composition of the Earth's upper mantle. Geochim. Cosmochim Acta 49, 2123-2132.

Peng Z.C., Zartman R.E., Futa K. and Chen D.G., 1986. Pb-, Sr- and Nd-isotopic systematics and chemical characteristics of Cenozoic basalts, Eastern China. Chemical Geol. 59, 3-33.

Perry F.V., Balaridge W.S. and Depaolo D.J., 1987. Role of asthenosphere and lithosphere in the genesis of Late Cenozoic basaltic rocks from the Rio Grande Rift and adjacent regions of the southwestern United States. J. Geophys. Res. 92, 9193-9213.

Perry F.V., Balaridge W.S. and Depaolo D.J., 1988. Chemical and isotopic evidence for lithospheric thinning beneath the Rio Grande rift. Nature 332, 432-434.

Preß S., Witt G., Seck H.A., Ionov D. and Kovalenko V.I., 1986. Spinel peridotite xenoliths from the Tariat Depression/Mongolia. I: Major element chemistry and mineralogy of a primitive mantle xenolith suite. Geochim. Cosmochim. Acta 50, 2587-2599.

Prinzhofer A. and Allegre C.J., 1985. Residual peridotitea and the mechanism of partial melting. Earth Planet. Sci. Lett. 74, 251-265.

Raheim A. and Green D.H., 1974. Experimental determination of the temperature and pressure dependence of the Fe-Mg partition coefficient for coexisting garnet and clinopyroxene. Contrib. Mineral Petrol. 48, 179-203.

Rhodes, J.M., 1983. Mantle heterogeneity associated with the Hawaiian melting anomaly: Evidence from Mauna Loa lavas. Eos. Trans. AGU. 64, 348.

Richard P., Shimizu N., and Allegre C.J. 1976. $^{143}Nd/^{144}Nd$, a natural tracer: an application to oceanic basalts. Earth Planet. Sci. Lett. 31, 269-278.

Richardson S.H., Erlank A.J., Duncan A.R. and Reid D.L., 1982. Correlated Nd, Sr and Pb isotope variation in Walvis Ridge basalts and implication for the evolution of their mantle source. Earth Planet. Sci. Lett. 59, 327-342.

Richter F.M., 1986. Simple models for trace element fractionation during melt segregation. Earth Planet. Sci. Lett. 77, 333-344.

Roden M.F., Frey F.A. and Francis D.M., 1984. An example of consequent mantle metasomatism in peridotite inclusions from Nunivak Island, Alaska. J. Petrol. 25, 546-577.

Roden M.F., Irving A.J. and Murthy V. R., 1988. Isotopic and trace element composition of the upper mantle beneath a young continental rift, Results from Kilbourne Hole, New Mexico. Geochim. Cosmochim. Acta 52, 461-474.

Roex A.P., Dick H.J.B. and Fisher R.L., 1988. Petrology and geochemistry of MORB from 25°E to 46°E along the southwest Indian Ridge: Evidence for contrasting styles of mantle enrichment. J. Petrol. in press.

Rutter M.J., 1987. Evidence for crustal assimilation by turbulently convecting, mafic alkaline magmas: Geochemistry of mantle xenolith-bearing lavas from Northern Sardinia. J. Volcanology Geothermal Res. 32. 343-354.

Sato H., 1977. Nickel content of basaltic magmas: identification of primary magmas and a measure of the degree of olivine fractionation. Lithos 10, 113-120.

Schneider M.E. and Eggler D.H., 1984. Compositions of fluid in equilibrium with peridotites: Implications for alkaline magmatism-metasomatism. In Kimberlites and Related Rocks (ed. J.Kornprobst), pp383-394. Amsterdam, Elsevier.

Schulze D.J., 1987. Megacrysts from alkalic volcanic rocks. In Mantle Xenolith. (ed. P.M. Nixon), pp433-451. Wiley, London.

Schwarzer R.R. and Rogers J.J.W., 1974. A worldwide comparison of differentiation trends. Earth Planet. Sci. Lett. 23, 286-296.

Smith D., 1977. The origin and interpretation of spinel-pyroxene clusters in peridotite. J. Geol. 85, 476-482.

Song Y., 1983. The geochemistry of selected Cenozoic basalts of Northeastern China. M.S. dissertation, Boston College. 182p

Song Y. and Frey F.A., 1989. Geochemistry of peridotites in basalt from Hannuoba, Eastern China: Implications for subcontinental mantle heterogeneity. Geochim. Cosmichim. Acta 53, 97-113.

Song Y., Frey F.A. and Zhi X., 1987. Geochemistry of basalts and peridotite xenoliths from Hannuoba Region, Eastern

China: Implication for Subcontinental Mantle Heterogeneity. (abstr.) EOS. 68, 1547.

Sparks R.S.J., Pinkerton H. and MacDonald R., 1977. The transport of xenoliths in magmas. Earth Planet. Sci. Lett. 35, 234-238.

Spera F.J., 1984. Carbon dioxide in petrogenesis III: role of volatiles in the ascent of alkaline magma with special reference to xenolith-bearing mafic lavas. Contrib. Min. Petrol. 88, 217-232.

Spera F.J., 1987. Dynamics of translithospheric migration of metasomatic fluid and alkaline magma. In Mantle Metasomatism (eds. M.A.MENZIES and C.J.HAWKESWORTH), pp1-20. Academic Press.

Stosch H.-G. and Seck H.A., 1980. Geochemistry and mineralogy of two spinel peridotite suites from Dreiser Weiher, West Germany. Geochim. Cosmichim. Acta 44, 457-470.

Stosch H.-G. and Lugmair G.W., 1986. Trace element and Sr and Nd isotope geochemistry of peridotite xenoliths from the Eifel (West Germany) and their bearing on the evolution of the subcontinental lithosphere. Earth Planet. Sci. Lett. 80, 281-298.

Stosch H.-G., Carlson R.W. and Lugmair G.W., 1980. Episodic mantle differentiation: Nd and Sr isotopic evidence. Earth Planet. Sci. Lett. 47, 263-271.

Stosch H.-G. Lugmair G.W. and Kovalenko V.I., 1986. Spinel peridotite xenoliths from the Tariat Depression, Mongolia. II: geochemistry and Nd and Sr isotopic composition and their implication for the evolution of the subcontinental lithosphere. Geochim. Cosmochim. Acta 50, 2601-2614.

Stucklee J.S. and Irvin J.A., 1976. Strontium isotope geochemistry of megacrysts and host basalts from southeastern Australia. Cosmochim. Acta 40, 209-213.

Suen C.J. and Frey F.A., 1987. Origins of the mafic and ultramafic rocks in the Ronda peridotite. Earth planet. Sci. Lett. 85, 183-202.

Sun S.-S. and McCullough F.M., 1988. Chemical and isotopic systematics of oceanic basalts: implications for mantle composition and processes. In: Magmatism in Ocean Basins (eds. A.D. SAUNDERS and M.J. NORRY).

Sun S.-S., McDonough W.F. and Ewart A., 1989. Four-component dynamic model for East-Australian basalts. In Intraplate Volcanism in Eastern Australia and New Zealand. (eds. R.W. JOHNSON and S.R. TAYLOR). Australian Academy Sci., in press.

Taylor S.R. and McLennan S.M., 1985. The continental crust: Its composition and evolution. (ed. A. HALLAM). Blackwell Sci. Publication. 312pp.

Thirlwall M.F. and Jones N.W., 1983. Isotope geochemistry and contamination mechanisms of Tertiary lavas from Skye, Northwest Scotland. In Continental Basalts and Mantle Xenoliths. (ed. C.J. Hawkesworth). Shiva Geol Ser, pp 186-208.

Thompson R.N., 1974. Some high-pressure pyroxenes. Mineral Mag. 39, 768-787.

Thompson R.N., Morrison M.A., Dickin A.P. and Hendry G.L., 1983. Continental flood basalts... Arachnids Rule OK? In: Continental basalts and mantle xenoliths, (eds C.J. HAWKESWORTH and M.J. NORRY), 158-185.

Thompson R.N., Morrison M.A., Hendry G.L. and Parry S.J., 1984. An assessment of the relative roles of crust and mantle in magma genesis: an elemental approach. Philosophical Transactions of the Royal Society of London. 310. 549-590.

Todt W., Dupre B. and Hofmann A.W., 1983. Pb isotope measurements using a multicollection: application to standard and basalts. Terra Cognita. 3.

Toramaru A. and Fujii N., 1986. Connectivity of melt phase in a partially molten peridotite. J. Geophys. Res. 91, 9239-9252.

Wang H., Dai T., Hong A., Fan S. and Yang X., 1982. K-Ar dating of Hannuoba basalts, Zhangjiakou. Proceeding (Abstract) of 2nd National Symposium of Isotope Geochemistry. Committee of Isotope Geochemistry, Mineralogy, Petrology and Geochemistry Society of China, 481-483. (in Chinese).

Wang Y., Xiao Z., and Zhao D., 1983. Garnet megacrysts in the Cenozoic basaltic rocks from Jiangsu-Anhui-Shandong Provinces. Petrol. Research 3, 89-94. (in Chinese with English abstract).

Watson E.B., 1979. Calcium content of forsterite coexisting with silicate liquid in the system Na_2O-CaO-MgO-Al_2O_3-SiO_2. Am. Mineral. 58, 998-1008.

Weaver B.L., Wood D.A., Tarney J. and Joron J.L., 1986. Role of subducted sediment in the genesis of ocean-island basalts: Geochemical evidence from South Atlantic Ocean islands. Geology. 14, 275-278.

Wedepohl K.H., 1985. Origin of the Tertiary basaltic volcanism in the northern Hessian Depression. Contrib. Mineral Petrol. 89, 122-143.

Wells P.R.A., 1977. Pyroxene thermometry in simple and complex systems. Contrib. Mineral. Petrol. 62, 129-139.

Wright T.L., 1971. Chemistry of Kilauea and Mauna Loa lava in space and time. U.S. Geol. Surv. Prf. Paper, p735.

White W.A. and Hofmann A.W., 1982. Sr and Nd isotope geochemistry of oceanic basalt and mantle evolution. Nature. 196, 821-825.

Wilshire H.G., 1987. A model of mantle metasomatism. In Mantle Metasomatism and Alkaline Magmatism (eds. E.M.MORRIS and J.D. PASTERIS), pp 47-60. Geol. Society of America, Inc Publ.

Worner G., Staudigel H. and Zindler A., 1985. Isotopic constraints on open system evolution of the Laacher See magma chamber (Eifel, W-Germany.. Earth Planet. Sci. Lett. 75, 37-49.

Worner G., Zindler A., Staudigel H. and Schmincke H., 1986. Sr, Nd, and Pb isotope geochemistry of Tertiary and Quaternary alkaline volcanics from West Germany. Earth Planet. Sci. Lett. 79, 107-119.

Wood B.J. and Banno S., 1973. Garnet-orthopyroxene and orthopyroxene-clinopyroxene relationships in simple and complex systems. Contrib. Mineral Petrol. 42, 109-124.

Wright T.L., and Doherty P.C., 1970. A linear programming and least-squares method for solving petrologic mixing problems. Geol. Soc. Amer. Bull. 81,1995-2008.

Yoder H.S. and Tilley C.E. 1962. Origin of basalt magmas: an experimental study of natural and synthetic rock system. J. Petrol. 3, 342-532.

Zartman R.E. and Doe B.R. 1981. Plumbotectonics-the model. Tectonophys. 75, 135-162.

Zartman R.E. and Haines S.M. 1988. The plumbotectonic model for Pb isotopic systematics among major terrestrial reservoirs-A case for bi-directional transport. Geochem. Cosmochim. Acta 52, 1327-1339.

Zhai M., 1983. The genesis and evolution of Hannuoba basalts, Hebei province. (In proceeding of M.S. dissertation of IGAS of 1981, IGAS eds.), 250-256. Beijing Science and Technology Press, Beijing. (in Chinese).

Zhai M., 1984. The study of plagioclases of Hannuoba basalt in Hebei province. Petrological Research. 4, 57-66. (in Chinese with English abstract).

Zhan R. and Cong B., 1984. Mineralogy of peridotitic inclusions, xenocrysts and megacrysts in basaltic rocks from Silong, Qu County, Zhejiang Province. Scientia Geol. Sinica 1, 58-71. (in Chinese with English abstract).

Zhang Q.W. and Huang H.Z., 1982. The evolution of magmato-tectonic activation of the Meso-Cenozoic Era in eastern China. Acta Geol. Sinica. 56, 111-122. (in Chinese).

Zhao R., 1983. Study of the megacrysts in Hannuoba basalts. M.S. dissertation (in Chinese).

Zheng X., 1980. Some problems on basalts and their ultramafic xenoliths in the North China Fault Block. Institite of Geology, Academica Sinica, Chinese Science Press, 335-347. (in Chinese).

Zhi X., Song Y., Frey F.A., Feng J. and Zhai M., 1989. Geochemistry of Hannuoba basalts, Eastern China: constraints on the origin of continental alkali and tholeiitic basalt. Submitted to Chemical Geol.

Zhi X. and Frey F.A., 1986. Geochemistry of ultramafic inclusion-bearing basalts from Hannuoba (Eastern China). Implication for their mantle source. EOS. 67, 390.

Zhou X. and Armstrong R.L., 1982. Cenozoic volcanic rocks of eastern China-secular and geographic trends in chemistry and strontium isotopic composition. Earth Planet. Sci. Lett. 58, 301-329.

Zhou X. and Carlson R.W., 1982. Isotopic evidence for temporal variability of mantle characteristics beneath the North China Fault Block. Carnegie Institution Annual Report. Dep. Terrestrial Magnetism. 81, 505-508.

Zhou X. and O'Nions R.K., 1986. Pb-Nd-Sr systematics of xenoliths from E. China. (Abstr). TERRA Cognita. 6, 244.

Zindler A. 1980. Geochemical processes in the earth's mantle and the nature of crust-mantle interactions: Evidence from studies of Nd and Sr isotope ratios in mantle-derived igneous rocks and lherzolite nodules. Ph.D. dissertation, Mass. Inst. Tech., 263p

Zindler A. and Hart S.R., 1986. Chemical geodynamics. Ann. Rev. Earth Planet. Sci. 14, 493-571.

Zindler A. and Jagoutz E., 1988. Mantle cryptology. Geochim. Cosmochim. Acta 52, 319-333.

Zindler A., Hart S.R., Frey F.A. and Jakobsson S.P., 1979. Nd and Sr isotope ratios and REE abundances in Reykjanes Peninsula basalts, Evidence for mantle heterogeneity beneath Iceland. Earth Planet. Sci. Lett. 45, 249-262.

Zindler A., Jagoutz E. and Goldstein S., 1982. Nd, Sr and Pb isotopic systematics in a three-component mantle: a new perspective. Nature 298, 519-523.

Zindler A., Staudigel H., Hart S.R., Endres R. and Goldstein S., 1983. Nd and Sr isotopic study of a mafic layer from Ronda ultramafic complex. Nature. 304, 226-230.

Zindler A., Staudigel H. and Batiza R., 1984. Isotope and trace element geochemistry of young Pacific seamounts: Implications for the scale of upper mantle heterogeneity. Earth Planet. Sci. Lett. 70, 175-195.

Zindler A. and Hart S.R., 1986. Chemical geodynamics. Ann. Rev. Earth Planet. Sci. 14, 493-571.

APPENDIX

A-1. Classification and Nomenclature

Hannuoba basalts could be classified into four groups simply based on CIPW normative compositions: the basanite, alkali olivine (Ol) basalt, olivine tholeiite and quartz (Qtz) tholeiite. The nomenclature adopted here is the one based on the chemical classification of Irvine and Baragar (1971). In a Ne-Ol-Cpx-Opx-Qtz tetrahedral diagram (Fig. 1-3; Yoder and Tilley, 1962) of Hannuoba basalts:

1) all ultramafic xenolith-bearing basalts are fallen on a limited area, where it has almost consistent relative norm of clinopyroxene (Cpx) of 40% (ranging of 30-45%) and variable relative norm of olivine and nepheline (Ne), ranging of 25-55% and 0.6-40% respectively.

2) Most of quartz tholeiites and olivine tholeiites are concentrated near the Cpx-Opx division line within a limited area in Fig. 1-3. For quartz tholeiite, the relative norm of Qtz of most of them is less than 5%, except one sample (Bai-13) with that of 10%; the relative norm of orthopyroxene (Opx) is 55-70%, and the relative norm of clinopyroxene is 30-40%, except one sample (Bai-8) with that of 25%. For olivine tholeiite, the relative norm of Ol of most of them is less than 15%, except one sample (Bai-15) with that of 19%; the relative norm of Opx is 40-65%; and the relative

norm of clinopyroxene is 30-45%, except one sample (Zh-21) with that of 50%.

3) In addition to these two limited areas, there are five samples in Ne-Ol-Cpx triangular diagram with relative norm of clinopyroxene of more than 45%, even up to 60% (Bai-24), and there are six samples in Ol-Cpx-Opx triangular diagram with relative norm of Ol of more than 25%, even up to 47% (Bai-20), and relative norm of Opx of less than 35% even down to 12% (B-20), except one sample (Bai-21) up to 40%. Most of these samples usually have different major and trace element geochemical characteristics from that in both limited area.

Therefore, in this thesis, the term alkaline basalt is used for ultramafic xenolith-bearing basalts including basanite and alkali olivine basalt (Fig. 1-3, alkali basalt-area), the term tholeiite or subalkali basalt is used for the sample fallen into the area indicated tholeiites (Fig. 1-3), and the term transitional basalt is used for other eleven samples where are beyond these two areas (Fig. 1-3).

A-2. Analytical Techniques

XRF ANALYSES

Major Element Analyses:

Ignited whole-rock powders were fused within a Pt-Au crucible in an oven, and pressed into glass disks. Duplicated disks were made and analyzed for each samples by X-ray fluorescence at the University of Massachusetts (Rhodes, 1983). The averages of these two measurement are reported in Table 1-1 and Table 4-1 as final results. BHVO-1 was included as a standard in each run of four samples. The relative deviation based on 13 replicated BHVO-1 analysis is reported in Table 1-3.

Trace Element Analysis:

Whole-rock powders were pressed to pellet disks with boric acid. Duplicated disks were made and analyzed for each samples. The elements V, Ni, Zn, Ba, Zr, Nb and Sr were determined by XRF (Au tube), and the elements Rb, Sr, Ga and Y were determined by XRF (Mo tube). The averages of two measurement for each sample are reported in Table 4-2 and Table 4-5. (The Sr values determined by Mo tube and Au tube XRF analysis are very close, and the Sr values from Mo tube analysis are arbitrarily reported.) BHVO-1 was included as a standard in each run. The relative deviation based on 13 or 14 replicated BHVO-1 analysis is reported in Table 1-3.

INAA ANALYSES

Sc, Cr, Co and Hf of all samples (basalts and xenoliths), and REE, Ta and Th of basalts were determined by INAA. Neutron activation Cr data are reported here rather than XRF data. In addition to synthetic standards, MkCore was included in each set of analyses by INAA in order to evaluate analytical precisions (Table 1-3).

RNAA ANALYSES

To obtain accurate data for peridotite xenoliths with very low REE concentration, REE abundances of Hannuoba peridotites were determined by radiochemical neutron activation analysis (RNAA) in F. Frey's laboratory at MIT. The RNAA procedure adopted was that developed by Hickey and Chen, and is described in Hickey and Frey (1981). The author and A. Leinbach have co-worked for the peridotites from Horoman, Japan and Hannuoba, China using RNAA method. See Leinbach (1987) for detailed description of the RNAA techniques.

The smooth nature of the REE patterns is a rough indication that the data is of good quality. Five REE elements (La, Sm, Eu, Yb and Lu) are high quality data with relative accuracy of ~3% and relative precision based on the duplicate analyses of peridotite 62210 of less than 10%[7]. The Ce, Nd and Tb data are poorer quality. The real

7. Relative precision based on mean and standard deviation from five repeat analyses of Horoman peridotite 62210 which were analyzed during the same RNAA procedures as the Hannuoba peridotites (Table 4-6).

precision is difficult to quantify, and is not extremely useful without more duplicate analyses. However, the accuracy of individual measurements could be approached by comparing data from different analytical techniques. Isotope dilution (ID) technique generally has greater accuracy than RNAA. The Nd and Sm abundances of the six Hannuoba peridotites have been measured by ID (Table 4-8), and REE abundances of two bulk peridotites (DM1-2 and DM1-7) have been measured by ID (Table 4-6). The relative deviations of REE abundances determined by RNAA and isotope dilution are listed in (Table 4-6).

ISOTOPIC ANALYSES

Sr and Nd Isotopes:

The Rb, Sr, Sm and Nd concentrations in xenoliths (whole rock and Cpx) were measured using isotope dilution (ID) techniques. Two mixed spike solutions were used: the MSEIII contained K, Rb, Cs, Sr and Ba, and the NdSmI contained Sm and Nd. The MSEI and SmNd II was used for garnet megacryst.

The alkali metals, Sr, REE and Ba were separated by a cation exchange (AG-50W-X8 resin) procedure described by Hart and Brooks (1977). A quartz column was used for xenoliths in this separation. Sm and Nd were separated in two steps using the technique adapted from Richard et al (1976) and Zindler (1980). The REE were firstly separated as

a group on a cation column (AG-50W-X8 resin) between Sr and Ba. Then Sm and Nd were separated using a reverse-phase chromatography, a column of teflon powder and HDEHP (Di(2-ethylhexyl) orthophosphoric acid). Due to the low concentration of Nd in mantle xenoliths, where samples greater than 60 mg were dissolved, the samples were split and run through two or more columns in the first step, then the REE elutions would be recombined before the second step.

Sr was loaded in mixed 0.1N HNO_3 and TAHFPH onto single W filaments. The alkali metals were loaded in 2-bottle water onto single Ta filaments. Nd and Sm were loaded with 1:1 0.1N phosphoric acid and 2.5N hydrochloric acid onto Ta side filament of a double filament assembly (center filament is Re).

The isotopic compositions and the concentrations of Sr and Nd were measured by NIMA-B, a computer-controlled, 9 inch, 60^{o} mass spectrometer designed and built by S.R. Hart and K. Burrhus.

Six procedural blanks run during xenolith (whole rock and Cpx) analyses, resulting in average of 0.1 ng for Sr and 0.05 ng for Nd, well below the level of significance.

Pb isotope:

500-1000 mg of basaltic powders were dissolved for Pb isotope analyses. The chemical procedures for separation of Pb were described by Manhes et al (1978) and Pegram (1986) using anion exchange chromatography (AG-1-X8 resin in bromide form).

Pb was loaded in phosphoric acid onto a single Re filament which was coated by silica gel on center of the filament. The detailed loading and flashing procedures were described by Pegram (1986). The isotopic compositions and the concentrations of Pb were run on TIMA, a 60 °, 12 " r.o.c. mass spectrometer.

All acids used in dissolution and column work for xenoliths and Pb isotopes were distilled in teflon according to the subboiling 2-bottle techniques (Mattinson, 1972).